Advances in biophysical methods for protein detection and characterisation

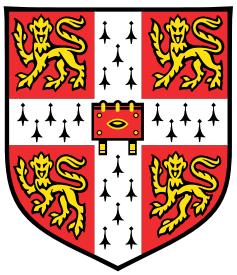

Quentin Alexis Eric Peter

Department of Chemistry
University of Cambridge

This dissertation is submitted for the degree of
Doctor of Philosophy

Queens' College August 2021

I would like to dedicate this thesis to Marie-Hélène and my loving parents Nathalie and Clarence.

Declaration

I hereby declare that except where specific reference is made to the work of others, the contents of this thesis are original and have not been submitted in whole or in part for consideration for any other degree or qualification in this, or any other university. This thesis is my own work and contains nothing which is the outcome of work done in collaboration with others, except as specified in the text and Acknowledgements. This thesis contains fewer than 60,000 words as prescribed for the Department of Chemistry Degree Committee.

Quentin Alexis Eric Peter
August 2021

Acknowledgements

I would like to thank Professor Tuomas Knowles for giving me the chance to work in such an interesting and interdisciplinary environment. His support and scientific insights are of incommensurable value to me. I have been fortunate enough to learn about a wide variety of subjects while working under his lead. It has been a pleasure to work with many fellow researchers who shared their knowledge and invaluable advices with me. I would like to thank the entire Knowles group and the researchers of the Center for Misfolding Diseases of the University of Cambridge for welcoming me and making me feel at home during all these years. My family and friends showed indefectible support over the years. I couldn't be more thankful to them. I want to particularly acknowledge my love Marie-Hélène, as well as my parents, Nathalie and Clarence, for always being there for me.

Of course, it all would not have been possible without the support of the European Union's Horizon 2020 research and innovation programme Marie Skłodowska-Curie actions, which financed the NANOTRANS Innovative Training Networks under ETN grant 674979-NANOTRANS. It gave me the opportunity to live in the United Kingdom and experience the local culture and way of life, in addition to providing me with invaluable education in this interdisciplinary research topic.

The research presented here has received funding from the European Research Council under the European Union's Seventh Framework Programme (FP7/2007-2013) through the ERC grant PhysProt (agreement n° 337969). The work presented in the chapter *Scalable integration of nano-, and microfluidics with hybrid two-photon lithography* was supported by the Engineering and Physical Sciences Research Council [grant number EP/L015889/1], the European research Council, the Winton Programme for the Physics of Sustainability and the Newman Foundation. NanoDTC and the ERC Consolidator Grant (DesignerPores 647144) are acknowledged for additional funding. Moreover, the Maxwell Community is acknowledged for scientific support. Finally, insightful discussions with Professor Daan Frenkel are acknowledged for the chapter *Microscale diffusiophoresis of proteins*.

Abstract

Proteins are the building blocs of life and mediate nearly every function in the cell. They are therefore a major and incredibly wide research topic. Their functions and malfunctions have serious impacts on a wide range of diseases. Proteins may be used as extremely versatile tools for biology such as for gene editing or biological medical products. Developing novel methods for protein detection and characterisation may thus have a tremendous impact on modern medicine and research. The present thesis discusses advances in biophysical methods for protein detection and characterisation. First, the possibility of detecting proteins label-free is addressed. A label may change the behaviour of the target protein. Two approaches are investigated: An ultraviolet light based autofluorescence microscope is described; and scattering based detection is explored by expending on the existing interferometric scattering (iSCAT) technique. An oblique illumination approach helps with increasing the contrast of the data, and a time correlation technique is used for local sizing on chip. Second, microfluidic techniques are routinely used to create protein assays. These assays minimise the amount of sample required and the absence of turbulences enable new techniques. A method to easily add nanofluidics elements to microfluidic designs is discussed. Finally, three characterisation methods are described. First, diffusional sizing uses a microfluidic chip to create a concentration gradient. The protein diffusion coefficient is extracted from the time evolution of this gradient. Second, the diffusiophoretic coefficient of the protein can be extracted by diffusiophoresis, which is the motion of proteins driven by the concentration gradient of another solute. This could be an important protein motion mechanism, as many gradients are present in cells and in living beings. Finally, the spatial propagation of the protein amyloid-beta 1-42, a protein associated to neurodegenerative disorders, is observed in a capillary.

Publications

This thesis is based on the following papers and manuscripts:

1. Pavan Kumar Challa*, **Quentin A. E. Peter***, Maya A. Wright, Yuewen Zhang, Kadi L. Saar, Jacqueline A. Carozza, Justin L.P. Benesch & Tuomas P. J. Knowles. "Real-time intrinsic fluorescence visualization and sizing of proteins and protein complexes in microfluidic devices". Analytical Chemistry 90.6 (2018): 3849-3855 (* contributed equally) [53].

2. **Quentin A. E. Peter***, Pavan Kumar Challa*, Zenon Toprakcioglu*, Kadi Liis Saar, Jeremy J. Baumberg & Tuomas P. J. Knowles. "Oblique illumination interferometric scattering". Manuscript in preparation (* contributed equally).

3. **Quentin A. E. Peter***, Raphael Jacquat*, Georg Krainer* & Tuomas P. J. Knowles. "Interferometric scattering correlation (iSCORR) microscopy". Manuscript in preparation (* contributed equally).

4. Oliver Vanderpoorten*, **Quentin A. E. Peter***, Pavan K. Challa*, Ulrich F. Keyser, Jeremy Baumberg, Clemens F. Kaminski & Tuomas J. P. Knowles. (2019). "Scalable integration of nano-, and microfluidics with hybrid two-photon lithography". Microsystems & Nanoengineering, 5(1), 1-9 (* contributed equally) [261].

5. **Quentin A. E. Peter**, Kadi Liis Saar, Therese W. Herling, Thomas Mueller & Tuomas P. J. Knowles. "Fast numerical integration of diffusional sizing basis functions". Manuscript in preparation.

6. **Quentin A. E. Peter***, Raphael P. B. Jacquat*, Therese W. Herling, Pavan Kumar Challa, Tadas Kartanas & Tuomas P. J. Knowles. "Microscale diffusiophoresis of proteins". Manuscript in preparation (* contributed equally).

7. **Quentin A. E. Peter***, Chris Taylor*, Urszula Łapińska*, Thomas Michaels, Paolo Arosio, Sara Linse & Tuomas P. J. Knowles. "Prion-like spatial transmission of

the Alzheimer's amyloid beta peptide by oligomers". Manuscript in preparation (* contributed equally).

In addition to the projects described in this thesis, I had the chance to collaborate with numerous talented researchers durning my PhD at the University of Cambridge. Here is a list of papers that resulted from these collaborations:

1. Francesco Simone Ruggeri, Jerome Charmet, Tadas Kartanas, **Quentin A. E. Peter**, Sean Chia, Johnny Habchi, Christopher M. Dobson, Michele Vendruscolo, and Tuomas P. J. Knowles. "Microfluidic deposition for resolving single-molecule protein architecture and heterogeneity". Nature Communications, 9(1):1–12, 2018. [222]

2. Christian Bortolini, Tadas Kartanas, Davor Copic, Itzel Condado Morales, Yuewen Zhang, Pavan K. Challa, **Quentin A. E. Peter**, Tamás Jávorfi, Rohanah Hussain, Mingdong Dong, Giuliano Siligardi, Tuomas P. J. Knowles & Jérôme Charmet. "Resolving protein mixtures using microfluidic diffusional sizing combined with synchrotron radiation circular dichroism". Lab on a Chip, 19(1):50–58, 2019. [40]

3. Kadi L Saar, **Quentin A. E. Peter**, Thomas Müller, Pavan K. Challa, Therese W. Herling, and Tuomas P. J. Knowles. "Rapid two-dimensional characterisation of proteins in solution". Microsystems & Nanoengineering, 5(1):1–10, 2019. [226]

4. Philip R Lindstedt, Francesco A Aprile, Maria J. Matos, Michele Perni, Jean B. Bertoldo, Barbara Bernardim, **Quentin A. E. Peter**, Gonzalo Jiménez-Osés, Tuomas P. J. Knowles, Christopher M. Dobson, Francisco Corzana, Michele Vendruscolo, and Gonçalo J. L. Bernardes. "Enhancement of the anti-aggregation activity of a molecular chaperone using a rationally designed post-translational modification". ACS central science, 5(8): 1417–1424, 2019. [166]

5. Yuewen Zhang, Therese W Herling, Stefan Kreida, **Quentin A. E. Peter**, Tadas Kartanas, Susanna Törnroth-Horsefield, Sara Linse, and Tuomas P. J. Knowles. "A microfluidic strategy for the detection of membrane protein interactions". Lab on a Chip, 20(17):3230–3238, 2020. [284]

6. Tom Scheidt, Tadas Kartanas, **Quentin A. E. Peter**, Matthias M Schneider, Kadi L. Saar, Thomas Müller, Pavan Kumar Challa, Aviad Levin, Sean Devenish, and Tuomas P. J. Knowles. "Multidimensional protein characterisation using microfluidic post-column analysis". Lab on a Chip, 20(15): 2663–2673, 2020. [234]

7. Mandy Koopman, **Quentin A. E. Peter**, Renée I. Seinstra, Michele Perni, Michele Vendruscolo, Christopher M. Dobson, Tuomas P. J. Knowles, and Ellen A. A. Nollen. "Assessing motor-related phenotypes of Caenorhabditis elegans with the wide field-of-view nematode tracking platform". Nature Protocols, 15 (6):2071–2106, 2020. [150]

8. William E. Arter, Yuriy Yusim, **Quentin A. E. Peter**, Christopher G. Taylor, David Klenerman, Ulrich F. Keyser & Tuomas P. J. Knowles. "Digital Sensing and Molecular Computation by an Enzyme-Free DNA Circuit". ACS nano, 14(5):5763–5771, 2020. [20]

9. Kimberley L. Callaghan, **Quentin A. E. Peter**, Janet R. Kumita, Tuomas P. J. Knowles, and Christopher M. Dobson. "Quantifying the Thermodynamic Stability of Amyloid Fibrils". Biophysical Journal, 118(3):492a, 2020. [49]

Some projects led to patents being filed and licensed. Here is a list:

GB1819033.0 Tuomas Pertti Jonathan KNOWLES, Pavan Kumar CHALLA, Kadi Liis SAAR, Quentin Alexis PETER, Clemens KAMINSKI, Oliver VANDERPOORTEN, "Particle Characterization Using Optical Microscopy". Filed (2018) and licensed (2019)

GB2010411.3 Tuomas Pertti Jonathan KNOWLES, Georg KRAINER, Raphael Phillipe Bernard JACQUAT, Quentin Alexis Eric PETER, "Interferometric Scattering Optical Microscopy". Filed (2020)

GB1819029.8 and GB1913536.7 Tuomas Pertti Jonathan KNOWLES, Pavan Kumar CHALLA, Kadi Liis SAAR, Quentin Alexis PETER, Zenon TOPRAKCIOGLU, "Optical Microscopy". Filed (2018 and 2019). Licensed (2019)

GB1820870.2 Tuomas Pertti Jonathan KNOWLES, Kadi Liis SAAR, Quentin Alexis Eric PETER, Pavan Kumar CHALLA, Thomas MUELLER, "Detection of Components". Filed (2018). Licensed (2019)

GB1815360.1 and GB1910277.1 Tadas KARTANAS, Tuomas Pertti Jonathan KNOWLES, Quentin Alexis Eric PETER, Kadi Liis SAAR, Tom SCHEIDT, Thomas MUELLER, Sean DEVENISH, "Improvements in or relating to profiling of particles using microfluidic devices". Filed (2018 and 2019), Licensed (2019)

GB1803724.2 Tuomas Pertti Jonathan KNOWLES, Pavan Kumar CHALLA, Kadi Liis SAAR, Quentin Alexis PETER, Clemens KAMINSKI, Oliver VANDERPOORTEN, "Particle characterization using optical microscopy". Filed (2018), Licensed (2018)

Table of contents

List of figures

Chapter 1

Introduction

1.1 Protein science

Proteins are the building blocks for virtually all functions in living organisms. These components of the cellular machinery are incredibly complex and versatile [8]. The production of new proteins is one of the most fundamental subsystems they enable. Protein-coding genes in DNA contains the blueprint for proteins. These genes are translated into amino acid chains by ribosome protein complexes. Proteins in all known living systems are built with the same 22 amino acids, 20 of them being used by human cells. The human genome consists of 20 000 - 30 000 genes coding for over 500 000 proteins [33]. The amino-acid chains fold into a functioning proteins, which are almost always the most thermodynamically stable conformation [74]. This is the most fundamental and universal example of biological self-assembly. Even then, the number of possible conformations is incredibly large, which prevents any systematic search [73]. The fact that nature finds the minimum of the energy landscape so quickly is a stunning feat. While the structure of a protein should be fully determined by the amino acid sequence [14], predicting their 3D structure has proven extraordinarily difficult. Recent developments in artificial intelligence have lead to impressive advances in solving this problem [133]. However, these techniques still struggle with multi-protein complexes, as interactions might change their shape [50]. Less than one fifth of proteins carry their function without interacting with other proteins [33]. Many proteins arrange into functional modules to achieve natural wonders [219]. Protein interactions are key to their function. They interact with genetic code, other proteins, or other biomolecules such as lipids. These interactions are dynamic and transient. Detecting and quantifying these interactions without alteration is therefore a very important challenge [190].

Functional proteins are fundamental for the survival of a cell. Therefore, the cell has many quality control mechanisms in place, such as molecular chaperones, to ensure correct

folding of amino acid chains into proteins [46, 108]. Many sources of stress, such as the macromolecular crowding inside cells, contribute to creating misfolded proteins [178, 83]. Failures of the quality control mechanisms is a common feature of a wide range of diseases [73]. Understanding these failures is one of the main challenges of modern science [263]. For example, the Prion protein (PrP), associated to several mammalian prion diseases, exists as the functional PrPC (cellular) form, and as the aggregated, infectious PrPSc (Scrapie) form. PrPSc has a self-replicating nature, with the ability to "seed" the conversion of PrPC into the aggregated form [208]. Other pathological conditions such as Parkinson's or Alzheimer's diseases are linked to fibrillar protein aggregates called amyloid [58]. Amyloid state exists for many proteins. These amyloid fibrils can be created either by primary nucleation of monomers, or by secondary pathways mediated by existing fibrils, as illustrated in Figure 1.1 for Alzheimer's Aβ42 peptide. These secondary pathways turn amyloid fibrils into self-propagating assemblies, which leads to a cascade cytotoxic process [146]. Amyloid fibrils may also have a practical use for some organisms. A wide range of bacterial pathogens form biofilm structures which helps them survive environmental stresses, such as antibiotics. Unlike the runaway mechanisms of amyloid diseases, these functional amyloid fibrils do not self-replicate to any significant degree. Bacterias can control the creation of amyloid fibrils through primary nucleation and elongation of fibrils, without the uncontrolled secondary nucleation found in pathological amyloid fibrils [13]. Understanding the conditions under which these aggregates form and propagate is therefore crucial to the development of effective treatments for this class of diseases [167].

Understanding the biology of proteins not only gives insights into the mechanisms of living things, but also provides scientists with incredibly versatile tools. Gene editing has become much easier with the discovery of CRISPR-Cas9 [69]. Monoclonal antibodies can be used to detect almost any biological component [239], allowing - among other things - early detection of pregnancy or cancer [28]. Antigenes such as SARS-COV-2's spike protein can similarly be used to detect antibodies in patient's blood, revealing past infections [86]. Proteins are also used as biological medical products to cure a wide range of conditions [270]. In general, it is hard to overstate the importance of protein science for modern medicine. The goal of this thesis is to contribute to the development of biophysical methods for protein detection and characterisation. Current challenges in protein science must be addressed to enable new leaps in knowledge and technical capabilities.

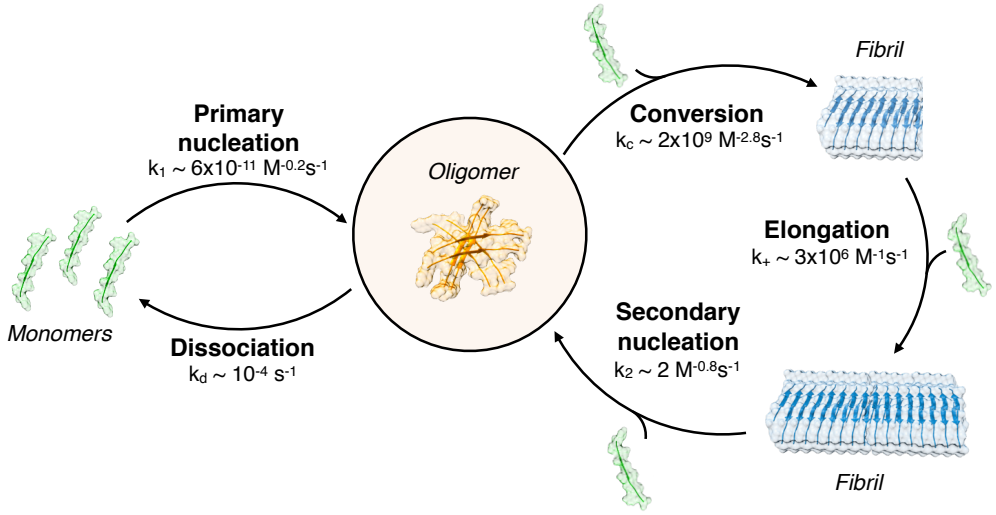

Fig. 1.1 Aggregation pathway of Alzheimer's Aβ42 peptide. The primary pathway is very unlikely and consists of primary nucleation of monomers into oligomers, that are then converted into amyloid fibrils. Once fibrils are present, they elongate and may catalyse the creation of new fibrils through secondary nucleation. While this secondary pathway is dominant for Aβ42 peptide, other pathways exist, such as fibril fragmentation. Image reproduced with permission from [177].

1.2 Biophysical tools for protein characterisation

A plethora of methods exist to detect and analyse proteins depending on their size, electrical charge, conformation, composition, or interactions. The structure of proteins can be probed to atomic-resolution using X-ray crystallography [142], cryogenic electron microscopy [129, 31, 94], or nuclear magnetic resonance spectroscopy [74]. This last technique is useful for studying samples in solution [205, 139]. Scanning probe microscopy is similarly used to probe the structure of larger complexes such as amyloid fibrils [222]. While these techniques enable getting highly resolved structural information on the proteins, interactions between them are often harder to probe. Probing dynamic interactions would be almost impossible for crystallised or frozen proteins, as is required for some of these techniques. For many applications, the presence of a protein or a single biophysical parameter is often a sufficient readout. Working in gas phase, mass spectrometry [235, 175] is a popular tool to obtain the mass-to-charge ratio of the components of a solution. It is often coupled with a separation technique to help with the identification of the components, such as ion mobility spectrometry [32]. It can be used to probe protein interactions [159]. However, knowing if an ionised sample corresponds to the physiological state is challenging. Many techniques can be used in solution under physiological conditions. Due to the transient nature of interactions,

a rapid analysis in a native environment is needed to get accurate results. Thermodynamic properties of binding can for example be probed by measuring the heat created by a reaction in solution using Isothermal titration calorimetry (ITC) [202] or Surface plasmon resonance (SPR) [232]. However, these techniques often require large amounts of sample and do not work well with complex backgrounds, as it is the case with biologic fluids.

Direct detection of particles is achieved optically by detecting absorption, scattering, or fluorescence. The absorption of a protein of circularly polarized light can provide information on the protein structure, such as the presence of alpha-helix and beta-sheets, using Circular dichroism (CD) [40, 140]. Similarly, the infrared absorption spectrum is used in Infrared spectroscopy [29]. These techniques can be used to probe protein folding and conformation [48]. Light scattering is used to detect the presence of proteins but the signal intensity scales with the sixth power of the particle size, making small particles challenging to detect at low concentrations [154]. This problem can be solved by using Interferometric scattering microscopy (iSCAT) that detects the interference of a scattered signal with a carrier wave [189], or by attaching a gold nanoparticle as a scattering label [251]. Fluorescence uses a physical phenomenon that shifts the wavelength of light, allowing the usage of optical filters to separate excitation and emission wavelengths. Proteins are usually fluorescent under UV light due to aromatic amino acid tryptophan and tyrosine [180]. Fluorescent labels can also be attached to particles to increase the signal ratio or use different wavelengths, which is especially useful for multicolour detection [122, 100]. For cases where only certain conformations are of interest, latent dye such as thioflavin-T (ThT) can be used to detect amyloid fibrils, but not monomers [36]. Finally, when proteins are captured on a surface, surface effects can be used for their detection. Evanescent waves can be detected using Surface plasmon resonance [232]. Changes to the surface interference pattern are detected by Bio-layer interferometry (BLI) [216]. In general, detecting interactions on surfaces might lead to errors, as competitive low affinity binding from the surface might affect the results [128].

1.3 Protein identification and characterisation

Detecting a protein is a crucial step for their identification and characterisation. While some detection methods intrinsically measure particle properties, such as scattering that depends strongly on the particle size, most techniques work best when coupled to another physical phenomenon. When in solution, particles are constantly bouncing against water molecules, as illustrated in Figure 1.2, resulting in a random travel called Brownian motion [82]. The amplitude of this motion depends on the drag applied to the particle by the medium and is

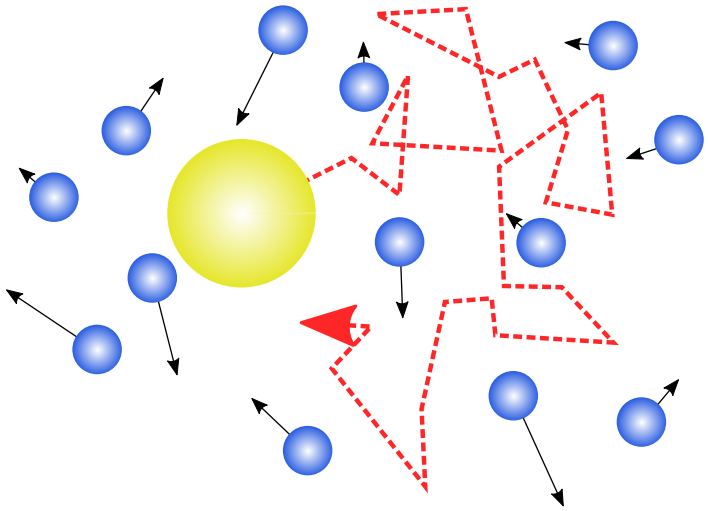

Fig. 1.2 Illustration of Brownian motion. Water particles (in blue) bounce around under the effect of temperature. A particle (in yellow) is pushed by this agitation and follows a random path (in red). The average distance travelled by the particle is measured by the diffusion coefficient, which depends on the water temperature and viscosity, as well as on the size of the particle.

described by the diffusion coefficient. It can be measured from the path of a single particle tracked over time [154]. If detecting a single molecule proves to be challenging, the signal from many molecules may be used. The diffusion coefficient is linked to the time correlation of fluorescence and scattering signal. Interferences variation between scattering particles is measured with Dynamic light scattering (DLS) [34] and fluorescence variation with Fluorescence correlation spectroscopy (FCS) [84]. The diffusion coefficient can be measured by the temporal evolution of a concentration field. For example, a microfluidic chip can be used to create a concentration gradient by simply merging two flows with different concentrations. This technique is called Diffusional sizing [101, 18], and may be used to probe heterogenous solutions or oligomerization of proteins [241, 51]. However, deconvolution of the signal from several different species is an ill-posed inverse problem [233]. A large difference in size is therefore needed to separate the signal from different species [283]. This highlights the need to couple characterisation methods with separation methods in order to analyse heterogeneous mixtures.

Many other physical phenomena can be used to measure the physical properties of proteins. The motion of proteins in a thermal gradient can be probed by Microscale thermophoresis [182, 273]. The motion of proteins in a solute gradient may be probed by Diffusiophoresis [89]. An electric field can probe the electrophoretic mobility using Free flow electrophoresis [149]. When the separation between species is sufficient, these phenomena may be used for Chromatography. Electrokinetic separation is widely used to separate

proteins. It covers techniques such as Capillary electrophoresis [141], Gel electrophoresis (PAGE) [274], Isoelectric focusing (IEF) [38], or Micellar electrokinetic chromatography (MEKC) [106]. Residence time in pores are probed in Size-exclusion chromatography (SEC) [90]. In general, many types of liquid, gas, or gel chromatography exist. They require a separation power sufficient to overcome diffusion.

Another method to handle polydispersity is to use chemical specificity. This consists in using an affinity probe to bind to the target protein. Antibodies are affinity probes created by the immune system to target foreign objects and are used in a wide range of techniques such as Enzyme Linked Immunosorbent Assay (ELISA) [267, 160] or Western blots [47, 169]. Affinity probes are generally used when working with patient samples, as they allow detecting low concentration of a target protein in a very heterogeneous solution. Other particles may be engineered to mimic antibodies. Nanobodies such as antibody fragments are smaller than antibodies [168, 88]. Aptamers are DNA- or RNA-based antibodies replacements [72], and DARPins are protein-based antibody mimetic proteins [204].

1.4 Micro- and nanofluidics as tools for protein characterisation

Microfluidics is the study and manipulation of sub-millimetre scale flow. It is an incredibly versatile tool and shows considerable promises to improve biology and biomedical research. The micro-scale physics not only allows to reduce the volume, cost, and time of traditional macroscale assays, it also opens horizons for new experiments [229]. The absence of turbulences, as explained below, means that the flow is regular and laminar, enabling the microfluidics technology to have good predictability and control over the dynamics of experiments [43]. Another important feature is the relatively low importance of gravity compared to a macro-scale experiment. Capillary and surface tension forces are dominant and can be used for a wide variety of applications, such as filtering analytes, passive pumping of fluids, as well as creating mono-disperse droplets [229, 248]. The laminar flow property can be used to extract e.g. the hydrodynamic radius from diffusion [18]. Complex protocols can be streamlined e.g. by labelling a biomolecule after doing an experiment on the same chip [278]. Other examples include DNA sequencing, polymerase chain reaction, DNA separation, immunoassays, cell counting and sorting, cell culture, and capillary electrophoresis [23, 44, 174, 135, 110].

A logical continuation of microfluidics is nanofluidics, which is characterised by an even higher surface to volume ratio [249], and which gives rise to unique phenomena.

It is interesting to note that most of the biological organisms function in a nanofluidic environment [81]. The discrete nature of molecules becomes important at such a scale, but if the smallest dimension is at least 10 nm, continuous theory is still a good approximation [249, 81]. The major difference with microfluidics comes from the interactions with the walls, as the electrical double layer size is no longer negligible [249]. The surface roughness might strongly affect the flow, and some particles may be attracted in or excluded from the channel. Another consequence of the high surface to volume ratio is the wall absorption, which can greatly reduce the transport rate [249]. Applications range from flow detection, liquid transport, control of molecular transport, to separation [249].

1.4.1 Materials

Polydimethylsiloxane (PDMS) has been extremely important for the development of microfluidics for four reasons [229]: it is cheap and easy to fabricate small quantities of devices from PDMS; it is relatively easy to tune its hydrophobicity; it can be bonded to glass; and its elasticity makes it easy to remove chips from moulds. Another feature of the PDMS is gas permeability, which is useful in some experiments such as cell culture. On the other hand, several issues can be noted. Uncross-linked monomers can contaminate the fluids processed within the device, and it can absorb small molecules [215]. Evaporation can occur because of the small volumes used and because of the PDMS gas permeability [229, 35]. Finally, it is not ideal for large scale production, as the cost does not scale well with the quantity produced [30]. This is why plastics such as polystyrene, cyclic olefin copolymers (COC) and polycarbonate are sometimes considered as an alternative, in addition to the fact that they are widely used in biology already [229]. Other materials - such as wax, paper, or glass - have also been used.

1.4.2 Fabrication

Microfluidic chips are typically created using a soft lithography technique [76]. The process is described in Figure (1.3). The first step is to design a mask that will be used to create a master. Then, the master is created from a silicon wafer. SU-8 photoresist is uniformly distributed with a spin coater. After heating the SU-8 to solidify it, the master is exposed to UV light with the mask preventing parts of the master from being exposed, which are removed during the development of the photoresist. PDMS can then be poured on the master and peeled off after a curing agent solidified the liquid. A glass slide is then bonded with a plasma oven to seal the chip. The same plasma oven can be used to treat the PDMS and

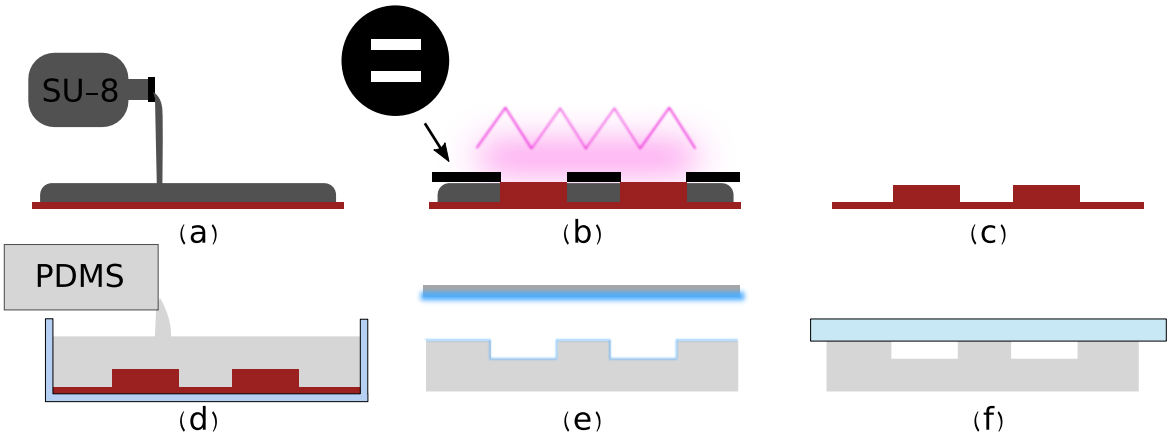

Fig. 1.3 Simplified process of creation of a microfluidic chip using PDMS. (a) SU-8 photoresist is poured on a silicon wafer. (b) The photoresist is then exposed to UV light while some areas are protected by a mask. (c) After developing, only the exposed areas remain and the master is ready. (d) The master is then placed into a petri dish, and covered by PDMS. (e) After baking the microfluidic chip and peeling it off the master, the chip is exposed to a plasma oven, (f) which will allow a glass slab to be bonded on top.

make it hydrophilic. Different coatings may be used to change the properties of PDMS such as the affinity to protein adhesion.

1.4.3 The physics at the microscale

The equations in this section are taken from [43]. The governing equations of microfluidics are the continuity equation, the Navier-Stokes equation, and the heat-transfer equation. The continuity equation states that nothing can appear or disappear in a fluid:

$$\partial_t \rho = -\nabla \cdot (\rho \boldsymbol{v}) \tag{1.1}$$

where ρ is the density and $\boldsymbol{v}$ the velocity field. If the fluid is incompressible, this reduces to:

$$\nabla \cdot \boldsymbol{v} = 0 \tag{1.2}$$

The Navier-Stokes equation is the corresponding equation of fluid motion. it is given by:

$$\rho[\partial_t \boldsymbol{v} + (\boldsymbol{v} \cdot \nabla)\boldsymbol{v}] = -\nabla p + \eta \nabla^2 \boldsymbol{v} + \beta \eta \nabla(\nabla \cdot \boldsymbol{v}) + \rho \boldsymbol{g} \tag{1.3}$$

where p is the pressure, η is the viscosity, β is a coefficient related to the ratio between the dynamic shear viscosity of an incompressible fluid (η) and compressibility-induced dilatational viscosity, and $\boldsymbol{g}$ describes external sources. For incompressible fluids, it reduces

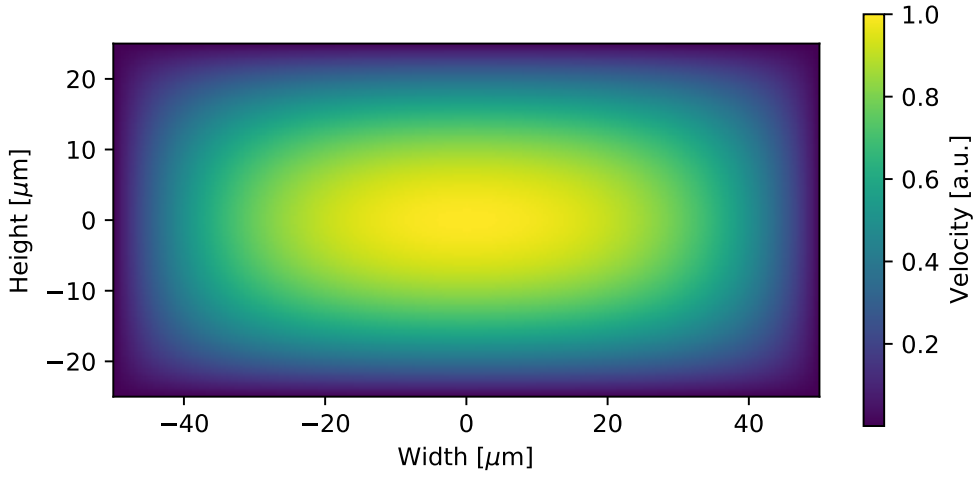

Fig. 1.4 Velocity profile of a Poiseuille flow in a channel with an aspect ratio of $1/2$.

to:

$$\rho[\partial_t \boldsymbol{v} + (\boldsymbol{v}\cdot\boldsymbol{\nabla})\boldsymbol{v}] = -\boldsymbol{\nabla}p + \eta\nabla^2\boldsymbol{v} + \rho\boldsymbol{g} \tag{1.4}$$

The non linear term of this equation ($(\boldsymbol{v}\cdot\boldsymbol{\nabla})\boldsymbol{v}$) creates a lot of interesting and complex effects. It is responsible for turbulences and complicates the mathematical analysis of the flow. It is negligible when the Reynolds number is low. The Reynolds number is defined by normalising all the units in the Navier-Stokes equation by a length scale L_0 and a velocity scale V_0. Considering the case without external sources, the Navier-Stokes equation becomes, where unit-less variables are marked with $\sim$:

$$Re[\tilde{\partial}_t \tilde{\boldsymbol{v}} + (\tilde{\boldsymbol{v}}\cdot\tilde{\boldsymbol{\nabla}})\tilde{\boldsymbol{v}}] = -\tilde{\boldsymbol{\nabla}}\tilde{p} + \tilde{\nabla}^2\tilde{\boldsymbol{v}} \tag{1.5}$$

$$Re = \frac{\rho V_0 L_0}{\eta} \tag{1.6}$$

If $Re \ll 1$, the left hand side can be neglected. If the time scale is controlled by an external factor, $\tilde{\partial}_t\tilde{\boldsymbol{v}}$ is not negligible. A low Reynolds number means that there will be no turbulences in the channel, this situation being called laminar flow. The laminar flow in a rectangular channel may be solved as shown in Figure (1.4) [250].

Under laminar flow, the non-linear term is negligible ($(\boldsymbol{v}\cdot\boldsymbol{\nabla})\boldsymbol{v} \approx 0$). The volumetric flow rate Q over a surface S with normal vector $\boldsymbol{n}$ is defined as:

$$Q \equiv \int_S \mathrm{d}S\boldsymbol{v}\cdot\boldsymbol{n} \tag{1.7}$$

The volumetric flow rate is proportional to the pressure gradient. An analogy with electrical circuits can be drawn. In this analogy, the electric potential is the pressure and the electrical current is the volumetric flow rate Q. A hydraulic resistance R_{hyd} is defined from Ohm's law:

$$R_{hyd} \equiv \frac{\Delta p}{Q} \tag{1.8}$$

R_{hyd} describes the loss of pressure along the channel. Similarly, an electric capacitor can be compared with the hydraulic compliance, where an addition of pressure increases the available volume (W):

$$C_{hyd} = \frac{\mathrm{d}W}{\mathrm{d}p} \tag{1.9}$$

As in the electrical counterpart, the presence of hydraulic compliance prevents the pressure from varying too abruptly. Finally, the hydraulic inductance represents the inertia. It is defined with the cross section area A of the channel as:

$$L_{hyd} = \frac{\rho L}{A} = \frac{\Delta p}{\partial_t Q} \tag{1.10}$$

1.5 Summary of the thesis

In this thesis, I discuss the contributions I made to the development of protein detection and characterisation methods with the fellow researchers I had the chance to work with. First, the detection of label-free proteins using their intrinsic fluorescence or scattering is discussed. In chapter 2, a novel deep-UV fluorescence microscope is presented. This microscope can detect the protein autofluorescence emitted by aromatic amino acids. An alternative approach to label-free protein detection is presented in chapter 3. Interferometric scattering microscopy (iSCAT) may detect the light scattered by a single protein. An interference pattern is created between the scattered light and a reference light. The presented microscope uses oblique illumination to separate these two light sources. This enables a modulation of the reflected light, increasing the recorded contrast. This technique works best when the protein is immobilised. In chapter 4, a time correlation technique is presented to use this interferometric approach for particles in solution. The size of label free proteins and single protein complexes can be measured. In addition to having improved the detection of protein, advances have been made in microfluidics fabrication. In chapter 5, a two-photons based lithography technique is described. This technique enables the addition of nanofluidics elements to microfluidic designs. Finally, this thesis focuses on protein characterisation techniques. In chapter 6, advances to diffusional sizing are presented. In chapter 7, diffusiophoresis - the motion of

proteins in a solute gradient - is used to characterise a range of proteins. Finally, chapter 8 describes research in spatial propagation of aggregation, which is relevant for the propagation of amyloid diseases. These chapters present a range of advances in biophysical methods for protein detection and characterisation.

Chapter 2

Real-time intrinsic fluorescence visualisation and sizing of proteins and protein complexes in microfluidic devices

2.1 Summary

This chapter is based on the paper: Pavan Kumar Challa, Quentin A. E. Peter*, Maya A. Wright, Yuewen Zhang, Kadi L. Saar, Jacqueline A. Carozza, Justin L.P. Benesch & Tuomas P. J. Knowles. "Real-time intrinsic fluorescence visualization and sizing of proteins and protein complexes in microfluidic devices". Analytical Chemistry 90.6 (2018): 3849-3855 (* contributed equally). [53] My work consisted in creating a data analysis and processing pipeline, as well as in analysing the data acquired by my colleagues and myself. One of my critical contributions lies in the background subtraction algorithm that aligns the images and removes background features when the experimental conditions are not stable, notably when the field of view moves or when the intensity pattern changes. I contributed to the data acquisition by running calibration experiments and by advising colleagues on how to best acquire data for my data analysis pipeline. I moreover contributed to the creation of the setup, notably by electronically linking the UV-LED and the camera to synchronise the shutter and to minimize the UV-radiation. Finally, I contributed to writing the paper.*

Optical detection has become a convenient and scalable approach to read out information from microfluidic systems. For the study of many key biomolecules, however, including peptides and proteins which have low fluorescence emission efficiencies at visible wavelengths, this approach typically requires labelling of the species of interest with extrinsic fluorophores to enhance the optical signal obtained – a process which can be time-consuming, requires

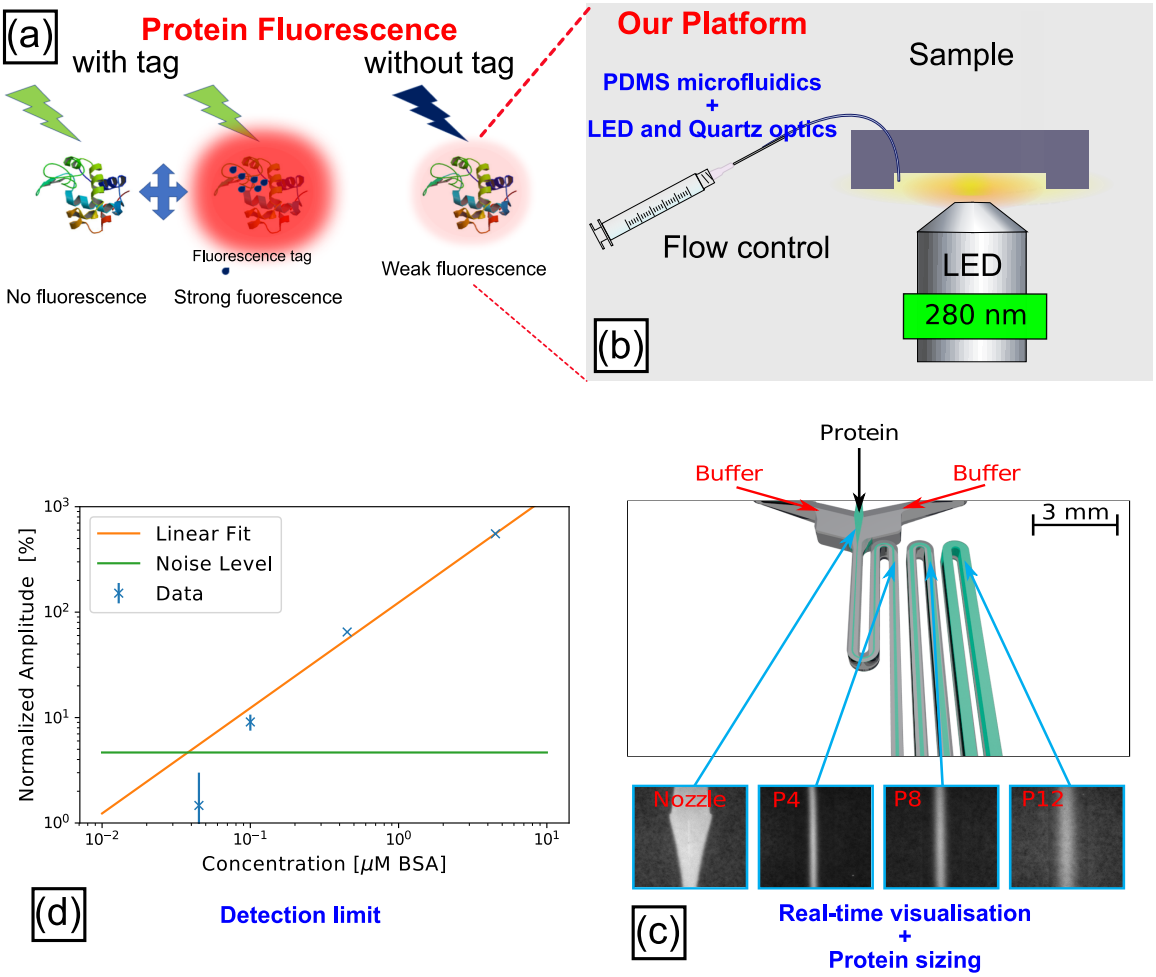

Fig. 2.1 Summary of the chapter. (a) With a label, a protein fluoresces strongly. Without label, it auto-fluoresces weakly. (b) Our platform uses PDMS microfluidics, a deep-UV LED, and quartz optics to detect this autofluorescence. (c) Using a diffusion device in conjunction with this platform, proteins can be sized label-free. (d) The lowest concentration that can be detected for BSA using this technique on our setup is hundreds of nanomolars.

purification steps, and has the propensity to perturb the behaviour of the systems under study due to interactions between the labels and the analyte molecules. As such, the exploitation of the intrinsic fluorescence of protein molecules in the UV range of the electromagnetic spectrum is an attractive path to allow the study of unlabelled proteins. However, direct visualisation using 280 nm excitation in microfluidic devices has to date commonly required the use of coherent sources with frequency multipliers and devices fabricated out of materials that are incompatible with soft-lithography techniques. Here, a simple, robust and cost-effective 280 nm LED platform that allows real-time visualisation of intrinsic fluorescence from both unlabelled proteins and protein complexes in polydimethylsiloxane microfluidic channels fabricated through soft-lithography is developed. Using this platform, intrinsic fluorescence visualisation of proteins at nanomolar concentrations on is demonstrated chip, and visualisation is combined with micron-scale diffusional sizing to measure the hydrodynamic radii of individual proteins and protein complexes under their native conditions in solution in a label-free manner.

2.2 Introduction

Proteins underpin most of the key functional processes in cells, and there has thus been a sustained and long-standing interest in developing tools capable of studying proteins under native conditions in solution. Microfluidic platforms are highly attractive in the context of protein science; they minimise sample consumption, cost, and measurement time. Moreover, exploitation of laminar fluid flow to integrate multiple functions onto a compact microfluidic chip platform enables miniaturisation, thus leading to the ability to readily perform studies that are impractical in conventional bulk studies. These characteristics lead to the potential of such systems to impact fields ranging from medical diagnostics, genetic analysis and drug discovery to proteomics. Applications including DNA sequencing, polymerase chain reaction, capillary electrophoresis, DNA separation, enzymatic assays, immunoassays, cell counting, cell sorting, and cell culture have been successfully miniaturised onto a chip [174, 23, 44, 135, 110].

A variety of methods have been developed to obtain information about the conformational states and folding pathways of biomolecules in solution, most notably these of proteins [196, 80, 59, 75, 242, 138]. Among these methods, fluorescence spectroscopy, where changes in the fluorescence intensity at a fixed wavelength or shifts in the wavelength at maximum intensity are observed, has been used successfully to study conformational changes of proteins due to the high sensitivity of this approach [256]. For such biophysical characterisation, protein molecules are generally studied with extrinsic labels due to the high signal-to-noise ratios that

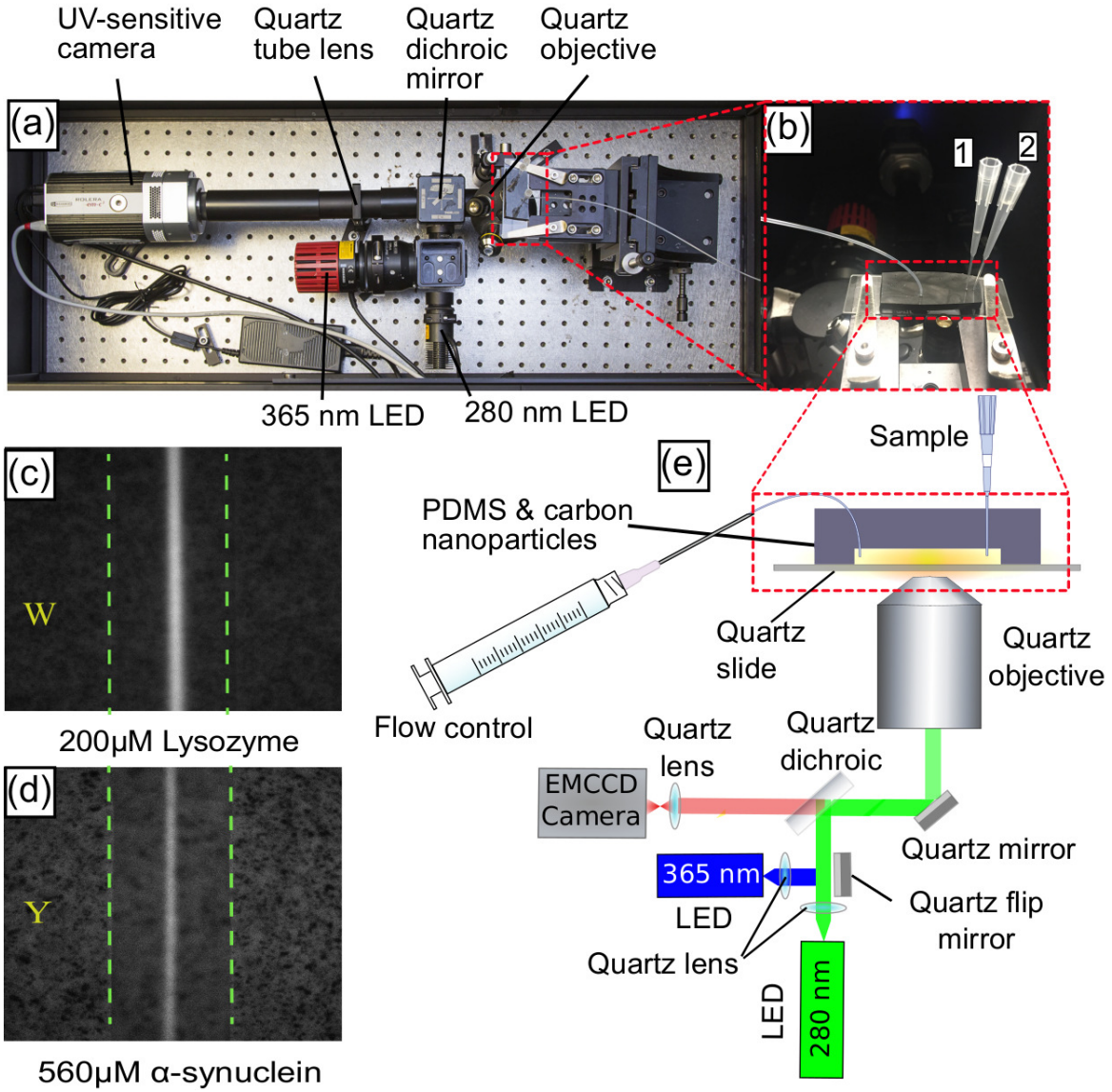

Fig. 2.2 (a) Deep-UV LED fluorescence platform to detect and quantify the intrinsic fluorescence from proteins in microfluidic systems. Photograph of the experimental set-up. (b) A microfluidic device bonded to a quartz slide is placed on the detection stage. The protein sample and buffer are flowed through inlets 1 and 2. (c) Autofluorescence of 200μM Lysozyme from Tryptophan [W] emission, (d) Autofluorescence of 560 μM α-synuclein from Tyrosine [Y] emission. (e) Schematic illustration of the optical set-up. Green dotted lines in (c) and (d) denote the ends of the microfluidic channels, where the protein samples only occupy the middle of the channels.

they afford. Despite the fact that there have been significant technological developments in the photochemistry and photophysics of modern dye molecules, labelling remains inherently a time-consuming and labour intensive process. Furthermore, extrinsic labelling has the propensity to perturb the folding processes and kinetics of proteins [256, 227, 278]. Hence, label-free techniques have in principle great advantages for studying protein conformations and can play a key role in numerous other bio-detection applications [85]. Typically, when excited with UV light below 300 nm proteins exhibit intrinsic fluorescence from the aromatic amino acids tryptophan, tyrosine, and phenylalanine [156].

As such, label-free techniques have clear inherent advantages over label-based ones, particularly in the context of the study of protein-protein interactions which can be perturbed by the labels. However, integration of intrinsic fluorescence visualisation with lab on a chip platforms has remained challenging due to the inherently low sensitivity confounded by the constraint of limited optical path lengths in reduced volumes. Nevertheless, even though visualisation applications have remained challenging, detection through UV-absorption-based measurements of native proteins in microfluidic chips have been demonstrated successfully [200, 161, 184, 237]. Due to the limited path lengths achievable in microfluidic devices, high levels of sensitivity remain challenging to achieve. To overcome these limitations several groups have used laser-based technologies through frequency doubled, tripled or quadrupled continuous wave and pulsed lasers for native fluorescence detection of proteins in a fused silica and PDMS microchips using a photomultiplier tube detectors [237, 148, 211, 255, 238, 112]. In particular, high speed laser scanners with a frequency quadrupled laser for deep UV fluorescence detection and visualisation of proteins has been demonstrated in a free flow electrophoresis fused silica chip [148]. Moreover, the frequency tripled output of Ti:Sapphire laser has been integrated to a fused silica microchip to study quenching and refolding kinetics in a laser machined flow mixer device using time correlated single photon counting (TCSPC) fluorescence detection system [37]. In addition, frequency quadrupled Nd:YAG lasers (266 nm) have been exploited to explore protein separation and detection [113]. In order to alleviate the complexity of frequency multiplying approaches conventionally required for generating high power coherent radiation at 280 nm non-coherent sources, including 230 nm high intensity deuterium lamps [287], or more recently UV-LED at 280 nm have been used to perform detection in capillary electrophoresis of native proteins using photomultiplier tubes [247, 258]. These systems represent significant advances as they allow unlabelled proteins to be studied in microfluidic systems, but in cases where high sensitivity is required such approaches have relied on materials and devices which are not compatible with rapid soft lithography fabrication techniques. Light emitting diodes (LED's) are simple, stable, cost-effective, have long lifetimes, and small sizes. However, the

low output power of the LEDs has hindered their use as a light source for intrinsic fluorescence visualisation of proteins in real time flowing through PDMS microfluidic devices using charge coupled device (CCD) cameras.

Here a compact 280 nm high power LED microchip based fluorescence visualisation platform which is fully compatible with rapid soft lithography microfabrication approaches is designed and implemented, opening up the possibility of using label-free protein studies in a wide range of device designs and architectures. Excitation at 280 nm enables visualisation of proteins molecules via the autofluorescence of their tryptophan and tyrosine amino acid residues. To illustrate the power of this method, autofluorescence detection is combined with diffusional sizing to measure the hydrodynamic radius of monomeric proteins bovine serum albumin (BSA), lysozyme and oligomeric clusters of the molecular chaperone αB-crystallin in free solution in a label-free manner by following their mass transport in real time in microchannels.

2.3 Experimental details

2.3.1 Intrinsic fluorescence visualisation platform

A robust and compact 280 nm-LED based epifluorescence microfluidic station is built for label-free fluorescence visualisation of proteins on chip, using fluorescence from the aromatic amino acids tryptophan and tyrosine (Figure (2.2)). Light from a 280 nm LED (Thorlabs M280L3) is passed through an aspherical lens of focal length 20 mm to obtain a nearly collimated beam. This beam is incident on a dichroic filter cube, which consists of an excitation filter (Semrock FF01-280/20-25) centred at a wavelength of 280 nm, and a dichroic mirror (Semrock FF310-Di01-25x36). The light is again reflected by a UV-enhanced aluminium mirror (Thorlabs CCM1-F01/M) and focused onto the sample flowing in a microfluidic device by an infinity corrected UV objective lens (magnification 10X, numerical aperture = 0.25). The fluorescence from the sample is collected through the same objective and passed through an emission filter (Semrock FF01-357/44-25) centred at a wavelength of 357 nm, and finally focused onto a EMCCD camera (Rolera EM-C2) by an air-spaced achromatic doublet lens (Thorlabs ACA254-200-UV) of focal length 200 mm. The exposure time used in our experiments is about 500 ms. The data in this chapter are available online [54].

2.3.2 Device fabrication

Microfluidic devices for intrinsic fluorescence visualisation experiments are cast using polydimethylsiloxane (PDMS) (Sylgard 184 kit, Dow Corning) from a silicon wafer master imprinted with 50 μm high channels fabricated using conventional UV lithography [210, 52]. Carbon black nano-powder (Sigma-Aldrich) is added to the PDMS before curing to create black devices, thus minimising unwanted autofluorescence from PDMS under 280 nm-LED illumination during the measurements. Devices are bonded to a quartz slide (Alfa Aesar, 76.2 x 25.4 x 1.0 mm) using a plasma bonder (Electronic Diener Femto, 40% power for 15 s) and subsequently plasma treated for 500 s to render the channels hydrophilic. The channels are filled from the outlet with buffer using a glass syringe (Hamilton, 500 μL), equipped with a needle (Neolus Terumo, 25 gauge, 0.5 x 16 mm), and polyethene tubing (Scientific Laboratory Supplies, inner diameter 0.38 mm, outer diameter 1.09 mm). The microfluidic devices used in this study are the diffusional sizing devices described in [183, 18].

2.3.3 Background correction

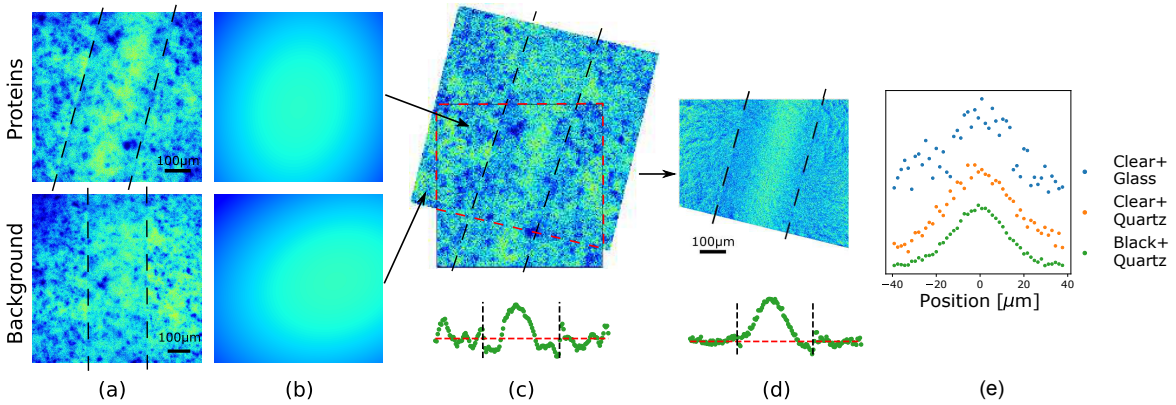

Fig. 2.3 Quantitative background correction significantly improves signal-to-noise ratios of intrinsic fluorescence on chip. (a) Images taken with the CCD camera of both the channel containing protein BSA and of the background alone at position 12 (Figure (2.4a)). The tilt and scale difference is exaggerated to make the process easier to visualise. (b) First, the intensity is fit with a polynomial and the images are flattened, as can be seen when comparing (a) and (c). (c) Second, the difference in angle, scale, and x-y offset is detected, resulting in an overlap between the two images. (d) As the images are flat and are overlapping, they can be subtracted to extract the relevant data. The change in profile is outlined on the bottom of (c) and (d). The topological noise introduced by the black nano-powder is removed. (e) Profiles at position 0 (Figure (2.4a)) in the microfluidic diffusional sizing device. Three microfluidic sizing chips are compared: clear PDMS bonded to glass, clear PDMS bonded to quartz, and black PDMS bonded to quartz.

An autofluorescence image of a protein sample in a microfluidic device taken on the deep UV set-up can be separated into three contributions: the signal from the protein, the signal from the background, and noise. A better signal-to-noise ratio can be obtained by generating a larger volume of statistically independent data, for example through longer exposure times and by acquiring series of pictures, or by decreasing the resolution by binning and Gaussian filtering, approaches which both reduce statistical noise. The background signal, by contrast, is constant across images and can thus be removed by comparing an image with and without sample present. Here, this process is implemented in three steps (Figure (2.3)). First, the non-uniform illumination distribution is extracted from the outside of the channel, which is expected to be flat on the large scale despite local variations due to the carbon nano-powder. This distribution, obtained with fitting a second order 2D polynomial (Figure (2.3b)), is then divided from the image. Second, the two images (with and without fluorescence signal from proteins) are registered. They might present a relative translation, rotation or scale difference, which are corrected through analysis in Fourier space [214]: given a function f_2 that is a translation of a function f_1, the Fourier transforms F_1 and F_2 are related by:

$$\begin{aligned} f_2(x,y) &= f_1(x-x_0, y-y_0) \\ F_2(\xi,\eta) &= e^{-2\pi i(\xi x_0+\eta y_0)} F_1(\xi,\eta) \end{aligned} \tag{2.1}$$

The phase term can be isolated. Using $\|F_1\| = \|F_2\|$:

$$e^{-2\pi i(\xi x_0+\eta y_0)} = \frac{F_2(\xi,\eta)F_1^*(\xi,\eta)}{\|F_2(\xi,\eta)F_1(\xi,\eta)\|} \tag{2.2}$$

x_0 and y_0 are found by taking the Fourier transform of Eq. (2.2). Given f_2 a rotated and rescaled version of f_1, a change of coordinates to log-polar yields a translation of the form:

$$\begin{aligned} f_2(x,y) &= f_1(x/a \cdot \cos\theta_0 + y/a \cdot \sin\theta_0, ...) \\ f_2(\log\rho,\theta) &= f_1(\log\rho - \log a, \theta - \theta_0) \end{aligned} \tag{2.3}$$

The angle and scale difference can therefore be found by using the same method. Eq. (2.1) shows that the magnitude of the Fourier transform does not depend on translation, and can therefore be used to find the relative angle and scaling. The offset can be found after rotation and scaling. The logarithm of the log-polar representation of the magnitude is used to find the angle and scale to avoid over-attributing importance to large-scale features [214]. Finally, the signal and background images are subtracted. The units of the resulting image are a ratio between the signal and the background amplitude. This is conserved between different lamp intensities, but not between devices. Therefore, a calibration step for each new device

is necessary. The code used for correcting the background in Figure (2.3) is accessible online [55].

2.3.4 Protein samples

Bovine serum albumin (BSA) was purchased from Sigma-Aldrich (product number #A9418; lyopholised powder used without further purification) and dilutions were prepared in 25 mM sodium phoshpate buffer pH 8.0. Chicken lysozyme (Sigma-Aldrich L6876; lyophilised powder used without further purification) was dissolved in 2.5 mM phosphate buffer at pH 8.0 to a final concentration of 200 µM with the concentrations similarly determined by NanoDrop spectrophotometer. 560 µM α-synuclein solutions were prepared in 25 mM phosphate solution buffer (pH 7.4) [121]. 120 μM αB-crystallin solutions were prepared in 2.5 mM phosphate buffer (pH 8).

2.4 Results and discussion

Visualisation of low intensity autofluorescence from proteins using excitation with 280 nm radiation poses challenges for the commonly used materials in soft lithography, including PDMS and glass, which absorb most of this light and exhibit significant background fluorescence, that decreases the imaging contrast. In order to address this challenge, a number of technical steps are required. First, all optical components are selected, including the microscope slide to which the microfluidic device is bonded, from quartz to avoid absorption by NBK7 glass. In addition, black carbon nano-powder is mixed with the PDMS during device fabrication to minimise unwanted autofluorescence from the PDMS [112]. Since statistical noise is proportional to the square root of the signal amplitude, a large background signal produces a large associated noise that decreases the signal-to-noise ratio dramatically. Moreover, although the presence of the black carbon nano-powder reduces the overall background, it introduces spatial irregularities in the measured signal. This can be observed in Figure (2.2c-d). This limitation is addressed with an image processing approach that included a specifically incorporated background subtraction (Figure (2.3)). These three steps can be used with almost any PDMS microfluidics device designed to allow analysis of unlabelled proteins that previously needed to be labelled with extrinsic fluorophores. By using black devices bonded to quartz and subjecting the images to our processing steps, the signal-to-noise ratio is improved by a factor of 10 over imaging in a conventional clear PDMS device bonded to glass (Figure (2.3)).

To test if our approach is sufficiently sensitive to be applied to study proteins, a representative set of proteins was chosen. It included BSA (Figure (2.4)), lysozyme (Figure (2.2c)) and αB-crystallin, which contain tryptophan residues, as well as α-synuclein (Figure (2.2d)), which does not contain any tryptophan residues, but has 4 tyrosine residues. Our results in Figure (2.2d) show that the autofluorescence from α-synuclein can certainly be visualised.

2.4.1 Detection limit

Having established the principles for operating the 280 nm-LED microfluidic platform, the limits of visualisation afforded through this approach are explored. Our data show that for BSA, the lowest concentration where the signal-to-noise ratio is large enough to image a profile at position 0 in the device design shown in Figure (2.4a) is 100 nM (Figure (2.5)). The lowest concentration of BSA that is visible at all positions, thus allowing for label-free sizing, is 500 nM, the amplitude at position 12 being approximatively five times lower than position 0, as seen in higher concentration measurements (Figure (2.4c)). The hydrodynamic radius of BSA measured through this approach is 3.3 $\pm$ 0.6 nm, which is close to the literature value determined at higher concentrations [25, 278] in bulk systems or by using labelling approaches.

The sensitivity of our platform can be estimated for a generic protein that has tryptophan and tyrosine amino acids as follows. The average abundance of tryptophan in the human proteome is c.a 1.3% [144, 79] and apparently, the average sequence is c.a 480 amino acids, which means that an average protein has $480 \times 0.013 = 6$ tryptophan residues. 100 nM BSA corresponds to 300 nM of tryptophan residues according to Figure (2.5). Taking this value as the detection limit, the concentration that can be measured for an average protein is c.a 300 nM / 6 = 50 nM. A similar argument can be applied for tyrosine; the average abundance in this case is around 3.3% [144, 79], so that for an average protein there are approximately $480 \times 0.033 = 15$ tyrosine residues. As such, for an average protein the detection limit from the signal of tyrosine residues alone is 2.1 μM / 15 = 140 nM.

2.4.2 Microfluidic diffusional sizing with fluorescence visualisation

To demonstrate the potential of our 280 nm-LED fluorescence visualisation platform, the microfluidic device shown in Figure (2.4a) is used to monitor the micron-scale diffusive mass transport of native proteins in space and time to determine their hydrodynamic radii [183, 18, 278]. To this effect, 12 images are taken along a 100 mm diffusion channel and processed into a set of lateral scan profiles, which are then fitted to a set of simulated basis functions [183]. Information about the spatial diffusion, transverse to the flow, and temporal diffusion,

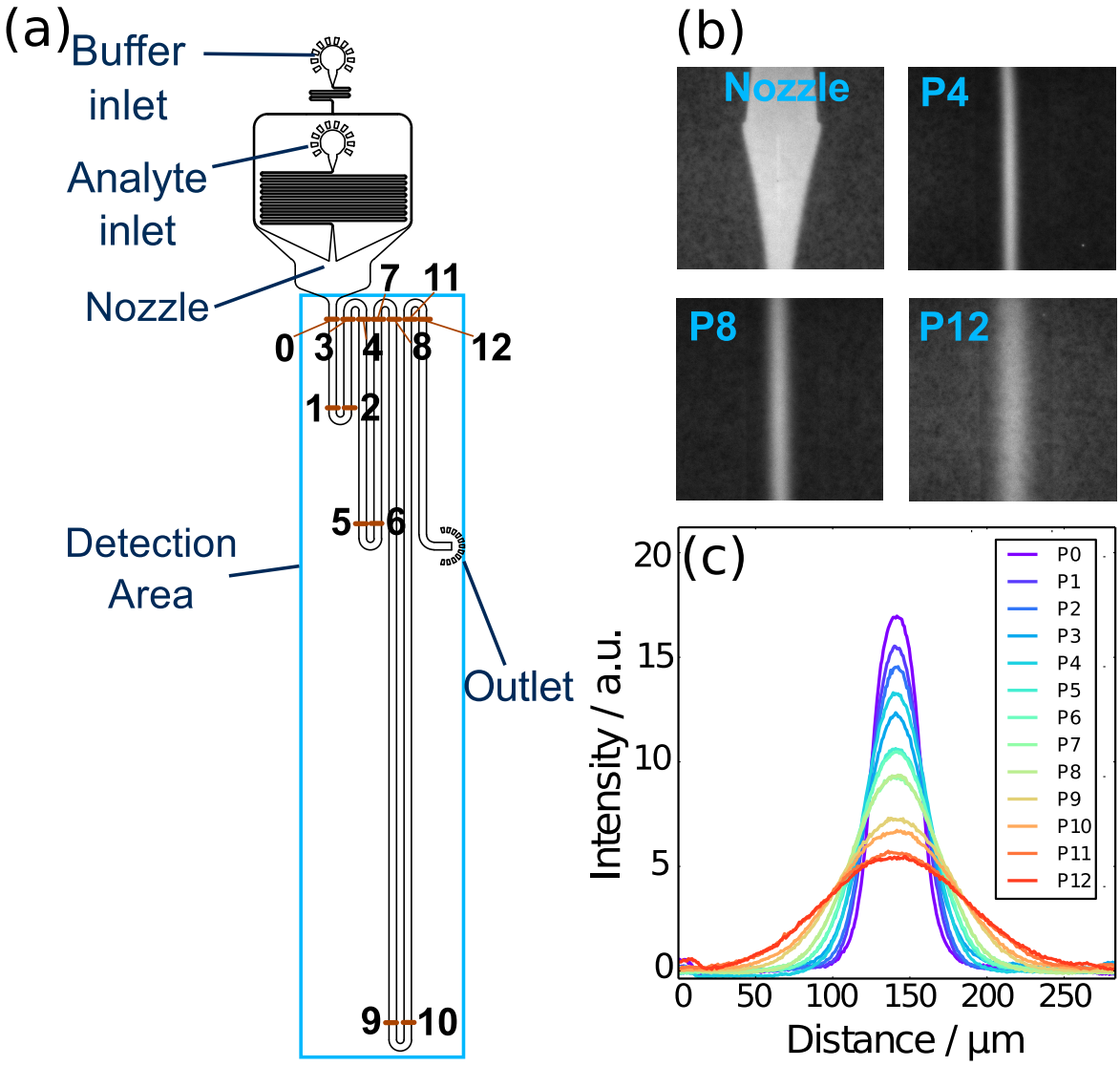

Fig. 2.4 Overview of the microfluidic diffusional sizing measurements. (a) Channel geometry of the microfluidic diffusion device. The buffer and sample are loaded in their respective inlets and drawn through the device through the device with a syringe and pump connected to the outlet. Images of the lateral diffusion of sample into buffer are taken at positions 0-12 in the detection area. (b) Images of 15 µM BSA taken at the nozzle and positions 4, 8 and 12. The extent of diffusion is greater further along the length of the diffusion channels. (c) Lateral scans of the imaged diffusion profiles in (b) from positions 0 through 12. These profiles are fit to a linear combination of simulated basis functions in order to extract the sample's diffusion coefficient. The data was taken by Maya A. Wright and Yuewen Zhang.

along the advective direction, is obtained from the diffusion profiles by deconvolving the experimental profiles into a linear combination of profiles expected for particles with known diffusion coefficients. A least-squares error algorithm is used to find the linear combination yielding the lowest residuals, allowing the average radius of the analyte to be determined [183, 18]. First, the hydrodynamic radii of bovine serum albumin (BSA), a transport protein with 583 amino acids (∼66,500 Da) present in blood plasma, and chicken lysozyme - an antimicrobial enzyme that forms part of the innate immune system - are measured. The results in Figure (2.4) and 2.5 show that, using this approach, spatio-temporal distribution of unlabelled BSA on chip may be visualised directly. Figure (2.4b) shows typical microscopy images of diffused 15 μM BSA at different positions along the microfluidic channels.

2.4.3 Fluorescence visualisation and sizing of protein complexes

Next, αB-crystallin (αB-C) which is a 175 amino acid long polypeptide chain with molecular mass of 20.1 kDa is examined. Our results show that the measured hydrodynamic radius for this system is significantly larger than the one expected from a scaling relationship between molecular mass and radius (Figure (2.6)). These findings, obtained under fully native conditions and for unlabelled molecules, indicate that the monomeric protein is forming complexes under these conditions. Sizing of self-assembled protein-structures can be challenging with many conventional techniques as such non-covalent complexes held together via weak interactions that have the propensity to be altered as soon as the proteins are moved away from under native conditions. The present results therefore open up the possibility of studying not only individual protein molecules, but also nanoscale protein complexes under fully native conditions in an entirely label-free manner.

These results on the size of αB-crystallin complexes under native conditions allow us to access an estimate of the number of monomer units self-assembled into a cluster. To this effect, the hydrodynamic radii of proteins [264, 96] is combined with our data and plotted as a function of their molecular mass (Figure (2.6)). The data is then fitted using the formula, $M_w = R_h^3/\alpha$ where R_h is the hydrodynamic radius of the proteins, α is the scaling coefficient, and M_w is the molecular mass. Then, using the fitted values $\alpha = 0.083749 \pm 0.00175\ nm^3/Da$ and measured hydrodynamic radius $R_h = 6.69\ nm \pm 0.63$, the overall molecular mass of the cluster is estimated to be $510 \pm 148kDa$ and thus the aggregation number to be $510 \pm 148kDa/20.1kDa = 25.4 \pm 7.3$. These values, measured under native conditions in free solution, are consistent with other measurements performed both in the solution and the gas phase in which αB-crystallin has been observed to form polyhedral oligomers with sizes ranging from 10-mers to 40-mers, with the species of highest abundance in the range between 24-32 subunits [119]. These results are thus in

(a)

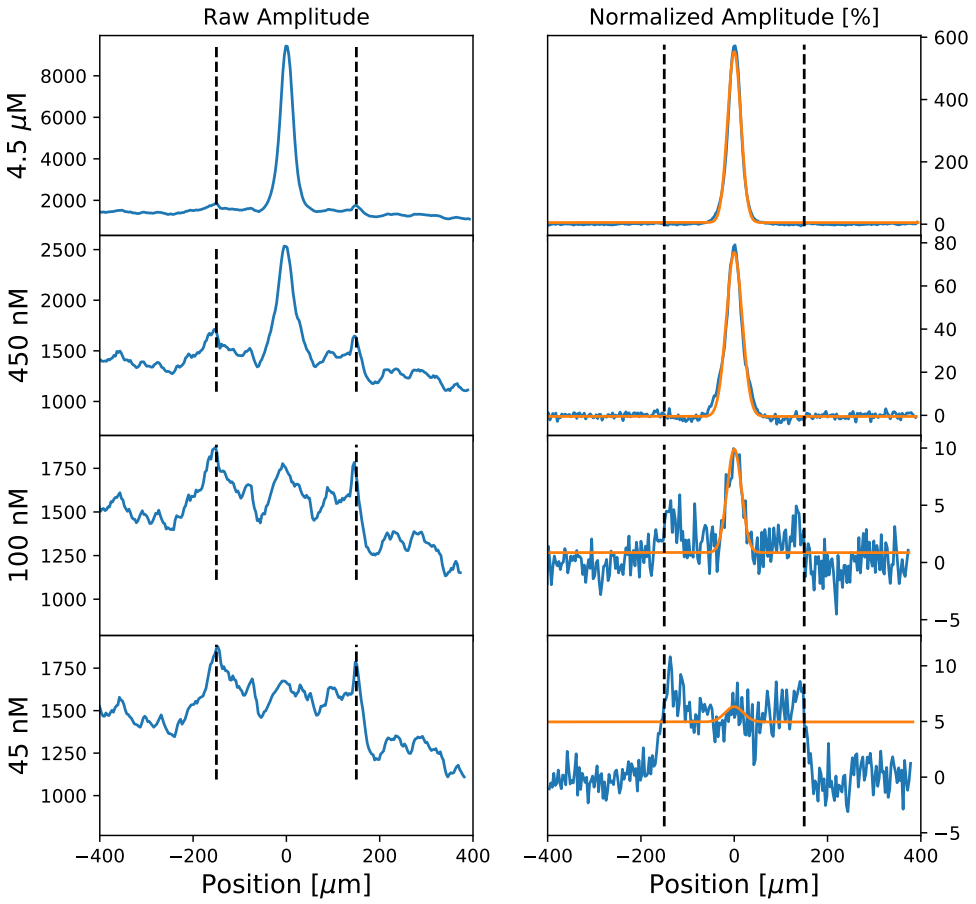

(b)

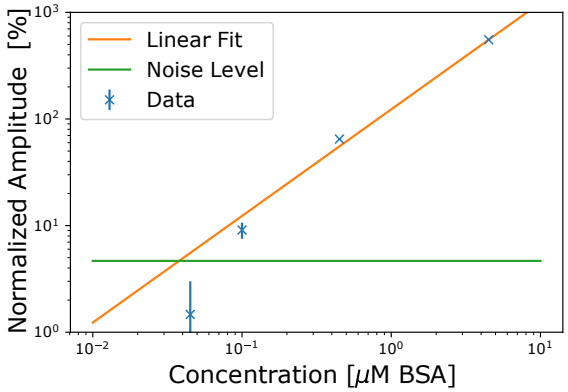

Fig. 2.5 (a) Profiles at position 0 (Figure (2.4a)) of the diffusion device for different BSA concentrations. The positions of the channel walls are indicated by two dashed black lines. Left: raw profiles. Right: background-corrected profiles. The orange line on the corrected background corresponds to the Gaussian fit, and the amplitude of that fit is reported plotted in (b). The baseline in the channel (-150 to 150 μm) is slightly higher than outside the channel. (b) Amplitude of the profile plotted against BSA concentration on a log-log scale. The lowest detected amplitude is 100 nM BSA. Representative profiles are shown in (a). The errors bars correspond to the standard deviation of the noise, and the green line corresponds to 3 standard deviations of the noise.

good agreement with biophysical characterisation performed in the gas phase using native mass spectrometry experiments [27, 16]. The intrinsic fluorescence set-up developed here is thereby demonstrated to be a powerful tool for the analysis of key biomolecules of physiological importance and, moreover, can be coupled with microfluidics to observe the self-assembly phenomena of proteins under native conditions in free-solution.

2.5 Conclusion

Analytical tools for characterising proteins and their complexes in solution phase without extrinsic labels are actively sought after for molecular biology and structural biology applications. The intrinsic fluorescence from proteins originates mainly from the aromatic residues tryptophan and tyrosine. A novel 280 nm-LED based fluorescence visualisation platform for characterising unlabelled proteins at nanomolar concentrations in the solution phase within microfluidic devices fabricated using soft-lithography has been described, designed, and built. This platform allowed us to visualise in real time the spatial distribution on the micron scale of intrinsic fluorescence of nanoscale proteins and protein complexes within microfluidic channels. Our results highlight the potential of this approach for label-free fluorescence and size measurements which consumes a small amount of sample, has fast processing times, and is robust for large scale integration of multiple components on a single chip. As an illustration of the power of this approach, fluorescence imaging is combined with diffusional sizing on chip to measure the hydrodynamic radius of proteins and self-assembled protein clusters of biological interest under their native conditions. The ability to image unlabelled proteins in solution in PDMS microfluidic chips has the potential to enable further studies of protein folding and unfolding pathways, kinetics, protein-protein interactions, and opens up the possibility of studying unlabelled proteins in a variety of microfluidic devices and architectures.

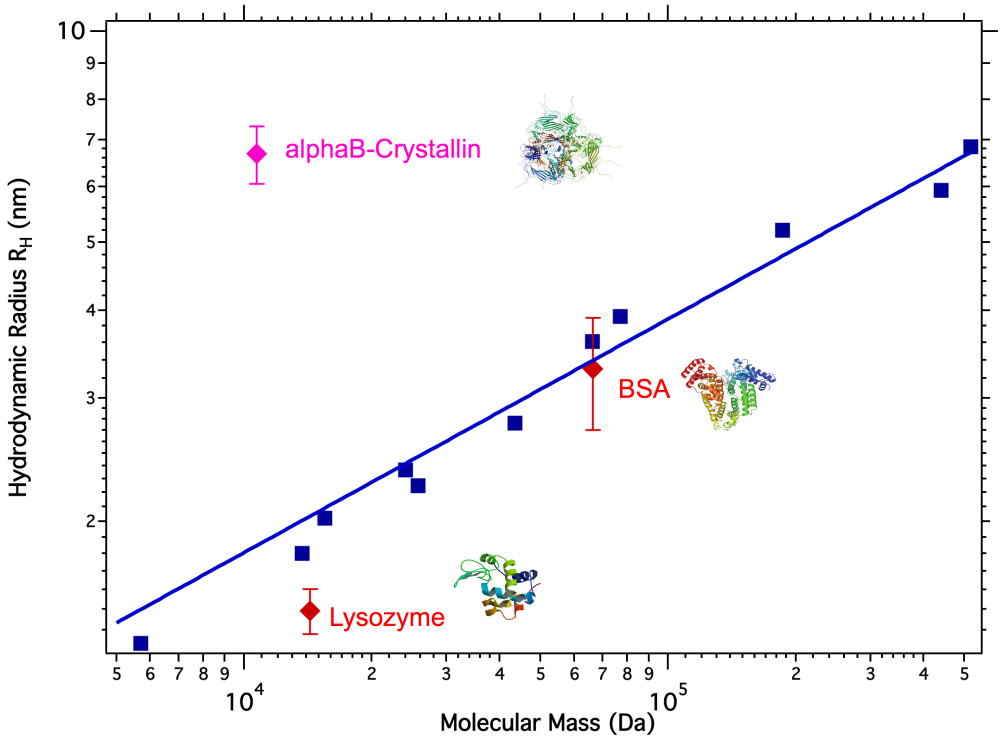

Fig. 2.6 Blue squares are the hydrodynamic radii of different monomeric proteins plotted as a function of their molecular mass from reference [264, 96] and the blue solid line is the corresponding fit. Red data points are of BSA and lysozyme monomers, and the pink data point corresponds to alphaB-crystallin obtained using our platform. The size of alphaB-crystallin deviates significantly from the expected hydrodynamic radius calculated from its monomeric molecular weight, and thus the measured protein size provides strong solution-phase evidence of protein complex formation under native conditions. The structure of the proteins [57, 231, 127] is shown next to their corresponding data point. Error bars denote the standard deviation of triplicate measurements repeated in separately fabricated devices or under different flow rates. The data was taken and processed by Pavan Kumar Challa, Maya A. Wright, and Yuewen Zhang.

Chapter 3

Oblique illumination interferometric scattering

3.1 Summary

This chapter is based on the manuscript: Quentin A. E. Peter, Pavan Kumar Challa*, Zenon Toprakcioglu*, Kadi Liis Saar, Jeremy J. Baumberg & Tuomas P. J. Knowles. "Oblique illumination interferometric scattering". Manuscript in preparation (* contributed equally). I analysed and processed the data. In addition to that, I participated to the data acquisition. I also explained the results using the mathematical framework presented in this chapter and had the realisation that oblique illumination would enable the usage of a spatial mask on the back focal plane. Finally, I contributed to writing the paper.*

Single molecule detection techniques enable crucial research in biological sciences. While fluorescence microscopy has been very successful, it suffers limitations that can be overcome by using light scattering. Interferometric scattering (iSCAT) microscopy is a recent technique that allows the detection of a single unlabelled protein. One limitation of this technique is the large number of photons that must be collected. Here, a novel technique is discussed that consists of sub-critical oblique illumination. By imaging the system with p-polarised light close to the Brewster's angle, the reflected fraction of the laser can be decreased without affecting the signal-to-noise ratio. Furthermore, oblique illumination removes spurious reflections that might be present in some setups, improving the signal further.

3.2 Introduction

Single molecule detection is crucial to further our understanding of biological systems [130, 132]. Fluorescence techniques [179] have revolutionised the field, but fluorescent labels have some limitations such as blinking and photo-bleaching [280]. Furthermore, adding a label to a molecule might perturb its natural function. Scattering microscopy methods are therefore of interest, but the extremely small signal from proteins has limited this approach. Interferometric scattering (iSCAT) microscopy [280, 19, 154] was developed to solve this problem by recording the interference of the scattered light with a carrier wave. The carrier wave is chosen so that the interference pattern is much brighter than any background, placing the system in the shot-noise limited regime. It should be noted that the shot-noise increases as well. As a consequence, the signal to shot-noise ratio is not dependent on the carrier wave. The signal is improved because the background contribution becomes negligible. This technique led to the detection of single unlabelled proteins [203, 279, 188]. The molecular weight can be estimated from the scattering contrast by recording thousands of landing events of proteins on a coverslip.

The carrier wave is created by the reflection on the interface between the coverslip and the solution. This has the advantage that the path length difference is very small, allowing the usage of short correlation-length lasers, which avoid interferences with other optical elements. The reflected fraction is fixed by Fresnel equations. The reflection is typically too strong to be imaged directly and requires combining frames from a high frame rate camera to increase the effective well depth. There is therefore a strong interest in decreasing the intensity of the carrier wave. A possible technique is to use the spatial separation of the reflected and scattered light on the back focal plane of the objective and apply a custom spatial filter [163, 63].

Here, the possibility to use sub-critical oblique illumination to modulate the reflected fraction is explored. The Fresnel equations predict a decrease in reflected intensity for p-polarised light when increasing the incidence angle. This technique does not require custom built optical filters. Furthermore, oblique illumination can remove spurious reflections that may degrade the signal on some setups. Finally, a technique based on Fourier transforms to measure reliably the illumination angle and the pixel size of an iSCAT setup is discussed.

3.3 Theory

3.3.1 Reflection coefficient modulation

An interferometric scattering (iSCAT) typically has an interface between coverslip and solution where 0.45% of the light is reflected. In the solution, usually very close to the surface, a particle scatters the transmitted light. Both the scattered light and the reflected light are collected on the detector which creates an interference pattern. The incident light ($I_0 = |E_{inc}|^2$) is reflected at the interface which creates a reflected electric field ($E_r = rE_{inc}$). The transmitted light is scattered on a particle which creates a scattered field ($E_s = sE_{inc}$). The collected intensity (I) is the interference between these two fields:

$$I = |E_r + E_s|^2 \approx I_0[|r|^2 + 2|r||s|\cos\phi] \tag{3.1}$$

where ϕ is the interference phase. As the scattering is much weaker than the reflection ($|s| \ll |r|$), the pure scattering term ($|s|^2$) is neglected. The scattering coefficient (s) is described by Rayleigh scattering and depends on the particle size. Ideally, the reflected coefficient (r) would be modulated so that the interference term ($I_0|r||s|$) is much larger than any background light, and that the reflected term ($I_0|r|^2$) does not saturate the camera. This is possible by varying the incidence angle. From Fresnel equation, the reflection coefficient r for p-polarised light depends on the incidence angle θ as:

$$r = \frac{n_g\sqrt{1-\left(\frac{n_g}{n_w}\sin\theta\right)^2} - n_w\cos\theta}{n_g\sqrt{1-\left(\frac{n_g}{n_w}\sin\theta\right)^2} + n_w\cos\theta} \tag{3.2}$$

with n_g and n_w the glass and water refractive index, respectively. $|r|^2$ decreases until reaching zero at Brewster's angle ($\theta_B = \arctan(n_w/n_g)$). The reflection coefficient does not affect the signal-to-noise ratio as the shot-noise is proportional to the square root of intensity:

$$S/N = \frac{I_0 2|r||s|\cos\phi}{\sqrt{I_0|r|^2}} = 2\sqrt{I_0}|s|\cos\phi \tag{3.3}$$

While a higher laser intensity improves the signal-to-noise ratio, the reflection coefficient does not have any effect. It can therefore be reduced to avoid over-exposing the camera, while still being large enough to stay in the shot-noise limited regime.

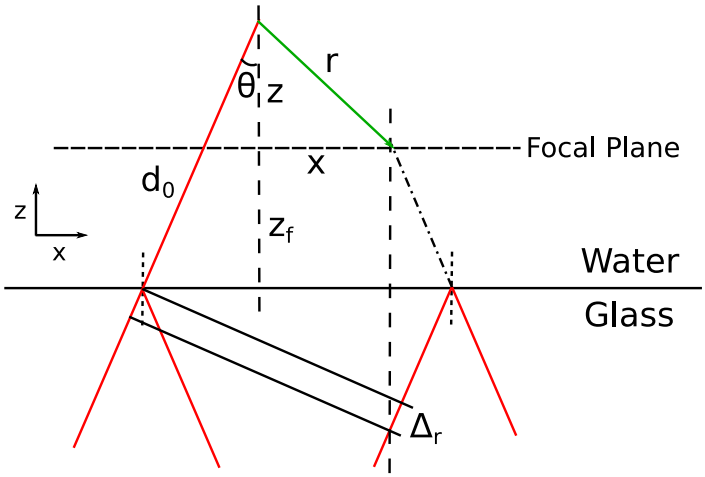

Fig. 3.1 Hologram geometry. The "Glass" part is assumed to have a reflective index equal to the water, so that the length can be compared. This does not apply if the focal plane is below the interface. Theta is the angle in the water, related to the other angle by Snell's law.

3.3.2 Spurious and interfering reflections

The laser is partly reflected on any interface where the refractive index changes. This reflection does not interfere with scattered light if the path difference is larger than the coherence length of the laser, typically hundreds of micrometers for laser diodes. For example, the back of the objective could reflect part of the light despite an anti-reflection coating. Equation (3.1) can be rewritten with the reflected intensity separated into interfering (r_i) and spurious (r_s) reflections:

$$I = |E_{ri} + E_{rs} + E_s|^2 \approx I_0[|r_i|^2 + |r_s|^2 + 2|r_i||s|\cos\phi] \tag{3.4}$$

where the spurious electric field E_{rs} does not interfere with the scattered signal or the signal reflected from the interface. Therefore, the signal-to-noise ratio is reduced:

$$S/N \propto 2\sqrt{I_0}|s|\cos\phi \Big/ \sqrt{1 + \frac{|r_s|^2}{|r_i|^2}} \tag{3.5}$$

3.3.3 Interference pattern hologram

The interferences are created by the difference of path between the reflected and the scattered light, as illustrated in Figure (3.1). The optical system is assumed to be relaying the magnified hologram to the camera [102]. The scattered light goes a distance d_0 from the glass-water interface to the particle, and a distance r from the particle to the focal plane. The reflected light

never crosses the focal plane, but the reflection seems to be coming from it, at a distance Δ_r, which is negative for small θ angles. Here, the coherence length is assumed to be large enough for parallel lines to have the same phase. The path difference is $\Delta \equiv \Delta_s - \Delta_r \equiv d_0 + r - \Delta_r$. The geometry gives for the reflected path distance:

$$-\Delta_r = \frac{z_f}{\cos\theta} - \sin\theta[x + \tan\theta(z + 2z_f)] \tag{3.6}$$

and for the scattered path distance:

$$\Delta_s = \frac{z + z_f}{\cos\theta} + \sqrt{x^2 + y^2 + z^2} \tag{3.7}$$

Therefore, the path length difference is:

$$\Delta = \sqrt{x^2 + y^2 + z^2} + (z + 2z_f)\cos\theta - x\sin\theta \tag{3.8}$$

By defining d as:

$$d \equiv \frac{\Delta}{\cos\theta} - (z + 2z_f) \tag{3.9}$$

Equation (3.8) can be rewritten as:

$$\frac{(x - d\tan\theta)^2}{A^2} + \frac{y^2}{B^2} = 1 \tag{3.10}$$

where A and B are defined as:

$$B^2 \equiv d^2 - z^2; \qquad A^2 \equiv \frac{B^2}{\cos^2\theta} \tag{3.11}$$

The hologram therefore looks like ellipsis of eccentricity $e = |\sin\theta|$ centered around $(x, y) = (d\tan\theta, 0)$. The innermost ellipse is centered around the smallest possible value of Δ, which corresponds to $x = |z|\tan\theta$. This is where the light would come if it was reflected by the particle. The iSCAT signal is given by $I \approx I_0[|r|^2 + 2|r||s|\cos\phi]$. The normalised interference pattern hologram is defined by:

$$H \equiv 1 + 2\frac{|s|}{|r|}\cos\phi \tag{3.12}$$

where $\phi = \frac{2\pi n_m}{\lambda}\Delta$.

3.3.4 Fourier transform of interference pattern

The hologram spatial frequencies are lead by the $\cos\phi$ term. Focusing on the x,y plane, $\phi(x,y) = 2\pi(r(x,y) - ax)n_m/\lambda + C$. In the case where $z = 0$, x, y, and r are linked by:

$$x = r\cos\theta; \qquad y = r\sin\theta$$

The Fourier transform of the following equation is of particular interest:

$$f(r,\theta) = \cos(2\pi r(1 - a\cos\theta)n_m/\lambda + C) \tag{3.13}$$

The Fourier transform of $\cos(2\pi rf)$ and $\sin(2\pi rf)$ are known [9] and correspond to an impulsion on a circle in Fourier plane, plus some small contributions. Therefore, a similar result for Equation (3.13) should be obtained. A cosine with an offset can be written as a sum of complex exponentials. The function of interest is now:

$$f(r,\theta) = \exp(\pm i2\pi r(1 - a\cos\theta)n_m/\lambda) \tag{3.14}$$

The 2d Fourier transform is given by [9, 26]:

$$F(u,v) = \int_{-\infty}^{\infty}\int_{-\infty}^{\infty} f(x,y)\exp(-i2\pi(ux+vy))dxdy \tag{3.15}$$

By offsetting the definition of the Fourier variables:

$$u' = \rho\cos\psi + u_0; \qquad v = \rho\sin\psi$$

The exponential term is:

$$\begin{aligned} -i2\pi\left[(u'x+vy) \pm r(1+a\cos\theta)\frac{n_m}{\lambda}\right] = \\ -i2\pi\left[r\rho\cos(\theta-\phi) + u_0 r\cos\theta \pm r(1-a\cos\theta)\frac{n_m}{\lambda}\right] \end{aligned} \tag{3.16}$$

Therefore, by setting $u_0 = \pm an_m/\lambda$, the equation is similar to the $a = 0$ case. The result therefore is two rings created by the Fourier impulsions with radius $\frac{n_m}{\lambda}$ and center $\pm\sin\theta_w n_m/\lambda$.

3.3.5 Illumination angle

By focusing the laser at the back focal plane of the objective, one can apply an oblique illumination to the sample, as it is done with a total internal reflection microscope. If the

particles of interest are relatively far from the surface, one needs to operate at subcritical angles to get some intensity from inside the channels. The focal length of the objective (F_{obj}) can be computed from the focal lens of the tube lens (f_{tl}) and the magnification (Ma). They are related by:

$$f_{obj} = \frac{f_{tl} n_{oil}}{Ma} \tag{3.17}$$

where n_{oil} is the refraction index of the immersion oil. The incidence angle is then computed from the laser position on the back-aperture from the middle (ΔX).

$$\sin(\theta_{oil}) = \frac{\Delta X}{f_{obj}} \tag{3.18}$$

where sin is used instead of tan because the objective is corrected for the Abbe sine condition. The angle in the water can then be computed from Snell's law:

$$\sin(\theta_{water}) = \frac{n_{oil}}{n_{water}} \sin(\theta_{oil}) = \frac{n_{oil}}{n_{water}} \frac{\Delta X}{f_{obj}} \tag{3.19}$$

3.3.6 Reflection at interfaces

The Fresnel equations are describing the reflected and transmitted coefficient from a medium 1 to a medium 2 depending on the incidence angle. They are, for s-polarized light:

$$R_s = \left| \frac{\cos\theta_i/n_2 - \cos\theta_t/n_1}{\cos\theta_i/n_2 + \cos\theta_t/n_1} \right|^2, \tag{3.20}$$

And for p-polarized light:

$$R_p = \left| \frac{\cos\theta_t/n_2 - \cos\theta_i/n_1}{\cos\theta_t/n_2 + \cos\theta_i/n_1} \right|^2, \tag{3.21}$$

One interesting angle, called the Brewster's angle, does not reflect light for p-polarisation. The light from a real laser is typically not perfectly collimated and polarised so some reflection would still occur.

3.3.7 Numerical aperture

The numerical aperture (NA) describes the maximum incidence angle (θ_{max}) in a medium with refraction index n that is accepted by the objective. It is given by:

$$NA = n \sin\theta_{max} \tag{3.22}$$

It is related to the maximum resolvable frequency by the Abbe diffraction limit:

$$f_{max,Abbe} = \frac{2NA}{\lambda} \tag{3.23}$$

This can be used to compute the useful image pixel size (px). The maximum frequency that can be resolved is:

$$f_{max,px} = \frac{1}{2px} \tag{3.24}$$

Therefore, the pixel size must be smaller than:

$$px < \frac{\lambda}{4NA} \tag{3.25}$$

In order to detect the Fourier circle described above, the numerical aperture must verify:

$$\frac{n(1+\sin\theta)}{\lambda} < f_{max,Abbe} \tag{3.26}$$

$$NA > n\frac{1+\sin\theta}{2} \tag{3.27}$$

3.3.8 Coherence length

In the previous paragraph, a single reflection that is perfectly interfering with the scattering signal is assumed. In reality, laser diodes have relatively broad spectrums, typically $\Delta\lambda = 2$ nm. The coherence length is given by [7]:

$$L = \sqrt{\frac{2\ln 2}{\pi}}\frac{\lambda^2}{\Delta\lambda} \tag{3.28}$$

For a typical laser diode, this can be as short as 100 um. Therefore, if there is a reflection from the back of the objective, this reflection would not interfere with the scattered signal.

3.4 Methods

3.4.1 Setup

A commercial TIRF microscope from Nikon (Ti2) is used below the total internal reflection angle. A drop of solution is placed on a coverslip. This is similar to a state-of-the-art iSCAT setup where the laser is off-axis. The principle of the setup is sketched in Figure (3.2). An oil immersion objective is used for its high numerical aperture and to avoid creating interfaces

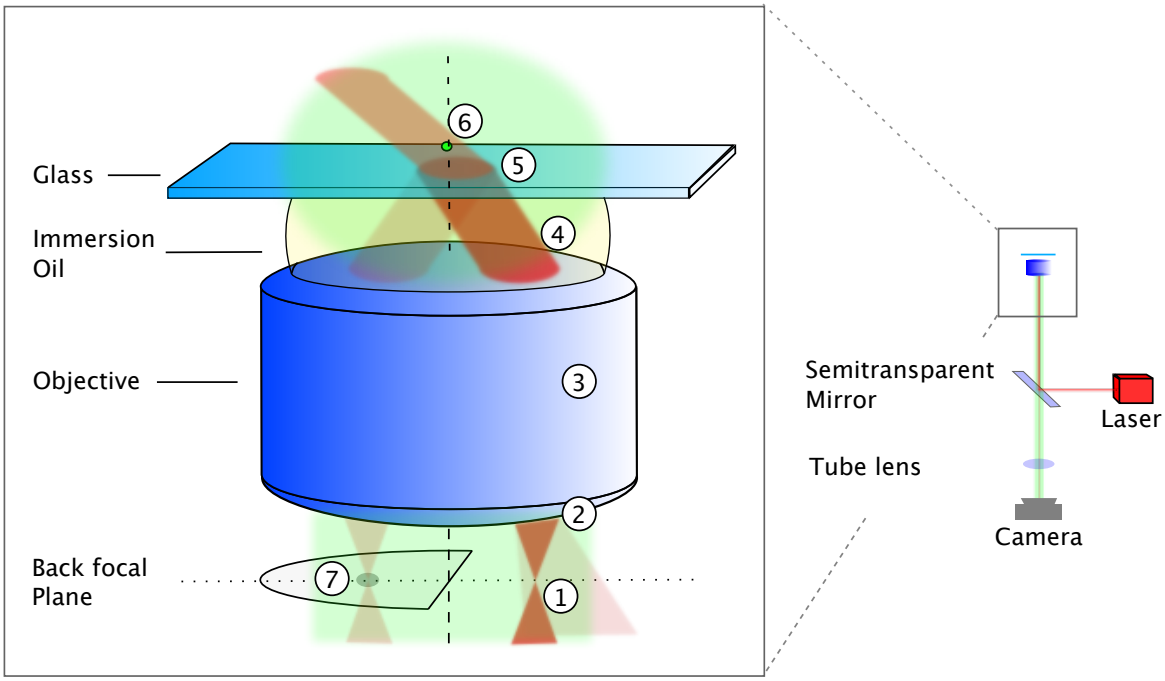

Fig. 3.2 Sketch of the setup. The light is emitted by the laser and reflected on a semitransparent mirror. It is focussed on the back focal plane (1) and passes through the objective (3). On the way, the interfaces in the objective will reflect a little light (2). The light passes through a refractive index matched oil (4) to avoid extra interfaces. At the glass-water interface (5) the light is separated into transmitted and reflected components. The transmitted light reaches particles that scatter (6). This scattered light interferes with the reflected light from the laser. Finally, a spatial mask can be placed on a semi disk on or near the back focal plane to improve the contrast (7).

between the objective and the cover slip. A laser is focused on the back focal plane of an objective, Figure (3.2.1). The laser or an optical element is mounted on a stage to allow a translation of the laser focal spot on the back focal plane, while keeping the laser parallel to the objective optical axis. The back of an objective is usually not flat, and a reflection of light coming with an offset will not be reflected in the optical path, Figure (3.2.2). Focusing the laser on the back focal plane of the objective collimates the laser, Figure (3.2.4). The emplacement of the back focal plane can be found by minimising the size of the spot on the ceiling. The collimated angle depends on the offset between the laser and the optical axis of the objective. Upon reaching the coverslip solution interface, Figure (3.2.5), a fraction of the light is reflected, depending on the incidence angle as well as on the laser polarisation. The transmitted light is scattered by particles in solutions, Figure (3.2.6), and collimated by the objective. The reflected light is focused on the back focal plane of the objective, Figure (3.2.7). The focus position of the reflected light is separated from the incident light on the back focal plane by twice the offset. This creates the opportunity to use a spatial Fourier mask [163, 63]. Placing the mask on the back of the objective removes the requirement of modifying the setup, as the mask can simply be taped to the back of the objective, and does not require a custom setup.

3.4.2 Data processing

Removing the reflected intensity ($|r|^2$) and the surface scattering - caused by the surface roughness - is essential to detect the particle of interest if it does not scatter strongly. To that end, the stability of the background and of the surface scattering is used. The signal of the particle of interest changes over time, while the background remains constant. The difference between an unbounded particle and a bounded particle is used for landing events. For diffusing particles, the median value of a stack of nearby frames can be used to extract a background. Once a static background (Bg) is extracted, the dynamical contribution can be extracted from a frame (I):

$$\frac{I-Bg}{\sqrt{Bg}} = \frac{I_0 2|r||s|\cos\phi}{\sqrt{I_0|r|^2}} = 2\sqrt{I_0}|s|\cos\phi \tag{3.29}$$

In the Fourier space, the functional form of $\cos\phi$ is described by a circle near the interface, and by a disk otherwise. The radius of the disk (R_d) depends on the wavelength (λ) and on the pixel size (p_x) as:

$$R_d = \frac{p_x n_m}{\lambda} \tag{3.30}$$

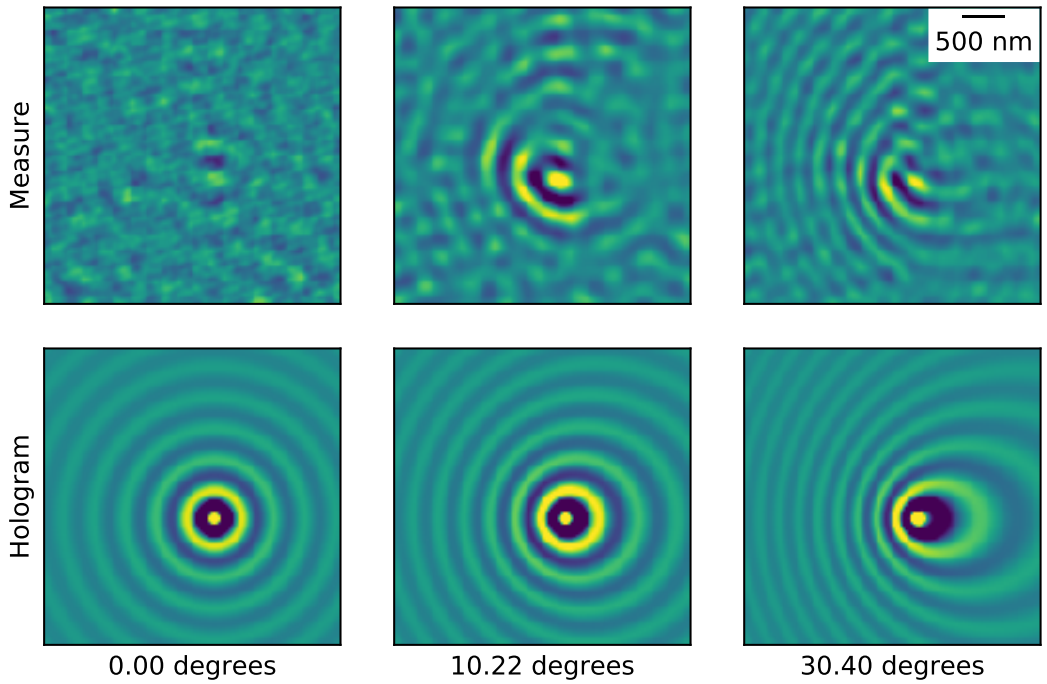

Fig. 3.3 Images of a strong scatterer compared to the predicted hologram at a fixed position. At normal incidence, the spurious reflection hides the signal. At higher angles, the spurious reflection is not present, but the image becomes more distorted. The color scale ranges from the lowest to the highest value for each image and is therefore not the same for each panel. The normal incidence, for example, has a much stronger intensity, as illustrated in Figure (3.4).

where n_m is the medium refraction index. The position of the center of the disk (X_d) depends on the incidence angle θ:

$$X_d = R_d \sin\theta \tag{3.31}$$

The pixel size and incidence angle can therefore be easily measured from the Fourier transform of an iSCAT image.

3.5 Results and discussion

The iSCAT signal from a strong scatterer has been recorded at different incidence angles. Because the scattering signal from this particle is strong enough, it can be detected without removing a static background, and therefore does not need to be dynamic. A few representative frames are shown in Figure (3.3). The corresponding recorded intensity is shown in Figure (3.4). As expected, despite the decrease in reflected intensity, the signal intensity at 10°

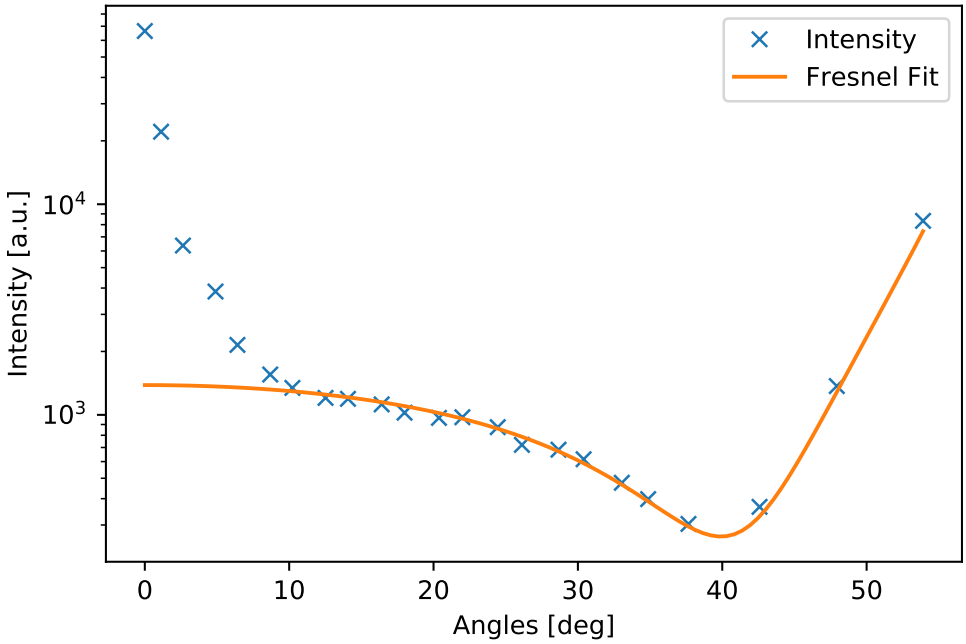

Fig. 3.4 Scattering intensity versus incidence angle. The measured intensity is composed of the reflected intensity (orange fit) and of spurious reflections near the normal angle.

and at 30° is very similar, while the eccentricity of the ellipses increases. More surprisingly, the signal is completely hidden at a 0° angle. This can be understood by fitting the data in Figure (3.4) to the Fresnel equations (3.20 and 3.21). A large discrepancy can be observed near normal incidence. This discrepancy can only be explained by a spurious reflection. As this spurious reflection has a path length which is longer than the coherence length of the laser, the interference signal is hidden. This explains why the particle is not visible on the normal incidence image in Figure (3.3).

Analysing the Fourier transform of the iSCAT image reveals a disk as shown in Figure (3.5). Knowing precisely the size of the pixels is useful as the diameter depends on the ratio of the pixel size to the medium wavelength. The position of the disk depends on the incidence angle, which means that the incidence angle can easily be measured. Spurious reflections that are not present at larger incidences can be seen at a normal angle. The variation from the laser and from the scattering signal are clearly defined. As expected, 40 nm polystyrene colloids have a lower signal than 100 nm.

In comparison to established iSCAT techniques, this setup arrangement makes it easier to avoid spurious reflections. This has the potential to massively improve the signal-to-noise ratio, provided that these spurious reflections are significant, as is the case in the present

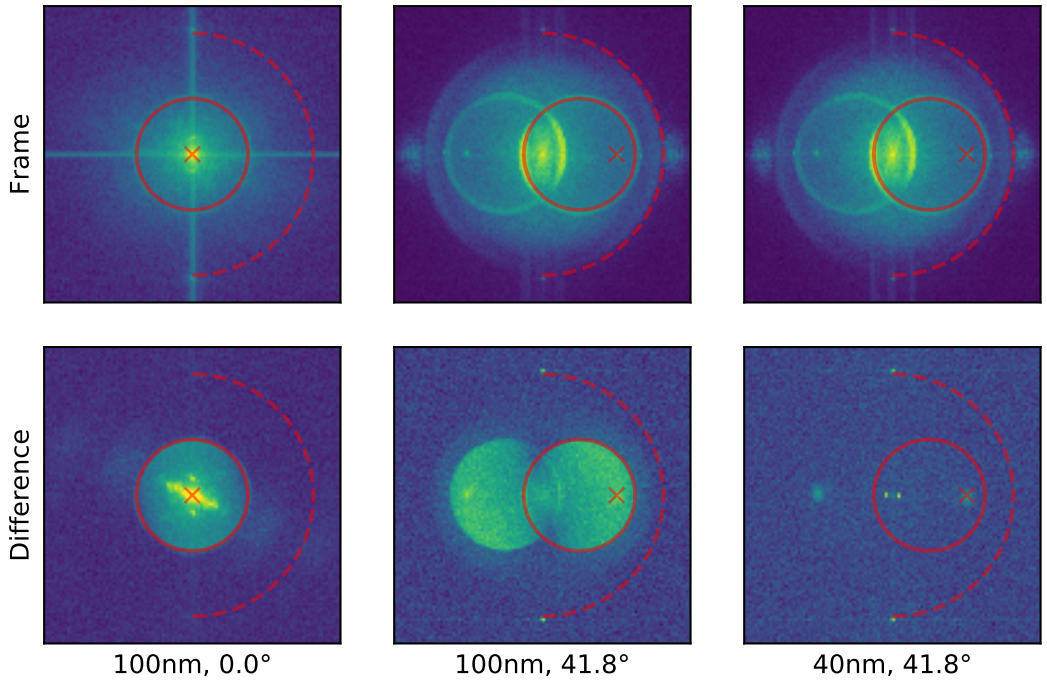

Fig. 3.5 Fourier Transform of iSCAT images. The top row is the transform of a single frame, while the bottom row is the transform of the difference of two consecutive frames. The frame rate is adjusted to 125 FPS by summing consecutive frames of a faster video. The dashed circle indicates the Abbe diffraction limit. The solid red line indicates the expected scattering circle, and the red cross indicates the position of the reflected laser. At normal incidence, the reflected laser dominates both Fourier transforms. By increasing the angle, the interfering scattering becomes dominant. For the present settings, the signal from 100 nm scatterers is stronger than the camera shot-noise, while 40 nm scatterers are mostly hidden in the noise.

system. Furthermore, new options to control the reflected fraction of excitation light are available. This is an important challenge in iSCAT systems. For p-polarized light, the reflected fraction can be arbitrarily attenuated by approaching Brewster's angle. If the reflected fraction is too low, the system is not shot-noise limited and the signal is hidden in the background light. If the reflected fraction is too high, the contrast on the raw images is poor, which makes aligning the microscope challenging. Furthermore, the high number of photons requires a camera with either a high frame rate or a large well depth. It is important to note that - perhaps surprisingly - while the contrast of the raw images depends on the reflected fraction of incident light, the signal ratio of the processed images does not, as explained in the theory. Established iSCAT techniques usually suffer from the latter issue, where too much light is reflected into the camera. The usual approach to mediate this issue lies in the addition of a spatial mask in the optical path. [163, 63] This approach requires placing the mask in a region where the incident, reflected, and scattered lights are spatially separated. Indeed, if the scattered or incident lights are attenuated, the signal-to-noise ratio decreases. Oblique illumination is particularly well suited to solve this problem, as illustrated in Figure (3.2). The excitation and reflected lights are completely separated on the back focal plane. As the reflected light is focussed on the back focal plane, the spatial mask can be as small as the focal spot, resulting in a reduction of the amount of filtered scattered light. Finally, The mask can be placed right below the objective. This makes the addition of a mask easy on a commercial microscope, where most of the light path is not easily accessible. Here, we used a commercial TIRF microscope that has a built-in mechanism to change the angle of the incident light.

3.6 Conclusion

Oblique illumination is a convenient way of modulating the reflected coefficient of iSCAT setups in order to improve the contrast without modifying the signal-to-noise ratio. Furthermore, it can dramatically improve the signal if spurious reflections are present. In addition, a method to quantify spurious reflections by measuring the intensity at different incidence angles is presented. The potential to measure the system pixel size and incidence angle by Fourier analysis of iSCAT images was also discussed.

Chapter 4

Interferometric scattering correlation (iSCORR) microscopy

4.1 Summary

This chapter is based on the manuscript: Quentin A. E. Peter, Raphael Jacquat*, Georg Krainer* & Tuomas P. J. Knowles. "Interferometric scattering correlation (iSCORR) microscopy". Manuscript in preparation (* contributed equally). I had the realisation that iSCAT signal temporal correlations could be used to size particles in solution. In addition to that, I derived the mathematical framework needed to extract the size and the concentration from the correlation time described in this chapter. Moreover, I created the data analysis and processing framework and used it to analyse the data. I also contributed to the creation of the setup and to the acquisition of the data. Finally, I contributed to writing the paper.*

Methods for particle detection and characterisation are crucial for enabling research in many fields. Leading edge research in protein science for amyloid diseases is interested in the detection of single particles in solution. This is usually done with fluorescence based microscopy technology that requires modifying the protein by attaching a label to it. Here, a novel technique is described to detect and size proteins in solution using interferometric scattered light. The size of the proteins is measured by interferometrically measuring the diffused distance, and the concentration by measuring the scattering intensity. This technique is able to detect single particles as well as large concentration of particles. The results shown here demonstrate the capabilities of the technique and open up a path towards a better physical understanding of proteins.

4.2 Introduction

Detection and identification of small bio-molecules is extremely important to understand biological processes [179]. Biophysical research has been transformed by the ability to covalently attach a fluorescent label to a single protein which allows single particle detection. This requires modifying the particle, in turn affecting its properties. Moreover, fluorescent labels tend to blink and photo-bleach [280]. In this context, scattering is a promising alternative. The scattering signal of a particle or of an attached scattering label such as a gold nanoparticle does not bleach or blink [280, 251]. While the scattering signal of a single atom in vacuum was successfully detected [253], the strong dependence of the scattering signal on the size of the particle (volume squared) makes it very hard to distinguish the scattering signal from the background light.

Interferometric scattering (iSCAT) [280, 154] was developed to increase the scattering signal above the background. Excitation light is excluded by most microscopy techniques, either by optical filters for fluorescence microscopy or by separating the detection and excitation paths for dark field microscopy. Instead, iSCAT uses part of the excitation light to interfere with the scattered signal, improving the size dependence of the signal - proportional to volume - and making it easy to surpass the background noise. This regime is called shot-noise limited, as the background noise is negligible compared to the shot-noise. It should be noted that the shot-noise is increased as well, which implies that the signal-to-noise ratio is not better than a shot-noise limited dark field scattering experiment. iSCAT led to the detection of label-free proteins as small as $19kDa$ [203, 279, 188]. The well depth of the camera - the number of photons it can collect for each frame - is a limiting factor due to the large number of detected photons. The camera used for iSCAT experiment therefore has a high frame rate and frames are averaged together to increase the effective well depth [251]. More advanced techniques have been used to reduce the number of detected photons without affecting the signal-to-noise ratio. They consist in modulating the collected fraction of excitation light. For example, a spatial filter has been used on the Fourier plane where reflected and scattered light are separated [163, 63].

iSCAT is limited to detecting particles bound to a surface because the interferometric phase varies very rapidly in solution, making it impossible to detect diffusing particles for long exposure times. There are however several disadvantages in measuring scattering on the surface. First, scattering from the surface is very strong compared to scattering from a small particle, hiding the signal under some conditions. Second, the scattering intensity of the particles depends exponentially on the distance to the surface. This might explain why thousands of landing events are needed to accurately size a protein [203, 279]. When the

particle is sufficiently close to surface - typically within one wavelength - evanescent waves are transmitted, which increases the scattered signal exponentially by up to 65% [187, 162].

Here, interferometric scattering correlation (iSCORR) microscopy is presented. This novel technique combines image correlation analysis of single particles and the improved signal of interferometric scattering microscopy (iSCAT) to enable label-free sizing of small colloids and biomolecules at very low concentration of particles in solution. A high speed camera is used to capture iSCAT images away from the surface with a frame rate faster than diffusion by a fourth of the wavelength. This resolves the well depth limitation and uses the strong dependence of the interference phase on the position to interferometrically size particles. These frames are then combined by a Fourier-space-based analysis algorithm and, through image correlation analysis, iSCORR allows the sizing of particles down to the single molecule level. This technique is compatible with single particle measurements in cells and microfluidic chips. Another major advantage of this technique over detecting a single landing event is that a measurement can be done by detecting many diffusion steps of the same molecule.

4.3 Theory

Rayleigh scattering describes the scattering from small particles, typically much smaller than the light wavelength (λ). The intensity at a distance R and angle θ of a particle of diameter d is proportional to the incident intensity I_0:

$$I_s = I_0 \frac{1+\cos^2\theta}{2R^2} \left(\frac{2\pi n_m}{\lambda}\right)^4 \left(\frac{n_p^2 - n_m^2}{n_p^2 + 2n_m^2}\right)^2 \left(\frac{d}{2}\right)^6 \tag{4.1}$$

where n_m is the refractive index of the surrounding medium and n_p is the refractive index of the particle. Because of the d^6 dependency on the particle size, this signal is very hard to separate from background light. This is solved by adding a coherent carrier wave and by detecting the interferometric pattern, a technique called iSCAT. Part of the excitation light is reflected on the glass-water interface (reflection coefficient r) and part is scattered (scattering coefficient s given by Equation (4.1)):

$$I \approx I_0(|r|^2 + 2|r||s|\cos\phi) \tag{4.2}$$

where I_0 is the excitation intensity and $|s|^2$ is assumed to be negligible. The interference phase (ϕ) is provided by the path difference between the excitation light reaching the focal plane directly and the one being scattered by the particle. This depends on the particle

distance to the focal plane (Z), on the distance of the focal plane from the interface (Z_f), and on the horizontal distance of the particle (ρ), as shown in Figure (4.1):

$$\phi = \frac{2\pi}{\lambda_m}\left(\sqrt{\rho^2+Z^2}+Z+2Z_f\right) \tag{4.3}$$

where λ_m is the laser wavelength in the medium ($\lambda_m = \lambda/n_m$). Interestingly, this is almost independent on Z for $Z<0$. Indeed, being scattered by a particle does not add path length if the particle is on the way to the focal plane. For $Z>0$, the Z dependence is very strong, inverting the interference pattern by moving by a quarter wavelength. Detecting particles therefore requires image correlation analysis. Combining frames which each have a small amount of information is the key idea behind iSCORR. A correlation function is created by averaging over all couples of frames separated by a correlation time Δt (See below for derivation):

$$g^2 \equiv \frac{\left\langle \left(\Delta\sqrt{I}\right)^2 \right\rangle_T}{I_0} = |s|^2\left(1-\exp\left(-\frac{\Delta t}{\tau}\right)\right)+\frac{\sigma_n^2}{2I_0} \tag{4.4}$$

where σ_n^2 is the normalised variance of the noise. The correlation time τ is defined as:

$$\tau \equiv (q^2 D)^{-1} \qquad q = \frac{2\pi}{\lambda_m}\sqrt{2\left(1+\frac{Z}{\sqrt{\rho^2+Z^2}}\right)} \tag{4.5}$$

The standard deviation of the correlation function is given by the sampling error when averaging over n frames [5]:

$$\sigma_{g^2} = \sqrt{\frac{2}{n}}\frac{\sigma_n^2}{2I_0} \tag{4.6}$$

Interestingly, the noise depends linearly on the exposition time ($\propto I_0$) and on the square root of the number of frames ($\propto \sqrt{n}$). This means that the noise is lower if the frames are first combined and then correlated. On the other hand, the signal from the particles is substantially reduced if the frames are combined for a total integration time larger than the correlation time (τ). This is indeed the reason why iSCAT can't detect diffusing particles without the iSCORR technique. The signal-to-noise reaches a maximum for a single frame exposure time lower than half the correlation time.

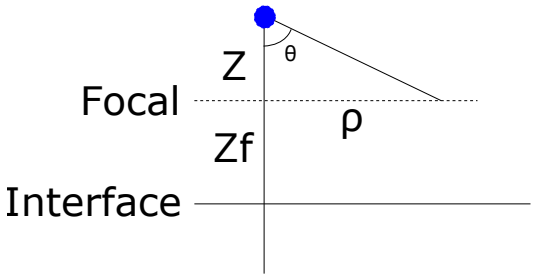

Fig. 4.1 iSCORR geometry used to compute path.

4.3.1 Derivation of the correlation function

An iSCAT signal is created when a reflected fraction (r) and a scattered fraction (s) of an incident wave with intensity I_0 interfere:

$$I = I_0(|r|^2 + 2|r||s|\cos\phi) \tag{4.7}$$

where $|s|^2 \ll |r|^2$ is neglected and (ϕ) is the interference phase. The shot-noise variance of the measurement (σ_I^2) is assumed to be proportional to the intensity:

$$\sigma_I^2 = I\sigma^2 \approx I_0|r|^2\sigma^2 \tag{4.8}$$

where σ^2 is the normalised variance. The interference phase is calculated from Figure (4.1):

$$\phi = 2\pi/\lambda_m\left(\sqrt{\rho^2+Z^2}+Z+2Z_f\right) \tag{4.9}$$

where the wavelength in the medium is $\lambda_m \equiv \lambda/n_m$, with λ the wavelength of the light in vacuum and n_m the medium refraction index. Z is the distance from the focal plane to the particle, ρ is the horizontal distance, and Z_f is the distance from the focal plane to the coverslip-solution interface. The reflected (r) and scattered (s) contributions to the iSCAT signal in Equation (4.7) can be separated by using a square root series and $|r| \gg |s|$:

$$\sqrt{I} \approx \sqrt{I_0}\,(|r| + |s|\cos\phi) \tag{4.10}$$

The corresponding noise variance is:

$$\sigma^2_{\sqrt{I}} = \left(\frac{1}{2}\frac{1}{\sqrt{I}}\sigma_I\right)^2 = \frac{\sigma^2}{4} \tag{4.11}$$

From there, the correlation curve can be defined (g^2) as the normalised time average of the signal difference. Assuming I_0 and $|r|$ are constant, and that $|s|$ varies significantly slower than the phase:

$$g^2 \equiv \frac{\left\langle \left(\Delta\sqrt{I}\right)^2 \right\rangle_T}{I_0} = |s|^2 \left\langle (\Delta\cos\phi)^2 \right\rangle_T + \frac{\sigma^2}{2I_0} \tag{4.12}$$

where the signal and the noise are not correlated. The temporal average of the square of the noise is its variance. As two frames are combined by subtraction, the variance of the noise is doubled. Assuming n frames are combined to get this time averaged, the sampling error is given by:

$$\sigma_{g^2} = \sqrt{\frac{2}{n}} \frac{\sigma^2}{2I_0} \tag{4.13}$$

Diffusion is modelled by random walk with variance $\sigma_Z^2 = \left\langle (\Delta Z)^2 \right\rangle_T = 2D\Delta t$. The phase difference $\Delta\phi$ depends on the spatial differences ΔZ and $\Delta\rho$:

$$\begin{aligned} \Delta\phi &= k(\Delta Z + \sqrt{(\rho+\Delta\rho)^2 + (Z+\Delta Z)^2} - \sqrt{\rho^2+Z^2}) \\ &\approx k\left(\Delta Z\left(1 + \frac{Z}{\sqrt{\rho^2+Z^2}}\right) + \Delta\rho\frac{\rho}{\sqrt{\rho^2+Z^2}}\right) \end{aligned} \tag{4.14}$$

where $k = 2\pi/\lambda_m$. Because ΔZ and $\Delta\rho$ are Gaussian random variables with variances $\sigma_Z^2 = \sigma_\rho^2 = 2D\Delta t$, $\Delta\phi$ is as well.

$$\sigma_\phi^2 \equiv \left\langle (\Delta\phi)^2 \right\rangle_T \approx 4D\Delta t k^2 \left(1 + \frac{Z}{\sqrt{\rho^2+Z^2}}\right) \tag{4.15}$$

The first term in Equation (4.12) is developped by using $\left\langle \sin^2\phi(t) \right\rangle_T = 0.5$, $\left\langle \cos\phi(t) \right\rangle_T = 0$, and $2\cos x\cos y = \cos(x-y) + \cos(x+y)$:

$$\left\langle (\Delta\cos\phi)^2 \right\rangle_T = 1 - \langle\cos\Delta\phi\rangle_T \tag{4.16}$$

As $\Delta\phi$ follows a Gaussian distributions, $\left\langle (\Delta\phi)^{2n} \right\rangle_T = \sigma_\phi^{2n}(2n-1)!!$:

$$\langle\cos\Delta\phi\rangle_T = \sum_{n=0}^{\infty} \frac{(-1)^n \left\langle (\Delta\phi)^{2n} \right\rangle_T}{(2n)!} = \exp\left(\frac{-\sigma_\phi^2}{2}\right) \tag{4.17}$$

Therefore, the correlation function is finally given by:

$$g^2 = |s|^2 \left(1 - \exp\left(-\frac{\Delta t}{\tau}\right)\right) + \frac{\sigma_n^2}{2I_0} \tag{4.18}$$

where the correlation time τ is defined:

$$\tau = (q^2 D)^{-1} \qquad q = \frac{2\pi}{\lambda_m}\sqrt{2\left(1 + \frac{Z}{\sqrt{\rho^2 + Z^2}}\right)} \tag{4.19}$$

4.3.2 Measurement under flow

A constant translation can be detected from a stack of iSCORR images. This means that iSCORR can be used as a flow meter technique. Furthermore, this contribution can be removed, which allows iSCORR to size particles under flow.

In the Fourier plane, a translation is equivalent to a phase difference [214]. If f_{n+1} is just f_n with a translation $(\Delta x, \Delta y)$:

$$f_{n+1}(x,y) = f_n(x + \Delta x, y + \Delta y) \tag{4.20}$$

then the Fourier transforms F are related by:

$$F_{n+1}(\varepsilon, \eta) = \exp(i\theta) F_n(\varepsilon, \eta) \tag{4.21}$$

where $\theta \equiv 2\pi(\varepsilon \Delta x + \eta \Delta y)$. As described before, taking the square root of the iSCAT signal separates the reflected and scattered intensity. Assuming F_n is constant over time, the Fourier transform of the frame n can be written as:

$$F\{\sqrt{I_n}\} \approx F_r + F_{s,n} \tag{4.22}$$

$F_{s,n+1}$ is related to $F_{s,n}$ by a difference on the scattering pattern $\delta F_{s,n}$, from the diffusion, and by a translation:

$$F_{s,n+1} = \exp(i\theta) F_{s,n} + \delta F_{s,n+1} \tag{4.23}$$

The difference used to compute the iSCORR signal is therefore given by:

$$\Delta_{n+1} = F_{s,n+1} - F_{s,n} = (\exp(i\theta) - 1) F_{s,n} + \delta F_{s,n+1} \tag{4.24}$$

Similarly, a forward calculation can be done:

$$\Delta_n = F_{s,n} - F_{s,n-1} = \exp(-i\theta)\left((\exp(i\theta) - 1)F_{s,n} + \delta F_{s,n}\right) \tag{4.25}$$

If $\theta = 0$, this is the simple case with no translation. Δ_{n+1}/Δ_n can be used as a constant between all frames to detect the offset by assuming δF to be small:

$$\frac{\Delta_{n+1}}{\Delta_n} \approx \exp i\theta \tag{4.26}$$

The Fourier transform of $\exp i\theta$ is a delta function that can be used to compute the offset, and therefore the flow rate. When θ is known, a new difference is computed to extract the δF:

$$\Delta\Delta_n = \Delta_{n+1} - \exp(i\theta)\Delta_n = \delta F_{s,n+1} - \delta F_{s,n} \tag{4.27}$$

This is a sum of Gaussian random variables with the same variance. The derivation can therefore proceed as in the case with no flow.

4.3.3 Basis function amplitude

The light emitted by a horizontal electric dipole μ above an interface is separated between s-polarised and p-polarised light [187]. Because the p-polarised light is seen at an angle from the detection point, the intensity decreases relative to the detection angle θ as $\cos^2(\theta)$. The light is detected after passing through the coverslip-solution interface, which means that the transmission coefficients from Fresnel equation are applied. The intensity collected on the camera corresponds to the projected intensity on the focal plane, which corresponds to adding a $\cos(\theta)$ term. The intensity of scattering at an angle θ is therefore proportional to:

$$|s|^2 \propto \left(|t^s(\theta)|^2 + |t^p(\theta)|^2 \cos^2(\theta)\right) \frac{\cos(\theta)}{R^2(\theta)} \tag{4.28}$$

Note that the expression does not take into account the spherical aberration introduced by the interface.

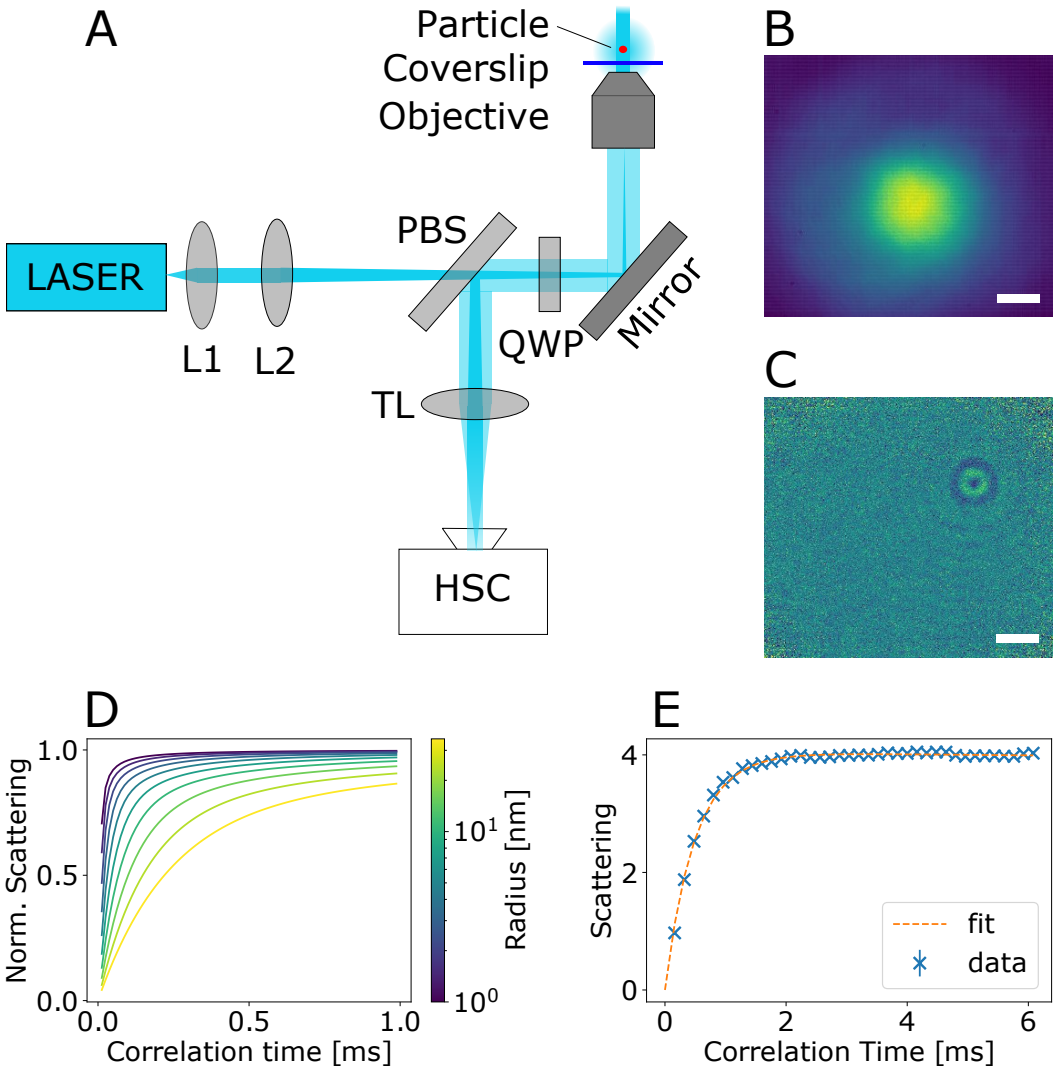

Fig. 4.2 (A) Sketch of an iSCAT setup. A laser is collimated by a first lens (L1) and focussed on the back focal plane of the objective by a second lens (L2). The light goes through a polarizing beam splitter (PBS) and a quarter wave plate (QWP) that transforms the linearly polarised light into a circularly polarised light. A mirror then reflects the light towards a high numerical aperture oil immersion objective. On the other side, the interface between the coverslip and the solution reflects part of the light, and particles in the solution scatter the transmitted light. These two lights go back through the objective, are reflected by the mirror, pass through the quarter wave plate, and are reflected by the polarising beam splitter towards the tube lens (TL) that focuses the scattered light on the high speed camera (HSC). As an example, a single 50 nm radius polystyrene colloid is imaged for 400 ms. (B) The recorded images are dominated by the reflected intensity. (C) The particles are visible after data processing by comparing two frames. The detected scattering depends on the temporal distance between the two frames, which is called the correlation time. (D) The scattering vs correlation time curve depends on the particle hydrodynamic radius. The curves here are normalised to the uncorrelated scattering intensity. (E) By processing the data with different correlation times, the radius of the particle is measured by fitting with the curves in (D).

4.4 Methods

4.4.1 Setup

The setup is based on state-of-the-art iSCAT capable of detecting label-free single proteins [99, 19], as illustrated in Figure (4.2A). Briefly, the setup is composed of a laser that is focused on the back focal plane of an oil immersion objective to illuminate the sample (dissolved or suspended in water), which is placed on a glass cover slip. The refractive index difference between the coverslip and the solution causes some of the laser intensity to be reflected. The laser then reaches particles in solution or suspension in water. These particles scatter the light. The reflected and scattered light is collected on a fast camera that records the interference pattern.

The laser intensity should be as strong as possible to increase the scattered light. Laser diodes are preferable as the coherence length is limited, which avoids interferences with other parts of the optical system. The coherence length should be at least twice the distance from the particle to the interface. The temporal coherence can be decreased with laser modulation to reduce the background [77]. The scattering signal depends strongly on the wavelength. Rayleigh scattering is much stronger for small wavelengths, but the quantum efficiency of most cameras is maximal around $\lambda \approx 600$ nm and glass optics transmittance falls quickly for small wavelengths. The wavelength of the laser must therefore be carefully selected to maximise the signal quality.

Careful selection of the camera is crucial for iSCORR. While the high frame rate is only a way to increase the effective well depth for iSCAT, it directly limits the ability to measure small particles for iSCORR. For example, a protein with hydrodynamic radius 3.5 nm - such as Bovine Serum Albumin - has a diffusion coefficient $D = 7 \cdot 10^{-11}\ m^2/s$. From Equation (4.5), the integration time should be at most 10 μs, which corresponds to a frame rate of 100 kHz. Assuming that the protein needs to be integrated for 0.4 s, as it has been documented in the literature [99], the field of view needs to be at least $\sqrt{2Dt} \approx 10\ \mu m$. By choosing the optics so that the pixel size is below $\lambda_m/2$ (160 nm) for example, the required number of pixels for detecting a single protein is 64x64. With a standard 12bit pixel, the camera acquisition rate must be above 0.4 Gpx/s or 0.6 GB/s. The RAM size then limits the experiment time. On some high speed cameras, there are two systems to read out the frames in alternation. This causes the even and odd numbered frames to be slightly different. As iSCORR is extremely sensitive to temporal effects, this requires combining the frames, effectively halving the frame rate of the camera but doubling the well depth. In practice, a lower frame rate can still be used. Here, we use a FASTCAM Mini UX100 type 800K-M-16G whose frame rate can go up to 80kHz.

4.4.2 Data analysis

iSCORR is based on a novel data analysis approach in which image correlation of the interference pattern is performed. This allows the extraction of the size and concentration of the particles. A typical raw iSCAT image is shown in Figure (4.2B). The scattering signal is extracted by taking the difference of the square root of two frames, as shown in Figure (4.2C). Several temporal distances are analysed and the mean intensity is plotted as the data in Figure (4.2E). To fit the data, a set of basis functions is calculated. Equation (4.4) describes the pattern created by a particle at a single position. However, the height of the particle is unknown. It is therefore assumed that the particle diffuses enough so that the position distribution is uniform between the interface position (Z_f) and above. The basis function ($B(\Delta t)$) is therefore defined as an average of the pattern for all the allowable positions (see the theory section 4.3):

$$B(\Delta t) \equiv \int_{Z_f}^{\infty} dZ \int_0^{\rho_{max}} \rho d\rho \left(|t^s(\theta)|^2 + |t^p(\theta)|^2 \cos^2(\theta) \right) \frac{\cos(\theta)}{R^2(\theta)} \left(1 - \exp\left(-\frac{\Delta t}{\tau(Z,\rho)} \right) \right) \tag{4.29}$$

The transmission coefficient for s- and p-polarised light are t^s and t^p, respectively. Figure (4.2D) illustrates how the correlation time of these basis functions depends on their radius. The data is fitted by a combination of these basis functions, of an offset corresponding to the noise variance, and of a linear dependence representing system contribution of correlations at a much slower time scale.

The Fourier transform is used to process the images, as the interferometric pattern intensity in the Fourier plane is concentrated on a disk. Fourier analysis also opens the possibility to detect and correct translation introduced by a flow, as discussed in section 4.3.2. In situ analysis of microfluidic chips under flow are therefore theoretically possible. This could also be used as a flow meter.

4.4.3 System contribution to the correlation

Any part of the system that is not constant in time can contribute to the correlation curve. Figure (4.3) compares fit for 50 nm radius polystyrene colloid, and for miliQ water. Obviously miliQ water should not have any particulates with 20 nm in size, but background contributions have the same correlation time. If these contributions are stable between experiments, they can be simply subtracted from the curve, improving the sensitivity of the system. Furthermore, a measurement with a strong periodic background signal is shown in Figure (4.4). These kind of background signals can typically arise from mechanical vibrations. The frequency that gave rise to this pattern can be extracted from the position of the first peak: $f = (2\Delta t_{max})^{-1}$.

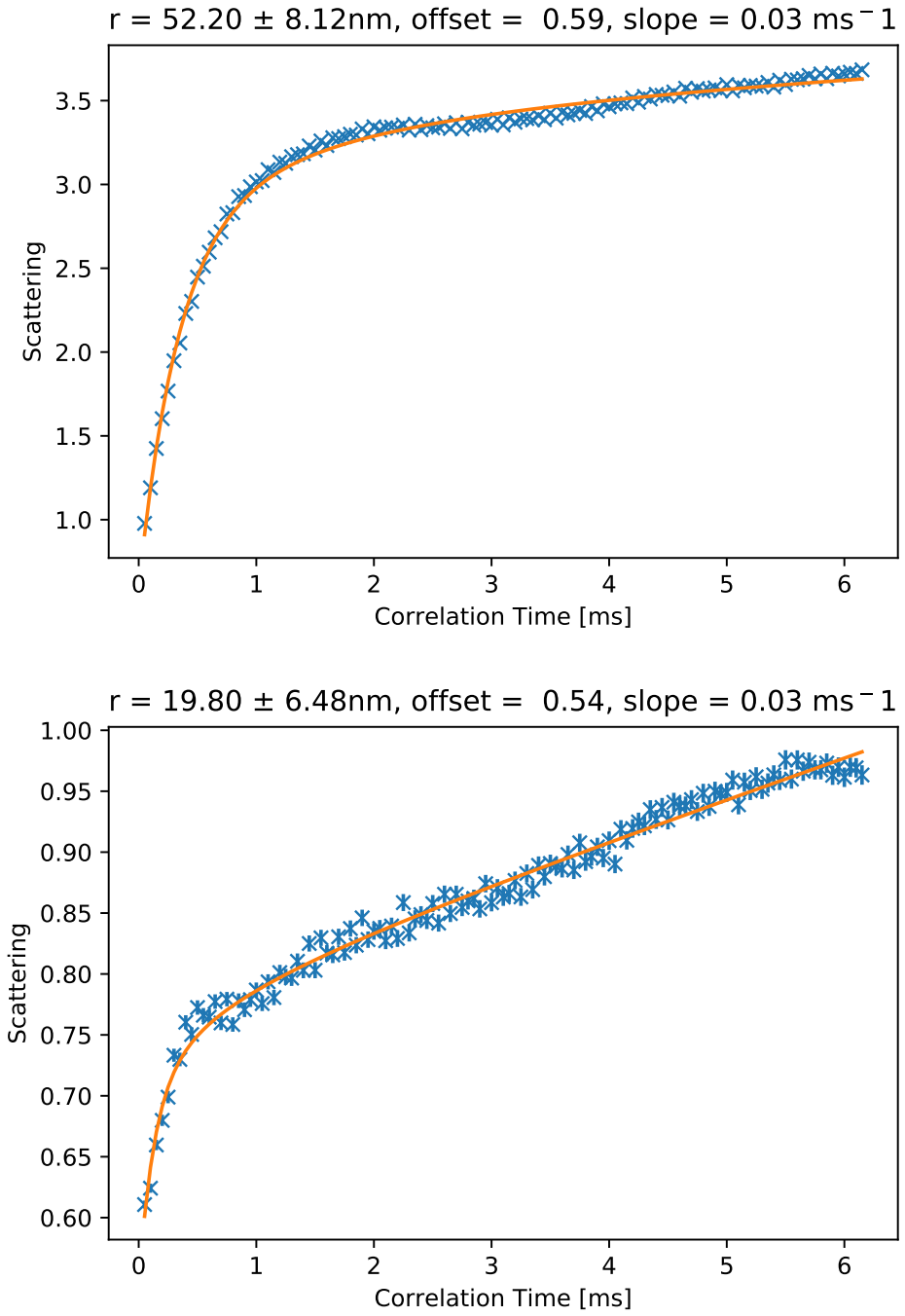

Fig. 4.3 Fits for 50 nm polystyrene colloid and for miliQ water. (top panel) The system is able to accurately size a single particle of radius 50 nm. (bottom panel) Some background correlation can be seen in the system. This should not be present for pure water. The correlation time corresponds to a diffusing particle of radius 20 nm but this could come from anywhere in the system. This system background correlation can be subtracted to improve the setup sensitivity.

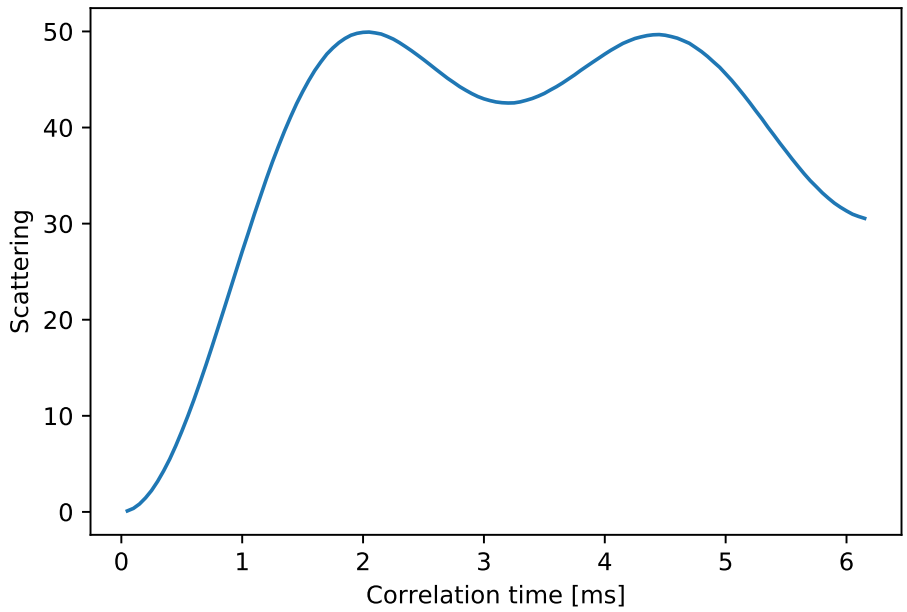

Fig. 4.4 Example of a correlation curve with a strong periodic noise of ≈ 200 Hz. Two harmonics can be seen.

4.5 Results and discussion

Knowing the qualitative behaviour of the correlation curves is crucial to optimally set up an experiment. To this end, an investigation of the basis functions is shown in Figure (4.5). Curves created by a single particle at a fixed position and corresponding intensity are shown in Figures (4.5A, C), respectively. As mentioned in the theory, the behavior of the system is very different above and below the focal plane. Above the focal plane, the correlation curves do not depend on the particle position. Therefore, the correlation time may be used to compute the particle size. Below the focal plane however, the correlation time depends strongly on the particle distance from the focal plane. This result indicates that it would be preferable to spatially confine the particles above the focal plane, for example by placing the focus on the interface. Another solution appears when assuming that the analysis time is long enough for the particle to diffuse uniformly in Z, or that several randomly distributed particles are present. In that case, the curves can be averaged above the interface position. The resulting curves and intensity are shown in Figures (4.5C-D), respectively. If the interface is on or above the focal plane, the curves are similar to a single particle diffusing at any position above the focal plane. However, placing the interface below the focal plane produces interesting results. The averaged curves first display a small dependence on the distance, but stabilises

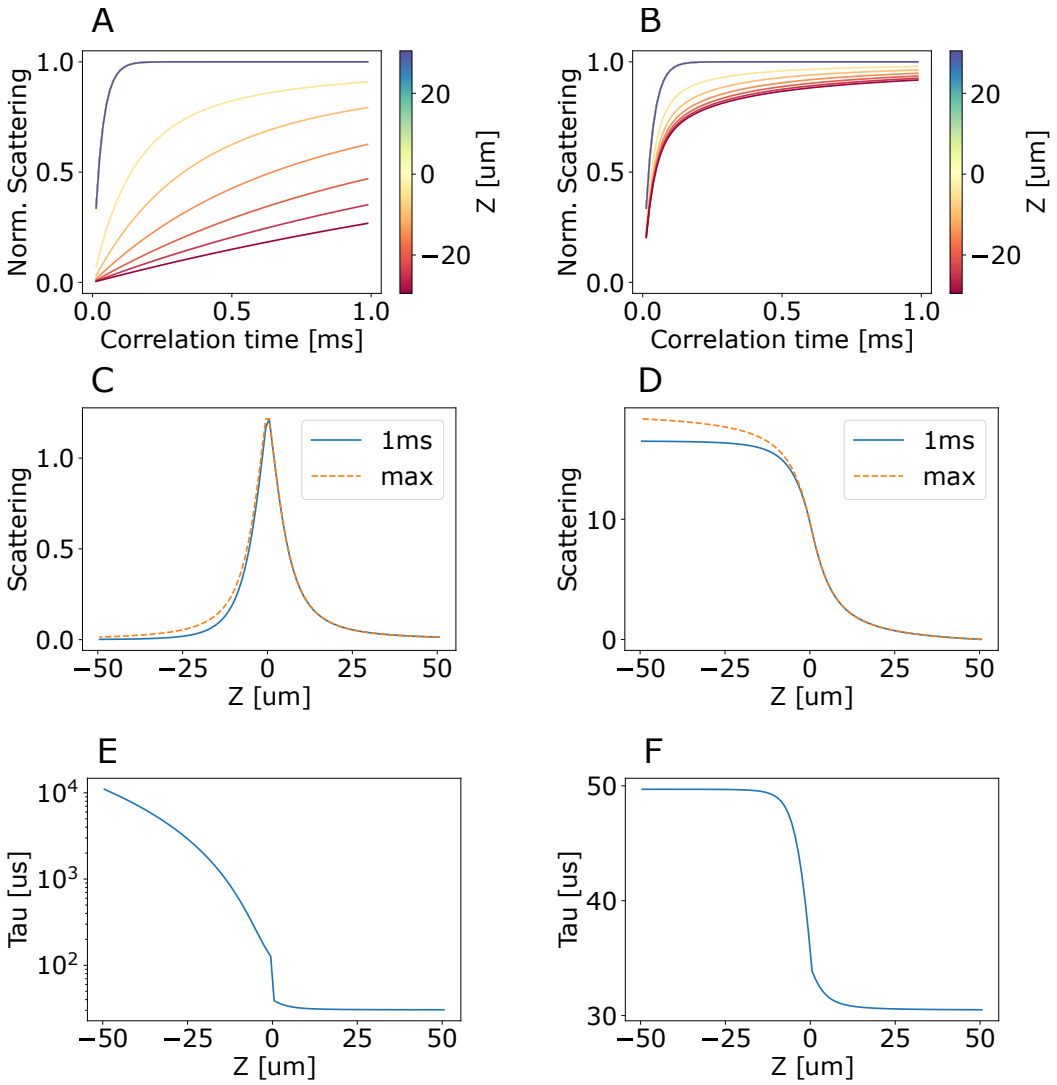

Fig. 4.5 Basis functions for particles of radius $r = 5$ nm. (A) Normalised curves for a range of particle Z positions. The normalisation factor is the scattering intensity shown in (C). (C) Scattering intensity corresponding to the curves in (A) at one millisecond and asymptotic. The intensity depends on the detector solid angle from the particle position. It decreases quickly when the particle Z position is larger than the field of view (12 um). (E) Correlation time for curves in (A). The correlation time is constant for particles above the focal plane ($Z > 0$). Below the focal plane, the effective correlation time increases quickly. (B) Integrated curves assuming that the particles diffuse uniformly above the interface. Here, Z is the position of the interface and the curves are integrated from Z to +50um. (D) Integrated scattering intensity as a function of the interface position. (F) Correlation time of the integrated curves. If the interface is placed below the focal plane ($Z < 0$), the effective correlation time increases by about 60% before stabilising at around $Z \approx -20$ um.

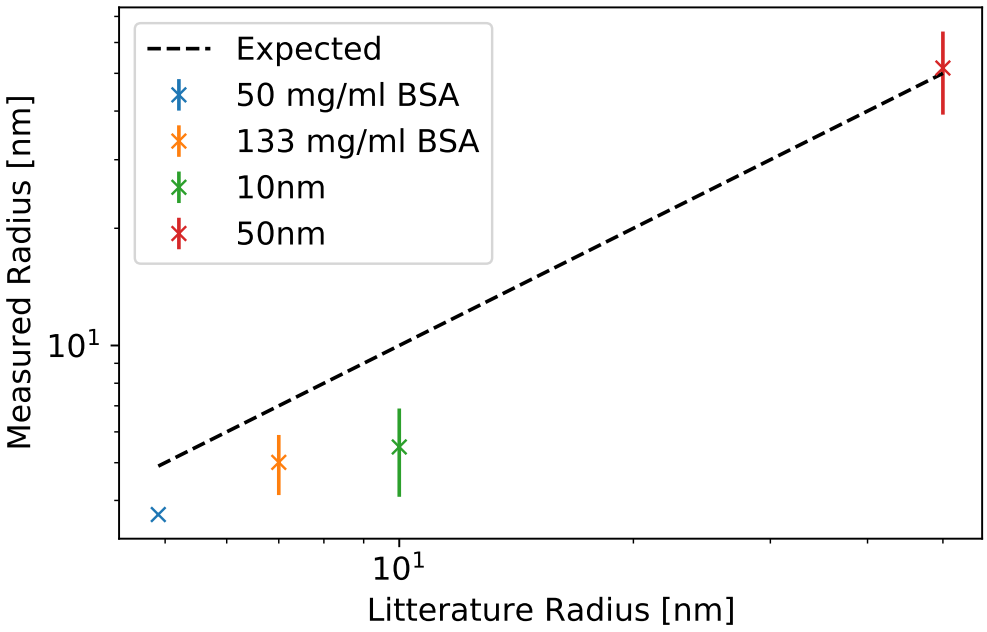

Fig. 4.6 Preliminary data for iSCORR sizing. Bovine serum albumin (BSA) and polystyrene colloids of 10 nm and 50 nm radius are detected and sized. The size of BSA depends on the concentration of BSA because of changes in the viscosity [17].

when the distance is large enough. Under this assumption, a measurement can be made in the bulk far from the interface and both the correlation time and the scattering intensity are good metrics. As an added benefit, the surface whose scattering can be significant is not in focus.

Using these insights, several particles have been successfully sized in solution, as shown in Figure (4.6). Here, the correlation time has been used. Some information could have been extracted from the scattering intensity as well, such as the scattering cross section for single particles or the concentration for denser analytes. Similarly to iSCAT and dark field scattering, the main advantage of iSCORR over other scattering correlation techniques such as dynamic light scattering (DLS) is the usage of a carrier wave to increase the signal above the background. Otherwise, iSCORR has similar properties to these techniques. Notably, the system is not expected to discriminate well between particles with similar sizes. This can be solved by upstream separation or by dilution down to single molecule levels, which are by definition mono-disperse. iSCORR is intrinsically a single molecule technique, unlike other correlation techniques, which record the interferences between particles.

The difficulty with interferometric scattering techniques lies in the separation of the scattering signal from the background and from the particle of interest. In state-of-the-art iSCAT, this is done by immobilising the particle of interest on a surface. The signal before

and after the landing event is the same, except for the addition of the particle. The particle signal can therefore be extracted by subtraction. Because the background scattering signal is extremely sensitive to drifts, the two frames that are subtracted must be taken with a small delay. This is much harder to achieve for diffusing particles, as no such sudden discontinuity exists. The key realisation for the technique presented in this chapter is that these two signals have different correlation times which can be used for separation. As shown in Figure (4.3), the diffusion timescale is usually sub-millisecond, while the drift timescale is orders of magnitude slower. The correlation signal from the background drift is therefore represented as a linear increase in the correlation plots, as the x-axis is much shorter than the background correlation time. One possible drawback of this approach is that the setup is sensitive to rapid vibrations that would have been integrated out in conventional iSCAT.

The diffusion along the Z axis is dominant, as shown in the theory. This might create problems when the particle is close to the channel surface, as interactions with the surface might break the isotropic diffusion assumption. The focal plane can however be placed far enough from the surface - typically a few tens microns - so that the interactions are negligible. This has the added benefit of avoiding the strong scattering from the surface. In this case, the particle can be positioned either above or below the focal plane. The correlation timescale changes dramatically when the particle crosses the focal plane, as explained in the theory. The measurement can either be made when the particle is above the focal plane, or by averaging and assuming that the particle diffuses uniformly. This is shown in Figure (4.5). The size estimation is more accurate for longer integration times. One could imagine many approaches for increasing the integration time, such as confining the particle in a region with an entropic trap. Alternatively, a higher concentration can be used to integrate the signal from many particles in parallel, as shown in Figure (4.6). This shows that this technique may be applied to a large range of concentrations. In comparison, state-of-the-art iSCAT typically requires thousands of landing events to get an accurate estimation of the size, while the technique presented here could size a single particle.

4.6 Conclusion

iSCORR is a single molecule technique that may be used to size a single diffusing particle. Using an iSCAT signal, a custom correlation algorithm is used to extract the correlation time and scattering intensity. While being fully compatible with iSCAT operations to detect single proteins on surfaces, this technique enables the detection of single particles diffusing in the bulk, as well as the characterisation of denser analytes. This technique is highly suitable

for integration with microfluidic chips or to select regions in cells, opening new method development opportunities.

Chapter 5

Scalable integration of nano-, and microfluidics with hybrid two-photon lithography

5.1 Summary

This chapter is based on the paper: Oliver Vanderpoorten, Quentin A. E. Peter*, Pavan K. Challa*, Ulrich F. Keyser, Jeremy Baumberg, Clemens F. Kaminski & Tuomas J. P. Knowles. (2019). "Scalable integration of nano-, and microfluidics with hybrid two-photon lithography". Microsystems & Nanoengineering, 5(1), 1-9 (* contributed equally). [261] I contributed to the design and the creation of the setup and of the experiments. In addition to that, I wrote the code to control the micro-writer and created a micro-language to specify the position, the speed, and the intensity of the writing laser. Moreover, I contributed to acquiring the data, notably the SEM images. Finally, I contributed to writing the paper.*

Nanofluidic devices have great potential for applications in areas ranging from renewable energy to human health. A crucial requirement for the successful operation of nanofluidic devices is the ability to interface them in a scalable manner with the outside world. Here, a methodology to produce master wafers is demonstrated for the fabrication of nanofluidic devices using soft-lithography approaches and the integration of nano-scale channels with conventional microfluidics using two-photon lithography. Using this approach, the fabrication of SU-8 moulds is demonstrated down to 230 nm lateral width and arbitrary channel heights from micron to sub-100 nm. Scanning electron microscopy and atomic force microscopy are used to characterize the printing capabilities of the system and show the integration of nanofluidic channels into an existing microfluidic chip design. The functionality of the

devices is demonstrated through super-resolution microscopy, allowing the observation of features below the diffraction limit of light produced using our approach. Single molecule localisation of diffusing Rhodamine 6G dye verifies the successful imprint of nanochannels of 420 nm width and spatial confinement of molecules to 200 nm across the channel. Nanoscale lab-on-chip development is accelerated by enhancing the current microscale fabrication capabilities through the combination of locally two-photon-written nano-sized functionalities with conventional mask whole-wafer UV-lithography. Our approach enables rapid nanofluidic chip prototyping in a non-cleanroom environment.

5.2 Introduction

Microfabrication and the patterning of nanostructures give new possibilities to analyse molecular processes with high precision. Microfluidics [272] has for instance become a powerful tool to study in-vitro the aggregation of proteins in lab-on-chip devices [124] in a controllable environment. Microdroplet generation [147], microfluidic diffusional sizing [53, 278, 40], and electrophoresis on chip [118, 225, 228] are now established techniques, but the nanofluidic regime has the potential to open up a whole new set of applications [39]. However - challenges remain in the routine fabrication and operation of such devices. Motivation for nanofluidic chip fabrication is given by selective transport mechanisms [236] occurring when channel widths reach diameters close to the Debye length [67]. Interactions between protein charges and the Debye layer can be used to confine, separate, and concentrate proteins [123], as well as for sorting exosomes and colloids according to their size down to 20 nm [24], but producing varying chip designs on wafer-scale is challenging and can slow progress in these areas. Additionally, nanofluidics provide high potential to increase efficiencies of blue energy conversion, where osmotic power is harvested from Gibbs free energy of a salt gradient between two solutions connected by nanopores, nanochannels, or membranes [246]. Performance of reverse electrodialysis (RED) depends largely on the geometry of the nanoscale confinements used, as has been studied by He et al. [111] in cylindrical and conical shaped nanochannels (ranging from 41 nm to 1200 nm diameter) whereas Kim et al. [143] studied the influence of channel height on RED for energy conversion in ion-selective silicon nanochannels with heights of 4 nm, 26 nm, and 80 nm. To produce lab-on-chip devices in the nanofluidic regime, electron beam lithography (EBL) and focused ion beam etching are used in clean room facilities to prototype nanochannels or nanopores in the sub-100 nm range in silicon/silicon nitride [282]. EBL can achieve channel sizes smaller than 10 nm [42], but cannot pattern as fast as mask-based lithography approaches [68]. The drawbacks of semiconductor technologies are their high costs for equip-

ment and maintenance due to special optical components and vacuum machinery required. Long writing times and high investment costs limit the adaption of nanofluidic devices. Methods to produce nanofluidic chips at wafer-scale in a non-clean room environment are therefore sought using other approaches. Common practice for lab-on-a-chip devices on a laboratory scale is UV mask photolithography followed by soft lithography [277]. There are two main photolithographic strategies to produce master moulds for soft lithography – large area mask patterning and direct laser-writing (DLW) [91, 195]. In general, both techniques work with UV-curable photoresists such as SU-8 spincoated onto a silicon wafer, with specified thicknesses of tens of microns. Uncrosslinked SU-8 is soluble in the developing agent PGMEA but becomes cross-linked and insoluble when exposed to UV radiation and post baking. UV attenuating masks with transparent sections in areas to be solidified are brought between the light source and the wafer, to project microfluidic chip designs onto the photoresist coated wafer. Unilluminated areas are then dissolved during the development process and only the UV-exposed areas remain. The wafer surface is then used as a mould for soft lithography using PDMS casting. DLW has the advantage that there is no need for masks. In this approach a laser is scanned over the wafer and is modulated accordingly to write the intended pattern. Both these technologies are limited to the fundamental diffraction limit and their sectioning capabilities are conventionally restricted by the thickness of the photoresist between 5 to 120 µm for common microfluidic fabrication, because each single UV photon initiates the polymerization process of the photoresist. Two-photon lithography overcomes this problem by using high power femtosecond pulse laser sources for the DLW process. Two infrared photons can interact with the photoinitiator molecule as if a single UV photon of half their wavelength had been absorbed [158]. This effect is a power dependent non-linear process and only occurs if pulses are highly correlated in space and time (in the order of femtoseconds) [170]. Therefore, just in the focal volume where high intensities are met, polymerization will occur and sub-diffraction limited features be be generated. Considering an additional non-linear photo response of the photoresist materials themselves and adjusting the laser intensity close to the energy threshold for polymerization, SU-8 nanorods of about 30 nm have been presented by Juodkazis et al. [134]. The fact that two incoming photons are unlikely to interact with a photoinitiator molecule before reaching the focal spot opens up arbitrary sectioning capabilities within the spincoated photoresist layer thickness. The application range of two-photon lithography is tremendeous and ranges from the fabrication of photonic crystals [254] and cell scaffolds [217], to metamaterials [98], biomimicry [173], and additive manufactured microfluidics [114]. Two-photon DLW has been used by Eschebaum et al. [87] to incorporate optical components (e.g. a total internal reflecting mirror) into a microfluidic chip design using soft lithography. Lin et al. [164] demonstrated the integration

of a 3-dimensional microfluidic mixer into photolithographically fabricated areas on a glass coverslip, using a commercial Nanoscribe system. In this chapter, the method of combining conventional UV-Lithography with two-photon direct laser writing is enhanced to approach the nanofluidic functionalities regime on a silicon surface. Silicon wafers are more common for microfluidic master fabrication than glass coverslips, due to their mechanical strength and surface quality. In the following, the successful master fabrication of nanofluidic chip devices on a silicon wafer using SU-8 with a channel size of 420 nm is introduced and experimentally demonstrated. In addition, arbitrary height channel mould fabrication down to 50 nm is demonstrated to be possible. A home-built two-photon setup is characterized with a calibration assay to determine the achievable minimal feature size of the system. Three system parameters are empirically evaluated to define the achievable resolution of the writing process: laser power, scanning speed, and focal spot offset from the wafer surface. To find the optimal values of these, test gratings are written in SU-8 at different conditions. Scanning electron microscopy (SEM) and atomic force microscopy (AFM) are used for the characterization of the polymerized features. The evaluated parameters are applied to incorporate nanofluidic channels into a microfluidic master. To show the successful imprinting of nanofluidic PDMS devices, their fluidic connectivity is demonstrated by flowing Rhodamine 6G dye through the channels and by imaging their lateral width on chip, using super-resolution microscopy. The procedure presented here fills the gap of affordable nanofabrication in biological laboratories in combination with conventional UV-lithography - overcoming low patterning speeds of DLW-technology but achieving sub-diffraction features in areas of interest.

5.3 Methods

5.3.1 Sample preparation and development

25 µm of SU-8 are spin-coated (BRUKER) at 3000 rpm onto a silicon wafer. The wafer is soft baked and treated according to the protocol of the photoresist distributor (Microchem). A microfluidic mask pattern is then projected onto the photoresist for 50 s with the setup described in Challa et al. [52]. The wafer is post-baked at 95°C so that the interfaces between developed and undeveloped regions become visible. After the two-photon writing process, the whole wafer is baked at 95°C again and finally rinsed with PGMEA and IPA.

5.3.2 Two-photon lithography setup

To produce the high intensities needed for two-photon excitation to occur, a Menlo System C-Fiber 780 HP Er:doped fibre oscillator with a repetition rate of 100 MHz with integrated

amplifier and second harmonic generation is used as a light source of the two-photon system. The laser pulse width is 120 fs. The setup is optimized to produce nanoscale features on a 100 µm x 100 µm field. The beam is expanded to fill the whole back aperture of the objective lens (Leica, PL APO, Magn. 100x, NA=1.4, oil) using a Thorlabs beam expander (AR coated: 650-1050 nm, GBE05-B). To make positioning of the focal spot over a whole 3" wafer possible, two PI linear-precision stages (M-404.2PD, Ball screw, 80 mm wide, ActiveDrive) are mounted perpendicularly on top of eachother with a suitable adaptor plate, connected to two individual PI Mercury DC Motor Controllers (C-863.11, 1 Channel, wide range power supply). On top, a PI NanoCube with a travel range of 100µmx100µmx100µm is mounted for high precision movement (pos. resolution: 2 nm) of the sample during the writing process. The wafer/photoresist interface is focused on using the back-reflection of the laser beam at low intensity (where polymerization will not occur), and the image is captured via a USB-camera (µEye ML, Industry camera, USB 3.0) with a tube lens (Thorlabs AC 254-100-A-ML, BBAR coating 400-700 nm, f=100.0 mm) mounted above the objective. The laser modulation is controlled by an acousto-optic modulator by AA Optoelectronics mounted after the laser output port and a fast switching power supply (ISOTECH,DC power supply, IPS 33030) controlled via USB. In order to provide an open-source setup, all the control programming, as well as the automated writing of a calibration assay of the system, are realized in Python.

5.3.3 Point spread function

While two-photon writing of features above 300 nm provides proper moulds for soft lithography, the formation of multiple lines is observed at positions where the voxel is deepened into the wafer. It is assumed that by overfilling the back aperture of the high-NA objective, an interference pattern is formed by the high spatial frequency components of the focused laser beam. These reflections cause major difficulties when nanofluidic channels below 300 nm height need to be written onto silicon wafers. To detect the interference patterns, the 3D PSF of the system is measured by overfilling the back aperture of the objective with a 5:1 beam expander and the far field back reflection of the laser beam from the silicon wafer surface is measured. An image stack is acquired with 50 nm step size while lowering the laser beam at low intensity into the wafer. From an orthogonal slice of the acquired z-stack (see Figure (5.1A)), one can see the interference patterns above the focal spot, which are caused by high spatial frequency components undergoing reflection due to the refractive index change from SU-8 to silicon. A pinhole in the laser beam path is adjusted so that the reflected interference patterns are minimized and another image stack is acquired, as shown in Figure (5.1B). By comparing the z-profile plots (see Figure (5.1C-D)) of both

PSFs, it becomes obvious that the intensity maxima above the wafer surface are reduced. Therefore, a variable beam expander (Thorlabs, BE02-05-B) is incorporated into the system; the calibration assay is repeated; and the parameters adjusted accordingly so that voxel truncation occurs. By reducing the numerical aperture, similar high resolution two-photon printing capabilities can be preserved and back-reflections reduced. This enables reliable channel fabrication at arbitrary heights from micron to the sub 300 nm regime on a silicon wafer. An improvement is demonstrated by changing the filling factor of a high NA objective and comparing calibration assays using SEM imaging. As shown in Figure (5.1E), multiple foci cause written lines to rip apart and renders them unsuitable for soft lithography. The improved and smooth printing capability can be seen in the SEM image (Figure (5.1F)), where lines decrease in width and height consistently without detaching parts.

Decreasing the power of the laser beam at constant offset allows the control of channel widths arbitrarily from the micron to the nano range (see Figure (5.2A)). According to the filling factor of the intended application or - in this case - intended channel size, the necessary power parameter can be read out from the assay. Figure (5.2B) shows a line profile plot of low NA two-photon written lines fabricated at 400 µm/s and illustrates how, by variation of the laser power from 58.5 mW to 70.0 mW, the channel width can be controlled from micron to 230 nm in size at the same offset of e.g. at -2.51 µm.

5.4 Results

5.4.1 Combining UV-lithography with two-photon DLW for wafer-scale nanofluidic chip fabrication

To explore the integration of nanofluidics with microfluidics, a prototypical nano/micro device is demonstrated, consisting of two microfluidic reservoirs that are connected via nanochannel junctions. These can be used for instance to exclude single molecules from a solution and to study their diffusion properties. On one side, a sample solution is pumped through while the other compartment of the device will be exposed to particles or proteins that fit through the nano-sized restriction connecting them.

Conventional methods to produce such nanofluidic devices are based on spincoating of sub 100 nm thin photoresist films and exposure through UV attenuating masks, or require electron beam lithography to push the lateral width down to the nanoscale [153]. Practical limitations of these methods are long writing times and variations in the photoresist thickness that render the integration of nanofluidics difficult. In our procedure presented here (see Figure (5.3)A-F), a single spin-coating process of a thick (e.g. 25 µm) SU-8 layer may be used. The wafer is

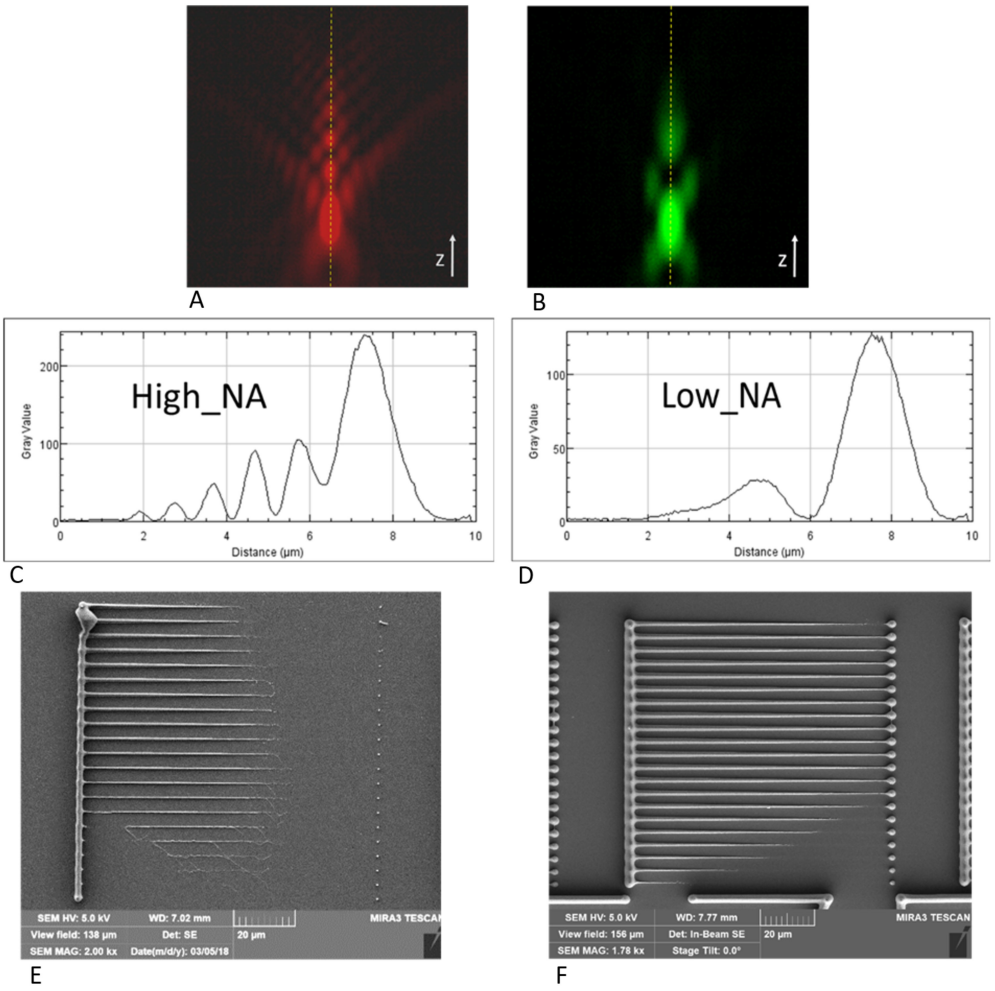

Fig. 5.1 (A) The orthogonal projection of the reflected PSF shows the interference patterns above the wafer surface; (B) Reducing the beam diameter coupled into the objective reduces the interference generated along the optical axis; (C) Line profile along z-axis for high NA case; (D) Line profile along z-axis for adopted beam diameter; (E) Calibration assay written at 200 µm/s, with an offset range from 0 µm to -3 µm using an overfilled back aperture; (F) Calibration assay written at 200 µm/s with an offset from -2 µm to -5 µm into the silicon wafer and adjusted beam diameter before the objective.

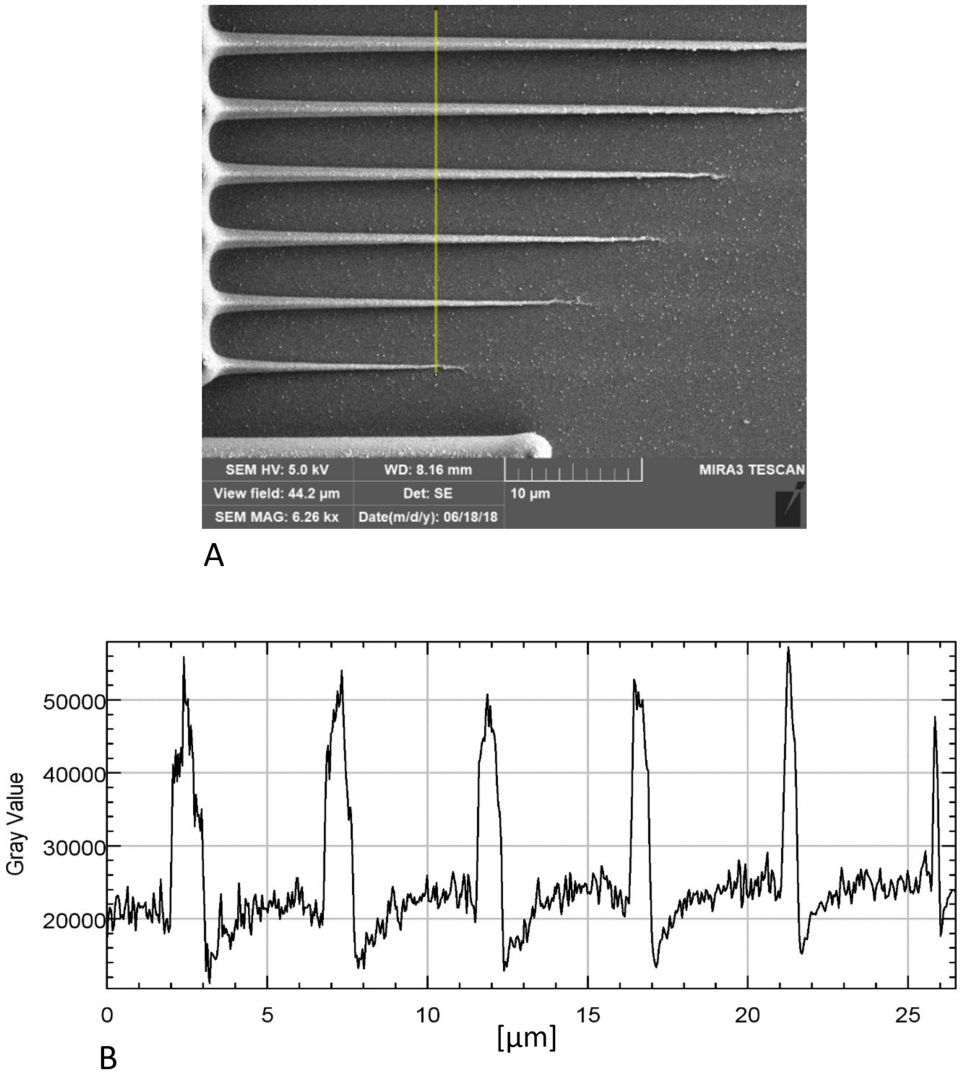

Fig. 5.2 (A) SEM image of NA-matched calibration assay written at 400 µm/s with laser intensities ranging from 58.5 mW to 70 mW and offset from -2 µm to -5 µm; (B) Line profile along power axis of calibration assay as indicated in (A). At constant offset and scanning speed, the channel width can be controlled in the sub-micron regime down to 230 nm.

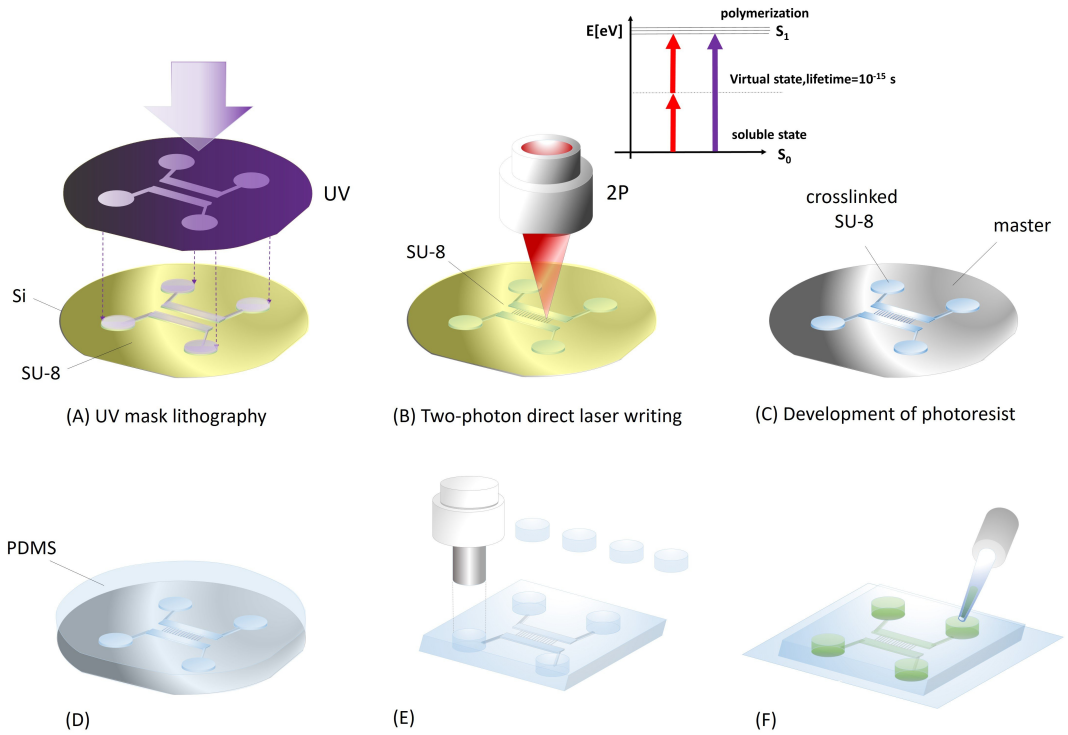

Fig. 5.3 Process outline for nanofluidic device fabrication via combination of two-photon lithography and mask UV-lithography; (A) Mask-based UV lithography is used to project an arbitrary microfluidic chip design onto a SU-8 coated silicon wafer; (B) Nanofluidic channels are added via two-photon lithography in areas of interest. The Jablonsky diagram illustrates that two spatially correlated IR-photons can interact with the photoinitiator like one single UV photon with half the wavelength if they are absorbed by the molecule within the lifetime of a virtual state excited by a single IR photon; (C) The wafer is developed and a microfluidic master wafer with integrated nanofluidics is obtained; (D) The wafer is covered with PDMS for soft lithography; (E) After curing of the PDMS, devices are peeled off the surface and inlets are added; (F) The final PDMS-chip is plasma bonded onto a glass coverslip and filled with e.g. fluorescent dye.

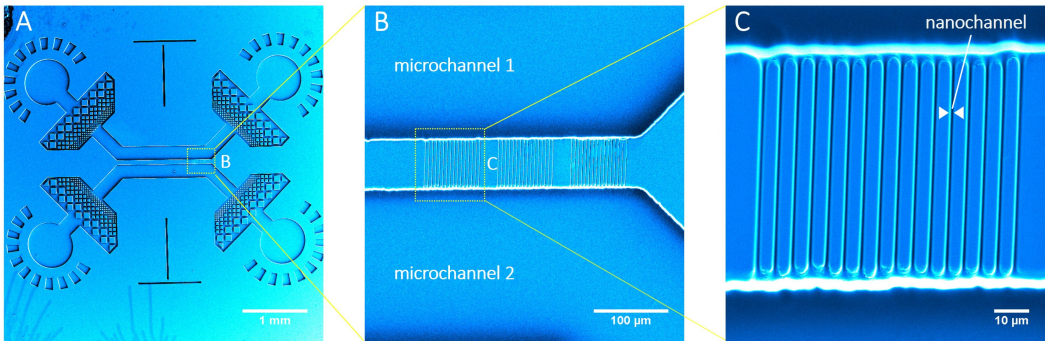

Fig. 5.4 (A) SEM micrograph of nanofluidic PDMS imprint fabricated by the combination of UV mask lithography and two-photon writing; (B) Three nanofluidic areas with nanochannels of 75 μm length joining the two microchannels; (C) Higher magnification shows 420 nm wide nanochannels imprinted in PDMS.

prebaked to remove solvent and UV-exposed through a film mask to pattern microfluidic areas on a waferscale. The wafer is then post-baked to polymerize the irradiated areas. The baking process induces a refractive index difference between exposed and unexposed areas. These refractive index edges are then used in the two-photon setup to find the regions of interest on the microfluidic master wafer, where the nanojunctions should be written. Since two-photon polymerization is induced only in the focal spot, the height of the printed channels may be arbitrarily controlled - the drawbacks of multiple spincoating steps within one development process of conventional techniques are overcome. In a second step, the master wafer is developed in PGMEA, cleaned with isopropanol, and dried using pressurized nitrogen. Through soft lithography, the pattern of the functionalised nanofiltration chips in PDMS is imprinted. The final PDMS imprint with additional microfluidic prefiltration sections can be seen in Figure (5.4A). Scanning electron microscopy images reveal the successful connection of the two microchannels with nanochannels of 420 nm width and 75 microns in length (see Figure (5.4B-C)). Due to double exposure by UV-lithography and two-photon writing, the nanochannels show broader joints at the intersection with the microfluidic area.

5.4.2 Calibration assay for micro-, to nano-scale two-photon writing

Since two-photon polymerization is a dose dependent process, the polymerized voxel scales with the intensity and the scanning speed of the laser beam in the photoresist. Additionally, since two-photon lithography is used here for 2.5 dimensional fabrication, the voxel truncation by the wafer surface also plays an important role on the lateral size of the written lines. A systematic approach is employed to evaluate the key factors in the system and to define

suitable operation parameters for micro- to nano-sized two-photon writing on the wafer surface. Faster scanning speed as well as lower laser intensity are observed to result in a smaller voxel size. Voxel truncation influences both and is furthermore important for the height of the channel moulds and proper attachment of the polymerized resin. Power ranging from 50 mW to 120 mW - as measured after the acousto-optic modulator - are evaluated. The laser focus is ascended into the wafer from 0 µm – 3 µm at a constant writing speed of 400 µm/s. An SEM image of the calibration print can be seen in Figure (5.5A). To improve SEM image quality and contrast, the sample is coated with 10 nm platinum. Along the vertical axis, the laser power for each line is varied, where the highest intensity is used at the top line. As expected, with increasing laser power the voxel size increases from bottom to top. At the lower end the effective laser dose does not reach the polymerization energy threshold, which does not result in polymerization. From left to right, a decrease in lateral width can be observed due to the laser focus being lowered 3 µm into the wafer over a distance of 100 µm. Using this calibration map, suitable parameters can be read out. Moreover, the spot size can be adjusted according to the filling factor of the pattern - or in this case - the channel dimensions to be written. Soft lithography compatible structures down to a size of 280 nm lateral width are found, as shown by SEM imaging in Figure (5.5B), and even 230 nm if the optical design is adopted (Figure (5.2)). AFM measurements of the region show heights down to 360 nm and are illustrated in Figure (5.5C) along with height profile measurements in Figure (5.5C*). Two-photon written nanochannels are by nature of hyperbolic shape, assuming a Gaussian intensity distribution in the focal spot, which limits this technology for the fabrication of rectangular channels. In comparison with other nanolithography techniques, the achievable lateral widths are relatively large. Based on AFM measurements, a height of down to 52 nm (see Figure (5.5B*)) and 35 nm height is verified at positions where the voxel is about to disappear into the sample (Figure (5.8)). Due to non-linear behaviour of the channel height when truncating the voxel on the surface, precise height control of the sample is required to approach fabrication in this regime (Figure (5.6)). High spatial frequency components of the focused laser beam are found to interfere above the wafer surface and to result in multiple polymerization locations, which can lead to detachment of the structures during the development process. Reducing the beam diameter before the objective result in an improvement of fabrication quality - showing similar lateral resolution and smooth lines when ascending the voxel into the wafer. (Figure (5.1))

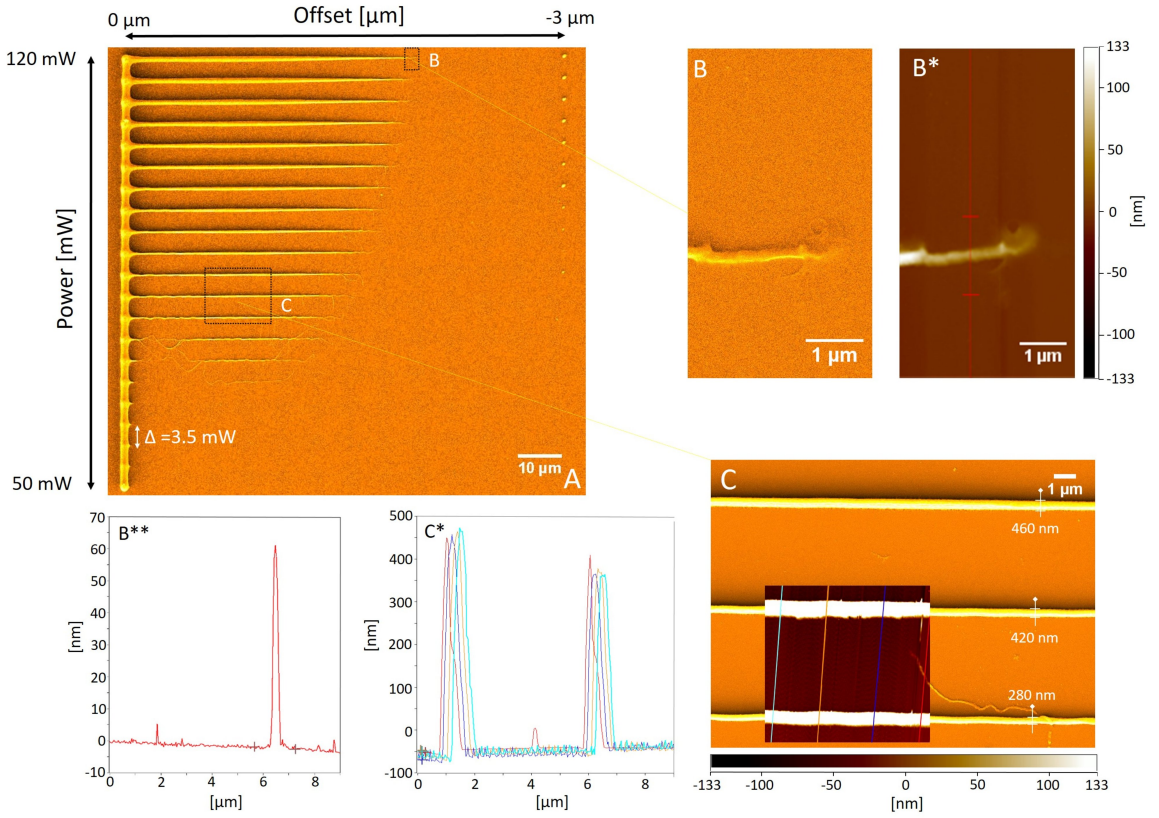

Fig. 5.5 Correlated SEM and AFM analysis of two-photon nano structures; (A) SEM image of power offset parameter test pattern at a writing speed of 400 µm/s. From bottom to top, the power is varied from 50 mW to 120 mW. Horizontally, from left to right the two-photon voxel is deepened into the wafer from zero offset - relating to the focal spot being on the wafer surface - to -3 µm, which relates to the focal spot being 3 microns inside the silicon from the wafer surface. One can see that at constant power just by varying the height, the lateral line width can be pushed to the nanoscale; (B) SEM-image of the position where the polymerization inducing voxel is disappearing into the wafer; (B*) Correlated AFM image of position B; (B**) AFM line plot of height profile measurement along red line as indicated in Figure (5.5B*) verifying a size down to 52 nm; (C) Detailed SEM imaging verifies soft lithography compatible structures down to 280 nm in width and illustrates how channel size can be controlled at constant offset by variation of power; (C*) AFM height profiles along coloured lines as indicated in Figure (5.5C).

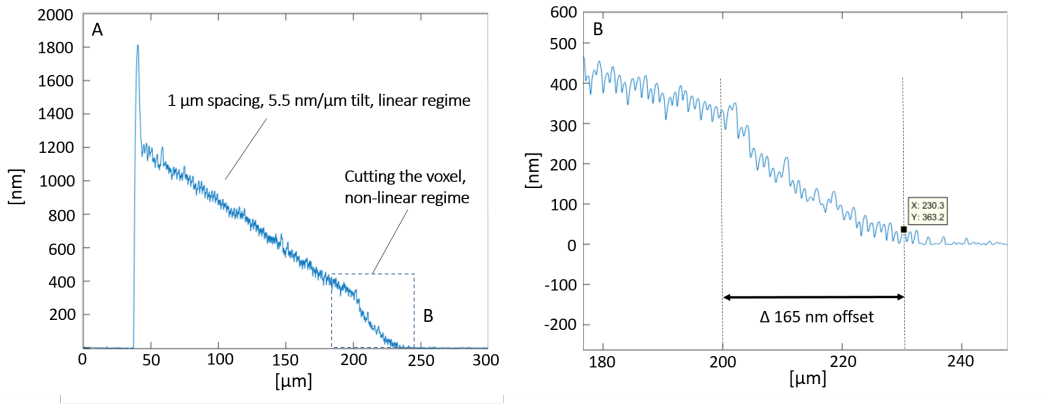

Fig. 5.6 (A) Height profile plot acquired with a Dektak BRUKER profilometer. A sample wafer with at 25 µm thick SU-8 layer is mounted in the system. The laser is focused onto the surface and the motor stages used to write a meander pattern with 1 µm spacing, under a slope of 5.5 nm/µm, at a writing speed of 400 µm/s and 120 mW laser power into the wafer. As can be seen, the printed heights range from micron to the nanoscale and show a linear slope. Especially when reaching the sub 300 nm regime, a non-linear dependence on the offset can be found when the polymerization inducing voxel is truncated by the silicon surface; (B) Detailed view of the non-linear regime shows regions with heights down to 36 nm. This curve implies the need for highly precise positioning for reliable fabrication on the nanoscale. The piezo technology used in this setup has a positioning resolution of 1 nm in closed loop mode and allows therefore precise control of channel heights within this fabrication window. The data was acquired and analysed by Oliver Vanderpoorten.

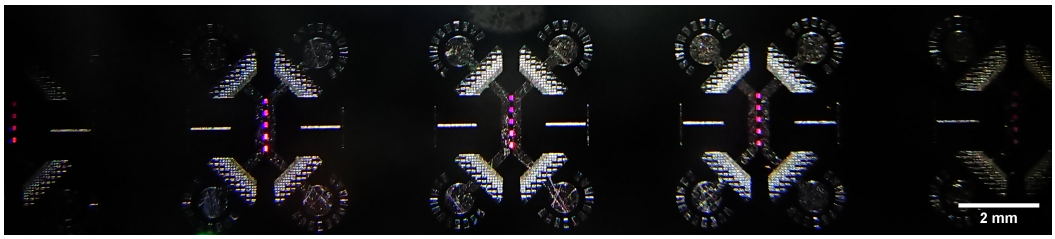

Fig. 5.7 Light microscope image showing a nanofluidic master wafer fabricated by the combination of UV-lithography and two-photon direct laser writing using SU-8. Microfluidic reservoirs of independent devices are joined with nanochannels on a millimetre scale using Python-based control software and the custom-built optical hardware described in the methods section. The nanochannels can be easily observed due to their grating-like diffraction when illuminated with a white light source.

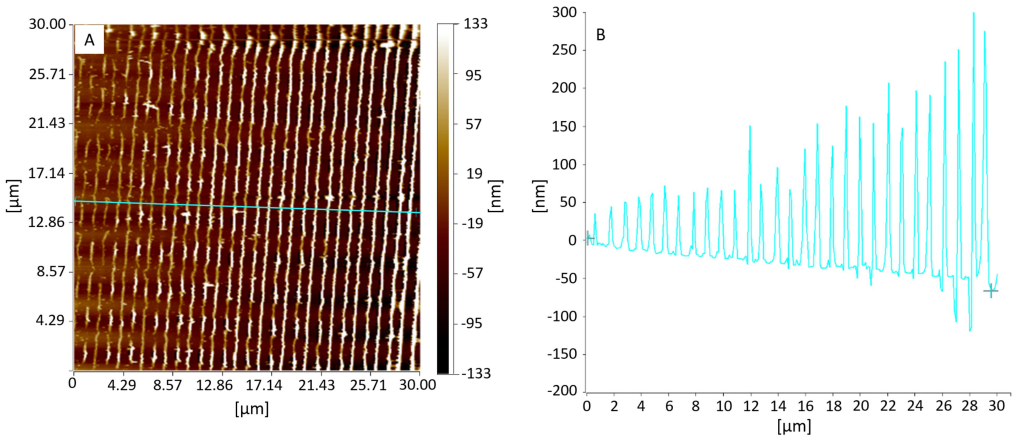

Fig. 5.8 The translational motor stages are used to write lines into SU-8 at 120 mW and 400 µm/s - slowly deepening the focus into the wafer, following a meander pattern with a spacing of 1 micron. AFM data shows polymerized lines with a height down to 35 nm, but also shows detachment due to the linear stages not moving smooth enough for this fabrication regime. The data was acquired and analysed by Oliver Vanderpoorten.

5.4.3 TIRF-super-resolution imaging of Rhodamine 6G molecules in nanochannels

In order to test the fluidic connectivity of the nanofluidic devices, an aqueous solution of a dye is flushed from the microfluidic inlet, (A) in Figure (5.9). Since the channels' dimensions are of the order or smaller than the wavelength of light, super resolution microscopy is used to image the nanofluidic channels. To this effect, total internal reflection (TIRF) illumination is used to restrict the excitation area of a fluorescence microscope to an area of approx. 100 nm above the coverslip. Since out of focus fluorophores are not excited, this technique has a much higher signal-to-noise ratio and is perfectly suitable for nanochannel measurements due to spatial confinement of molecules close to the coverslip. To verify the correct bonding and size consistency of the channels on chip, the reservoirs are filled with Rhodamine 6G solution at femto molar concentration dissolved with 200 µM MEA in PBS. The solution is adjusted with KOH to a pH of 10 in order to induce blinking of the fluorescent dye molecules and to enable breaking the resolution limit of conventional fluorescence microscopy by using the STORM principle [70]. By taking thousands of images, localizing the fluorescent emitters in each image, and overlaying the data, a super resolved image can be reconstructed. A description of the setup that is used for imaging can be found in Rowlands et al. [221]. Single molecule localization is a useful method for the characterization of nanofluidic devices after the plasma bonding step to verify fluidic connectivity. Moreover, it offers an alternative to clean room equipment such as electron microscopy or AFM. From

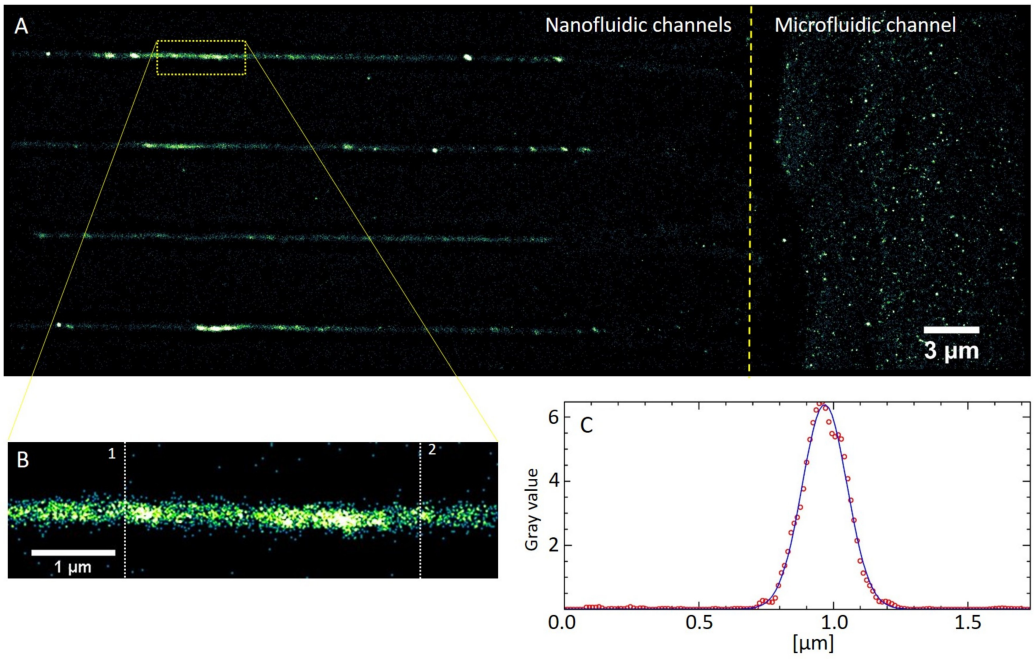

Fig. 5.9 (A) Super-resolved dSTORM image of a nanofluidic PDMS chip with Rhodamine 6G diffusing through two-photon written nanochannels. (B) Zoomed in region, verifying the successful imprinting of fluidically connected nanochannels in PDMS; The channel size is measured by averaging the vertical line profiles reaching from position 1 to position 2; (C) Plot of averaged line profiles as indicated in (B) - verifying the intended channel width of 420 nm on chip and a FWHM of 200 nm. Reconstruction is computed with the ThunderSTORM software plugin for ImageJ [191]. The data was acquired and analysed by Oliver Vanderpoorten.

the super-resolved fluorescence microscopy image, the effective channel size is measured to be 200 nm (FWHM) (see Figure (5.9A-B)), is consistent with the expected channel size read out from the calibration data acquired by SEM, and demonstrates the reliability of this technique. Small distortions induced by sample handling during the bonding process can be visualized on chip and show the importance of careful attachment of the PDMS during the bonding process. The detected molecules show a Gaussian distribution along the channel width, which could be due to the increased channel height towards the nanochannel centre. This causes an increase in the amount of detected molecules in the centre in comparison to positions close to the walls.

5.5 Discussion

In this chapter, two-photon lithography is shown to be capable of fabricating nanofluidic channels of arbitrary heights from micron to sub-100 nm using materials conventionally employed for microfluidic fabrication, as well as to integrate these structures with microfluidics. Two-photon lithography provides a reliable technique that decouples the influence of varying photoresist thicknesses from nanofluidic fabrication. The method reaches the upper boundary of the ultrananoscale with 35 nm to 50 nm channel heights, where new charge-induced transport mechanisms start to appear, but their lateral resolution remains one order of magnitude larger than EBL and RIE. Also, the round shape of the polymerization voxel inhibits the fabrication of rectangular shaped channels, which is achievable using RIE. Another technique, e.g. crack induced nanochannels, provides a simple and non-clean room technique with channel sizes in the sub 100 nm regime. Approaches such as generating mechanically induced cracks in chips have a high fabrication speed and can rapidly generate nanochannels up to milimeters length. However, this method cannot be easily interfaced with traditional PDMS microfluidics. The combination of EBL and UV-lithography is possible, but it is challenging without extending write times and costs, whereas two-photon lithography provides high flexibility for the effective integration of arbitrary two-dimensional nanofluidic functionalities into microfluidic masters. Although two-photon lithography cannot achieve as small features as electron-beam lithography, its fabrication range is useful for a variety of biophysical and blue energy applications e.g. charge measurements of proteins in solution using nanotraps with dimensions of 600 nm width and 160 nm height [223]. Nano electroporation (NEP) uses 90 nm wide channels for precise dose control for the injection of nanoparticles, plasmids, and siRNA on a single cell basis. NEP demonstrates the improvement of the process when channels in the submicron regime are used [41]. In blue energy research, a nanofluidic device with a power density of 705 W/m2 using a silicon nanochannel of dimensions 715 nm x 350 nm x 40 nm was demonstrated by Zhang et al. [285]. However, one must be careful when comparing soft lithography devices with silicon applications. Handling the PDMS correctly during the bonding process is crucial in order to avoid bending or collapsing nanostructures on the final substrate. Silicon chips are more reliable and stable during operation, but PDMS is cost-effective and offers the advantage of fast replacement. The lateral resolution of the two-photon effect can be pushed to its limit by using the STED principle [275]. Using photoresists consisting of tri- and tetra-acrylates and 7 Diethylamino-3-thenoylcoumarin and surrounding the focal spot with a depletion beam pushes the polymerized features size to 55 nm at a resolution of 120 nm, which shifts two-photon lithography technology further towards EBL resolution for nanofabrication.

5.6 Conclusion

Nanofluidic functionalities are successfully integrated into microfluidic chips by combining two-photon lithography with mask based UV-lithography on a silicon wafer in a non-clean room environment. Pre-exposed areas undergo a refractive index change, which can be used to find and align the two-photon writing process. It is demonstrated that the two-photon lithography setup presented here is capable of producing features down to 230 nm lateral width on a silicon wafer surface in SU-8 photoresist and successfully integrating 420 nm wide nanochannels into a microfluidic master design. By ascending the voxel, reliable nanochannel moulds of sub 100 nm in height are fabricated. This regime allows the usage of the EDL overlay to control particle translocation and has the potential to produce PDMS devices that are comparable to EBL or RIE-etched chips. In contrast to other techniques e.g nanochannel fabrication by cracking, where mechanics and reagents define the shape of the formed nano junctions, two-photon lithography allows the integration of arbitrary nano-sized patterns and complex shapes (e.g. varying channel sizes) into microfluidic devices. The reliability of the fabrication process is verified by comparing SEM images of a SU-8 calibration sample with TIRF fluorescence super-resolution imaging in the final PDMS devices. Improvement in resolution of the process could be achieved by a change in photoresist composition or post-processing of the photoresist via temperature and plasma treatments to thin out written structures. With this method, we hope to provide a fast, reliable and flexible pathway for nanofluidic chip fabrication. This may enable biophysical research laboratories to study protein transport effects on the nanoscale in a laboratory environment.

Chapter 6

Fast numerical integration of diffusional sizing basis functions

6.1 Summary

This chapter is based on the manuscript: Quentin Peter, Kadi Liis Saar, Therese W. Herling, Thomas Mueller & Tuomas P. J. Knowles. "Fast numerical integration of diffusional sizing basis functions". Manuscript in preparation. I developed the data processing pipeline and the algorithms to process and to analyse the data. In addition to that, I analysed the data. Moreover, I contributed to the design of the experiment and to the data acquisition. Finally, I wrote the paper.

Diffusional sizing is a microfluidics technique that measures diffusion coefficients of particles and complexes under flow. It can give critical insights into many biological systems such as molecular interactions. Here, the method to choose the right experimental conditions to maximise the sensitivity, accuracy, and dynamic range of experiments is discussed. Efficient numerical methods simulate the system to provide insight into the assay and to fit experimental data.

6.2 Introduction

Proteins are the key elements in the machinery of life. They mediate most of the cellular functions. Studying their interactions is therefore critical to further our understanding in biomedical sciences. Microfluidics technologies have proven successful in this endeavour [117]. In particular, diffusional sizing techniques enable measurement of the size of complexes in solution [151]. This is especially useful to study molecular interactions [109, 97, 18, 152, 227] or

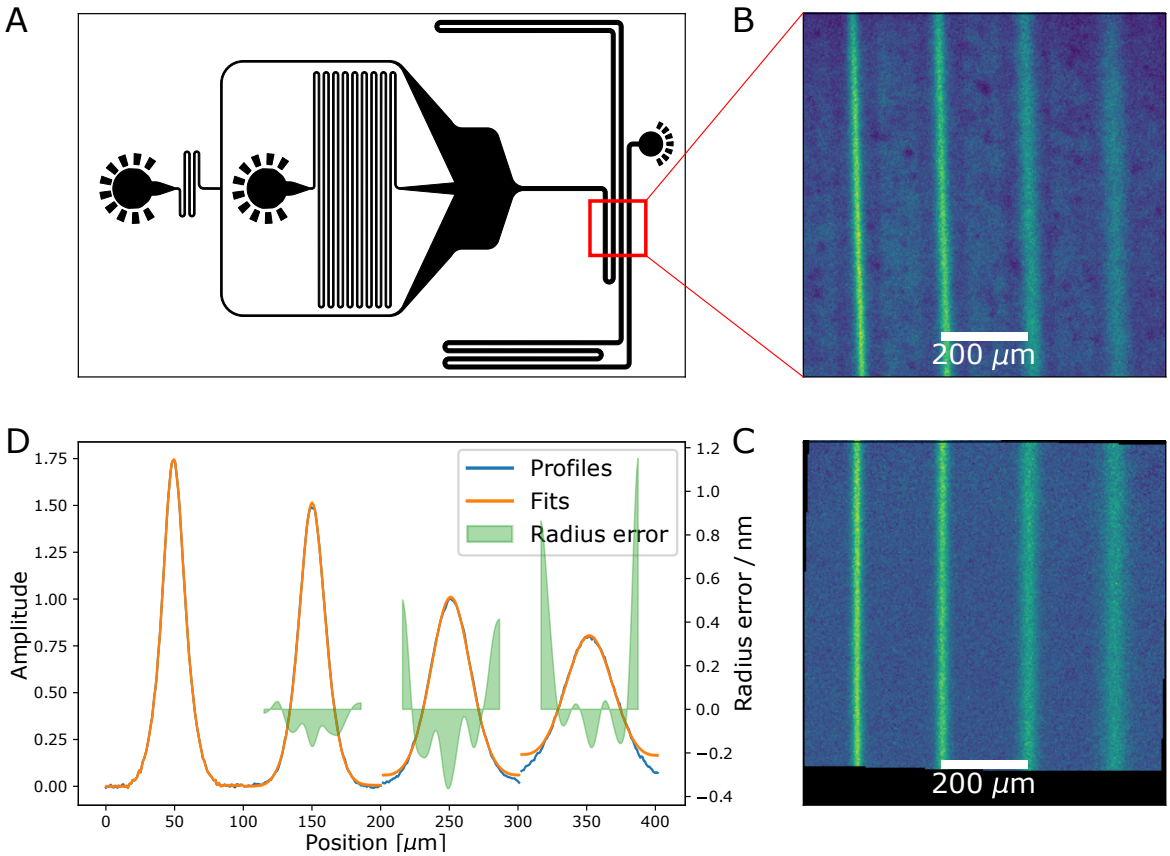

Fig. 6.1 (A) A microfluidic device is designed to inject a sample centrally into a diffusion channel. The diffusion channel is folded so that several positions are visible in the same field of view, as illustrated by a red square. (B) A UV-based protein autofluorescence image of the four positions is acquired. (C) This image can be processed by removing a reference background image, and by correcting for rotation. (D) The diffusion profiles are extracted and fitted to extract the sample diffusion coefficient. Here, a small error can be seen on the side of the profiles. This indicates that the sample is sticking to the walls.

protein folding states [286]. The diffusion of analytes perpendicular to a steady flow allows a measurement of the diffusion coefficient [136, 137, 66]. This technique can also be used as a viscometer [17] or combined with other techniques such as synchrotron radiation circular dichroism [40] to obtain multidimensional data.

A typical diffusional sizing assay is shown in Figure (6.1). Channels containing a sample and a buffer are merged together into a long diffusion channel. An initial diffusion profile is thereby created and diffuses towards equilibrium. By recording the profile at several positions along the diffusion channel, the sample diffusion coefficient is measured. A significant deviation can be observed between the fit and the data in Figure (6.1D). This is likely caused by protein absorption on the walls. The model indeed assumes reflecting boundary conditions. However, this discrepancy is not problematic as the fit is global and covers several positions where the sample did not reach the walls. Furthermore, the most significant part of the profiles corresponds to the largest slope, which is the most sensitive to a change in diffusion. As the largest slope is distant from the walls in this example, the effect of adhesion is limited. In this work, the initial profile shape and the position of recording are optimised. Data analysis techniques and fitting strategies are presented to enhance the quality and the speed of the assay. As an example, the process by which multi-position sizing in the same field-of-view increases the dynamic range and enables better scale estimations - which are critical to accuracy - is discussed.

6.3 Theory

The diffusion profile depends on the channel cross section, the flow rate (Q), the detection position along the diffusion channel (x), and the sample diffusion coefficient (D). All these quantities can be combined to a dimensionless variable that is introduced as the amount of diffusion (ϕ):

$$\phi \equiv x\frac{D\beta}{Q} \tag{6.1}$$

This variable, together with the channel height over width ratio (β), uniquely describes the diffusion system. A unique variable can therefore be analysed, which reduces drastically the search space for an optimum solution. The corresponding dimensionless diffusion equation can be integrated numerically from an initial profile to form a set of basis functions $B(\phi)$. These numerical simulations can be used by a least-square algorithm to fit data. The accuracy of the amount of diffusion fit σ_ϕ is found by Taylor expansion of the least square

equation: [218]

$$\sigma_\phi^2 = 1 \Big/ \sum_i \left(\frac{\partial B_i(\phi)}{\partial \phi} \frac{1}{\sigma_i(\phi)} \right)^2 \tag{6.2}$$

where σ_i is the noise on the pixel i. Two cases are considered: If the system is shot-noise limited, the variance of the noise is proportional to the signal intensity ($\sigma_i^2(\phi) = \alpha B_i(\phi)$):

$$\sigma_{\phi,sn}^2 = \alpha \Big/ \sum_i \left(\frac{\partial B_i(\phi)}{\partial \phi} \right)^2 \frac{1}{B_i(\phi)} \tag{6.3}$$

If the system is instead limited by background noise, σ_i is independent on the signal and possibly position. Assuming $\sigma_i(\phi) = \sigma$:

$$\sigma_{\phi,bn}^2 = \sigma^2 \Big/ \sum_i \left(\frac{\partial B_i(\phi)}{\partial \phi} \right)^2 \tag{6.4}$$

6.3.1 Dimensionless diffusion equation

The problem of particles diffusing in a fully developed flow in a rectangular microfluidic channel of width and height $W \times H$ is considered. A flow ($\boldsymbol{v}$) is created by a pressure field (p). The flow in such a setting is called Poiseuille flow. The incompressible Navier-Stokes equation relates the pressure and viscosity (η) to the velocity:

$$\rho[\partial_t \boldsymbol{v} + (\boldsymbol{v} \cdot \boldsymbol{\nabla})\boldsymbol{v}] = -\boldsymbol{\nabla} p + \eta \nabla^2 \boldsymbol{v}$$

Applying time invariance ($\partial_t \boldsymbol{v} = 0$) and translational invariance ($(\boldsymbol{v} \cdot \boldsymbol{\nabla})\boldsymbol{v} = 0$), the equation is simplified:

$$\eta[\partial_y^2 + \partial_z^2] v_x(y,z) = \partial_x p$$

where x is the direction of the flow, and z is the height. Normalising the distances by the width, and the flux with the flow rate (Q), $v_x' = v_x WH/Q$, the dimensionless stokes equation is obtained:

$$[\partial_{y'}^2 + \partial_{z'}^2] v_x'(y',z') = 1$$

This equation is solved by the series:

$$v_x'(y',z',\beta) = \sum_{nm} A_{nm}(\beta) \sin(n\pi y') \sin(m\pi \frac{z'}{\beta}) \tag{6.5}$$

This form of the solution is symmetrical and converges quickly [250]. The series coefficient (A_{nm}) is defined:

$$A_{nm}(\beta) \equiv -\frac{16}{\pi^4}\frac{1}{nm\left(n^2+\frac{m^2}{\beta^2}\right)}\delta_{(n \bmod 2),1}\delta_{(m \bmod 2),1} \tag{6.6}$$

and the aspect ratio (β):

$$\beta \equiv \frac{H}{W} \tag{6.7}$$

The general convection-diffusion equation for the local concentration $c(x,y,z)$ and diffusion coefficient D under dilute conditions is given by: [252]

$$\frac{\partial c}{\partial t} = \nabla\cdot(D\nabla c) - \nabla\cdot(\boldsymbol{v}c)$$

The diffusion coefficient is related to the hydrodynamic radius by the Einstein relation [82]:

$$D = \frac{k_b T}{6\pi\eta R_h} \tag{6.8}$$

By time invariance, and by assuming that diffusion in the x direction is negligible ($D\partial_x^2 c \ll v_x\partial_x c$):

$$\partial_x c = \frac{D}{v_x}(\partial_y^2+\partial_z^2)c$$

The dimensionless amount of diffusion ϕ is defined as follows:

$$\phi \equiv x\frac{D\beta}{Q} \tag{6.9}$$

leading to the dimensionless differential equation describing the diffusion of species in a poiseuille flow:

$$v_x'\partial_\phi c = (\partial_{y'}^2 c + \partial_{z'}^2 c) \tag{6.10}$$

This equation can be numerically integrated using a Crank-Nicholson method [78].

6.3.2 Monodisperse fitting

Equation 6.10 can be numerically integrated from an initial profile for given ϕ and β. β is the aspect ratio of the channel and is therefore known. The theoretical initial profile could be calculated from the chip design. However, in practice, variations in hydrodynamic resistances and in non-intuitive non-slip boundary conditions make this difficult. Instead, the

first recorded profile can be used as an initial profile. For any given ϕ, a basis function $B(\phi)$ can therefore be numerically integrated and compared with the measured data.

It is assumed that each position has a different amplitude because of illumination non-uniformity, and eventually that a random offset is applied. After normalisation, the profiles are compared to a set of basis functions $B(\phi)$. The least square error is computed, which allows to quickly find the best fit.

6.3.3 Polydisperse fitting

Here, the method to fit polydisperse profiles from basis functions is discussed. It is assumed that each position has a different amplitude because of illumination non-uniformity, and eventually that a random offset is applied. Let us assume a data point $D_{k,px}$ at position k along the channel and pixel px across the channel. This can be fitted by a basis function $B_{k,px}(r)$ with r being the hydrodynamic radius. The problem is that there is no functional form for $B(r)$. However, $B(r)$ can be numerically estimated for any r. The strategy is therefore to simulate a range of test radii and then to interpolate their resulting basis functions in order to estimate the profile for any radius. A least square fitting can therefore be computed with fitting function $Y_{k,px}(\overrightarrow{r}) = \sum_i a_i B_{k,px}(r_i) + b_k$:

$$\chi^2 = \sum_{px}\sum_{k}\left(\sum_i a_i B_{k,px}(r_i) + b_k - D_{k,pk}\right)^2 \tag{6.11}$$

The sum over the pixels can be done once to save processing time. The "pre-summed" variables are introduced:

$$(\overrightarrow{B_k})_i \equiv \sum_{px} B_{k,px}(r_i); \qquad (\overleftrightarrow{BB_k})_{i,j} \equiv \sum_{px} B_{k,px}(r_i)B_{k,px}(r_j)$$

$$D_k \equiv \sum_{px} D_{k,px}; \qquad (\overrightarrow{BD_k})_i \equiv \sum_{px} B_{k,px}(r_i)D_{k,px}$$

$$N_{px} \equiv \sum_{px} 1; \qquad DD_k \equiv \sum_{px} D_{k,px}D_{k,px}$$

The least square equation becomes:

$$\begin{aligned}\chi^2 = \vec{a} \times \sum_k \overleftrightarrow{BB_k} \times \vec{a} - 2\vec{a} \times \sum_k \overrightarrow{BD_k} + \sum_k DD_k \\ + 2\vec{a} \times \sum_k \overrightarrow{B_k} b_k - 2\sum_k D_k b_k + N_{px}\sum_k b_k^2\end{aligned} \tag{6.12}$$

where the second line is null if offsets are not taken into consideration. By taking the derivate with respect to a_i and b_k, the optimal value for the offset is found to be:

$$b_k = \frac{1}{N_{px}} \left(D_k - \vec{a} \times \overrightarrow{B_k} \right) \tag{6.13}$$

and the amplitude parameter:

$$\vec{a} = \left(\sum_k \overleftrightarrow{BB_k} - \frac{1}{N_{px}} \sum_k \overrightarrow{B_k} \otimes \overrightarrow{B_k} \right)^{-1} \times \left(\sum_k \overrightarrow{BD_k} - \frac{1}{N_{px}} \sum_k \overrightarrow{B_k} D_k \right) \tag{6.14}$$

which is a ratio of covariances. This is enough to test a given $\vec{r}$, as this allows us to compute the best a_i and b_k for it. To optimise $\vec{r}$, one needs to find the Jacobian of χ^2 assuming a_i and b_k are optimised.

$$\partial_i \chi^2 = \vec{a} \times \sum_k \partial_i \overleftrightarrow{BB_k} \times \vec{a} - 2\vec{a} \times \sum_k \partial_i \overrightarrow{BD_k} + 2\vec{a} \times \sum_k \partial_i \overrightarrow{B_k} b_k \tag{6.15}$$

The derivatives are computed from the interpolation of B. For a given r_i, let us assume the previous test radii is $\underline{r_i}$ and the next is $\overline{r_i}$. c_i is introduced so that:

$$r_i = \underline{r_i}(1 - c_i) + c_i \overline{r_i} \tag{6.16}$$

The basis function can therefore be interpolated with:

$$B_{k,px}(r_i) \approx B_{k,px}(\underline{r_i})(1 - c_i) + c_i B_{k,px}(\overline{r_i}) \tag{6.17}$$

The derivatives over r_i can therefore be transformed into derivatives over c_i:

$$\partial_i (\overrightarrow{B_k})_l = \delta_{i,l} \left((\overrightarrow{B_k})_{\overline{l}} - (\overrightarrow{B_k})_{\underline{l}} \right) \tag{6.18}$$

Similarly for $\overrightarrow{BD_k}$:

$$\begin{aligned} \partial_i (\overleftrightarrow{BB_k})_{l,m} = \delta_{i,m} \big[& (1 - c_l) \left((\overleftrightarrow{BB_k})_{\underline{l},\overline{m}} - (\overleftrightarrow{BB_k})_{\underline{l},\underline{m}} \right) \\ & + c_l \left((\overleftrightarrow{BB_k})_{\overline{l},\overline{m}} - (\overleftrightarrow{BB_k})_{\overline{l},\underline{m}} \right) \big] \\ + \delta_{i,l} \big[& (1 - c_m) \left((\overleftrightarrow{BB_k})_{\overline{l},\underline{m}} - (\overleftrightarrow{BB_k})_{\underline{l},\underline{m}} \right) \\ & + c_m \left((\overleftrightarrow{BB_k})_{\overline{l},\overline{m}} - (\overleftrightarrow{BB_k})_{\underline{l},\overline{m}} \right) \big] \end{aligned} \tag{6.19}$$

The solution can then be found by minimisation over the radii only, which massively decreases the number of variables to fit. The errors are found from Taylor expansion of the least square equation [218]:

$$\begin{aligned}\sigma^2_{r_{i,j}} &= \left(\sum_{px}\sum_{k}\frac{1}{\sigma^2_{px,k}}\frac{\partial Y_{k,px}(\overrightarrow{r})}{\partial r_i}\frac{\partial Y_{k,px}(\overrightarrow{r})}{\partial r_j}\right)^{-1} \\ &= \left(\sum_{px}\sum_{k}\frac{a_i a_j}{\sigma^2_{px,k}}\frac{\partial B_{k,px}(r_i)}{\partial r_i}\frac{\partial B_{k,px}(r_j)}{\partial r_j}\right)^{-1}\end{aligned} \tag{6.20}$$

6.4 Methods

6.4.1 Microfluidics

Microfluidic diffusion devices are made from patterned Polydimethylsiloxane (PDMS) bound to a glass slide. Briefly, a master is created by spin-coating SU-8 photoresist onto a 3" silicon wafer and exposing a pattern through a negative mask with a UV-LED [52]. After developing the photoresist, a mixture of PDMS and curing agent in a ratio 1:10 is poured on the master and cured for 2 hours at 60^oC. Holes are then punched to allow for fluidic connections and the device is bounded to a glass coverslip using a plasma oven. Black carbon nano-powder can be mixed to the PDMS to decrease the background fluorescence, and the glass slide can be replaced by a quartz slide if UV detection is used. A typical design for the photolithographic mask is shown in Figure (6.1A). The holes for fluidic connections are surrounded by diffraction markers so they become more visible while punching. The resistances on the inlet channel (the initial meandering channels) are designed to control the ratio of the central injection. The chip is operated by applying a flow rate with a neMESYS syringe pump in either pushing or pulling mode. The sample diffuses into the buffer over the diffusion channel length. The diffusion channel is folded to group the detection positions in a single detection region. This allows the detection of an initial profile from which basis functions can be derived. This also allows detecting several detection positions, which increases the dynamic range of the assay.

6.4.2 Detection and data processing

Fluorescence microscopy is used to record the diffusion profile. The particles of interest can either be labelled with a fluorescent marker, or a UV-LED based autofluorescence method can be used to detect unlabelled proteins [53]. In addition to conventional fluorescence microscopy, confocal microscopy has been used to scan across the channels and extract diffusion profiles with a high signal-to-noise ratio. An example of UV-autofluorescence image

is shown in Figure (6.1B). Fluorescence images are processed by acquiring a background image at the same position on the device. A non-uniform illumination map is extracted by fitting the background with a multidimensional 2nd order polynomial fit (a 2D parabolla) and is used to flatten the illumination by division. The background image is then subtracted. Finally, the angle of the image is detected by using the image translational symmetry. It is extracted by correlating the top and bottom half of the image. The result is illustrated in Figure (6.1C). For scanning confocal microscopy data, the illumination is uniform by design. The filtered background scan only needs to be subtracted. Having a good background is crucial. It will allow to detect the baseline of the profiles, one of the largest contributors to fitting error.

6.4.3 Profiles processing

While each position could be detected individually, a better strategy is to group all the positions in one detection region. In addition to enabling the acquisition of time stacks, it allows for a better detection of the channels position and scale. The scale might vary because the magnification of a microscope depends on the focus in the case of fluorescence microscopy or because the scan was not perfectly perpendicular to the channels for scanning confocal microscopy. The algorithm is illustrated in Figure (6.2). First, two masks are created from the known channel and inter-channel width. These are denoted as "channel" and "wall" in Figure (6.2A). These masks are shaped as the top of a Gaussian function to decrease interfaces effects. The correlation of these masks with the profile is shown in Figure (6.2B). The fluorescence from the channels is maximised, while the fluorescence from the walls is minimised. The same procedure can be repeated for a range of pixel sizes around the expected value. The pixel size with the best channel-to-wall fluorescence ratio is selected as being the most probable value, as shown in Figure (6.2C). This allows for the extraction of each position as shown in Figure (6.2D). Once the profiles are extracted, a first fitting can occur. This fitting can be used to refine the positioning of the profiles by detecting any remaining offset between the data and the fit.

6.4.4 Simulations

The flow in the channel is assumed to be under steady state. The concentration field does not change explicitly with time but instead over the length of the channel. The dimensionless advection diffusion equation describes how the concentration field changes (see SI):

$$v_x' \partial_\phi c = (\partial_{y'}^2 c + \partial_{z'}^2 c - \mu' \partial_{y'} c) \tag{6.21}$$

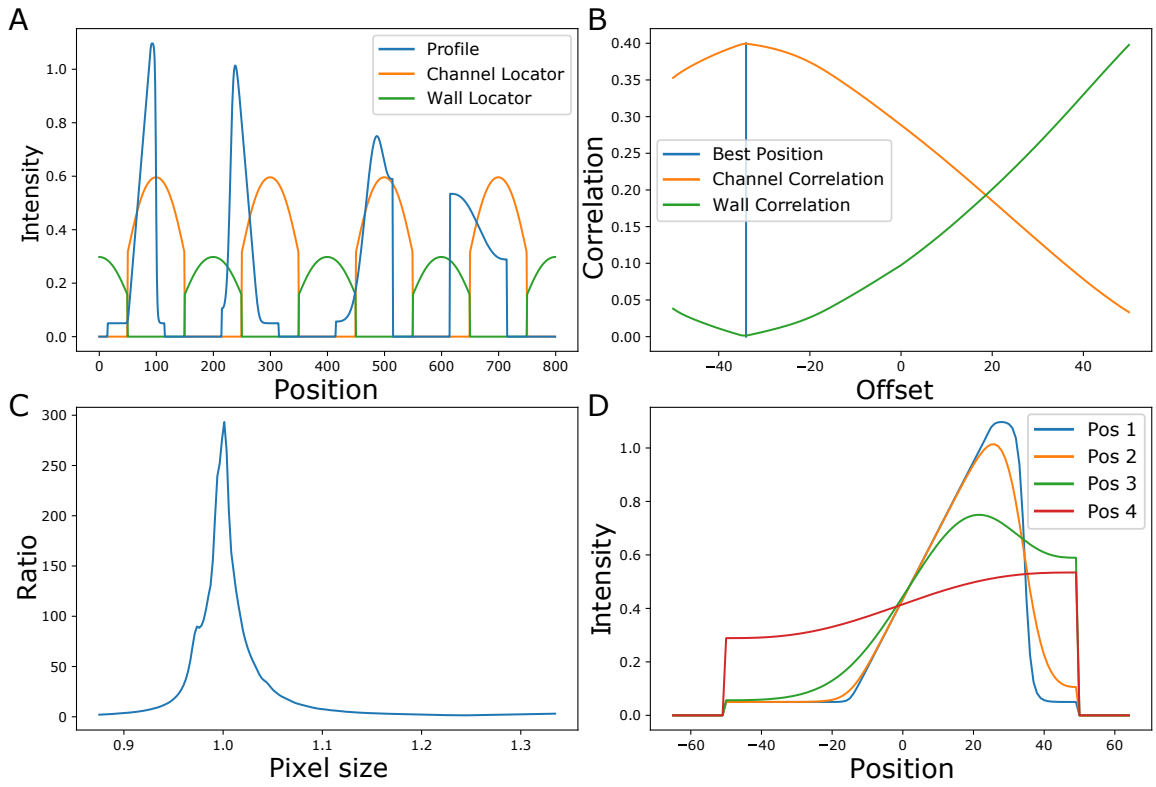

Fig. 6.2 Algorithm to detect the diffusion channel and scale changes. The overall profile contains four reading positions. The profiles are inverted in each reading position as the flow direction changes. (A) A rounded mask is created for the channels and the walls. The round top decreases the side effects. (B) The rounded masks are applied at several offsets to find the maximal intensity from the channel and minimal intensity from the background. (C) The same procedure is repeated for small variations on the scale. The ratio of channels intensity to background intensity reveals the real scale of the image. (D) Finally, all the positions are extracted. The profiles in this simulation are highly asymmetrical to illustrate that this technique can fit imperfect experimental data.

This problem was previously solved by Monte Carlo simulations of diffusing particles, [183] but this is very time consuming. Here, numerical integration of an ordinary differential equation is used instead. A Crank-Nicholson method is used, which has the advantage to be numerically stable and accurate [78]. A step matrix which, when multiplied by a concentration profiles, advances the simulation by an amount of diffusion $\delta\phi$, is computed. The diffusion profile corresponding to an amount of diffusion $\phi = N\delta\phi$ can therefore be computed by multiplying the matrix N times with the initial profile. To save time, a matrix exponentiation method which decreases the number of steps needed logarithmically is used. For example, instead of multiplying the matrix 2^n times to simulate a profile, the matrix is squared n times then multiplied by the initial profile.

6.4.5 Fitting

The fit is based on at least two positions. The first position is used to simulate some basis functions and the following positions are compared with the simulations. A global fitting is used to find the best solution over all positions. For a monodisperse fitting, a set of simulations corresponding to all positions is computed for a range of diffusion coefficients. The least square error between the recordings and the simulations is calculated. Using the property - discussed above and illustrated in Figure (6.4) - that the interpolation of two profiles approximates well the intermediate profiles, the best solution can be extracted from the two best fitting profiles. One can estimate the error on ϕ with first order Taylor series, as discussed in the theory. For polydisperse fitting, the number of variables grows quickly and stochastic algorithms are needed to find the global minimum. The fitting script uses basin-hopping [268] on a carefully defined system. Once the amount of diffusion ϕ is obtained, the radius can be calculated from the reading position x, the flow rate Q, the aspect ration β, the temperature T, and the viscosity η as:

$$r = \frac{x}{Q\phi}\beta\frac{K_b T}{6\pi\eta} \tag{6.22}$$

The standard error on the radius not only comes from the error on ϕ, but also from all other errors:

$$\sigma_r^2 \approx r^2\left(\frac{\sigma_\phi^2}{\phi^2} + \frac{\sigma_x^2}{x^2} + \frac{\sigma_Q^2}{Q^2} + \frac{\sigma_\beta^2}{\beta^2} + \frac{\sigma_T^2}{T^2} + \frac{\sigma_\eta^2}{\eta^2}\right) \tag{6.23}$$

The fitting algorithm does not know about any of the other errors and will therefore only take the error on ϕ into account, but these other errors can and will have an effect on the radius estimation. The scripts used for the fitting can be found online [199].

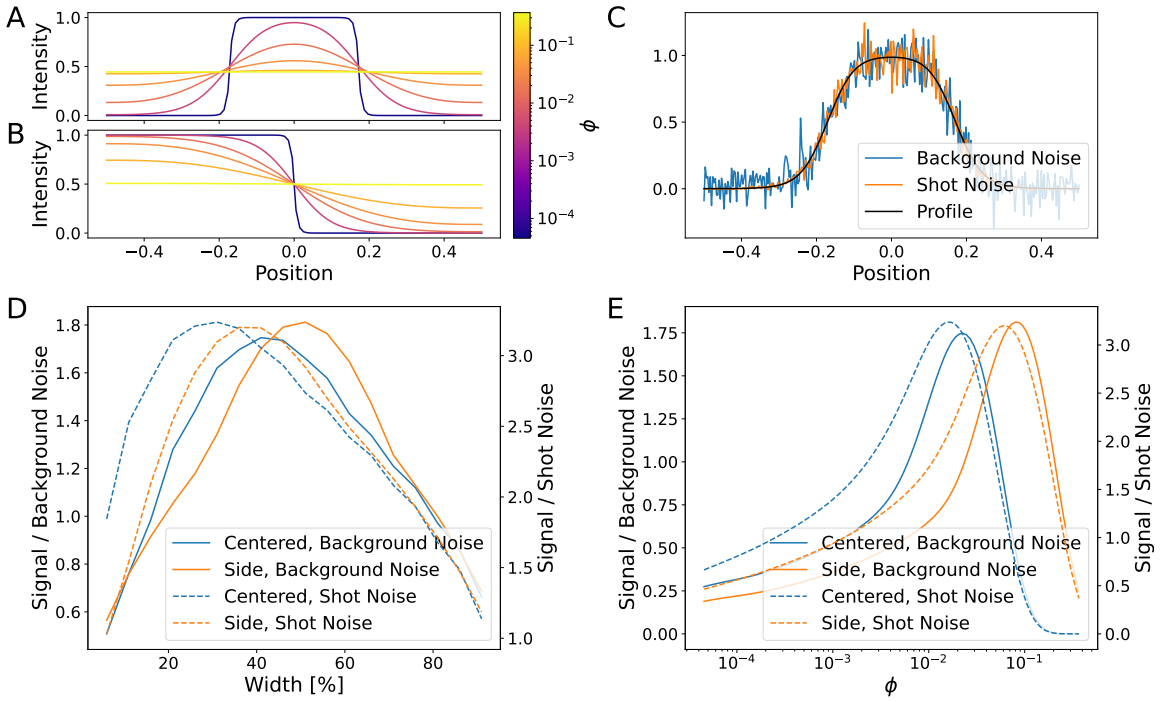

Fig. 6.3 Diffusion profiles are created by injecting a sample in the centre (A) or on the side (B) of a diffusion channel. The diffusion profile slowly flattens until reaching a flat concentration distribution. The colour of the diffusion profiles depends on the amount of diffusion ϕ, which is proportional to the diffusion coefficient. (C) When acquiring the data, noise is inevitable. Two cases are considered: shot-noise, that depends on the profile concentration, and uniform background noise. (D) The maximum signal-over-noise is plotted for both types of injection and noise. (E) The curves corresponding to the maximal injection width in (D) reveals an optimal amount of diffusion ϕ.

6.5 Results and discussion

The precision on the measurement is the main consideration when designing a diffusional sizing assay. When lacking an analytical solution for the diffusion profiles, efficient simulations are essential to estimate the signal-to-noise ratio of the measurement for all possible cases. Using Equations (6.3) and (6.4), the theoretical noise on a measurement can be extracted from the numerically integrated basis functions. The system is assumed to be either shot-noise or background noise limited, with the understanding that a realistic system would present both kind of noises, as illustrated in Figure (6.3C). Two types of initial profiles are particularly suited to microfluidic devices: central injection and side injection, as shown in Figures (6.3A) and (6.3B), respectively. The measurement signal-to-noise ratio depends on the injection width and on the reading position, as shown in Figures (6.3D) and (6.3E), respectively. If the injection width is too small, a low amount of sample is injected, which decreases the signal

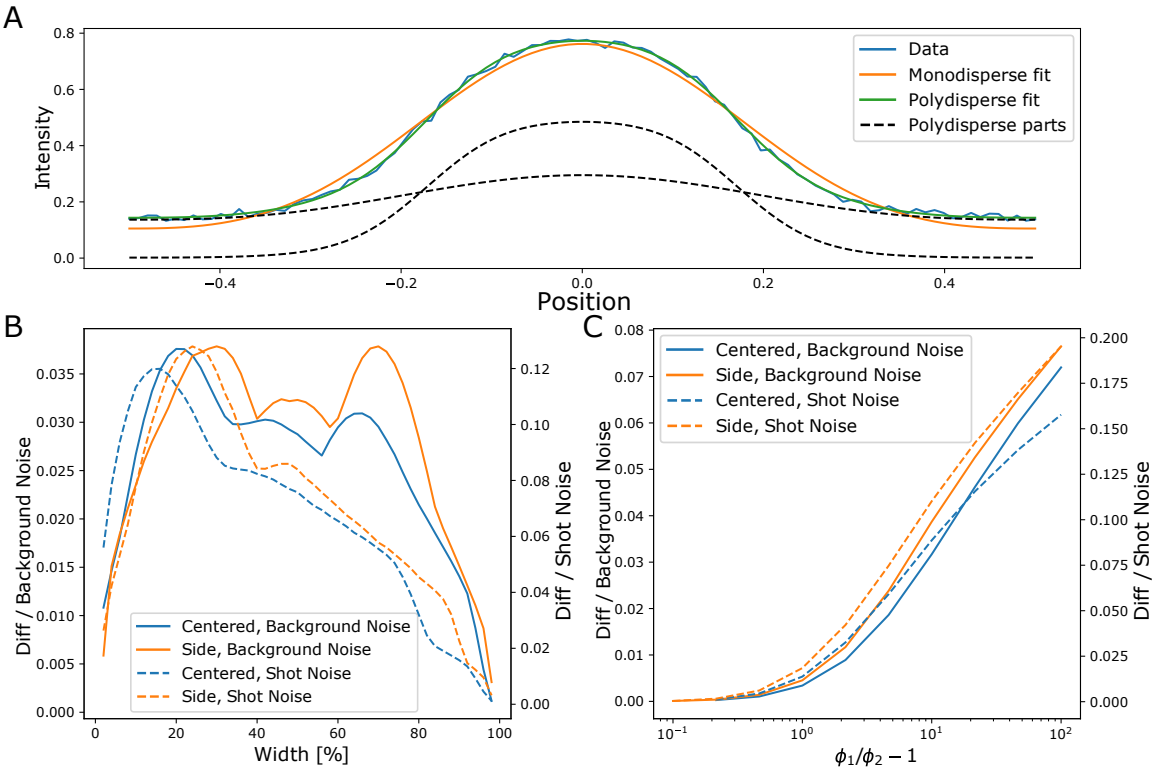

Fig. 6.4 (A) The monodisperse fit of a polydisperse diffusion profile is really close to the polydisperse fit. The diffusion coefficients of the two components are separated by a factor 10. (B) The difference between monodisperse and polydisperse fits is normalised by the acquisition noise. It is dependent on the initial profile and on the noise type, shown here for a ratio of 10. (C) The difference, shown here at the optimal width, grows with the diffusion ratio of the two components. A moderate amount of noise can easily preclude the separation of a polydisperse profile.

strength. If instead the injection width is too large, the profile quickly reaches the channel walls and flattens, loosing all information. An optimal injection width therefore exists. This optimum width is larger for central injection as the front is further from the walls. Shot-noise amplitude is smaller for low concentrations. This favors narrower injections compared to background noise. The dependence of this optimal profile on the amount of diffusion (ϕ), which is proportional to the reading position, is shown in Figure (6.3E). The strong peak around the optimal amount of diffusion has a long tail on the low diffusion side and stops abruptly on the high diffusion side. Indeed, when the diffusion profile reaches equilibrium, the signal is lost. The width of the peak means that a given flow rate in an experiment is suitable to measure a dynamic range of approximatively one order of magnitude in diffusion coefficient. To improve the dynamic range, several reading positions can be used.

Another important consideration is the discrimination capability of the assay for polydispersity. Many systems of interest are not monodisperse. The combination of two profiles whose samples have an order of magnitude difference in their diffusion coefficients is shown in Figure (6.4A). The profiles sum is almost indistinguishable from the monodisperse fit. This is quantified by the root mean square difference between a polydisperse profile (P_i) and its corresponding monodisperse fit (M_i) normalised by the noise (σ_i):

$$\Delta_{PM} \equiv \sqrt{\sum_i \frac{(M_i - P_i)^2}{\sigma_i^2}}$$

As for the sensitivity above, this difference depends on the initial profile, as illustrated in Figure (6.4B). Shot-noise favors small injection width while constant noise is more uniform. Figure (6.4C) shows that below a factor two difference in diffusion coefficient, the difference between polydisperse and monodisperse diffusion profiles is easily hidden by even a modest acquisition noise. Above that value, the difference increases as the log of the diffusion ratio. This has two important implications. First, polydisperse fitting is only possible if the diffusion coefficients are significantly different. A noise amplitude of 3% would hide an order of magnitude difference in diffusion coefficients. Second, this means that a combination of profiles leads to a profile that can be fitted by a monodisperse function. The resulting diffusion coefficient corresponds to a weighted average of all the components. If one were to analyse a polydisperse system, a difference in mean radii would be detected easily.

6.5.1 Maximum signal-to-noise ratio

The diffusion coefficient signal-to-noise ratio dependence on injection width and reading position is shown in Figure (6.5). As discussed above, the maxima first increases with

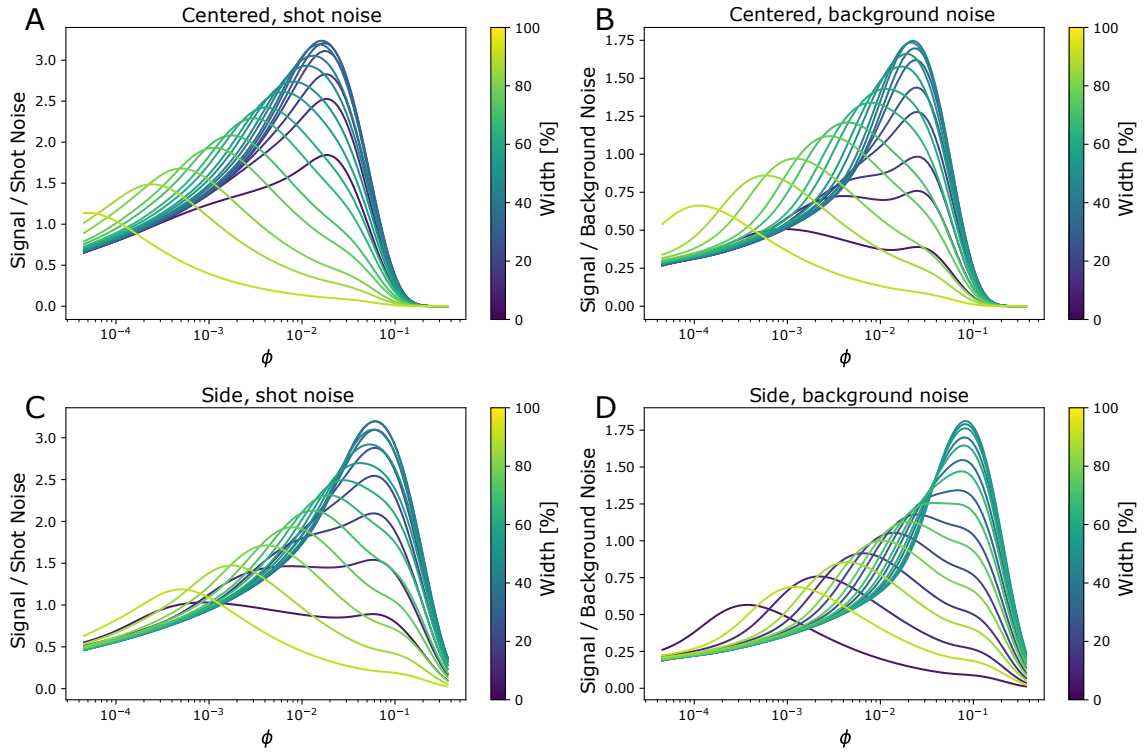

Fig. 6.5 Signal-to-noise ratio corresponding to diffusion coefficient fitting. The colour corresponds to the injection width. The graphs correspond to central injection, (A) shot-noise, and (B) background noise, and side injection (C) shot-noise, and (D) background noise. The height-to-width ratio is 0.5.

increasing width as more sample is injected. When the peak becomes too large, the front reaches the walls faster and the maxima is shifted to lower diffusions. Figure (6.3D) plots the maxima of each of these curves. Figure (6.6A) shows the largest peak for each case. Side injection profiles have to diffuse twice the distance to reach the walls. This corresponds to 4 times the diffusion. Figure (6.6B) shows that, by shifting the diffusion by a factor 4, the cures for central and side injections overlap. The difference between polydisperse diffusion profiles and monodisperse fit is shown in Figure (6.7) for a diffusion coefficient ratio of 10. The same curves are shown for a fixed injection width of 34% and varying diffusion coefficient ratio in Figure (6.8). The diffusion coefficient ratio unsurprisingly changes the amplitude of the curves considerably. Finally, the height-over-width ratio can be investigated. The system is defined by both the amount of diffusion (ϕ) and the height-to-width ratio (β). This ratio however does not play a large role, as shown in Figure (6.9). The difference in signal-to-noise ratio is less than 10% over two orders of magnitude.

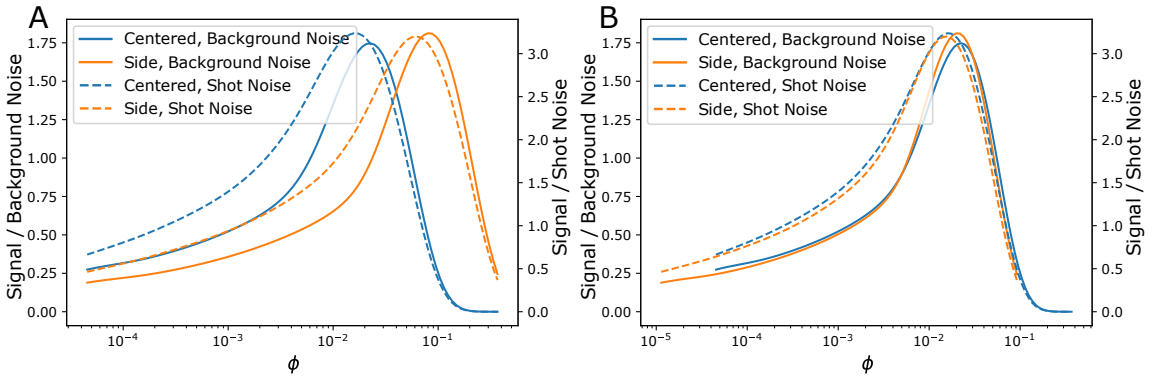

Fig. 6.6 (A) Comparison of the largest curves from Figure (6.5). (B) If the amount of diffusion ϕ is shifted by a factor 4, the curves overlap. This is expected as the distance to be diffused is twice as large for the side injection.

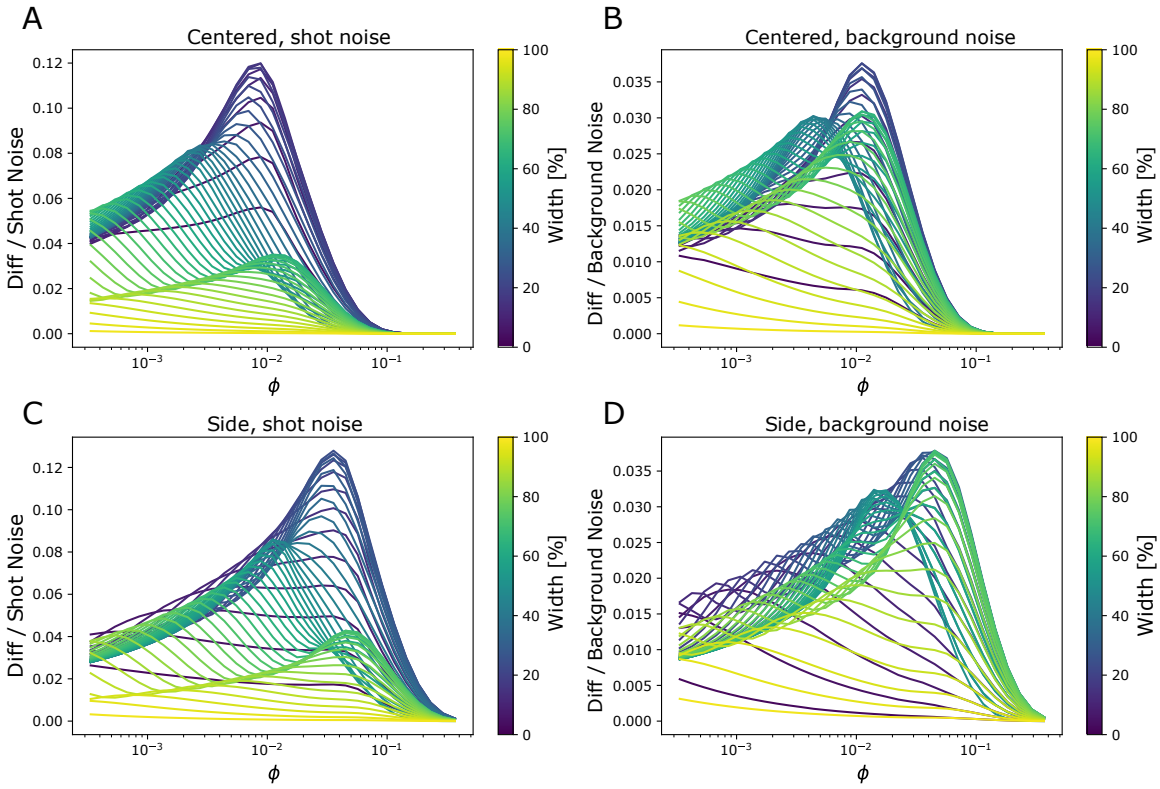

Fig. 6.7 Difference between polydisperse profiles and monodisperse fit normalised by noise. The colours correspond to the injection width. The ratio between the two combined profiles diffusion coefficients is 10. The graphs correspond to central injection, (A) shot-noise, and (B) background noise, and side injection (C) shot-noise, and (D) background noise.

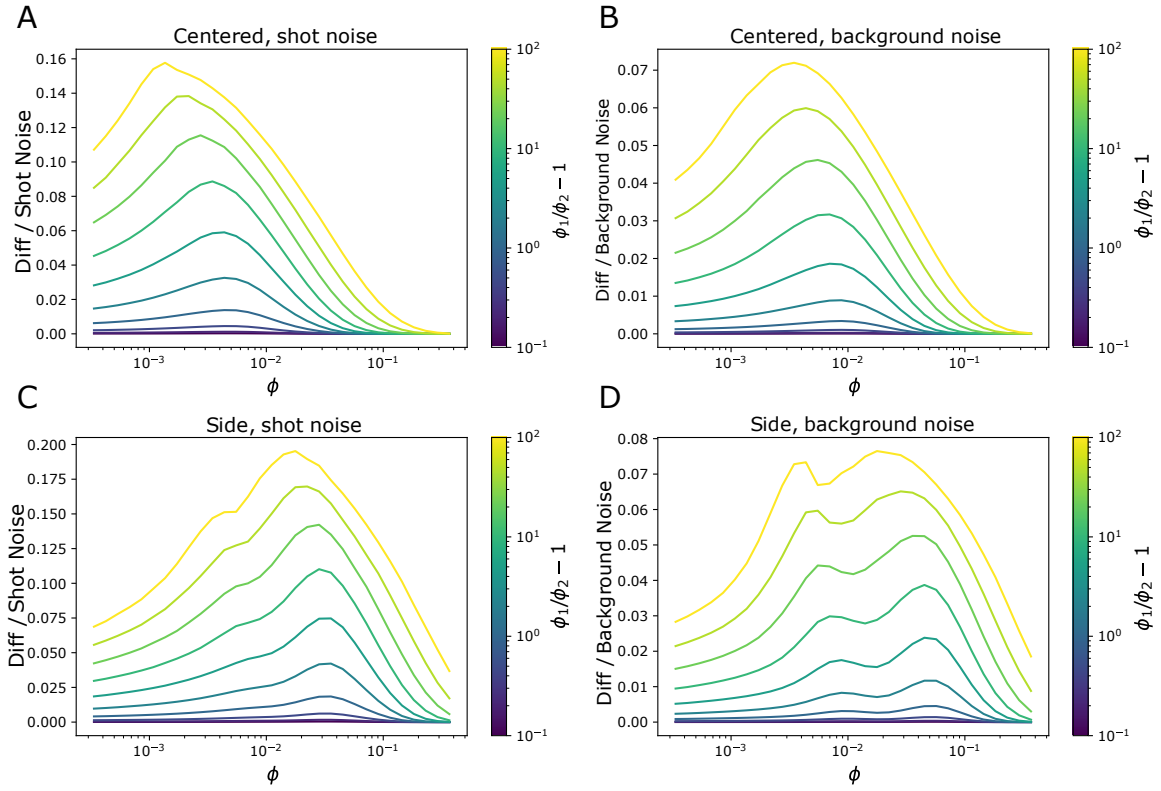

Fig. 6.8 Difference between polydisperse profiles and monodisperse fit normalised by noise. The colours correspond to the ratio between the two combined profiles diffusion coefficients. The injection width is 34%. The graphs correspond to central injection, (A) shot-noise, and (B) background noise, and side injection (C) shot-noise, and (D) background noise.

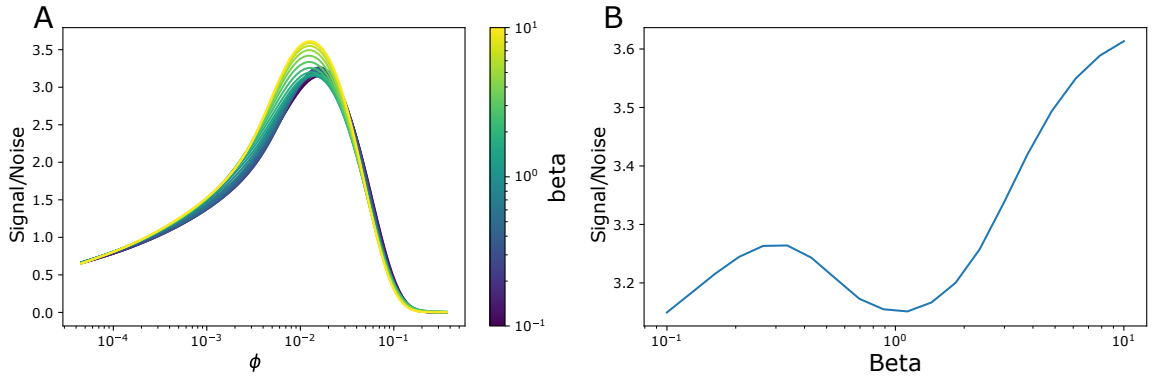

Fig. 6.9 (A) Signal-to-noise ratio corresponding to the diffusion coefficient fitting. The colours correspond to the height-to-width ratio (β). (B) Maximum of the curves in (A) as a function of the height-to-width ratio.

6.6 Conclusion

The methods to size a sample by analysing the diffusion profiles have been presented. The microfluidic chip design should combine several positions in the same field of view to improve detection accuracy and acquisition speed. The flow rate should be adjusted to match the best sensitivity for a given sample, and the detection position spaced properly to increase the dynamic range of the assay. For polydisperse samples, separation is very challenging, unless the diffusion coefficients of the components are separated by orders of magnitude. Sizing however can easily be performed where the result is a weighted average of the components, which is sufficient for many applications.

Chapter 7

Microscale diffusiophoresis of proteins

7.1 Summary

This chapter is based on the manuscript: Quentin Peter, Raphael P. B. Jacquat*, Therese W. Herling, Pavan Kumar Challa, Tadas Kartanas & Tuomas P. J. Knowles. "Microscale diffusiophoresis of proteins", Manuscript in preparation (* contributed equally). I designed the experiments. In addition to that, I largely contributed to acquiring the data. Moreover, I created a data processing and analysis pipeline. I also analysed the data and created simulations to extract the diffusiophoretic and the diffusion coefficients from the data. Finally, I wrote most of the paper.*

Living systems are characterised by their spatially highly inhomogeneous nature, which is susceptible to modify fundamentally the behaviour of biomolecular species, including the proteins that underpin biological functionality in cells. Spatial gradients in chemical potential are known to lead to strong transport effects for colloidal particles, but their effect on molecular scale species such as proteins has remained largely unexplored. Here, a demonstration is made with microfluidic measurements that individual proteins can undergo strong diffusiophoretic motion in salt gradients in a manner which is sufficient to overcome diffusion and which leads to dramatic changes in their spatial organisation on the scale of a cell. Moreover, a demonstration is made that this phenomenon can be used to control the motion of proteins in microfluidic devices. These results open up a path towards a physical understanding of the role of gradients in living systems in the spatial organisation of macromolecules and highlight novel routes towards protein sorting applications on device.

7.2 Introduction

Living cells constantly work to remain out of equilibrium, a key requirement for life. One crucial aspect of the non-equilibrium nature of living systems is the ubiquitous presence of gradients in ionic strength, maintained using ion pumps and related molecular machinery. This situation is fundamentally different to the spatially largely homogeneous conditions that characterise protein studies *in vitro* under bulk solution conditions. Understanding the diffusiophoresis of proteins can therefore yield insights in the nature and regulation of protein transport in living organisms [240]. Although over the past few decades diffusiophoresis has been well studied for larger colloids [11, 10, 12, 71, 185, 157, 288], little is known about whether single protein molecules, which are much smaller than typical colloids, can also generally undergo diffusiophoresis and which factors can modulate this process. Diffusiophoresis is linked to osmotic processes that take place on the particles surface [171, 6]. Surprisingly, the force applied on the particle does not scale with the surface [172], explaining why proteins might undergo non-negligible diffusiophoretic effects, as previously shown for the high mobility protein Lysozyme [15, 89]. In biophysics and life sciences, microfluidic techniques are increasingly used to probe the nature of proteins [109, 56, 18, 151, 17]. The rapid growth of the use of microfluidic techniques in research and industry [2, 229] is in part motivated by the fact that, compared to bulk processes, microfluidic processes enable a significant decrease in the required volume of solution. Moreover, under the microfluidic regime, it is possible to create laminar flows [194], which enable a fine control of dynamic experiments and which allow measurements that are often not possible in bulk solution. Similar phoretic processes, electrophoresis [276, 259] and thermophoresis [265, 266], are used to develop novel microfluidic techniques in research and industry. Diffusiophoresis is showing promising results for a wide range of applications, from oil recovery [155] to in-line preconcentration techniques [95].

In this study, transient protein diffusiophoresis is explored using a microfluidic format, which allows to control protein mass transport by eliminating the influence of factors that are ubiquitous in bulk measurements, such as convection. Previous geometries used for the study of diffusiophoresis of colloids include two channels merging perpendicularly [21], parallel flow of two solutions [1], diffusion through an hydrogel [193, 192], or two parallel channels joined by a micro- [244] or nano-channel [120]. Here, a simple geometry consisting of a dead-end perpendicular to a main channel is exploited [245]. Measuring the key properties of proteins such as mobility, size, and isoelectric point is one of the main goals in developing tools for protein science. Diffusiophoresis can be used for sizing colloids and calculating their ζ-potential in microfluidics [213, 245, 243], and could therefore be extremely useful if this effect proved to be generally significant for proteins. Diffusiophoresis could give additional

insight into folding states, as suggested by short polymers simulation [212]. Here, label-free protein diffusiophoresis is measured in real space using a novel UV microscope [53]. The results emphasize the dominant contribution to diffusiophoresis, and are fitted to extract relevant properties of the target protein, such as the hydrodynamic radius and the electrophoretic mobility.

7.3 Theory

7.3.1 Colloids diffusiophoresis

In colloids experiments, diffusiophoresis is described as a result of two effects [11]: chemiophoresis and electrophoresis. The electrophoretic motion is caused by the difference of ionic diffusion coefficients ($D_{\pm}$) of a salt. An electric field (E) appears between cations and anions to prevent bulk separation. It depends on the differential ratio of the ion diffusion coefficients (β) [11]:

$$E = -\beta \frac{k_B T}{Ze} \frac{d \ln C}{dx} \qquad \beta = \frac{D_+ - D_-}{D_+ + D_-}. \tag{7.1}$$

where $k_B T$ is the thermal energy and Ze is the ionic charge. The second term, the chemiophoretic contribution, is due to pressure difference inside the double layers of protein [245], which is similar to osmosis. One could note that the size of a protein is typically much smaller than the Debye length, so that the applicability of this effect which has been described for large colloids might be doubtful. These two effects are described by the diffusiophoretic mobility of the protein (Γ_p) that controls the diffusiophoretic speed $u_p = \Gamma_p \nabla \ln C$. For a purely electrophoretical experiment, the diffusiophoretic mobility is proportional to the ζ-potential of the proteins (ζ_p) [230, 245, 207, 206] and to the electrophoretic mobility (μ_p):

$$\Gamma_p = \zeta_p \frac{\varepsilon}{\eta} \frac{k_B T}{Ze} \beta = \mu_p \frac{k_B T}{Ze} \beta \tag{7.2}$$

where ε is the permittivity and η is the viscosity of the solvent. The diffusiophoresis therefore depends on the protein through its mobility, and on the salt through the charge of its ions and its β coefficient. The charge (q_p) can be related to the mobility using the Einstein relation:

$$\mu_p = \frac{q_p}{k_B T} D_p \tag{7.3}$$

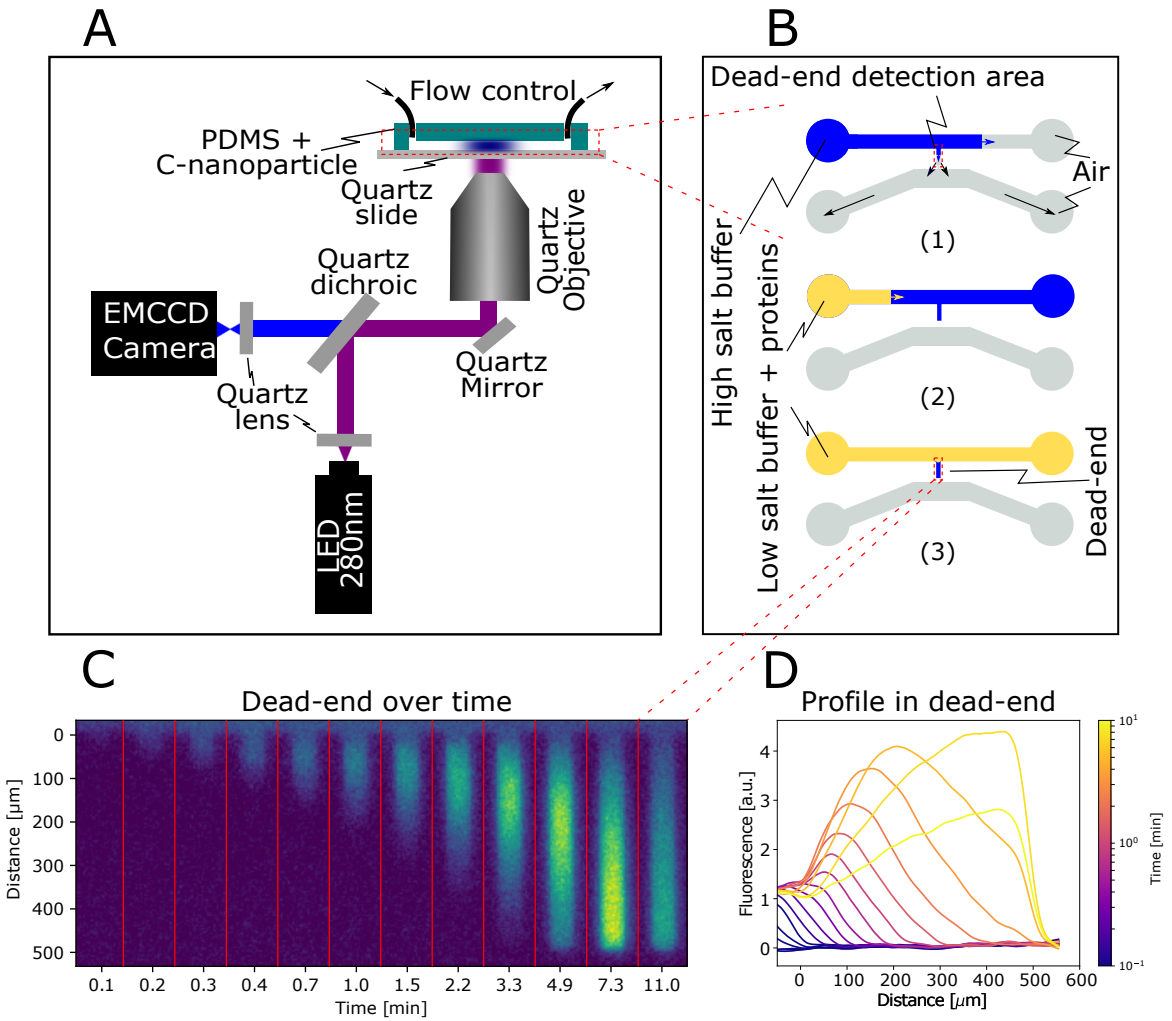

Fig. 7.1 (A) Schematic of the UV label-free microscope used to image a microfluidic device with a dead-end geometry. (B) Microfluidic device design used in this study. (B1) Firstly, the device is filled with a high-salt buffer. The air in the dead-end is pushed through the Polydimethylsiloxane (PDMS) in an empty lower channel. (B2) A protein solution is then pushed in the main channel, (B3) leaving only the high salt solution inside the dead-end. (C) A video of the dead-end is taken with logarithmically spaced time points to reduce photobleaching. (D) The channel is detected in each frame and the average over the width is extracted to form a profile.

7.3.2 Polyvalent ions

The description of diffusiophoresis in the literature [230, 245, 207, 206] for electrophoresis based diffusiophoresis usually depicts a salt whose two ions have the same valence or charge number ($Z_{\pm}$). This is not always the case, especially if - to optimise the β parameter - one uses a large and highly charged molecule with many counter-ions. Here, the general case of ions polyvalence is derived. An electric field is assumed to appear to prevent the charge density from being non-zero. The diffusion of small ions is slowed down, while the diffusion of larger ions is accelerated by this field. As the density of charge is assumed to be zero, $\vec{\nabla}\cdot\vec{E}=0$ from Maxwell equations. Each ionic specie i has a concentration c_i, a diffusion coefficient D_i, and a mobility μ_i. The motion is controlled by the convection-diffusion equation:

$$\frac{\partial c_i}{\partial t} = D_i\nabla^2 c_i - \mu_i\vec{E}\cdot\vec{\nabla}c_i$$

The mobility μ_i depends on the charge and on the diffusion coefficient:

$$\mu_i = \frac{D_i q_i}{k_B T} \tag{7.4}$$

The condition of charge neutrality can be written as $\sum c_i q_i = 0$. Taking the derivative with respect to time and integrating over space leads to a formula for the electric field needed to avoid charge separation:

$$\vec{E} = k_B T \frac{\sum q_i D_i \vec{\nabla} c_i}{\sum q_i^2 D_i c_i} \tag{7.5}$$

This is further simplified in the case of a single anion and a single cation with charge $q_{\pm} = \pm Z_{\pm} e$, where e is the elementary charge. In this case, the concentration of the ions are proportional to the salt concentration c:

$$\vec{E} = \frac{D_+ - D_-}{D_+ Z_+ + D_- Z_-}\frac{k_B T}{e}\vec{\nabla}\ln c \tag{7.6}$$

This leads to the definition of a new unit-less parameter β_Z that describes uniquely the salt contribution to the diffusiophoresis.

$$\beta_z = \frac{D_+ - D_-}{D_+ Z_+ + D_- Z_-} \tag{7.7}$$

If the ions have the same valence ($Z_+ = Z_-$), the usual result is recovered, and $\beta_Z = \beta/Z$. The diffusiophoretic coefficient therefore only depends on the protein mobility μ_p and on the

salt β_Z coefficient:

$$\Gamma_p = \frac{k_B T}{e} \mu_p \beta_Z \tag{7.8}$$

A similar derivation can be used to derive the salt diffusion coefficient D_s:

$$D_s = D_+ D_- \frac{Z_+ + Z_-}{D_+ Z_+ + D_- Z_-} \tag{7.9}$$

The unitless coefficient that controls diffusiophoresis is Γ_p / D_s:

$$\frac{\Gamma_p}{D_s} \propto \frac{1}{Z_+ + Z_-} \left(\frac{1}{D_-} - \frac{1}{D_+} \right) \tag{7.10}$$

The inverse of the diffusion coefficient is proportional to the hydrodynamic radius. Therefore, maximising the diffusiophoretic effect corresponds to maximising the difference between the ionic hydrodynamic radii.

7.4 Methods

7.4.1 Experimental setup

A microfluidic Polydimethylsiloxane (PDMS) device with a dead-end geometry, as shown in Figure (7.1), is used to create a gradient of salt. It is composed of three regions. The solution is flowed in the main channel, which is a straight channel with a cross section of 500×50 μm^2. The dead-end channel is perpendicular to this channel and its dimensions are $50 \times 50 \times 500$ μm^3. A second, unconnected channel is placed near the end of the dead-end to provide an escape to the air going through the PDMS, which is porous. The PDMS is casted on a master created by photo-lithography [52] and cured. It is then bounded to a quartz slide using a plasma oven.

The device is first filled with the solution which is intended for the dead-end channel. Pressure is applied until the air is evacuated through the PDMS in the second channel. A second solution is then pushed in the main channel, which comes into contact with the first solution at the base of the dead-end channel. The pressure is applied by hand for the priming of the chip and using a neMESYS syringe pump when pushing the protein solution at a flow rate of 600 ul/h.

A UV-LED based microscope is used to detect the proteins autofluorescence at 280 nm [53]. This is important as a covalently attached label might change the key properties of the protein. In practice, the observed fluorescence intensity at longer times is systematically lower, due to photo-bleaching. To reduce this effect, the images are logarithmically spaced in time.

The proteins have been obtained from Sigma-Aldrich. The proteins and product numbers are Myoglobin from equine skeletal muscle (M0630), Thyroglobulin from bovine thyroid (T1001), Lysozyme from chicken egg white (L6876), β-Lactoglobulin from bovine milk (L3908), and Bovine Serum Albumin (A7906). The concentrations used are 10 uM for Bovine Serum Albumin, β-Lactoglobulin, and Lyosyme, 1 uM for Thyroglobulin, and 30 uM for Myoglobulin. The experiments are made with three different salts - LiCl, KCl, KIO_3 - at 200 mM. All data can be found online [197].

7.4.2 Channel geometry

One might expect that inverting the solute concentration would result in an inversion of the diffusiophoretic velocity. In reality, the diffusiophoretic velocity u depends on $\nabla \ln(C) = \nabla C/C$ where C is the solute concentration [11]. Having the salt in the dead-end causes both the highest gradient and the lowest concentration to be localised at the inlet of the dead-end, therefore leading to the largest effect. In contrast, if the high solute concentration is in the main channel, there are only small guiding fields near the entrance. This greatly reduces the phenomenon.

7.4.3 Image analysis

The images of the dead-end are flattened to remove the non-uniform lightning by fitting a second-order two-dimensional polynomial to the outside of the channel. Detecting the background is only possible if the fluorescence of the proteins is not much higher than the background fluorescence. Otherwise, the fluorescence intensity is used as is. The channel sides are detected by using a Scharr edge detection algorithm. Finally, the intensity is normalised by the median value of the last five frames in the main channel.

The profiles are extracted by taking the average intensity over the center of the width of the channel, ignoring the sides to avoid wall effects. The resulting profiles are then filtered using a repeated Savitzki-Golay filter to reduce noise while conserving the shape. Finally, the profiles are plotted with a different colour for each frame time, as shown in Figure (7.1). All scripts can be found online [198].

7.4.4 Finite elements simulations

A finite elements software is used to simulate the system (Comsol multiphysics 5.2a with Microfluidics module and Optimization module). In one dimension, a Dirichlet boundary condition is used to fix the protein and salt concentrations at the inlet of the channel, and

a Neumann boundary condition is used on the closed end. In two and three dimensions, the main channel is simulated, allowing the main channel flow to enter the dead-end and allowing a local depletion to occur.

7.4.5 Fitting

Only profiles with a concentration peak are fitted. As seen on Figure (7.3), the experimental data fits the profiles well, except in two cases. First, if the peak reaches the end of the channel, the assumption of a semi-infinite channel is clearly broken. Therefore, frames with a significant fluorescence in the last fifth of the channel are not considered. Second, the large intensity difference between the data and the theoretical solution causes the normalised profile to start on a higher level at the channel inlet, as seen on Figure (7.3). Therefore, the part of the profile between the inlet and the peak is ignored as well. The selected data is illustrated by a solid line, and the ignored data by a dashed line. The solid line is almost completely hidden by the fit.

7.4.6 Free flow electrophoresis and diffusional sizing

Free flow electrophoresis is a technique that consists in applying an electric field perpendicularly to the direction of flow and by detecting the amount of deviation caused on a stream of particles. The deviation is proportional to the mobility of the particles. Diffusional sizing consists in looking at the diffusion speed under flow and extracting the diffusion coefficient from it. These techniques were used to compare the results with diffusiophoresis [220, 116].

7.5 Results and discussion

In order to explore whether or not proteins undergo a significant level of diffusiophoresis, a microfluidic device that enables the generation of a localised solute gradient is designed. The experiment is illustrated in Figure (7.1). After filling the device with a high solute concentration, this geometry allows the content of the main channel to be replaced by a protein solution with low ion concentration, while maintaining the high salt concentration in the dead-end. A strong solute gradient is therefore created at the dead-end inlet. The propagation of proteins over time in this solute gradient is captured by a UV-based autofluorescence microscope enabling label-free measurement of protein concentration [53]. The data in Figure (7.1C) reveals a significant effect on protein mass transport resulting from this solute gradient.

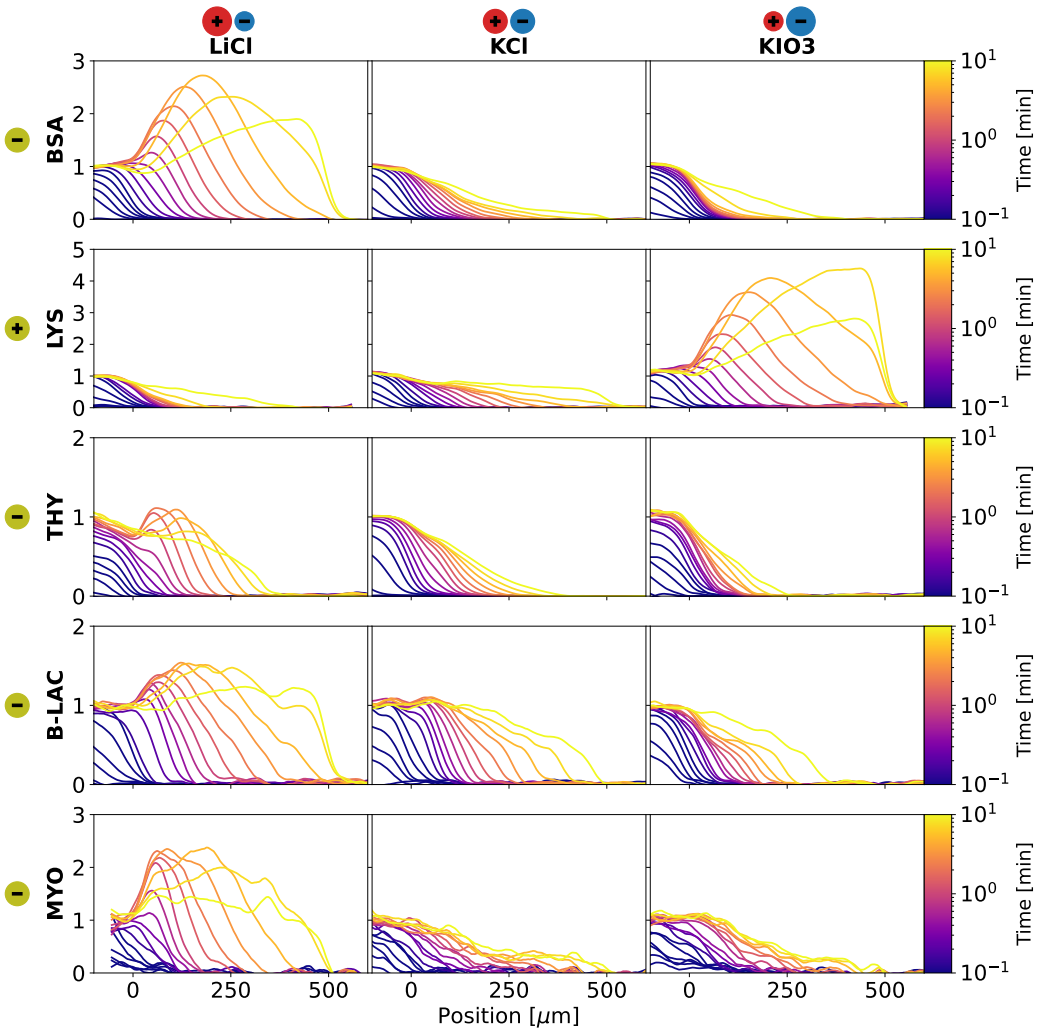

Fig. 7.2 Diffusiophoresis of proteins in different salt gradients. Four negatively charged proteins, Bovine Serum Albumin (BSA), Thyroglobulin (THY), Beta-Lactoglobulin (B − LAC), and Myoglobin (MYO), as well as a positively charged protein, Lysozyme (LYS), are placed into a salt gradient. The salts used to create this gradient are Lithium chloride (LiCl), Potassium chloride (KCl), and Potassium iodate (KIO_3). If the more diffusive salt ion has the same charge as the protein, a concentration peak appears in the channel. When the more diffusive salt ion has the same charge as the protein, the diffusion in the channel is reduced. If the two ions have a similar diffusivity, the effect is small. A sketch of the ions is shown on top of the figure to help visualize the relative diffusivities, where smaller means more diffusive.

In order to understand the origin of this remarkably large diffusiophoretic effect, the key physical parameters governing the motion of large scale objects such as colloids are considered. They exhibit two principal contributions to diffusiophoresis: electrophoresis and chemiophoresis (see the methods section 7.3.1). To investigate whether such effects or other related phenomena play a role for the behaviour of proteins whose surface are a factor $10^2 - 10^3$ smaller than typical colloids, a range of proteins and salts are selected. The importance of the surface area has been discussed in the literature [172]. In particular, the conjugated salts from strong bases and acids are selected to avoid affecting the pH of the solution. First LiCl and KIO_3, which have a strong difference in the diffusion coefficient of their ions, and then KCl, whose ions have similar diffusivities. This differential behaviour is captured by the β coefficient, which is the normalised difference between the ionic diffusion coefficients D_+ and D_-: $\beta \equiv (D_+ - D_-)(D_+ + D_-)^{-1}$. For example, LiCl has $D_{Li^+} = 1.03 \cdot 10^{-8}\ m^2/s$ and $D_{Cl^-} = 2.03 \cdot 10^{-8}\ m^2/s$, which gives a normalised difference of $\beta = -0.326$. The β coefficient of KIO_3 (0.298) has roughly the same magnitude and an opposite sign, and KCl (-0.019) has a much smaller magnitude [45]. Our experiments were designed to test whether the electrophoresis term dominates, resulting in a strong and opposite effect from LiCl and KIO_3, or if the chemiophoresis term dominates, resulting in a similar effect from all three salts. The results are shown in Figure (7.2). The first column shows LiCl which dissolves into a more diffusive Cl^- anion and a less diffusive Li^+ cation. An electric field pointing out of the dead-end is created by the difference in the ionic diffusion to avoid charge separation. Consistently with the electrophoretic description, Bovine Serum Albumin (BSA), whose charge is negative at pH 7, is attracted and concentrated in the dead-end, forming a visible concentrated peak. The data in the first column of Figure (7.2) further reveals that Lysozyme (LYS), whose charge is positive at pH 7, is by contrast prevented from entering the channel for a few minutes, until the strength of the salt gradient decreases. Next, the effect of KCl whose ions have approximatively the same size in the second column of Figure (7.2) are investigated. As the profiles are dominated by diffusion, the diffusiophoretic effect is almost negligible. To verify this conclusion, a third salt is tested. KIO_3 creates a roughly equal and opposite electric field compared with LiCl. As expected, the third column of Figure (7.2) reveals that BSA diffusion into the dead-end is significantly restricted for several minutes. Lysozyme is instead strongly concentrated and attracted into the dead-end. This result highlights the role of electrostatics and indicates that the electrophoresis is much stronger than the chemiophoretic contribution.

A concentration peak becomes visible when the charge sign of the protein matches the more diffuse salt ion. The position of the peak depends mostly on the diffusiophoresis strength and the width of the peak depends on the protein size. This opens up the possibility to

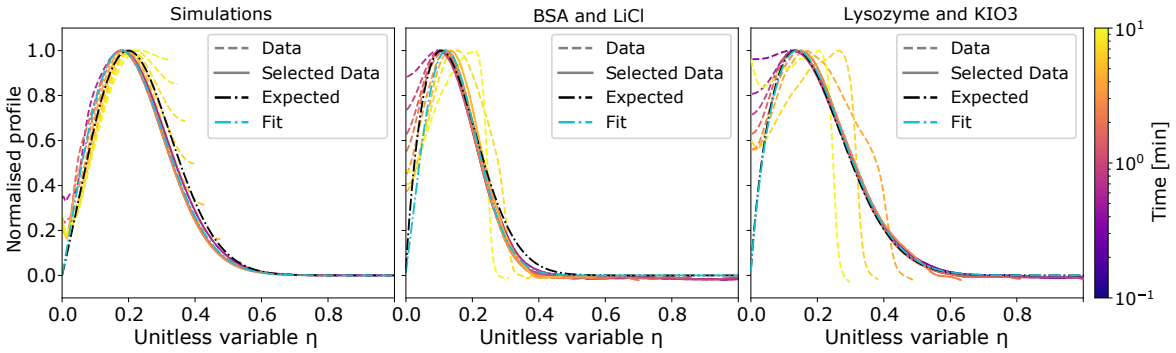

Fig. 7.3 Quantitative description of diffusiophoresis. A finite elements simulation and the two proteins from Figure (7.2) are plotted as a function of the dimensionless variable η. The finite elements simulation and the measurements give similar results. Most curves overlap with the 1D model. The differences are explained by two effects. The main channel is not a perfect reservoir. This can be seen on the left near $\eta = 0$. The dead-end channel is not semi-infinite. This is highlighted by the later, yellow curves not overlapping when reaching the end of the channel. Both the fitted profile (cyan) and the expected profile (black) are a good match to the measured data. The simulation is a 2D simulation with protein diffusion coefficient of $5.9 \cdot 10^{-11}\ m^2/s$ and diffusiophoresis coefficient of $-1.5 \cdot 10^{-10}\ m^2/s$. The corresponding expected profile is the solution of equation (7.11) for the same values. For BSA and Lysozyme plots, the expected profiles are the solution to the same equation with electrophoretic mobilities measured by free flow electrophoresis [115] of respectively $-0.988 \cdot 10^{-8}$ and $1.76 \cdot 10^{-8}\ m^2/Vs$ and hydrodynamic radii measured by diffusional sizing [226] of respectively 3.48 and 2.05 nm.

fit the peaks to extract this information about the proteins. The physics can be captured in one dimensional space by introducing a dimensionless parameter [22], $\eta = x/\sqrt{4D_s t}$, describing distances x relative to the mean diffusional distance of the salt with diffusion coefficient D_s at a time t. The protein concentration (N) depends on the diffusion ($D_p d^2N/d\eta^2$) and on a driving force from the gradient in the channel potential of the salt, creating a dimensionless velocity ($d\ln(C/C_{main})/d\eta$):

$$\frac{D_p}{D_s}\frac{d^2N}{d\eta^2} + 2\eta\frac{dN}{d\eta} - \frac{\Gamma_p}{D_s}\frac{d}{d\eta}\left(N\frac{d\ln(C/C_{main})}{d\eta}\right) = 0 \tag{7.11}$$

The dimensionless constants represent the ratio of the protein diffusion coefficient (D_p) and diffusiophoretic coefficient (Γ_p) with the salt diffusion coefficient (D_s). The salt diffusion coefficient captures the diffusion of both ions. This results in a weighted average of the ionic diffusivities. The diffusiophoretic coefficient depends on the protein and on the salt properties. In the dilute limit, the salt concentration C is given by a single constant ($0 \leq \alpha \leq 1$), which is the ratio of the concentration in the main channel (C_{main}) by the initial concentration in the dead-end:

$$C(\eta) = C_{main}(\alpha + (1-\alpha)\,\mathrm{erf}(\eta)) \tag{7.12}$$

Interestingly, this simple one-dimensional analysis predicts qualitatively the observed trends, thus capturing the essential physics, as shown in Figure (7.3). A quantitative comparison reveals that the predicted peak heights are higher than those observed in the experiments. To understand the origin of this effect, finite elements simulations for multidimensional systems are next performed. The reason for the observed differences in the peak heights is a depletion of analytes at the inlet of the dead-end that is not captured in the one dimensional analysis. However, when normalized by the height of the concentration peak, the profiles have the same shape, as illustrated in Figure (7.3). The cyan profiles, fitted with Equation (7.11), match well the measurements and the finite elements simulations. The width of the peak is directly related to the protein diffusion coefficient, and the protein mobility can be obtained from the location of the peak. The black profiles in Figure (7.3) indicate the expected curves from the mobility and radius measured by free flow electrophoresis [115] and diffusional sizing [226]. The same fitting is applied to the other protein experiments and the results are shown in Figure (7.4). The Lysozyme protein has the largest mobility, explaining why the effect is the strongest among tested proteins.

The advantage of this technique over the approaches presented in Chapters 2-4 is that multidimensional information about a single protein can be extracted in a single experiment. This allows the identification of species that have similar hydrodynamic radii but different electrophoretic mobilities. The accuracy on the hydrodynamic radius is however lower with

this technique. One limitation of the setup presented here is that the salt gradient is transient. A stable salt gradient would result in a larger effect, thereby improving the accuracy of the assay. This would however complicate the setup. A stable salt gradient requires two reservoirs of concentration, for example two channels connected by a H-junction. While having no bulk flow in a dead-end is easy, bulk flow in a junction is much more difficult to avoid. Any difference in pressure between the two ends will lead to a flow, flushing the protein peak away. Two designs were tried and rejected because of PDMS compliance and of pressure variations caused by syringe pumps: a design with a channel and a large reservoir, and a design with a channel on either side. These limitations are however not insurmountable and a future design using injection moulding to create a more rigid chip and pressure controllers could lead to more success. Another option would be to use nanochannels, as described in Chapter 5, to increase the hydrodynamic resistance in the junction.

The finite elements simulations are validated by experiments. Moreover, they provide us with an opportunity to query which experimental parameters can be optimized for future developments to maximise the strength of the diffusiophoretic effect. For example, these simulations show how the concentration power depends on the salt properties. Figure (7.7) summarises the strength of the effect while different experimental parameters are varied. The most impactful parameter is the diffusiophoresis coefficient, which can be maximised by choosing a salt with a large difference in ionic diffusion coefficient. This is achieved by maximising the difference in ionic hydrodynamic radii. Other optimisations include a small diffusion coefficient for the salt and a salt concentration difference of at least two orders of magnitudes between the main and side channels.

7.5.1 COMSOL simulations

The theoretical solution for the semi-infinite channel predicts a concentration that is much higher than what is seen in the experiments. To understand this discrepancy, COMSOL simulations are done in one, two, and three dimensions. In one dimension, the salt and protein concentrations are fixed at the dead-end inlet. In two and three dimensions, the main channel and the flow are simulated. An example of the protein distribution is shown in Figure (7.5). A half circle can be seen in two and three dimensions, where the main channel flow penetrates in the dead-end. While the intensity of the one dimensional simulation is very close to the intensity predicted by the theoretical solution, as shown in Figure (7.6), the intensities of the higher dimensional simulations are much lower. However, when the profiles are normalised, the solution seems to fit perfectly. In two and three dimensions, a small offset can be seen. It leads to a small underestimation of the diffusiophoresis coefficient, as discussed below.

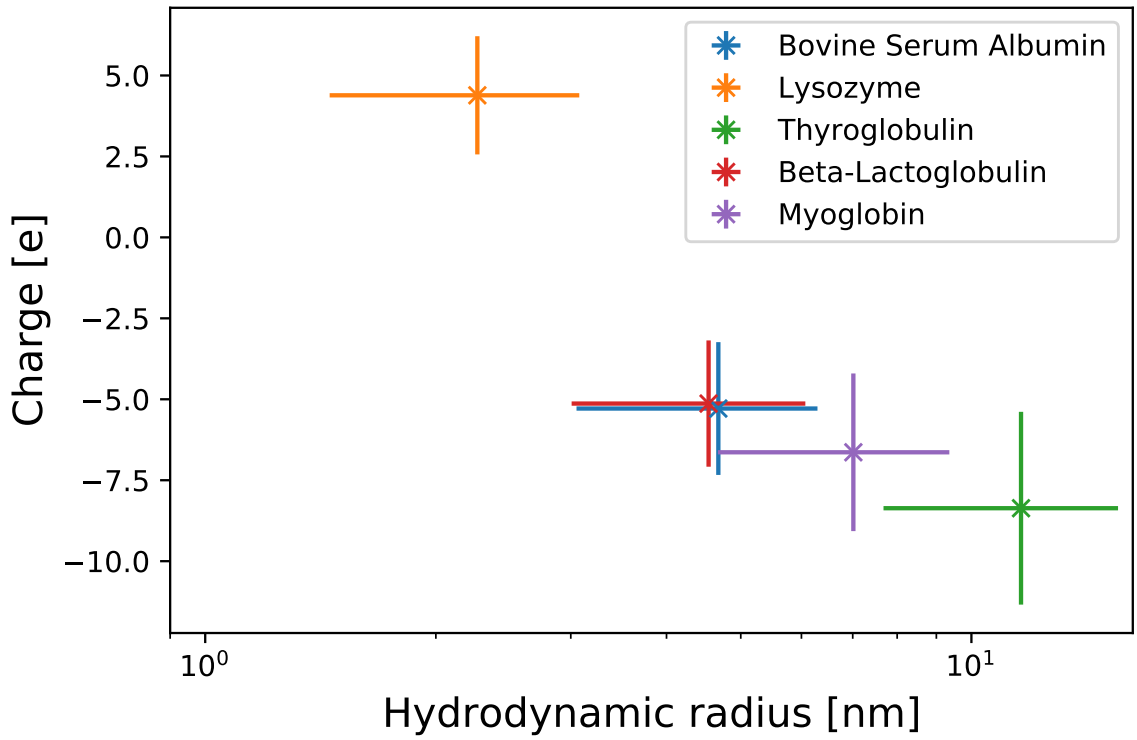

Fig. 7.4 Fitting results for the five proteins from Figure (7.2). The error bars are estimated from the fitting. The hydrodynamic radius is extracted from the fitted diffusion coefficient. The charge is extracted from both the diffusion and the diffusiophoresis coefficients, by making the assumption that the system is dominated by the electrophoretic contribution to diffusiophoresis. The relative error is about 34% for the radius and 38% for the charge.

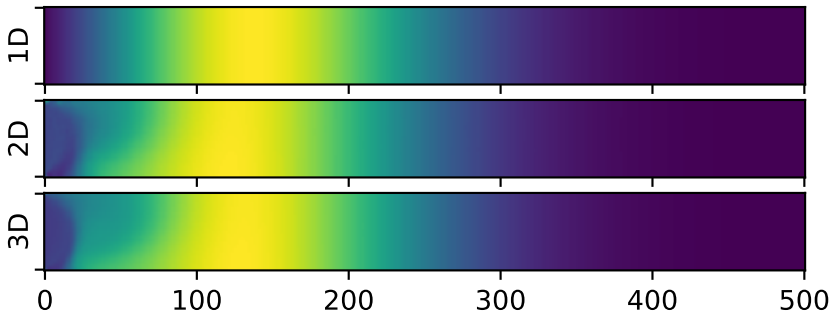

Fig. 7.5 Spatial distribution of the concentration in the channel for the COMSOL Figures after two minutes. The colourmaps are normalised for each plot, so that the intensities cannot be compared here.

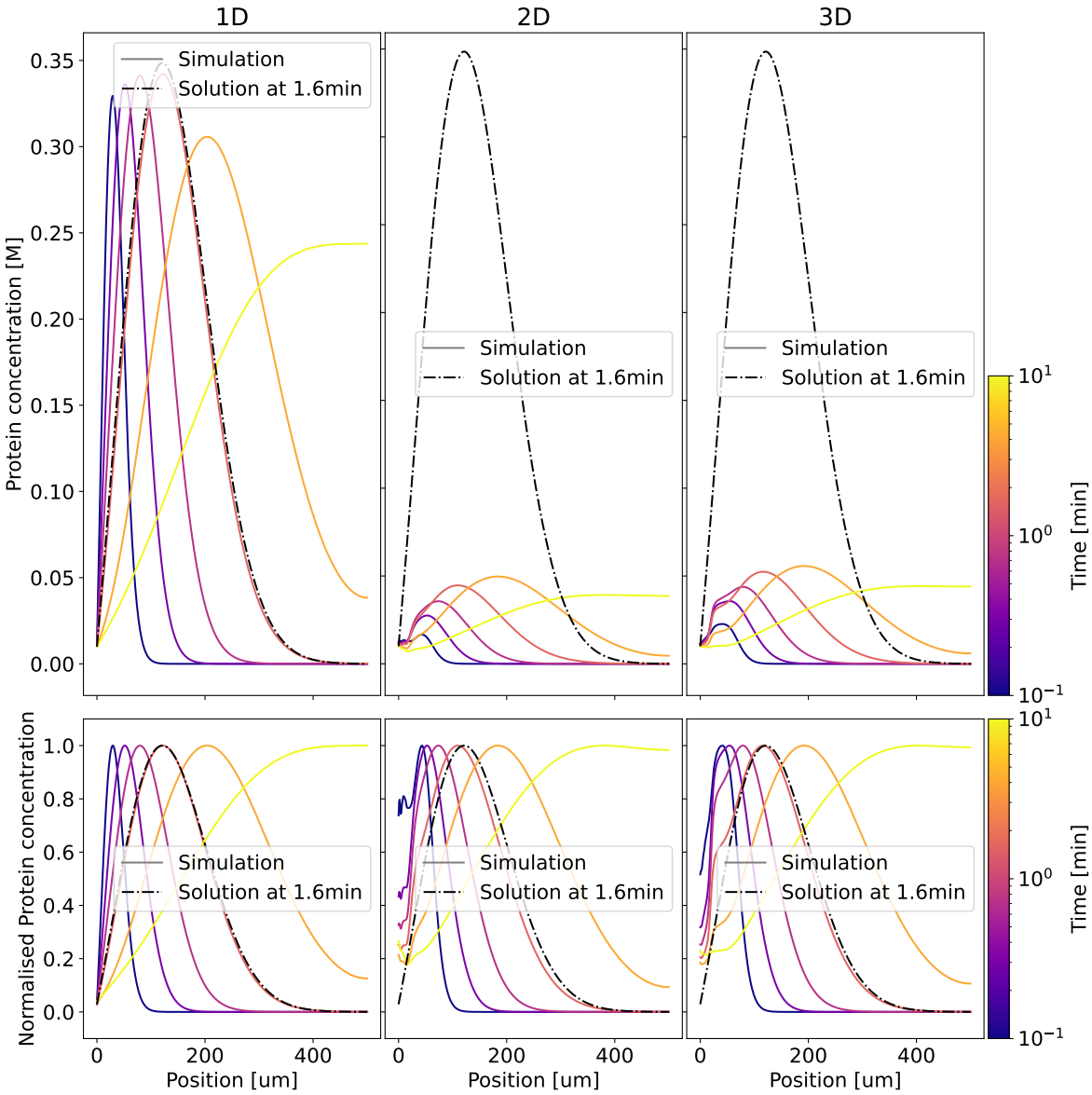

Fig. 7.6 Comparison of one, two, and three dimensional simulations. The intensity of the partial differential equation and of the one dimensional simulation are similar and much larger that of two and three dimensional simulations. When normalised, the three simulations are almost indistinguishable.

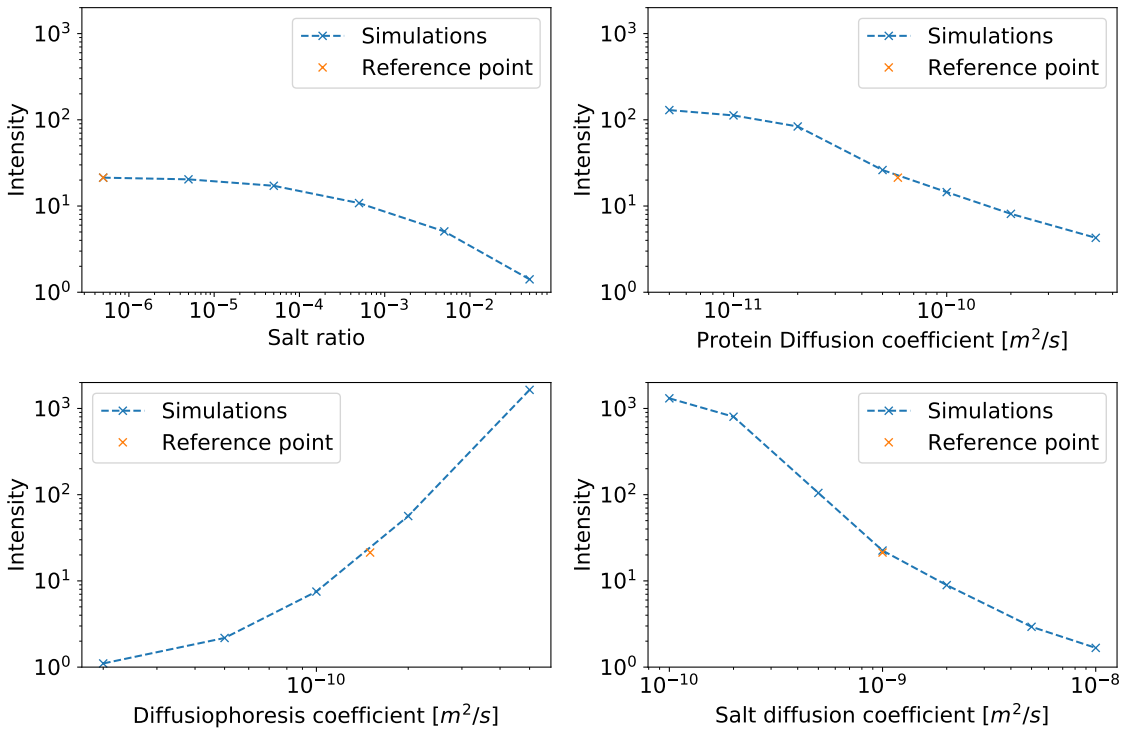

Fig. 7.7 Role of the physical properties of proteins on the strength of the diffusiophoresis effect. The maximum concentration of the simulations is shown as a function of (A) salt ratio, (B) protein diffusion coefficient, (C) diffusiophoresis coefficient, and (D) salt diffusion coefficient. The intensity is the ratio of the maximal concentration with the initial protein concentration. The reference point is the same between the four graphs.

Figure (7.7) shows the effect of varying several parameters on the strength of the diffusiophoresis effect. First, the effect of the salt concentration ratio between the main channel and the initial dead-end concentration are investigated, in Figure (7.7A). As expected, a ratio of one leads to no diffusiophoretic effect. As the ratio decreases, the effect becomes stronger but rapidly saturates when the main channel molarity is two to three orders of magnitude below the dead-end molarity. Further, a protein with a large diffusion coefficient is unsurprisingly harder to concentrate (Figure (7.7B)). As expected, the diffusiophoresis coefficient is a major contributor to the concentration (Figure (7.7C)). Therefore, to see a large effect, β should be maximised. A perhaps less intuitive result is shown in the final plot (Figure (7.7D)). As the salt diffusion coefficient increases, the intensity decreases. This is explained in Equation (7.11), as the unit-less parameter that controls the diffusiophoresis is Γ_p/D_s. An experiment designed to analyse proteins using the diffusiophoretic effect should therefore use a high concentration of a salt that has a large difference in ionic diffusion coefficient, and whose own diffusion coefficient is small.

7.5.2 Experiments

Plotting the experiments against the unitless parameter η can give a better vision of whether or not diffusiophoresis is taking place. This is shown in Figure (7.8). The small diffusiophoretic effect of KCl, while nowhere as large as the LiCl and KIO3 versions, can be seen.

The salt concentration ratio is an important parameter as it limits the concentration of buffer that can be used with the proteins. Even using proteins without buffer can significantly decrease the diffusiophoretic strength. BSA is itself an ionic molecule, and is accompanied by many counter-ions. The molecular weight of BSA is typically three orders of magnitude higher than a salt such as LiCl. Assuming that the concentration of counter-ions is a thousand times higher than the protein concentration, Figure (7.9) is consistent with the simulation results: decreasing the concentration from 1000 μM to 100 μM results in a peak ten times higher, while the next decrease of an order of magnitude only increases the peak height by 30%. The concentration of any salt or counter-ions should therefore be at least two orders of magnitude lower than the dead-end salt concentration. The next test consists in verifying if the diffusiophoresis coefficient dependence is really as strong as Figure (7.7) seems to indicate. To that end, $NaOH$ is compared with $LiCl$, as the β coefficient of $NaOH$ is twice as large as the one of $LiCl$. To avoid a large effect from the massive change in pH, thyroglobulin, whose electro-phoretical mobility is roughly constant for pH of 7 and above [260], is selected. As shown in Figure (7.10), the peak is 16 times higher when simply doubling the diffusiophoretic coefficient.

7.5.3 Fits

The simulations show a good agreement with the theoretical solutions after normalisation. Therefore, fitting the profiles appears to be a promising way of extracting information about the proteins. To validate this approach, the simulated profiles are fitted with the theoretical solution. As the theoretical solution assumes a semi-infinite channel, the profiles with significant intensity in the last fifth of the channel are excluded. Similarly, the part of the profiles between the main channel and the peak are not fitted as the intensity difference changes this part of the profiles. As can be seen in Figure (7.6), a slight offset in the fitted diffusiophoresis coefficient and a good agreement with the diffusion coefficient are expected. This is indeed what is shown in Figure (7.11). The error on the diffusion coefficient is consistently smaller than 10% and the error on the diffusiophoresis appears to have a constant offset of -25%. A closer look at a few simulations leads to a better understanding of these graphs. The diffusiophoresis coefficient seems to increase slightly with the salt ratio, as shown in Figure (7.11A). For ratios close to one, the concentration is much lower, as

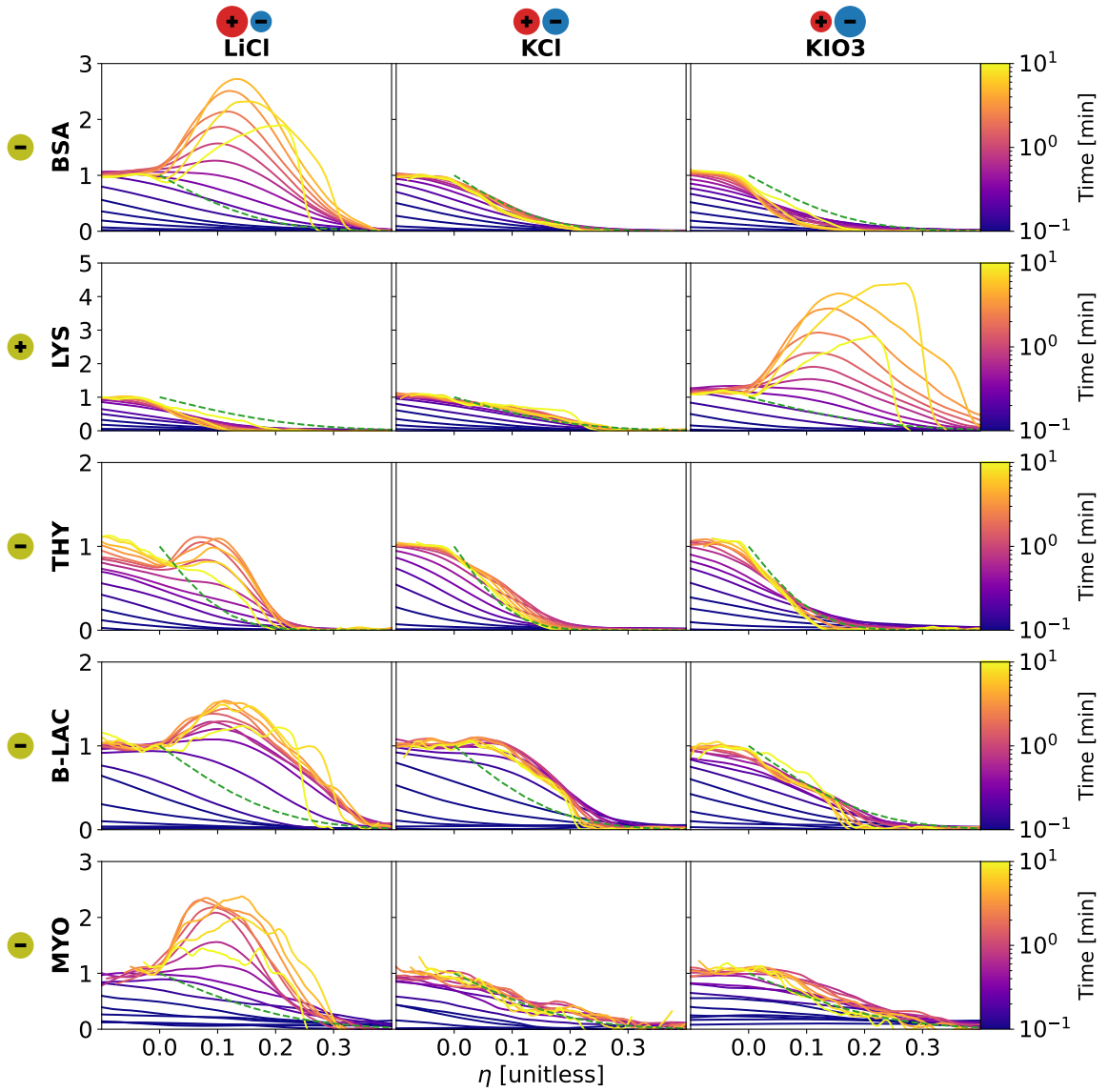

Fig. 7.8 Diffusiophoresis of proteins in salt gradient versus the unitless parameter η. The proteins are Thyroglobulin (Thy), Bovine Serum Albumin (BSA), Beta-Lactoglobulin (B-LAC), Myoglobin (MYO), and Lysozyme (LYS). The salts are Lithium chloride (LiCl), Potassium chloride (KCl), and Potassium iodate (KIO3). If the smaller salt ion has the same charge as the protein, a concentration peak appears in the channel. If the larger salt ion has the same charge as the protein, the diffusion in the channel is reduced. If the two ions have a similar charge, no effect is visible. The green dotted line shows the expected profile from diffusion alone, which should be the same at any time when plotting against η.

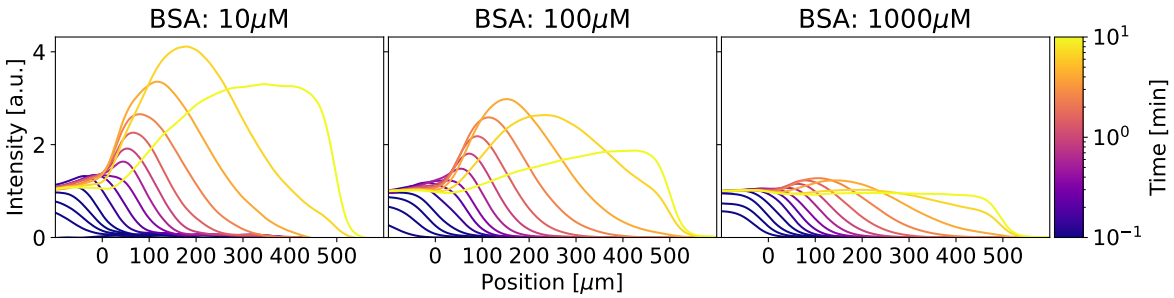

Fig. 7.9 Effect of protein concentration on diffusiophoresis for BSA. The salt is 2 M LiCl.

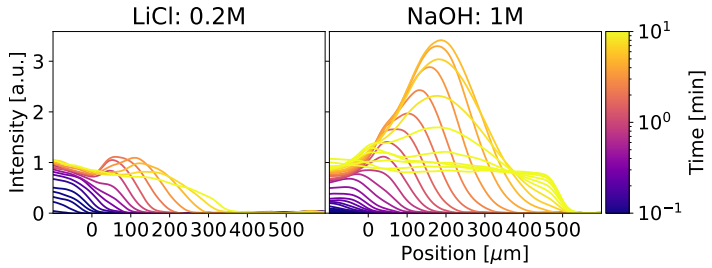

Fig. 7.10 Effect of diffusiophoretic coefficient on 1 uM Thyroglobulin. The salts are 0.2 M LiCl and 1 M NaOH.

shown in Figure (7.12A). The fitted coefficient increases when the diffusiophoretic effect disappears. The following simulations are done with the lowest channel salt concentration. In Figure (7.11B), the fitted diffusion becomes much higher when the diffusion coefficient is low. This is unsurprising as the slope becomes really steep and does not change much, as shown in Figure (7.12B). On the one hand, effects such as numerical diffusion could easily explain this change in fitted diffusion coefficient. On the other hand, the diffusiophoresis coefficient appears to be roughly constant. In Figure (7.11C), the diffusion coefficient is quite stable when varying the diffusiophoresis coefficient. The fitted diffusiophoresis coefficient itself however shows a relative increase for lower values of the simulated diffusiophoresis coefficient. As shown in Figure (7.12C), this could be explained by the simulation taking more time to converge to the theoretical solution. This problem is even more apparent in Figure (7.11D), where the fitted diffusiophoresis appears to be too large for low salt diffusion. Looking at Figure (7.12D), the problem appears: only the first time points do not have a significant fluorescence at the end of the channel. Unfortunately, these time points are before the simulation converged to the theoretical solution.

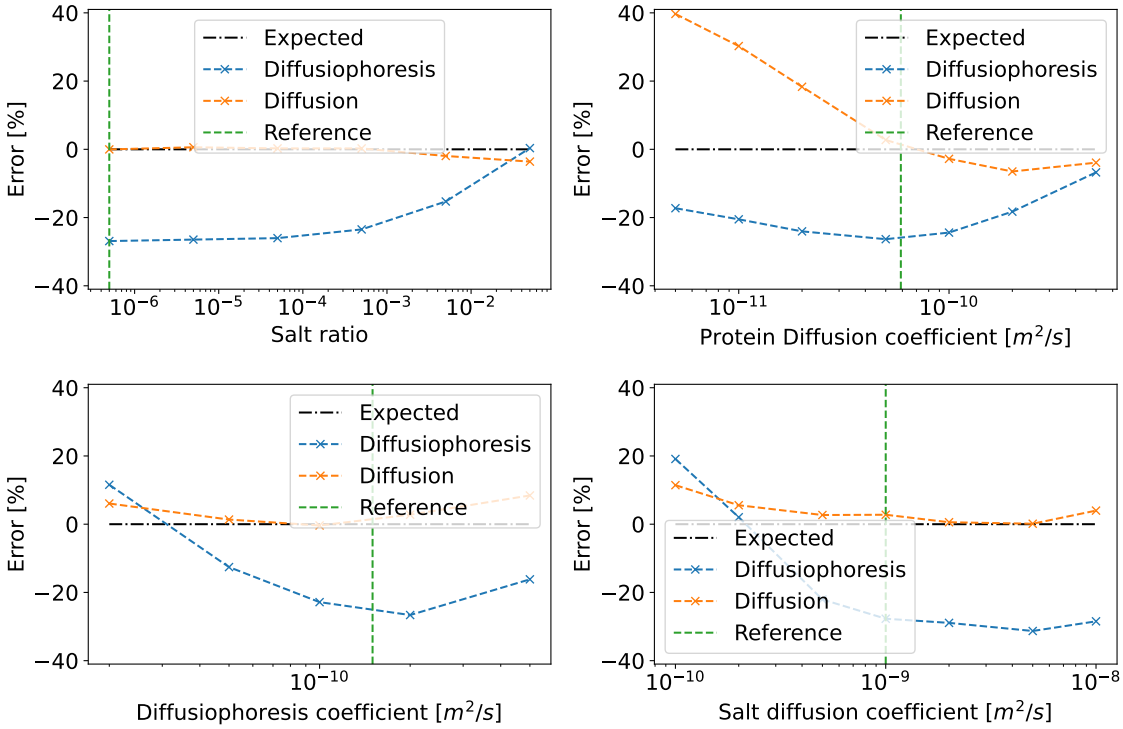

Fig. 7.11 Error in the fit of the simulations. The blue lines represent the error on the diffusiophoresis coefficient. The orange lines represents the error on the diffusion coefficient. The reference value is the same between the four graphs.

Salt	NaOH	LiCl	NaCl	KCl	CsCl	KIO_3	HCl
β	-0.597	-0.326	0.207	-0.019	0.005	0.298	0.642

Table 7.1 Values of different β coefficients at 25^{o}C. Values taken from [103, 281] for LiCl, CsCl and $KI0_3$. ; and from [262] for NaCl and KCl.

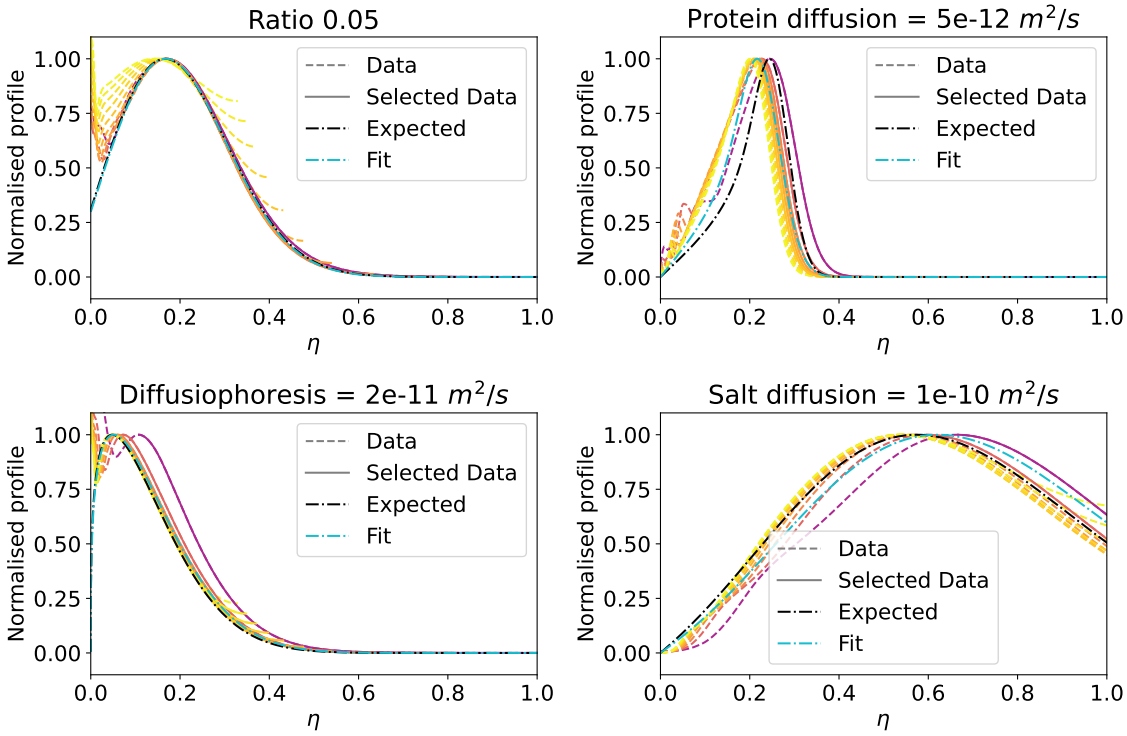

Fig. 7.12 Selected simulations profiles and fits.

7.6 Conclusion

This chapter describes a direct, real-space observation of diffusiophoresis of proteins. This spatial effect is commonly ignored in descriptions of biological systems. In this context, a method to measure protein diffusiophoresis could open the way to novel physiological discoveries. Diffusiophoresis, which is dependent on particle size, is significant for proteins and could have applications for the manipulation of proteins in microfluidic devices. In our diffusiophoretic experiments, proteins could be concentrated by up to a factor of four. Moreover, these proteins could be prevented from entering the channel during several minutes. The protein diffusion and diffusiophoretic coefficients were estimated. The electrophoretic contribution to diffusiophoresis is shown to be much more consequential than the chemiophoretic contribution. Finally, the methods to increase the effect by choosing a salt that is composed of ions with a large difference in relative diffusion coefficient has been discussed. This opens up the door to fundamentally new microfluidic approaches for protein detection and characterisation.

Chapter 8

Prion-like spatial transmission of the Alzheimer's amyloid beta peptide by oligomers

8.1 Summary

This chapter is based on the manuscript: Quentin A. E. Peter, Chris Taylor*, Urszula Łapińska*, Thomas Michaels, Paolo Arosio, Sara Linse & Tuomas P. J. Knowles. "Prion-like spatial transmission of the Alzheimer's amyloid beta peptide by oligomers". Manuscript in preparation (* contributed equally). I contributed to analysing the data. Moreover, I created a data analysis and processing pipeline, as well as simulations. I also developed a theory to explain data features such as the fluorescence gap. Finally, I contributed to writing the paper.*

The formation of amyloid fibrils of amyloid-beta peptides is a hallmark of Alzheimer's disease. Here, it is demonstrated that the aggregation of the peptide amyloid-beta 1-42 spreads in space and time following prion-like behaviour. Such spatial spreading is shown to occur via a diffusion mechanism involving soluble species, catalytically produced by secondary nucleation. These species act as seeds and dramatically accelerate the propagation velocity of the reaction wavefront. This result suggests that such soluble species, in addition to their implication in possible mechanisms of toxicity, play a key role in accelerating the spatial spreading of aggregation, and should therefore be considered primary targets of therapeutic intervention.

8.2 Introduction

The proliferation of amyloid-beta (Aβ) aggregates is thought to be a crucial factor in the development of Alzheimer's disease [107, 181]. It has been widely proposed that Aβ, along with other amyloidogenic proteins such as alpha-synuclein and tau, can propagate in a prion-like manner [125, 201, 271, 257, 131, 105]; resembling the deadly diseases where misfolded prion proteins spread and confer their irregular structure on previously-unaffected proteins, acting as distortive templates or seeds [209, 64, 3, 4]. In an analogous way, both morphology and molecular structure have been shown to self-replicate when Aβ aggregates grow from preformed seeds [201]. This has major implications on the pathology of the disease as toxic aggregates are able to rapidly impose their misshapen state on native Aβ monomers via spreading and seeding. As with prion diseases, this causes a cascade of misfolding and aggregation which ultimately overwhelms the cellular clearance mechanisms and perturbs the function of the central nervous system, eventually resulting in death for the affected individual [131].

The aggregation of amyloidogenic proteins is investigated in the hope of identifying targets for therapeutic intervention. Bulk experiments reveal several pathways for protein aggregation. Homogeneous nucleation forms aggregates from the binding of two monomers [126]. The runaway protein aggregation however is caused by secondary mechanisms [145] such as fibril fragmentation [65, 147] or heterogeneous (secondary) nucleation [92, 224, 60, 62], where existing fibrils catalyse the formation of new aggregates. In the case of amyloid-beta aggregates, the intermediate species - oligomers - are of particular interest [177]. Prior studies have largely focused on the temporal evolution of protein aggregates [186, 104, 165, 176]. However, the spatial propagation of aggregation is relevant to probe intermediate species and to distinguish the underlying microscopic driving force. Studies on the spatial propagation of the amyloidogenic protein insulin propose two scenarios depending on the specific dominant microscopic process [147, 61]. When free diffusion of protein aggregates is restricted, their propagation is driven by the growth of fibrils. In contrast, when the aggregates diffuse freely, they seed new aggregations in a process described by Fisher's wave [93]. This wave is expected to be much faster than fibril growth.

In this chapter, the spatial propagation of amyloid-beta 1-42 (Aβ42) is investigated. This is pertinent in relation to the pathogenesis of Alzheimer's disease. Unlike previous studies, spreading over a macro scale is observed. This ensures that an understanding of the proliferation of Aβ42 aggregates is attained. This understanding is relevant to the length-scales of the extracellular environment in the brain. Such a study into the spatial propagation of Aβ42 provides an understanding of the microscopic processes underlying the proliferation of the disease. Using capillary experiments, the aggregation of Aβ42 is confirmed to be

driven by secondary nucleation. The dominant component to spreading of Aβ42 is the diffusion of aggregate species. This supports the hypothesis that the spreading mechanism of Aβ42 is analogous to prion diseases.

8.3 Theory

Protein aggregation has been extensively studied in bulk [176]. The current theory predicts three mechanisms to create new fibrils. Primary nucleation describes the spontaneous creation of fibrils from monomers. Fractionation describes the formation of new fibrils by the separation of existing fibrils in several parts. Finally, secondary nucleation describes the creation of fibrils from monomers catalysed by existing fibrils. For alpha-synuclein, the dominant process is secondary nucleation. The fibril mass M is in this case described by the following equation: [61]

$$\frac{\partial M}{\partial t} = \kappa(m)M \tag{8.1}$$

Where κ is the aggregation rate that depends on the monomer concentration (m) as $\kappa = k_{agg}m^{3/2}$. The numerical value of k_{agg} depends on the temperature [62] and is, at 37^oC, $k_{agg} = 2.8 \times 10^5\ M^{-3/2}\ s^{-1}$. The diffusion of monomers and fibrils can be taken into account by introducing an effective diffusion coefficient $\bar{D}$ so that Equation (8.1) reads:

$$\frac{\partial M}{\partial t} = \kappa(m)M + \bar{D}\nabla^2 M \tag{8.2}$$

The diffusion coefficient for a fibril is given in [61] and depends on the temperature T, the viscosity η, and the fibril hydrodynamic radius according to Einstein's equation:

$$\bar{D} = \frac{k_B T}{6\pi\eta R_H} \tag{8.3}$$

For a fibril, the hydrodynamic radius depends linearly on the length of the fibril L up to a logarithmic correction factor γ:

$$R_H = \gamma L = \frac{L}{2\log(2L/d)} \tag{8.4}$$

where d is the diameter of the fibril.

8.3.1 Aggregation time

When analysing the data, the half point slope is used to define the aggregation time as the time the aggregation would take if the slope was constant. Equation (8.1) can be used to relate this aggregation time with the initial monomer concentration m_0:

$$T_{agg} = m_0 \Big/ \frac{\partial M}{\partial t}(M = m_0/2) = \frac{m_0}{k_{agg}(m_0/2)^{3/2}(m_0/2)} = \frac{2^{5/2}}{k_{agg}m_0^{3/2}} \tag{8.5}$$

Here, the diffusion effect is ignored. In reality, the monomers are expected to slowly be consumed as they diffuse into the front, and therefore the aggregation time to increase over time. m_0 should thus be seen as the effective monomer concentration the front is diffusing into. More specifically, the monomer and fibril masses might not add up to the initial monomer mass everywhere.

8.3.2 Fisher wave

Assuming a travelling wave, Equation (8.2) can be transformed into a Fisher equation [93]. The fibril mass M is related to the travelling wave function f by $M(x,t) = m_0 f(x - vt)$, where v is the propagation speed. The equation can therefore be rewritten as:

$$\bar{D}f'' + vf' + k_{agg}m_0^{3/2}(1-f)^{3/2}f = 0 \tag{8.6}$$

where the monomer concentration is assumed to be $m = m_0 - M$. This equation is a Fisher equation with an extra factor of $3/2$. The velocity for the Fisher equation is related to the front width w by $v = k_{agg}m_0^{3/2}w + \bar{D}/w$, so that the width is given by:

$$w = \frac{v \pm \sqrt{v^2 - 4\bar{D}k_{agg}m_0^{3/2}}}{2k_{agg}m_0^{3/2}} \tag{8.7}$$

The minimum velocity is therefore defined as $v_{min} = 2\sqrt{\bar{D}k_{agg}m_0^{3/2}}$. Narrower fronts are driven mostly by diffusion, while larger fronts are driven by aggregation. When $v = v_{min}$, both contributions are equal. One of the intriguing features of Fisher waves is that a travelling wave solution can be found for any velocity larger than v_{min}.

8.3.3 Fibril size

The average fibril length $L = \delta\mu$ is given by the average polymerisation number (μ) and the added length of a monomer δ. The average polymerisation number is the ratio of the fibril growth rate ($2k_+m$) and the overall aggregation rate κ:

$$\mu = \frac{2k_+m}{\kappa} \tag{8.8}$$

The expected dependence of the diffusion coefficient is therefore $D \propto \sqrt{m}$ from Equation (8.4). The minimal velocity of the Fisher wave is thus expected to scale as $v_{min} \propto m$.

8.3.4 Gaps size

An aggregation front propagating at a constant velocity v can be modeled as a sink for monomers. The monomer front will therefore extend until the number of monomers diffusing towards the front equals the number of monomers eaten by the front. For an initial concentration m_0, the front consumes $v\,dt\,m_0$ monomers at each time step dt. The diffusion flow depends on the slope, which is approximatively m_0/g, where g is the gap size, and on the monomer diffusion coefficient ($D_m = 1.5 \cdot 10^{-10}\ m^2/s$). Therefore, the gap size can be found as:

$$g = D_m/v \tag{8.9}$$

In the data, a typical velocity is around 1 mm/h. The expected gap size from this mechanism is therefore 0.5 mm, i.e. much smaller than the observed width. An alternative explanation is that the monomers are slowly depleted everywhere, for example due to adhesion on the surface. In that case, one would observe a decrease of the aggregation rate over time. This phenomenon is described in the next section.

8.3.5 Aggregation rate decrease

Figure (8.1) shows the aggregation rate over time. Interestingly, the aggregation rate decreases, which is consistent with the hypothesis of monomer depletion. This effect is more visible for unseeded fronts as the seeds affect the aggregation rate for early times.

8.3.6 Simulations

The spatial propagation of amyloid-beta aggregates is simulated based on the oligomer model described in [177]. Figure (8.2) shows a selection of results. By comparing these results with

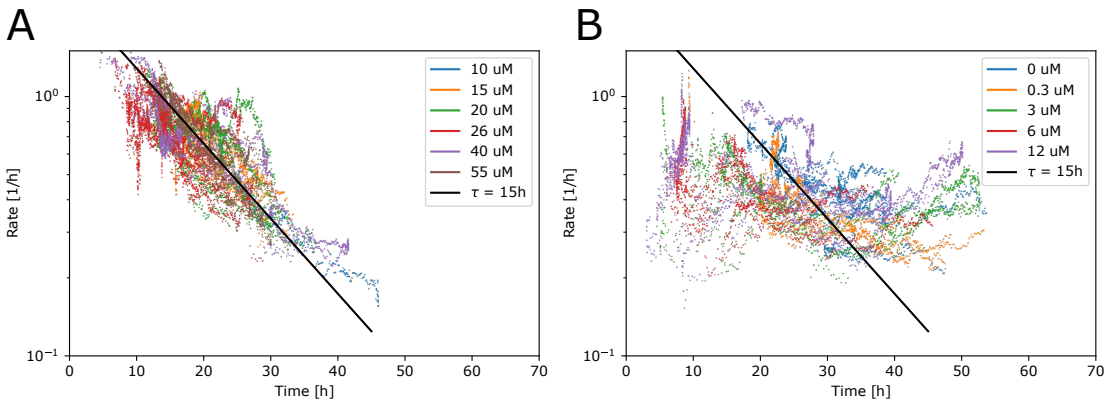

Fig. 8.1 Evolution of the aggregation rate over time. (A) Unseeded fronts. The aggregation rate decreases over time. For later times, the rate is stabilising. (B) Seeded fronts. For early times, the aggregation rate is modified by the presence of seeds.

Figure (8.4), two observations can be made. First, without assuming an adhesion rate, the front diffuses linearly to the other side of the capillary, reproducing neither the gaps nor the decreasing aggregation rate. Second, the aggregation rate in the data is much slower than the expected value from bulk experiments. This could for example be explained by the presence of the walls, as interfaces might promote aggregation.

8.4 Materials and methods

8.4.1 Expression and purification of recombinant Aβ42

Aβ42 recombinant protein is expressed and purified according to a previously described protocol [269]. Briefly, lyophilised Aβ42 is fully dissolved in guanadinium chloride (1 mL) on ice to give a 6 mM solution, pH 8. The Aβ42 solution (1 mL) is injected onto a column (GE Healthcare Superdex^{TM} 75, 10/300 GL Sweden, 25 mL). The buffer is exchanged with a pre-prepared de-gased phosphate buffer (20 mM Na_2HPO_4 / NaH_2PO_4, 0.2 mM EDTA, pH 8) under column flow 0.7 mL.min^{-1}, pressure 0.7 MPa. The obtained stock solution of Aβ42 is temporarily stored on ice during the preparation of capillaries.

8.4.2 Preparation of capillaries containing unseeded Aβ42

Monomeric Aβ42 solutions at 5 different concentrations (10 μM, 15 μM, 20 μM, 26 μM, and 40 μM) are prepared by diluting into the pre-prepared phosphate buffer with ThT (20 μM) in a low-bind Eppendorf. This solution is gently mixed by slow aspiration of a pipette. Each square borosilicate capillary (0.2 mm ID, $\approx$ 50 mm length, CM Scientific)

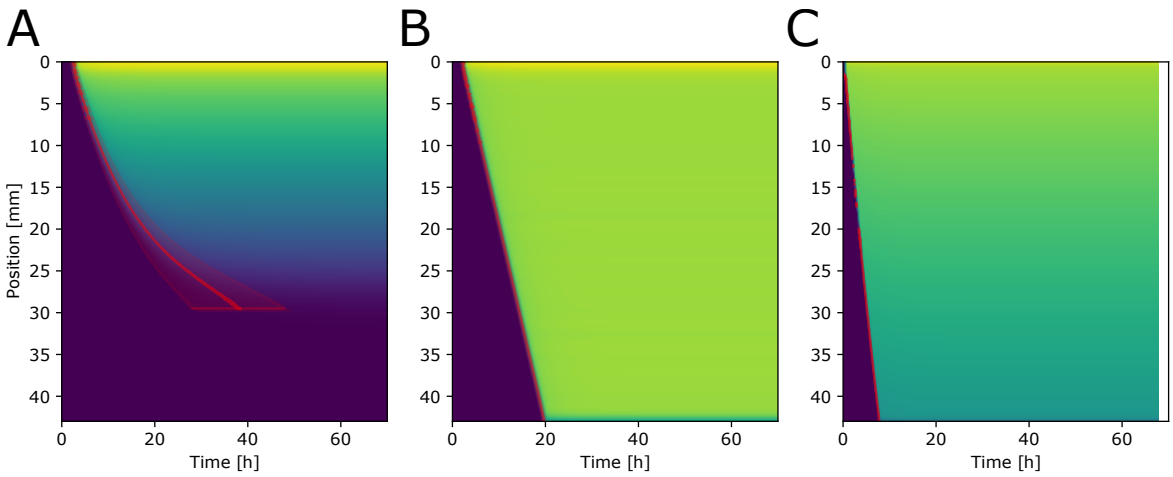

Fig. 8.2 Aggregation propagation simulations of amyloid-beta aggregates based on the oligomer model described in [177]. (A) 5 μM with an adhesion rate of 1 / 15h. (B) 5 μM without adhesion. (C) 20 μM with adhesion rate of 1 / 15h. The red line and region correspond to the detected aggregation time as returned by the data analysis pipeline. These are included here for comparison with the results.

is filled by capillary action and sealed with wax plugs to prevent evaporation; first at the raised end and then at the lower end, making sure to minimise the air trapped inside. Each experiment consist of multiple repeats for each concentration of protein. The capillaries are aligned on a glass slide and held in place with epoxy glue at the ends of the capillaries. The time frame between the removal of the samples from ice and the start of the measurement typically amounts to 30 minutes. (Capillaries of the lowest concentrations are always prepared first as these are expected to aggregate more slowly and therefore are least affected by the delay due to preparation time.)

8.4.3 Preparation of capillaries containing seeded Aβ42

A small aliquot of monomeric Aβ42 solution is diluted to a final concentration of 20 μM in pre-prepared phosphate buffer with ThT (20 μM) and incubated at 37 ^{o}C in a microplate (Corning 96 Well Half Area) in a plate reader (FLUOstar OPTIMA, BMG) until the aggregation curve reaches a plateau. Dilutions of these fully-converted monomer seeds are prepared and stored on ice. The time to half-completion (half-time) of the aggregation is identified and seeds, termed half-converted monomer seeds, are produced by repeating the aggregation in the microplate until this time-point, and by storing the appropriate dilutions on ice. For both types of seeded experiments, the capillaries are prepared by aspirating monomeric Aβ42 via capillary action to fill approximately 75% of the capillary. The remaining 25% is then filled with seeds in the same manner. The capillary is sealed with wax, at the end with seeds,

and then at the other end. The capillary preparation is always started from the lowest seed concentration. As for unseeded experiments, the time frame between the removing of the samples from ice to the start of the measurement is typically 30 minutes.

8.4.4 Epifluorescence instrument used in conjunction with an automated stage

An epifluorescence instrument is used for all experiments with an incorporated automated stage (MS-2000 FT, ASI). In brief, a 445 nm laser (MLD, Cobolt) beam is attenuated with neutral density filters, expanded and collimated. This beam is passed through an excitation filter (FF01-488/20-25, Laser2000) to remove any stray wavelength of light, then directed to the back aperture of the microscope (RAMM, ASI), aligned parallel to the optical axis. A lens is inserted to collimate the beam, reflected by the dichroic mirror (FF484-FDi01-25x36, Laser2000), on the sample through the objective (4X, 0.13 NA, Nikon). Emission is collected through the same objective and passed through the same dichroic mirror and a long-pass filter (BLP01-473R-25, Laser2000), before being directed to a camera (CoolSnap MYO, Photometrics).

8.4.5 Programming automated stage for capillary experiments

The automated stage is programmed (Micromanager) to scan the length of the capillaries which are aligned vertically on a glass slide in a meticulous manner such that they are perfectly parallel to the stage movement over the 5 cm distance scanned. This allowes 5 capillaries aligned adjacent to one another with minimal spacing to fit into one field of view (horizontally). Once the first set of 5 capillaries has been scanned, the stage is programmed to repeat equivalent scans starting from the top of the next set of 5 capillaries. This process is replicated until all capillaries for the experiment has been scanned (29 positions per capillary length). Using this method, a set of brightfield images are taken for each position to confirm that every single capillary remains in view. The brightfield LED is then blocked and fluorescence images taken using a 445 nm laser with a shutter. The whole scanning process is set to repeat every 5 minutes in order to track the position of the ThT dye-active species (Aβ42 aggregates) arising.

8.4.6 Data analysis

The data is analysed as described in Figure (8.3): In each image, the location of 5 capillaries is detected. The images are combined together by knowing the pixel size and the automatic

stage step size. The image of each capillary is then separated and an average is taken along the width. Each time point is then used as a column in a 2D map representing the space-time evolution of the propagation front. For each pixel line, the position and the slope at the half aggregation point are extracted. The half aggregation point is used because $\nabla^2 M \approx 0$ in Equation (8.2). The slope can be converted in an aggregation rate as described in Equation (8.5), and the velocity is extracted by comparing the half time between neighbouring points.

8.5 Results

To monitor the spatial propagation of aggregation of Aβ42 proteins, an epifluorescence microscopy setup using laser excitation at 445 nm is used, as shown in Figure (8.3). The benzothiazole salt thioflavin-T (ThT) binds to the aggregates and is used as a latent dye. Monomeric proteins at 6 different concentrations (10 μM, 15 μM, 20 μM, 26 μM, 40 μM, and 55 μM) are loaded into square borosilicate capillaries which are wax sealed, as shown in Figure (8.3A). Similarly, 5 concentrations of half-converted seeds (0 μM, 0.3 μM, 3 μM, 6 μM, and 12 μM) are added to a 20 μM Aβ42 capillary. The fluorescent intensity of up to 20 capillaries are recorded in parallel by scanning, using an automated stage at fixed time intervals, as shown in Figure (8.3C). Image processing is used to extract a 2D map of the florescence position over time. The front velocity and aggregation rate can be extracted from this 2D map, as shown in Figure (8.3D-F).

In total, more that 80 capillaries have been recorded. A selection of runs is shown in Figure (8.4). Two important parameters are extracted from the fronts: the aggregation rate and the velocity at each position. Several features can be observed in these, as well as in other capillaries. First, the aggregation usually starts from the ends of the capillaries, showing the importance of interfaces for the nucleation of aggregation. The first side to aggregate is usually the lower side in Figure (8.3A), top side in Figures (8.3F) and (8.4). A second observation is that the velocity changes dramatically between repeats, as shown in Figure (8.4A-B) for 20 μM Aβ42, and as shown in Figure (8.4C) with seeds. This is an expected feature of Fisher waves, as the velocity depends on the initial conditions [61]. A minimal velocity is however described by the theory. The next observation is that the aggregation time is larger than what would be expected from bulk experiments. Applying the rates from aggregation experiments would lead to an effective monomer concentration of approximatively 1 μM. This discrepancy can be explained by a larger surface-to-volume ratio in capillaries compared to bulk experiments. Finally, the aggregation run does not always fill the entire capillary, but instead forms a gap, as shown in Figure (8.4B-E). This gap can be explained by monomer depletion. One could expect that the monomers diffuse into the front,

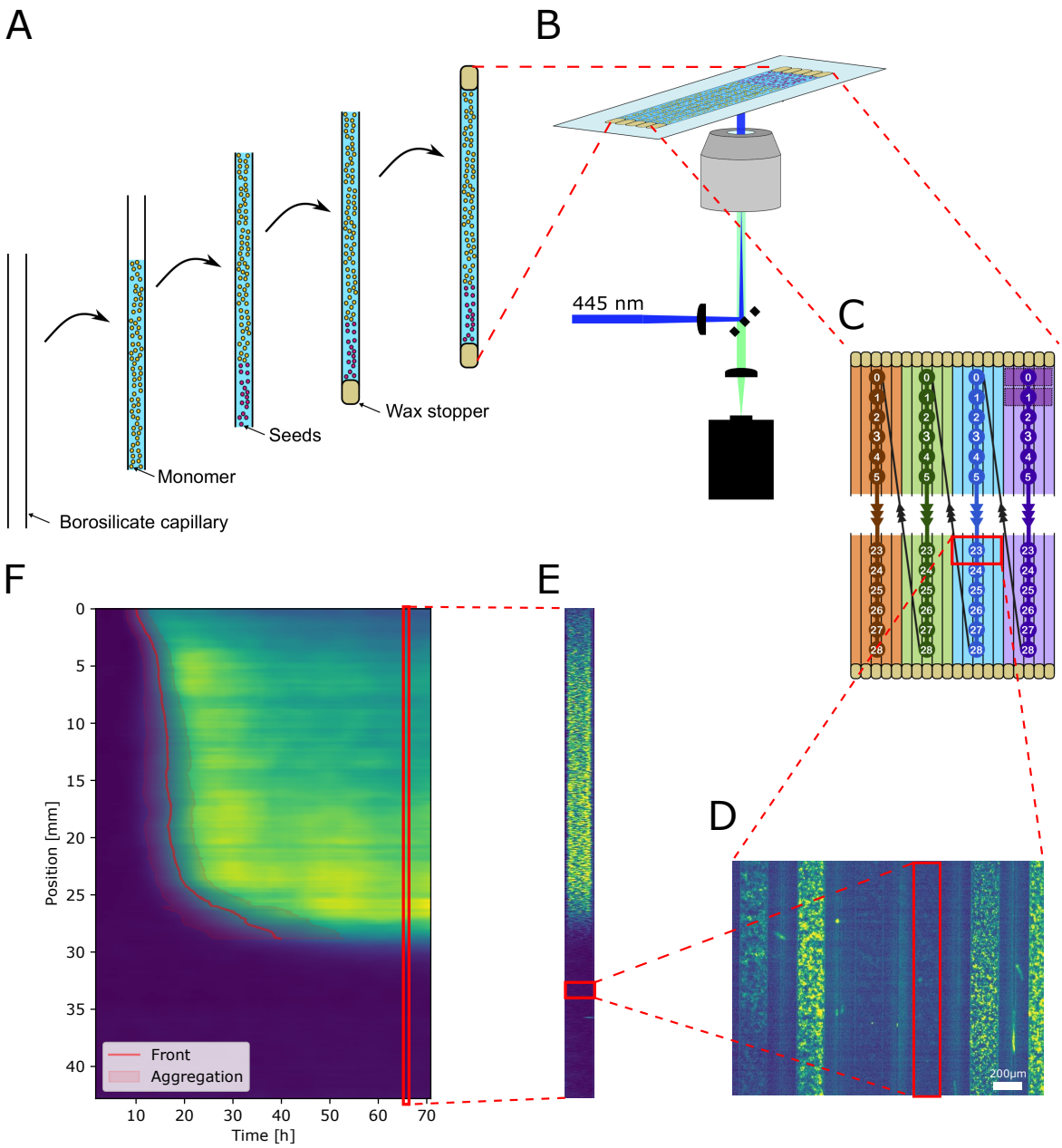

Fig. 8.3 Schematic of the experiments. (A) 5 cm long borosilicate capillaries are filled with a monomeric amyloid beta solution by capillary forces. A seeds solution is optionally added to one side before sealing both ends with wax. (B) The capillaries are mounted on a fluorescent microscope with excitation at 445 nm. (C) A motorised stage scans the capillaries, capturing a series of images at every position over several hours. (D) On each image, a small part of the capillaries is visible. The location of each capillary is detected using image analysis techniques. (E) An overall image of the capillary is reconstructed at each time. (F) The images are then merged together to form a 2D image of the fluorescence position over time. This image is used to detect the front position, the aggregation rate, and the velocity. The detected front position and the aggregation time are shown in red.

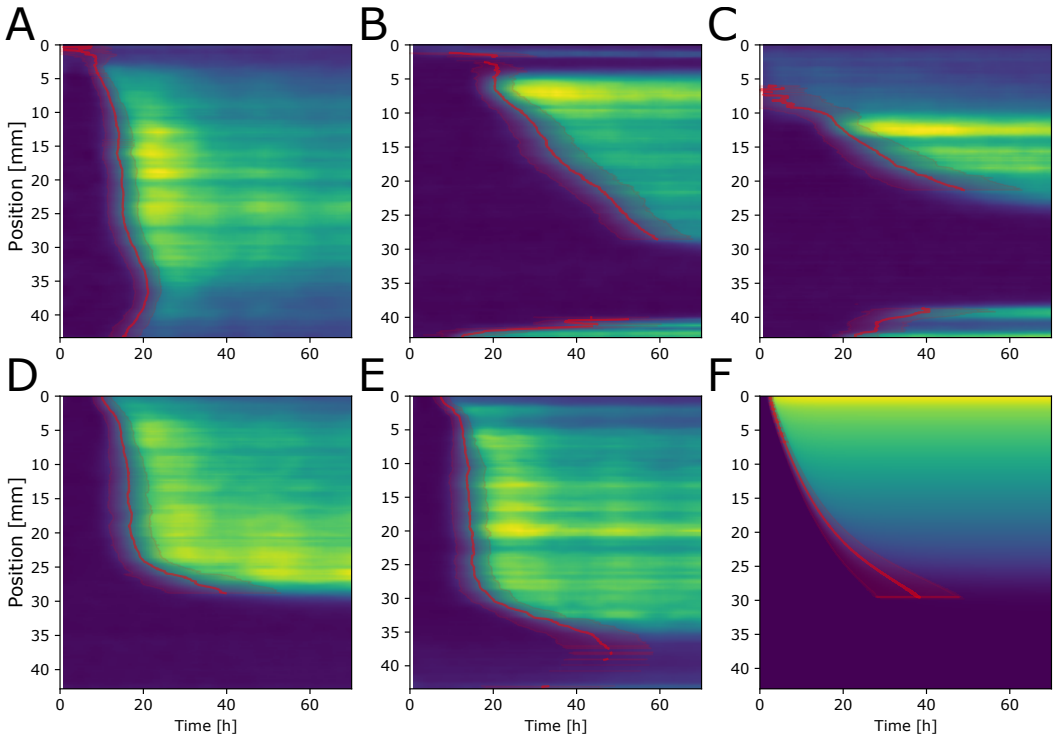

Fig. 8.4 Selected results of spatial aggregation of propagation. (A) and (B) 20 μM amyloid beta monomers aggregating. Because of the Fisher wave speed selection, the velocities can be very different. Interestingly, a gap appears at low velocities where the aggregation stops. In (B), a buffer solution is added to the top of the capillary, explaining the dark gap. (C) 20 μM amyloid beta monomers with the first 5 mm filled with 12 μM half-converted seeds. The seeds cause the aggregation to start immediately, but do not change the aggregation speed noticeably. (D) 26 μM and (E) 40 μM aggregation fronts. In these occurrences, the front started from one side, and a gap is present. (F) Simulation of a propagating front assuming a constant adhesion rate of the monomers on the walls. The gap behaviour is reproduced. The red line and region correspond to the detected aggregation time as returned by the data analysis pipeline.

and are therefore trapped in it. The gap size from this phenomenon depends on the monomer diffusion coefficient and on the front velocity. The predicted width is much smaller than the observed gap size. A more likely explanation is that monomers are adhering to the surface over time, decreasing the effective monomer concentration. This would also explain why the aggregation rate is decreasing over time, when one would expect it to remain constant. Figure (8.4F) shows the result of a Monte-Carlo simulation. The gap and the decreasing aggregation rate are reproduced by assuming a fixed adhesion rate.

8.5.1 Half-converted monomer seeds

To ensure that the type of seed is not a factor, it was decided to investigate the effect of seeds taken from the half-time of the aggregation timecourse in addition to the fully-converted monomer seeds. The presence of a larger proportion of small aggregate species would be expected at the half-time. This sample of half-converted monomer seeds was postulated to lead to an increase in the rate of propagation compared to its fully-converted monomer seed counterpart. This is due to the faster diffusion of small aggregate species - present in a higher proportion - propagating the aggregation more rapidly through the capillary. Capillaries containing 20 μM Aβ42 monomer seeded at one end with half-converted monomer seeds at 4 different concentrations (0.3 μM, 3 μM, 6 μM, and 12 μM) and a 20 μM Aβ42 unseeded monomer control are thus prepared. The half-converted monomer seeds do not affect the velocity of the reaction wavefront in the spatial propagation of Aβ42. The removal of the lag time of aggregation is observed when half-converted monomer seeds are present at concentrations of 3 μM and above. The seed concentration of 0.3 μM reduces the lag time only slightly from that of the unseeded conditions, implying that the critical concentration of aggregates required for secondary nucleation to dominate in the aggregation of Aβ42 is higher than this value (0.3 μM - 3 μM).

8.6 Discussion

Two phenomena are known to cause spatial propagation of aggregation [61]. Either the diffusion is restricted and the propagation is driven by the growth of the fibrils, or the intermediate species diffuse freely and nucleate new aggregations further down the capillary. If the spatial propagation is driven by the fibril growth, the velocity is given by $v = 2k_+ m\delta/\pi$, where k_+ is the growth rate measured by AFM measurements, and m is the monomer concentration. The local monomer concentration is not directly measured, but can be estimated from the aggregation rate κ: The bulk measurements give a relation of $\kappa = \sqrt{2} \cdot k_{agg} \cdot m^{3/2}$, where $k_{agg} = 2.8 \cdot 10^5\ M^{-3/2}\ s^{-1}$ at 35 Celsius [62, 177]. If the spatial propagation is driven by diffusion instead, the fibril mass (M) evolution is described by [61]:

$$\frac{\partial M(t,x)}{\partial t} = \kappa M(t,x) + \bar{D}\nabla^2 M(t,x) \tag{8.10}$$

where $\bar{D}$ is the effective diffusion coefficient. To extract the aggregation rate κ from the fluorescence curves, the slope at the half aggregation time is used, as $\nabla^2 M(t,x) \approx 0$. This equation describes a Fisher wave, whose velocity depends on the initial conditions. The minimum velocity is given by $v_{min} = 2\sqrt{\kappa \bar{D}}$.

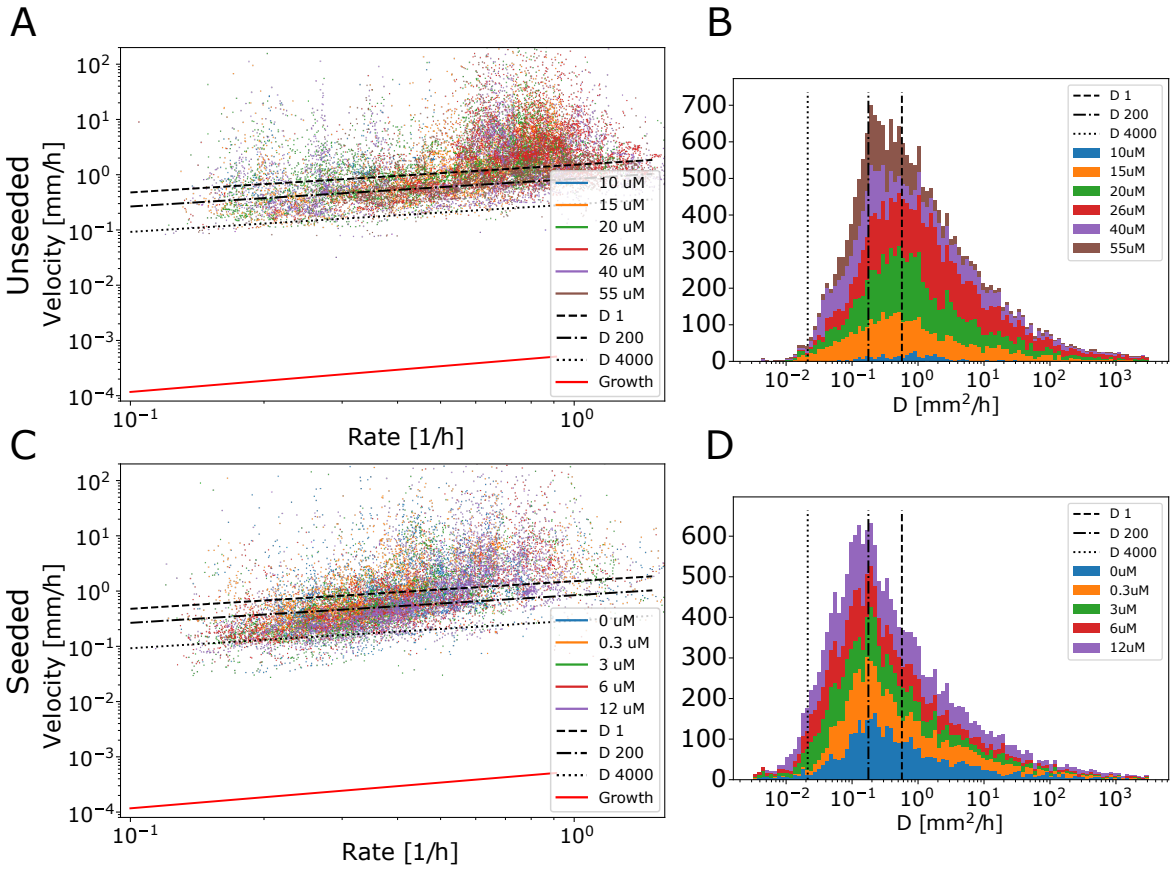

Fig. 8.5 Velocity vs rate of the aggregation front for (A) unseeded and (C) seeded capillaries. Assuming the minimum velocity of the Fisher wave, (B) and (D) respectively, represent the corresponding effective front diffusion coefficient. The red line represents growth limited velocity, which is orders of magnitude below what is observed in our experiments.

In order to identify which component is dominating the reaction-diffusion process of the spatial propagation of Aβ42, the velocity of the front is plotted against the aggregation rate in Figure (8.5A, C). It can readily be seen that the velocity described by growth limited propagation is orders of magnitude lower than the recorded velocity. The spatial propagation of aggregation is therefore diffusion limited. The effective diffusion coefficient can then be estimated. The diffusion coefficient corresponding to the aggregation rate and the velocity is shown in Figure (8.5B, D) for seeded and unseeded experiments, respectively. These are compared to the diffusion coefficient of a monomer, and of a 200 and 4000 monomer long fibril. As expected, a lot of the diffusion coefficients are smaller than the monomer diffusion coefficient, meaning that they do not correspond to a minimum velocity. The histogram however starts to decrease around a maximum occurrence corresponding to a fibril length of 200 units, and stops at around 4000 units.

8.7 Conclusion

The presence of Aβ aggregates in the brain is a hallmark of Alzheimer's disease. It is important to understand how these toxic aggregates form and spread both temporally and spatially. The spatial propagation of Aβ aggregates has largely been overlooked in the past. Here, the spatial spreading of aggregates is monitored on a macro length-scale, in addition to the temporal evolution of species. Diffusion is found to be the dominant microscopic driving force for the spreading of aggregate species using both experimental and theoretical methods. As detailed previously for Aβ42 and certain other amyloidogenic proteins [145, 147, 60], filaments catalyse the production of new aggregates on their surfaces. The diffusion of aggregates is proposed to proliferate these species to further propagate the aggregation of Aβ42. Our work underlines the impact of this mechanism for the proliferation of species. Secondary nucleation provides many small aggregates which can diffuse quickly, thus further driving the spatial propagation by diffusion. In this way, low molecular weight species may be crucial for controlling spreading behaviour and prion-like behaviour in the aggregation of Aβ42 and other amyloidogenic proteins. The approach developed here could be useful in directing drug design efforts. The technique offers an effective way to examine the role of various potential drug molecules on both the temporal and, crucially, the spatial development of Aβ42 aggregation. By identifying molecules which reduce the prion-like spreading of Aβ42, this could provide a significant addition to the tools available to combat the devastating effects of Alzheimer's disease.

Chapter 9

Conclusion

In this thesis, I presented several advances in biophysical methods for protein detection and characterisation. The first three chapters focused on label-free protein detection. This is critical for accurate characterisation of proteins, as labels or affinity probes change their biophysical properties. The following label-free methods were presented: First, a novel deep-UV protein autofluorescence microscope that can make use of the autofluorescence of aromatic amino acid Tryptophan and Tyrosine is discussed. Second, a method to increase the contrast of interferometric scattering microscopy using oblique illumination is examined. Third, the time correlation is used on the iSCAT signal to measure the sample diffusion coefficient. All these approaches enable novel assays to more precisely quantify unmodified proteins.

The fourth chapter focused on improving microfluidic methods by adding nanofluidic channels to microfluidic designs using two-photon techniques. Most nanofluidic devices require few nanofluidic elements, so that this advance eases the development and the integration of novel nanofluidic techniques in protein assays.

Finally, three biophysical methods are presented. The fifth chapter addressed diffusional sizing, which enables the sizing of proteins by observing the temporal evolution of a concentration gradient over time. Diffusional sizing is rapidly developing as an easy way of getting information on protein-protein interaction, and this chapter contributes to increasing the accuracy and ease of analysis of these assays. The sixth chapter presented diffusiophoresis, which measures the forces applied on proteins by a solute gradient. These gradients can be integrated to microfluidic devices in order to locally control the concentration of proteins or to determine their diffusiophoretic coefficient. The seventh chapter demonstrated the spatial propagation of aggregation of Alzheimer's Aβ42 peptide. This propagation is observed on large scales in capillaries by using a latent dye that revels the presence of aggregates. This is crucial to understand the propagation of amyloid diseases such as Alzheimer's in the brain.

In my opinion, the most impactful result of this thesis is the work I have done on improving the diffusional sizing workflow. This includes my work on the deep-UV protein autofluorescence microscope in Chapter 2 but is mostly covered in Chapter 6 on fast numerical integration of diffusional sizing basis functions. The python script referred to in this chapter was developed throughout my PhD by collaborating with multiple researchers that work with diffusional sizing. The expertise I developed helped to better understand the need of the data processing pipeline users, and allowed to me give advice to my collaborators on how to best acquire the sizing data. The python data processing pipeline first extracts a diffusional sizing profile and then uses this profile to give a size and an error. Here, the complexity lies in the wide array of conditions under which the data is acquired, and how to remove the background. The data is acquired with many methods, including epifluorescence microscopy, single molecule detection scanning, and even circular dichroism spectroscopy.[284, 40] Diffusional sizing can also be combined in-line with other techniques such as Free-flow electrophoresis or liquid chromatography.[226, 234] Improving this data processing analysis pipeline helped enable many novel research projects, which is why I think this aspect of my work was particularly impactful.

In conclusion, the methods presented in this thesis add new tools to the arsenal of biological research, enabling a further understanding of complex biophysical systems.

9.1 Outlook

The future most valuable direction for this work is likely the iSCORR technique presented in Chapter 4. While it is now a preliminary proof-of-concept, this technology could enable exiting new research in protein science. If the technique can be tuned to detect low concentration or even a single protein diffusing in solution, it could have a major impact. One could for example imagine a setup where proteins are separated and then detected by iSCORR in a totally label-free manner, and at extremely low concentrations. This separation would provide some information on the protein. The iSCORR would then detect and measure the size. This technique is particularly well suited for microfluidics and nanofluidics, as it could analyse the content of any solution flowing in a channel or trapped in a cavity.

The most important factor when doing biological research is having the right tools. A researcher could have the best ideas but still be limited by available techniques. At the same time, having the right assay may reveal unexpected features of biological systems and advance research significantly. My goal during my PhD was to contribute to these advances by developing novel approaches for high-impact research. Furthermore, I believe that there is a high value in integrating these advances in easy-to-use commercial systems. To that

end, I contributed to several patents and spent three months helping to develop a commercial product in a private company - Fluidic Analytics Ltd. - as part of my PhD program. I envision the projects presented here as basis for novel research and diagnosis applications to probe biological samples. Some projects have sparked interest and collaborations in my research group and beyond, as evidenced by the many projects I had the chance to collaborate on. The future of this research lies in commercial applications for biological research and medical diagnostics. I hope that these results will contribute to the betterment of human health.

References

[1] Abécassis, B., Cottin-Bizonne, C., Ybert, C., Ajdari, A. and Bocquet, L. [2008], 'Boosting migration of large particles by solute contrasts', *Nature Materials* **7**(10), 785–789.

[2] Abgrall, P. and Gue, A. [2007], 'Lab-on-chip technologies: making a microfluidic network and coupling it into a complete microsystem—a review', *Journal of Micromechanics and Microengineering* **17**(5), R15.

[3] Aguzzi, A. and Calella, A. M. [2009], 'Prions: Protein Aggregation and Infectious Diseases', *Physiological Reviews* **89**(4), 1105–1152.

[4] Aguzzi, A. and Falsig, J. [2012], 'Prion propagation, toxicity and degradation', *Nature Neuroscience* **15**(7), 936–939.

[5] Ahn, S. and Fessler, J. A. [2003], 'Standard errors of mean, variance, and standard deviation estimators', *EECS Department, The University of Michigan* pp. 1–2.

[6] Ajdari, A. and Bocquet, L. [2006], 'Giant amplification of interfacially driven transport by hydrodynamic slip: Diffusio-osmosis and beyond', *Physical Review Letters* **96**(18), 186102.

[7] Akcay, C., Parrein, P. and Rolland, J. P. [2002], 'Estimation of longitudinal resolution in optical coherence imaging', *Applied Optics* **41**(25), 5256–5262.

[8] Alberts, B. [1998], 'The cell as a collection of protein machines: preparing the next generation of molecular biologists', *Cell* **92**(3), 291–294.

[9] Amidror, I. [1998], 'The fourier-spectrum of circular sine and cosine gratings with arbitrary radial phases', *Optics Communications* **149**(1-3), 127–134.

[10] Anderson, J. L. [1989], 'Colloid transport by interfacial forces', *Annual Review of Fluid Mechanics* **21**(1), 61–99.

[11] Anderson, J. L. and Prieve, D. C. [1984], 'Diffusiophoresis: migration of colloidal particles in gradients of solute concentration', *Separation and Purification Methods* **13**(1), 67–103.

[12] Anderson, J. L. and Prieve, D. C. [1991], 'Diffusiophoresis caused by gradients of strongly adsorbing solutes', *Langmuir* **7**(2), 403–406.

[13] Andreasen, M., Meisl, G., Taylor, J. D., Michaels, T. C., Levin, A., Otzen, D. E., Chapman, M. R., Dobson, C. M., Matthews, S. J. and Knowles, T. P. [2019], 'Physical determinants of amyloid assembly in biofilm formation', *Mbio* **10**(1).

[14] Anfinsen, C. B. [1973], 'Principles that govern the folding of protein chains', *Science* **181**(4096), 223–230.

[15] Annunziata, O., Buzatu, D. and Albright, J. G. [2012], 'Protein diffusiophoresis and salt osmotic diffusion in aqueous solutions', *The Journal of Physical Chemistry B* **116**(42), 12694–12705.

[16] Aquilina, J. A., Benesch, J. L. P., Bateman, O. A., Slingsby, C. and Robinson, C. V. [2003], 'Polydispersity of a mammalian chaperone: mass spectrometry reveals the population of oligomers in alphaB-crystallin.', *Proceedings of the National Academy of Sciences of the United States of America* **100**(19), 10611–6.

[17] Arosio, P., Hu, K., Aprile, F. A., Müller, T. and Knowles, T. P. [2016], 'Microfluidic diffusion viscometer for rapid analysis of complex solutions', *Analytical Chemistry* **88**(7), 3488–3493.

[18] Arosio, P., Müller, T., Rajah, L., Yates, E. V., Aprile, F. A., Zhang, Y., Cohen, S. I., White, D. A., Herling, T. W., De Genst, E. J., Linse, S., Vendruscolo, M., Dobson, C. M. and Knowles, T. P. J. [2016], 'Microfluidic diffusion analysis of the sizes and interactions of proteins under native solution conditions', *ACS Nano* **10**(1), 333–341.

[19] Arroyo, J. O., Cole, D. and Kukura, P. [2016], 'Interferometric scattering microscopy and its combination with single-molecule fluorescence imaging', *Nature Protocols* **11**(4), 617.

[20] Arter, W. E., Yusim, Y., Peter, Q., Taylor, C. G., Klenerman, D., Keyser, U. F. and Knowles, T. P. [2020], 'Digital sensing and molecular computation by an enzyme-free dna circuit', *ACS Nano* **14**(5), 5763–5771.

[21] Ault, J. T., Shin, S. and Stone, H. A. [2018], 'Diffusiophoresis in narrow channel flows', *Journal of Fluid Mechanics* **854**, 420–448.

[22] Ault, J. T., Warren, P. B., Shin, S. and Stone, H. A. [2017], 'Diffusiophoresis in one-dimensional solute gradients', *Soft Matter* **13**(47), 9015–9023.

[23] Auroux, P.-A., Iossifidis, D., Reyes, D. R. and Manz, A. [2002], 'Micro total analysis systems. 2. analytical standard operations and applications', *Analytical Chemistry* **74**(12), 2637–2652.

[24] Austin, R., Wunsch, B., Smith, J., Gifford, S., Wang, C., Brink, M., Bruce, R., Stolovitzky, G. and Astier, Y. [2017], 'Nanoscale lateral displacement arrays for the separation of exosomes and colloids down to 20 nm', *Bulletin of the American Physical Society* **62**.

[25] Axelsson, I. [1978], 'Characterization of proteins and other macromolecules by agarose gel chromatography', *Journal of Chromatography A* **152**(1), 21 – 32.

[26] Baddour, N. [2011], Two-dimensional fourier transforms in polar coordinates, *in* 'Advances in Imaging and Electron Physics', Vol. 165, Elsevier, pp. 1–45.

[27] Baldwin, A. J., Lioe, H., Robinson, C. V., Kay, L. E. and Benesch, J. L. P. [2011], 'αB-crystallin polydispersity is a consequence of unbiased quaternary dynamics.', *Journal of Molecular Biology* **413**(2), 297–309.

[28] Bander, N. H. [2006], 'Technology insight: monoclonal antibody imaging of prostate cancer', *Nature Clinical Practice Urology* **3**(4), 216–225.

[29] Barth, A. [2007], 'Infrared spectroscopy of proteins', *Biochimica et Biophysica Acta (BBA)-Bioenergetics* **1767**(9), 1073–1101.

[30] Becker, H. [2009], 'It's the economy...', *Lab on a Chip* **9**, 2759–2762.

[31] Ben-Shem, A., de Loubresse, N. G., Melnikov, S., Jenner, L., Yusupova, G. and Yusupov, M. [2011], 'The structure of the eukaryotic ribosome at 3.0 å resolution', *Science* **334**(6062), 1524–1529.

[32] Benesch, J. L., Ruotolo, B. T., Simmons, D. A. and Robinson, C. V. [2007], 'Protein complexes in the gas phase: technology for structural genomics and proteomics', *Chemical Reviews* **107**(8), 3544–3567.

[33] Berggård, T., Linse, S. and James, P. [2007], 'Methods for the detection and analysis of protein–protein interactions', *Proteomics* **7**(16), 2833–2842.

[34] Berne, B. J. and Pecora, R. [2000], *Dynamic light scattering: with applications to chemistry, biology, and physics*, Courier Corporation.

[35] Berthier, E., Warrick, J., Yu, H. and Beebe, D. J. [2008], 'Managing evaporation for more robust microscale assays part 1. volume loss in high throughput assays', *Lab on a Chip* **8**, 852–859.

[36] Biancalana, M. and Koide, S. [2010], 'Molecular mechanism of thioflavin-t binding to amyloid fibrils', *Biochimica et Biophysica Acta (BBA)-Proteins and Proteomics* **1804**(7), 1405–1412.

[37] Bilsel, O., Kayatekin, C., Wallace, L. A. and Matthews, C. R. [2005], 'A microchannel solution mixer for studying microsecond protein folding reactions', *Review of Scientific Instruments* **76**(1), 014302–014302.

[38] Bjellqvist, B., Ek, K., Righetti, P. G., Gianazza, E., Görg, A., Westermeier, R. and Postel, W. [1982], 'Isoelectric focusing in immobilized ph gradients: principle, methodology and some applications', *Journal of Biochemical and Biophysical Methods* **6**(4), 317–339.

[39] Bocquet, L. and Charlaix, E. [2010], 'Nanofluidics, from bulk to interfaces', *Chemical Society Reviews* **39**(3), 1073–1095.

[40] Bortolini, C., Kartanas, T., Copic, D., Morales, I. C., Zhang, Y., Challa, P. K., Peter, Q., Jávorfi, T., Hussain, R., Dong, M. et al. [2019], 'Resolving protein mixtures using microfluidic diffusional sizing combined with synchrotron radiation circular dichroism', *Lab on a Chip* **19**(1), 50–58.

[41] Boukany, P. E., Morss, A., Liao, W.-c., Henslee, B., Jung, H., Zhang, X., Yu, B., Wang, X., Wu, Y., Li, L. et al. [2011], 'Nanochannel electroporation delivers precise amounts of biomolecules into living cells', *Nature Nanotechnology* **6**(11), 747.

[42] Bruno, G., Di Trani, N., Hood, R. L., Zabre, E., Filgueira, C. S., Canavese, G., Jain, P., Smith, Z., Demarchi, D., Hosali, S. et al. [2018], 'Unexpected behaviors in molecular transport through size-controlled nanochannels down to the ultra-nanoscale', *Nature Communications* **9**(1), 1–10.

[43] Bruus, H. [2015], Chapter 1 governing equations in microfluidics, *in* 'Microscale Acoustofluidics', The Royal Society of Chemistry, pp. 1–28.

[44] Buchholz, B. A., Doherty, E. A. S., Albarghouthi, M. N., Bogdan, F. M., Zahn, J. M. and Barron, A. E. [2001], 'Microchannel dna sequencing matrices with a thermally controlled "viscosity switch"', *Analytical Chemistry* **73**(2), 157–164.

[45] Buffle, J., Zhang, Z. and Startchev, K. [2007], 'Metal flux and dynamic speciation at (bio) interfaces. part i: critical evaluation and compilation of physicochemical parameters for complexes with simple ligands and fulvic/humic substances', *Environmental Science & Technology* **41**(22), 7609–7620.

[46] Bukau, B. and Horwich, A. L. [1998], 'The hsp70 and hsp60 chaperone machines', *Cell* **92**(3), 351–366.

[47] Burnette, W. N. [1981], '"western blotting": Electrophoretic transfer of proteins from sodium dodecyl sulfate-polyacrylamide gels to unmodified nitrocellulose and radiographic detection with antibody and radioiodinated protein a', *Analytical Biochemistry* **112**(2), 195–203.

[48] Calero, M. and Gasset, M. [2005], Fourier transform infrared and circular dichroism spectroscopies for amyloid studies, *in* 'Amyloid Proteins', Springer, pp. 129–151.

[49] Callaghan, K. L., Peter, Q., Kumita, J. R., Knowles, T. P. and Dobson, C. M. [2020], 'Quantifying the thermodynamic stability of amyloid fibrils', *Biophysical Journal* **118**(3), 492a.

[50] Callaway, E. [2020], ''it will change everything': Deepmind's ai makes gigantic leap in solving protein structures.', *Nature* .

[51] Chakraborty, M., Kuriata, A. M., Henderson, J. N., Salvucci, M. E., Wachter, R. M. and Levitus, M. [2012], 'Protein oligomerization monitored by fluorescence fluctuation spectroscopy: self-assembly of rubisco activase', *Biophysical Journal* **103**(5), 949–958.

[52] Challa, P. K., Kartanas, T., Charmet, J. and Knowles, T. P. J. [2017], 'Microfluidic devices fabricated using fast wafer-scale led-lithography patterning', *Biomicrofluidics* **11**(1), 014113.

[53] Challa, P. K., Peter, Q., Wright, M. A., Zhang, Y., Saar, K. L., Carozza, J. A., Benesch, J. L. and Knowles, T. P. [2018*a*], 'Real-time intrinsic fluorescence visualization and sizing of proteins and protein complexes in microfluidic devices', *Analytical Chemistry* **90**(6), 3849–3855.

[54] Challa, P. K., Peter, Q., Wright, M. A., Zhang, Y., Saar, K. L., Carozza, J. A., Benesch, J. L. and Knowles, T. P. [2018*b*], 'Research data supporting" real-time intrinsic fluorescence visualisation and sizing of proteins and protein complexes in microfluidic devices"', *https://doi.org/10.17863/CAM.18873* .

[55] Challa, P. K., Peter, Q., Wright, M. A., Zhang, Y., Saar, K. L., Carozza, J. A., Benesch, J. L. and Knowles, T. P. [2018*c*], 'Scripts supporting" real-time intrinsic fluorescence visualisation and sizing of proteins and protein complexes in microfluidic devices"', *https://doi.org/10.5281/zenodo.1155526* .

[56] Charmet, J., Arosio, P. and Knowles, T. P. [2017], 'Microfluidics for protein biophysics', *Journal of Molecular Biology* .

[57] Chinnathambi, S., Karthikeyan, S., Velmurugan, D., Hanagata, N., Aruna, P. and Ganesan, S. [2015], 'Effect of moderate uvc irradiation on bovine serum albumin and complex with antimetabolite 5-fluorouracil: Fluorescence spectroscopic and molecular modelling studies', **2015**, 1–12.

[58] Chiti, F. and Dobson, C. M. [2006], 'Protein misfolding, functional amyloid, and human disease', *Annual Review of Biochemistry* **75**, 333–366.

[59] Chiti, F., Taddei, N., van Nuland, N. A., Magherini, F., Stefani, M., Ramponi, G. and Dobson, C. M. [1998], 'Structural characterization of the transition state for folding of muscle acylphosphatase.', *Journal of Molecular Biology* **283**(4), 893–903.

[60] Cohen, S. I. A., Linse, S., Luheshi, L. M., Hellstrand, E., White, D. a., Rajah, L., Otzen, D. E., Vendruscolo, M., Dobson, C. M. and Knowles, T. P. J. [2013], 'Proliferation of amyloid-β42 aggregates occurs through a secondary nucleation mechanism.', *Proceedings of the National Academy of Sciences of the United States of America* **110**(24), 9758–63.

[61] Cohen, S. I. A., Rajah, L., Yoon, C., Buell, a., White, D., Sperling, R., Vendruscolo, M., Terentjev, E., Dobson, C., Weitz, D. and Knowles, T. [2014], 'Spatial Propagation of Protein Polymerization', *Physical Review Letters* **112**(9), 098101.

[62] Cohen, S. I., Cukalevski, R., Michaels, T. C., Šarić, A., Törnquist, M., Vendruscolo, M., Dobson, C. M., Buell, A. K., Knowles, T. P. and Linse, S. [2018], 'Distinct thermodynamic signatures of oligomer generation in the aggregation of the amyloid-β peptide', *Nature Chemistry* **10**(5), 523–531.

[63] Cole, D., Young, G., Weigel, A., Sebesta, A. and Kukura, P. [2017], 'Label-free single-molecule imaging with numerical-aperture-shaped interferometric scattering microscopy', *ACS Photonics* **4**(2), 211–216.

[64] Collinge, J. [2001], 'PRION DISEASES OF HUMANS AND ANIMALS : Their Causes and Molecular Basis', *Annual Reviews* **24**(McGowan 1922), 519–50.

[65] Collins, S. R., Douglass, A., Vale, R. D. and Weissman, J. S. [2004], 'Mechanism of prion propagation: Amyloid growth occurs by monomer addition', *PLoS Biology* **2**(10).

[66] Culbertson, C. T., Jacobson, S. C. and Ramsey, J. M. [2002], 'Diffusion coefficient measurements in microfluidic devices', *Talanta* **56**(2), 365–373.

[67] de la Escosura-Muñiz, A. and Merkoçi, A. [2016], 'Nanochannels for electrical biosensing', *TrAC Trends in Analytical Chemistry* **79**, 134–150.

[68] del Campo, A. and Greiner, C. [2007], 'Su-8: a photoresist for high-aspect-ratio and 3d submicron lithography', *Journal of Micromechanics and Microengineering* **17**(6), R81.

[69] Deltcheva, E., Chylinski, K., Sharma, C. M., Gonzales, K., Chao, Y., Pirzada, Z. A., Eckert, M. R., Vogel, J. and Charpentier, E. [2011], 'Crispr rna maturation by trans-encoded small rna and host factor rnase iii', *Nature* **471**(7340), 602–607.

[70] Dempsey, G. T., Vaughan, J. C., Chen, K. H., Bates, M. and Zhuang, X. [2011], 'Evaluation of fluorophores for optimal performance in localization-based super-resolution imaging', *Nature Methods* **8**(12), 1027.

[71] Derjaguin, B., Dukhin, S. and Korotkova, A. [1993], 'Diffusiophoresis in electrolyte solutions and its role in the mechanism of the formation of films from caoutchouc latexes by the ionic deposition method', *Progress in Surface Science* **43**(1-4), 153–158.

[72] Dieckmann, T., Fujikawa, E., XHAO, X., Szostak, J. and Feigon, J. [1995], 'Structural investigations of rna and dna aptamers in solution', *Journal of Cellular Biochemistry* pp. 56–56.

[73] Dobson, C. M. [2003], 'Protein folding and misfolding', *Nature* **426**(6968), 884–890.

[74] Dobson, C. M., Šali, A. and Karplus, M. [1998], 'Protein folding: a perspective from theory and experiment', *Angewandte Chemie International Edition* **37**(7), 868–893.

[75] Dousseau, F. and Pezolet, M. [1990], 'Determination of the secondary structure content of proteins in aqueous solutions from their amide i and amide ii infrared bands. comparison between classical and partial least-squares methods', *Biochemistry* **29**(37), 8771–8779.

[76] Duffy, D. C., McDonald, J. C., Schueller, O. J. and Whitesides, G. M. [1998], 'Rapid prototyping of microfluidic systems in poly (dimethylsiloxane)', *Analytical Chemistry* **70**(23), 4974–4984.

[77] Dulin, D., Barland, S., Hachair, X. and Pedaci, F. [2014], 'Efficient illumination for microsecond tracking microscopy', *PloS one* **9**(9).

[78] Dullemond, C. and Kuiper, R. [2008], 'Lecture numerical fluid dynamics', *University of Heidelberg, Summer Semester* .

[79] Dyer, K. F. [1971], 'The quiet revolution: A new synthesis of biological knowledge', *Journal of Biological Education* **5**(1), 15–24.

[80] Dyson, H. J. and Wright, P. E. [2004], 'Unfolded proteins and protein folding studied by nmr.', *Chemical Reviews* **104**(8), 3607–22.

[81] Eijkel, J. C. T. and Berg, A. v. d. [2005], 'Nanofluidics: what is it and what can we expect from it?', *Microfluidics and Nanofluidics* **1**(3), 249–267.

[82] Einstein, A. [1905], 'Über die von der molekularkinetischen theorie der wärme geforderte bewegung von in ruhenden flüssigkeiten suspendierten teilchen', *Annalen der Physik* **4**.

[83] Ellis, R. J. [2001], 'Macromolecular crowding: an important but neglected aspect of the intracellular environment', *Current Opinion in Structural Biology* **11**(1), 114–119.

[84] Elson, E. L. and Magde, D. [1974], 'Fluorescence correlation spectroscopy. i. conceptual basis and theory', *Biopolymers: Original Research on Biomolecules* **13**(1), 1–27.

[85] Emmelkamp, J., Wolbers, F., Andersson, H., Dacosta, R. S., Wilson, B. C., Vermes, I. and van den Berg, A. [2004], 'The potential of autofluorescence for the detection of single living cells for label-free cell sorting in microfluidic systems.', *Electrophoresis* **25**(21-22), 3740–5.

[86] Emmenegger, M., De Cecco, E., Lamparter, D., Jacquat, R. P., Ebner, D., Schneider, M. M., Morales, I. C., Schneider, D., Dogancay, B., Guo, J. et al. [2020], 'Population-wide evolution of sars-cov-2 immunity tracked by a ternary immunoassay', *medRxiv* .

[87] Eschenbaum, C., Großmann, D., Dopf, K., Kettlitz, S., Bocksrocker, T., Valouch, S. and Lemmer, U. [2013], 'Hybrid lithography: Combining uv-exposure and two photon direct laser writing', *Optics Express* **21**(24), 29921–29926.

[88] Esparza, T. J., Martin, N. P., Anderson, G. P., Goldman, E. R. and Brody, D. L. [2020], 'High affinity nanobodies block sars-cov-2 spike receptor binding domain interaction with human angiotensin converting enzyme', *Scientific Reports* **10**(1), 1–13.

[89] Fahim, A. and Annunziata, O. [2020], 'Amplification of salt-induced protein diffusiophoresis by varying salt from potassium to sodium to magnesium chloride in water', *Langmuir* **36**(10), 2635–2643.

[90] Fekete, S., Beck, A., Veuthey, J.-L. and Guillarme, D. [2014], 'Theory and practice of size exclusion chromatography for the analysis of protein aggregates', *Journal of Pharmaceutical and Biomedical Analysis* **101**, 161–173.

[91] Feng, R. and Farris, R. J. [2002], 'Influence of processing conditions on the thermal and mechanical properties of su8 negative photoresist coatings', *Journal of Micromechanics and Microengineering* **13**(1), 80.

[92] Ferrone, F. A., Hofrichter, J. and Eaton, W. A. [1985], 'Kinetics of sickle hemoglobin polymerization. II. A double nucleation mechanism', *Journal of Molecular Biology* **183**(4), 611–631.

[93] Fisher, R. A. [1937], 'The wave of advance of advantageous genes', *Annals of Eugenics* **7**(4), 355–369.

[94] Fitzpatrick, A. W., Debelouchina, G. T., Bayro, M. J., Clare, D. K., Caporini, M. A., Bajaj, V. S., Jaroniec, C. P., Wang, L., Ladizhansky, V., Müller, S. A. et al. [2013], 'Atomic structure and hierarchical assembly of a cross-β amyloid fibril', *Proceedings of the National Academy of Sciences* **110**(14), 5468–5473.

[95] Friedrich, S. M., Burke, J. M., Liu, K. J., Ivory, C. F. and Wang, T.-H. [2017], 'Molecular rheotaxis directs dna migration and concentration against a pressure-driven flow', *Nature Communications* **8**(1), 1–10.

[96] Frigon, R. P., Leypoldt, J. K., Uyeji, S. and Henderson, L. W. [1983], 'Disparity between Stokes radii of dextrans and proteins as determined by retention volume in gel permeation chromatography', *Analytical Chemistry* **55**(8), 1349–1354.

[97] Gang, H., Galvagnion, C., Meisl, G., Müller, T., Pfammatter, M., Buell, A. K., Levin, A., Dobson, C. M., Mu, B. and Knowles, T. P. [2018], 'Microfluidic diffusion platform for characterizing the sizes of lipid vesicles and the thermodynamics of protein–lipid interactions', *Analytical Chemistry* **90**(5), 3284–3290.

[98] Gansel, J. K., Thiel, M., Rill, M. S., Decker, M., Bade, K., Saile, V., von Freymann, G., Linden, S. and Wegener, M. [2009], 'Gold helix photonic metamaterial as broadband circular polarizer', *Science* **325**(5947), 1513–1515.

[99] Gemeinhardt, A., McDonald, M. P., König, K., Aigner, M., Mackensen, A. and Sandoghdar, V. [2018], 'Label-free imaging of single proteins secreted from living cells via iscat microscopy', *JoVE (Journal of Visualized Experiments)* (141), e58486.

[100] Gessner, T. and Mayer, U. [2000], 'Triarylmethane and diarylmethane dyes', *Ullmann's Encyclopedia of Industrial Chemistry* .

[101] Giddings, J. C. [1985], 'A system based on split-flow lateral-transport thin (splitt) separation cells for rapid and continuous particle fractionation', *Separation Science and Technology* **20**(9-10), 749–768.

[102] Goldfain, A. M., Garmann, R. F., Jin, Y., Lahini, Y. and Manoharan, V. N. [2016], 'Dynamic measurements of the position, orientation, and dna content of individual unlabeled bacteriophages', *The Journal of Physical Chemistry B* **120**(26), 6130–6138.

[103] Goswami, A., Acharya, A. and Pandey, A. [2001], 'Study of self-diffusion of monovalent and divalent cations in nafion-117 ion-exchange membrane', *The Journal of Physical Chemistry B* **105**(38), 9196–9201.

[104] Grey, M., Dunning, C. J., Gaspar, R., Grey, C., Brundin, P., Sparr, E. and Linse, S. [2015], 'Acceleration of α-synuclein aggregation by exosomes', *Journal of Biological Chemistry* **290**(5), 2969–2982.

[105] Guo, J. L. and Lee, V. M. Y. [2014], 'Cell-to-cell transmission of pathogenic proteins in neurodegenerative diseases', *Nature Medicine* **20**(2), 130–138.

[106] Hancu, G., Simon, B., Rusu, A., Mircia, E. and Gyéresi, Á. [2013], 'Principles of micellar electrokinetic capillary chromatography applied in pharmaceutical analysis', *Advanced Pharmaceutical Bulletin* **3**(1), 1.

[107] Hardy, J. and Selkoe, D. J. [2002], 'The amyloid hypothesis of Alzheimer's disease: progress and problems on the road to therapeutics.', *Science (New York, N.Y.)* **297**(5580), 353–6.

[108] Hartl, F. U. and Hayer-Hartl, M. [2002], 'Molecular chaperones in the cytosol: from nascent chain to folded protein', *Science* **295**(5561), 1852–1858.

[109] Hatch, A., Garcia, E. and Yager, P. [2004], 'Diffusion-based analysis of molecular interactions in microfluidic devices', *Proceedings of the IEEE* **92**(1), 126–139.

[110] Hatch, A., Kamholz, A. E., Hawkins, K. R., Munson, M. S., Schilling, E. A., Weigl, B. H. and Yager, P. [2001], 'A rapid diffusion immunoassay in a t-sensor', *Nature Biotechnology* **19**(5), 461–465.

[111] He, Y., Huang, Z., Chen, B., Tsutsui, M., Miao, X. S. and Taniguchi, M. [2017], 'Electrokinetic analysis of energy harvest from natural salt gradients in nanochannels', *Scientific Reports* **7**(1), 1–15.

[112] Hellmich, W., Greif, D., Pelargus, C., Anselmetti, D. and Ros, A. [2006], 'Improved native UV laser induced fluorescence detection for single cell analysis in poly(dimethylsiloxane) microfluidic devices', *Journal of Chromatography A* pp. 1130–195.

[113] Hellmich, W., Pelargus, C., Leffhalm, K., Ros, A. and Anselmetti, D. [2005], 'Single cell manipulation, analytics, and label-free protein detection in microfluidic devices for systems nanobiology.', *Electrophoresis* **26**(19), 3689–96.

[114] Hengsbach, S. and Lantada, A. D. [2014], 'Rapid prototyping of multi-scale biomedical microdevices by combining additive manufacturing technologies', *Biomedical Microdevices* **16**(4), 617–627.

[115] Herling, T., Müller, T., Rajah, L., Skepper, J., Vendruscolo, M. and Knowles, T. [2013], 'Integration and characterization of solid wall electrodes in microfluidic devices fabricated in a single photolithography step', *Applied Physics Letters* **102**(18), 184102.

[116] Herling, T. W., Arosio, P., Müller, T., Linse, S. and Knowles, T. P. [2015], 'A microfluidic platform for quantitative measurements of effective protein charges and single ion binding in solution', *Physical Chemistry Chemical Physics* **17**(18), 12161–12167.

[117] Herling, T. W., Levin, A., Saar, K. L., Dobson, C. M. and Knowles, T. P. [2018], 'Microfluidic approaches for probing amyloid assembly and behaviour', *Lab on a Chip* **18**(7), 999–1016.

[118] Herling, T. W., O'Connell, D. J., Bauer, M. C., Persson, J., Weininger, U., Knowles, T. P. and Linse, S. [2016], 'A microfluidic platform for real-time detection and quantification of protein-ligand interactions', *Biophysical Journal* **110**(9), 1957–1966.

[119] Hochberg, G. K. A., Ecroyd, H., Liu, C., Cox, D., Cascio, D., Sawaya, M. R., Collier, M. P., Stroud, J., Carver, J. A., Baldwin, A. J., Robinson, C. V., Eisenberg, D. S., Benesch, J. L. P. and Laganowsky, A. [2014], 'The structured core domain of αB-crystallin can prevent amyloid fibrillation and associated toxicity.', *Proceedings of the National Academy of Sciences of the United States of America* **111**(16), E1562–70.

[120] Hong, J., Kim, B. and Shin, H. [2018], 'Mixed-scale poly (methyl methacrylate) channel network-based single-particle manipulation via diffusiophoresis', *Nanoscale* **10**(30), 14421–14431.

[121] Hoyer, W., Antony, T., Cherny, D., Heim, G., Jovin, T. M. and Subramaniam, V. [2002], 'Dependence of α-synuclein aggregate morphology on solution conditions', *Journal of Molecular Biology* **322**(2), 383–393.

[122] Hu, C.-D. and Kerppola, T. K. [2003], 'Simultaneous visualization of multiple protein interactions in living cells using multicolor fluorescence complementation analysis', *Nature Biotechnology* **21**(5), 539–545.

[123] Inglis, D. W., Goldys, E. M. and Calander, N. P. [2011], 'Simultaneous concentration and separation of proteins in a nanochannel', *Angewandte Chemie International Edition* **50**(33), 7546–7550.

[124] Janasek, D., Franzke, J. and Manz, A. [2006], 'Scaling and the design of miniaturized chemical-analysis systems', *Nature* **442**(7101), 374–380.

[125] Jarrett, J. T., Berger, E. P. and Lansbury, P. T. [1993], 'The Carboxy Terminus of the β Amyloid Protein Is Critical for the Seeding of Amyloid Formation: Implications for the Pathogenesis of Alzheimer's Disease', *Biochemical Journal* **32**(18), 4693–4697.

[126] Jarrett, J. T. and Lansburry, P. T. [1993], 'Seeding "one-dimensional cristallization" of amyloid: a pathogenic mechanism in Alzheimer's disease and scrapie?', *Cell* **73**, 1055–1058.

[127] Jehle, S., Vollmar, B. S., Bardiaux, B., Dove, K. K., Rajagopal, P., Gonen, T., Oschkinat, H. and Klevit, R. E. [2011], 'N-terminal domain of αb-crystallin provides a conformational switch for multimerization and structural heterogeneity', *Proceedings of the National Academy of Sciences* **108**(16), 6409–6414.

[128] Jiao, M., Li, H.-T., Chen, J., Minton, A. P. and Liang, Y. [2010], 'Attractive protein-polymer interactions markedly alter the effect of macromolecular crowding on protein association equilibria', *Biophysical Journal* **99**(3), 914–923.

[129] Jimenez, J. L., Nettleton, E. J., Bouchard, M., Robinson, C. V., Dobson, C. M. and Saibil, H. R. [2002], 'The protofilament structure of insulin amyloid fibrils', *Proceedings of the National Academy of Sciences* **99**(14), 9196–9201.

[130] Joo, C., Balci, H., Ishitsuka, Y., Buranachai, C. and Ha, T. [2008], 'Advances in single-molecule fluorescence methods for molecular biology', *Annual Review of Biochemistry* **77**, 51–76.

[131] Jucker, M. and Walker, L. C. [2013], 'Self-propagation of pathogenic protein aggregates in neurodegenerative diseases.', *Nature* **501**(7465), 45–51.

[132] Juette, M. F., Terry, D. S., Wasserman, M. R., Zhou, Z., Altman, R. B., Zheng, Q. and Blanchard, S. C. [2014], 'The bright future of single-molecule fluorescence imaging', *Current Opinion in Chemical Biology* **20**, 103–111.

[133] Jumper, J., Evans, R., Pritzel, A., Green, T., Figurnov, M., Tunyasuvunakool, K., Ronneberger, O., Bates, R., Zidek, A., Bridgland, A. et al. [2020], 'High accuracy protein structure prediction using deep learning', *Fourteenth Critical Assessment of Techniques for Protein Structure Prediction (Abstract Book)* **22**, 24.

[134] Juodkazis, S., Mizeikis, V., Seet, K. K., Miwa, M. and Misawa, H. [2005], 'Two-photon lithography of nanorods in su-8 photoresist', *Nanotechnology* **16**(6), 846.

[135] Kameoka, J., Craighead, H. G., Zhang, H. and Henion, J. [2001], 'A polymeric microfluidic chip for ce/ms determination of small molecules', *Analytical Chemistry* **73**(9), 1935–1941.

[136] Kamholz, A. E., Schilling, E. A. and Yager, P. [2001], 'Optical measurement of transverse molecular diffusion in a microchannel', *Biophysical Journal* **80**(4), 1967–1972.

[137] Kamholz, A. E. and Yager, P. [2001], 'Theoretical analysis of molecular diffusion in pressure-driven laminar flow in microfluidic channels', *Biophysical Journal* **80**(1), 155–160.

[138] Kartanas, T., Ostanin, V., Challa, P. K., Daly, R., Charmet, J. and Knowles, T. P. [2017], 'Enhanced quality factor label-free biosensing with micro-cantilevers integrated into microfluidic systems', *Analytical Chemistry* **89**(22), 11929–11936. PMID: 28984439.

[139] Kay, L. E. [2011], 'Nmr studies of protein structure and dynamics', *Journal of Magnetic Resonance* **213**(2), 477–491.

[140] Kelly, S. M., Jess, T. J. and Price, N. C. [2005], 'How to study proteins by circular dichroism', *Biochimica et Biophysica Acta (BBA)-Proteins and Proteomics* **1751**(2), 119–139.

[141] Kemp, G. [1998], 'Capillary electrophoresis: a versatile family of analytical techniques', *Biotechnology and Applied Biochemistry* **27**(1), 9–17.

[142] Kendrew, J. C., Bodo, G., Dintzis, H. M., Parrish, R., Wyckoff, H. and Phillips, D. C. [1958], 'A three-dimensional model of the myoglobin molecule obtained by x-ray analysis', *Nature* **181**(4610), 662–666.

[143] Kim, D.-K., Duan, C., Chen, Y.-F. and Majumdar, A. [2010], 'Power generation from concentration gradient by reverse electrodialysis in ion-selective nanochannels', *Microfluidics and Nanofluidics* **9**(6), 1215–1224.

[144] King, J. L. and Jukes, T. H. [1969], 'Non-darwinian evolution', *Science* **164**(3881), 788–798.

[145] Knowles, T. P. J., Waudby, C. a., Devlin, G. L., Cohen, S. I. a., Aguzzi, A., Vendruscolo, M., Terentjev, E. M., Welland, M. E. and Dobson, C. M. [2009], 'An analytical solution to the kinetics of breakable filament assembly.', *Science (New York, N.Y.)* **326**(5959), 1533–7.

[146] Knowles, T. P., Vendruscolo, M. and Dobson, C. M. [2014], 'The amyloid state and its association with protein misfolding diseases', *Nature reviews Molecular cell biology* **15**(6), 384–396.

[147] Knowles, T. P., White, D. A., Abate, A. R., Agresti, J. J., Cohen, S. I., Sperling, R. A., De Genst, E. J., Dobson, C. M. and Weitz, D. A. [2011], 'Observation of spatial propagation of amyloid assembly from single nuclei', *Proceedings of the National Academy of Sciences* **108**(36), 14746–14751.

[148] Köhler, S., Nagl, S., Fritzsche, S. and Belder, D. [2012], 'Label-free real-time imaging in microchip free-flow electrophoresis applying high speed deep UV fluorescence scanning', *Lab on a Chip* **12**(3), 458–463.

[149] Kohlheyer, D., Eijkel, J. C., van den Berg, A. and Schasfoort, R. B. [2008], 'Miniaturizing free-flow electrophoresis–a critical review', *Electrophoresis* **29**(5), 977–993.

[150] Koopman, M., Peter, Q., Seinstra, R. I., Perni, M., Vendruscolo, M., Dobson, C. M., Knowles, T. P. and Nollen, E. A. [2020], 'Assessing motor-related phenotypes of caenorhabditis elegans with the wide field-of-view nematode tracking platform', *Nature Protocols* **15**(6), 2071–2106.

[151] Kopp, M. R. and Arosio, P. [2018], 'Microfluidic approaches for the characterization of therapeutic proteins', *Journal of Pharmaceutical Sciences* .

[152] Kopp, M. R., Villois, A., Capasso Palmiero, U. and Arosio, P. [2018], 'Microfluidic diffusion analysis of the size distribution and microrheological properties of antibody solutions at high concentrations', *Industrial & Engineering Chemistry Research* **57**(21), 7112–7120.

[153] Kovarik, M. L. and Jacobson, S. C. [2009], 'Nanofluidics in lab-on-a-chip devices'.

[154] Kukura, P., Ewers, H., Müller, C., Renn, A., Helenius, A. and Sandoghdar, V. [2009], 'High-speed nanoscopic tracking of the position and orientation of a single virus', *Nature Methods* **6**(12), 923–927.

[155] Lager, A., Webb, K. J., Collins, I. R., Richmond, D. M. et al. [2008], Losal enhanced oil recovery: Evidence of enhanced oil recovery at the reservoir scale, *in* 'SPE symposium on improved oil recovery', Society of Petroleum Engineers.

[156] Lakowicz, J. R., ed. [2006], *Protein Fluorescence*, Springer US, Boston, MA, pp. 529–575.

[157] Lechlitner, L. R. and Annunziata, O. [2018], 'Macromolecule diffusiophoresis induced by concentration gradients of aqueous osmolytes', *Langmuir* **34**(32), 9525–9531.

[158] Lee, K.-S., Kim, R. H., Yang, D.-Y. and Park, S. H. [2008], 'Advances in 3d nano/microfabrication using two-photon initiated polymerization', *Progress in Polymer Science* **33**(6), 631–681.

[159] Leney, A. C. and Heck, A. J. [2016], 'Native mass spectrometry: what is in the name?', *Journal of the American Society for Mass Spectrometry* **28**(1), 5–13.

[160] Lequin, R. M. [2005], 'Enzyme immunoassay (eia)/enzyme-linked immunosorbent assay (elisa)', *Clinical Chemistry* **51**(12), 2415–2418.

[161] Liang, Z., Chiem, N., Ocvirk, G., Tang, T., Fluri, K. and Harrison, D. J. [1996], 'Microfabrication of a Planar Absorbance and Fluorescence Cell for Integrated Capillary Electrophoresis Devices', *Analytical Chemistry* **68**(6), 1040–1046.

[162] Lieb, M. A., Zavislan, J. M. and Novotny, L. [2004], 'Single-molecule orientations determined by direct emission pattern imaging', *JOSA B* **21**(6), 1210–1215.

[163] Liebel, M., Hugall, J. T. and van Hulst, N. F. [2017], 'Ultrasensitive label-free nanosensing and high-speed tracking of single proteins', *Nano Letters* **17**(2), 1277–1281.

[164] Lin, Y., Gao, C., Gritsenko, D., Zhou, R. and Xu, J. [2018], 'Soft lithography based on photolithography and two-photon polymerization', *Microfluidics and Nanofluidics* **22**(9), 97.

[165] Lindberg, D. J., Wranne, M. S., Gilbert Gatty, M., Westerlund, F. and Esbjörner, E. K. [2015], 'Steady-state and time-resolved Thioflavin-T fluorescence can report on morphological differences in amyloid fibrils formed by Aβ(1-40) and Aβ(1-42)', *Biochemical and Biophysical Research Communications* **458**(2), 418–423.

[166] Lindstedt, P. R., Aprile, F. A., Matos, M. J., Perni, M., Bertoldo, J. B., Bernardim, B., Peter, Q., Jiménez-Osés, G., Knowles, T. P., Dobson, C. M. et al. [2019], 'Enhancement of the anti-aggregation activity of a molecular chaperone using a rationally designed post-translational modification', *ACS Central Science* **5**(8), 1417–1424.

[167] Linse, S., Scheidt, T., Bernfur, K., Vendruscolo, M., Dobson, C. M., Cohen, S. I., Sileikis, E., Lundqvist, M., Qian, F., O'Malley, T. et al. [2020], 'Kinetic fingerprints differentiate the mechanisms of action of anti-aβ antibodies', *Nature Structural & Molecular Biology* **27**(12), 1125–1133.

[168] Maeda, S., Koehl, A., Matile, H., Hu, H., Hilger, D., Schertler, G. F., Manglik, A., Skiniotis, G., Dawson, R. J. and Kobilka, B. K. [2018], 'Development of an antibody fragment that stabilizes gpcr/g-protein complexes', *Nature Communications* **9**(1), 1–9.

[169] Mahmood, T. and Yang, P.-C. [2012], 'Western blot: technique, theory, and trouble shooting', *North American journal of medical sciences* **4**(9), 429.

[170] Malinauskas, M., Farsari, M., Piskarskas, A. and Juodkazis, S. [2013], 'Ultrafast laser nanostructuring of photopolymers: A decade of advances', *Physics Reports* **533**(1), 1–31.

[171] Marbach, S. and Bocquet, L. [2019], 'Osmosis, from molecular insights to large-scale applications', *Chemical Society Reviews* **48**(11), 3102–3144.

[172] Marbach, S., Yoshida, H. and Bocquet, L. [2019], 'Local and global force balance for diffusiophoretic transport', *arXiv preprint arXiv:1910.13901* .

[173] Marino, A., Tricinci, O., Battaglini, M., Filippeschi, C., Mattoli, V., Sinibaldi, E. and Ciofani, G. [2018], 'A 3d real-scale, biomimetic, and biohybrid model of the blood-brain barrier fabricated through two-photon lithography', *Small* **14**(6), 1702959.

[174] McDonald, J. C. and Whitesides, G. M. [2002], 'Poly(dimethylsiloxane) as a material for fabricating microfluidic devices', *Accounts of Chemical Research* **35**(7), 491–499.

[175] Mehmood, S., Allison, T. M. and Robinson, C. V. [2015], 'Mass spectrometry of protein complexes: from origins to applications', *Annual Review of Physical Chemistry* **66**, 453–474.

[176] Meisl, G., Kirkegaard, J. B., Arosio, P., Michaels, T. C. T., Vendruscolo, M., Dobson, C. M., Linse, S. and Knowles, T. P. J. [2016], 'Molecular mechanisms of protein aggregation from global fitting of kinetic models', *Nature Protocols* **11**(2), 252–272.

[177] Michaels, T. C., Šarić, A., Curk, S., Bernfur, K., Arosio, P., Meisl, G., Dear, A. J., Cohen, S. I., Dobson, C. M., Vendruscolo, M. et al. [2020], 'Dynamics of oligomer populations formed during the aggregation of alzheimer's aβ42 peptide', *Nature Chemistry* **12**(5), 445–451.

[178] Mittal, S., Chowhan, R. K. and Singh, L. R. [2015], 'Macromolecular crowding: Macromolecules friend or foe', *Biochimica et Biophysica Acta (BBA)-General Subjects* **1850**(9), 1822–1831.

[179] Moerner, W. E. and Orrit, M. [1999], 'Illuminating single molecules in condensed matter', *Science* **283**(5408), 1670–1676.

[180] Monici, M. [2005], 'Cell and tissue autofluorescence research and diagnostic applications', *Biotechnology Annual Review* **11**, 227–256.

[181] Mucke, L. and Selkoe, D. J. [2012], 'Neurotoxicity of amyloid β-protein: Synaptic and network dysfunction', *Cold Spring Harbor Perspectives in Medicine* **2**(7), 1–17.

[182] Mueller, A. M., Breitsprecher, D., Duhr, S., Baaske, P., Schubert, T. and Längst, G. [2017], Microscale thermophoresis: a rapid and precise method to quantify protein–nucleic acid interactions in solution, *in* 'Functional Genomics', Springer, pp. 151–164.

[183] Müller, T., Arosio, P., Rajah, L., Cohen, S. I. A., Yates, E. V., Vendruscolo, M., Dobson, C. M. and Knowles, T. P. J. [2016], 'Particle-based monte-carlo simulations of steady-state mass transport at intermediate péclet numbers', *International Journal of Nonlinear Sciences and Numerical Simulation* **0**(0), 0.

[184] Nakanishi, H., Nishimoto, T., Arai, A., Abe, H., Kanai, M., Fujiyama, Y. and Yoshida, T. [2001], 'Fabrication of quartz microchips with optical slit and development of a linear imaging UV detector for microchip electrophoresis systems', *Electrophoresis* **22**(2), 230–234.

[185] Nery-Azevedo, R., Banerjee, A. and Squires, T. M. [2017], 'Diffusiophoresis in ionic surfactant gradients', *Langmuir* **33**(38), 9694–9702.

[186] Nielsen, L., Khurana, R., Coats, A., Frokjaer, S., Brange, J., Vyas, S., Uversky, V. N. and Fink, A. L. [2001], 'Effect of environmental factors on the kinetics of insulin fibril formation: Elucidation of the molecular mechanism', *Biochemistry* **40**(20), 6036–6046.

[187] Novotny, L. and Hecht, B. [2012], *Principles of nano-optics*, Cambridge university press.

[188] Ortega Arroyo, J., Andrecka, J., Spillane, K., Billington, N., Takagi, Y., Sellers, J. and Kukura, P. [2014], 'Label-free, all-optical detection, imaging, and tracking of a single protein', *Nano Letters* **14**(4), 2065–2070.

[189] Ortega-Arroyo, J. and Kukura, P. [2012], 'Interferometric scattering microscopy (iscat): new frontiers in ultrafast and ultrasensitive optical microscopy', *Physical Chemistry Chemical Physics* **14**(45), 15625–15636.

[190] Ou-Yang, L., Dai, D.-Q., Li, X.-L., Wu, M., Zhang, X.-F. and Yang, P. [2014], 'Detecting temporal protein complexes from dynamic protein-protein interaction networks', *BMC Bioinformatics* **15**(1), 335.

[191] Ovesnỳ, M., Křížek, P., Borkovec, J., Švindrych, Z. and Hagen, G. M. [2014], 'Thunderstorm: a comprehensive imagej plug-in for palm and storm data analysis and super-resolution imaging', *Bioinformatics* **30**(16), 2389–2390.

[192] Palacci, J., Cottin-Bizonne, C., Ybert, C. and Bocquet, L. [2010], 'Sedimentation and effective temperature of active colloidal suspensions', *Physical Review Letters* **105**(8), 088304.

[193] Palacci, J., Cottin-Bizonne, C., Ybert, C. and Bocquet, L. [2012], 'Osmotic traps for colloids and macromolecules based on logarithmic sensing in salt taxis', *Soft Matter* **8**(4), 980–994.

[194] Park, H., Pak, J. J., Son, S. Y., Lim, G. and Song, I. [2003], 'Fabrication of a microchannel integrated with inner sensors and the analysis of its laminar flow characteristics', *Sensors and Actuators A: Physical* **103**(3), 317–329.

[195] Park, S.-H., Yang, D.-Y. and Lee, K.-S. [2009], 'Two-photon stereolithography for realizing ultraprecise three-dimensional nano/microdevices', *Laser & Photonics Reviews* **3**(1-2), 1–11.

[196] Pelton, J. T. and McLean, L. R. [2000], 'Spectroscopic methods for analysis of protein secondary structure', *Analytical Biochemistry* **277**(2), 167–176.

[197] Peter, Q., Jacquat, R. P., Herling, T. W., Challa, P. K., Kartanas, T. and Knowles, T. P. J. [2021*a*], 'Data supporting "microscale diffusiophoresis of proteins"', *https://doi.org/10.17863/CAM.48786* .

[198] Peter, Q., Jacquat, R. P., Herling, T. W., Challa, P. K., Kartanas, T. and Knowles, T. P. J. [2021*b*], 'Scripts supporting "microscale diffusiophoresis of proteins"', *https://doi.org/10.5281/zenodo.3636078* .

[199] Peter, Q., Saar, K.-L., Herling, T. W., Muller, T. and Knowles, T. P. J. [2021], 'Scripts supporting "fast numerical integration of diffusional sizing basis functions"', *https://doi.org/10.5281/zenodo.3881940* .

[200] Petersen, N. J., Mogensen, K. B. and Kutter, J. P. [2002], 'Performance of an in-plane detection cell with integrated waveguides for UV/Vis absorbance measurements on microfluidic separation devices', *Electrophoresis* **23**(20), 3528–3536.

[201] Petkova, A. T., Leapman, R. D. and Guo, Z. [2005], 'Self-Propagating, Molecular-Level Polymorphism in Alzheimer's beta-Amyloid Fibrils', *Science* **307**(January), 262–266.

[202] Pierce, M. M., Raman, C. and Nall, B. T. [1999], 'Isothermal titration calorimetry of protein–protein interactions', *Methods* **19**(2), 213–221.

[203] Piliarik, M. and Sandoghdar, V. [2014], 'Direct optical sensing of single unlabelled proteins and super-resolution imaging of their binding sites', *Nature Communications* **5**, 4495.

[204] Plückthun, A. [2015], 'Designed ankyrin repeat proteins (darpins): binding proteins for research, diagnostics, and therapy', *Annual Review of Pharmacology and Toxicology* **55**, 489–511.

[205] Price, W. S. [1997], 'Pulsed-field gradient nuclear magnetic resonance as a tool for studying translational diffusion: Part 1. basic theory', *Concepts in Magnetic Resonance: An Educational Journal* **9**(5), 299–336.

[206] Prieve, D., Anderson, J., Ebel, J. and Lowell, M. [1984], 'Motion of a particle generated by chemical gradients. part 2. electrolytes', *Journal of Fluid Mechanics* **148**, 247–269.

[207] Prieve, D. C. and Roman, R. [1987], 'Diffusiophoresis of a rigid sphere through a viscous electrolyte solution', *Journal of the Chemical Society, Faraday Transactions 2: Molecular and Chemical Physics* **83**(8), 1287–1306.

[208] Prusiner, S. B. [1991], 'Molecular biology of prion diseases', *Science* **252**(5012), 1515–1522.

[209] Prusiner, S. B. [1998], 'Prions', *Proceedings of the National Academy of Sciences* **95**(23), 13363–13383.

[210] Qin, D., Xia, Y. and Whitesides, G. M. [2010], 'Soft lithography for micro- and nanoscale patterning', *Nature Protocols* **5**(3), 491–502.

[211] Quentmeier, S., Denicke, S. and Gericke, K.-H. [2009], 'Two-Color Two-Photon Fluorescence Laser Scanning Microscopy', *Journal of Fluorescence* **19**(6), 1037–1043.

[212] Ramírez-Hinestrosa, S., Yoshida, H., Bocquet, L. and Frenkel, D. [2020], 'Studying polymer diffusiophoresis with non-equilibrium molecular dynamics', *The Journal of Chemical Physics* **152**(16), 164901.

[213] Rasmussen, M. K., Pedersen, J. N. and Marie, R. [2020], 'Size and surface charge characterization of nanoparticles with a salt gradient', *Nature Communications* **11**(1), 1–8.

[214] Reddy, B. S. and Chatterji, B. N. [1996], 'An fft-based technique for translation, rotation, and scale-invariant image registration', *IEEE TRANSACTIONS ON IMAGE PROCESSING* **VOL. 5**(NO. 8), 1266–1271.

[215] Regehr, K. J., Domenech, M., Koepsel, J. T., Carver, K. C., Ellison-Zelski, S. J., Murphy, W. L., Schuler, L. A., Alarid, E. T. and Beebe, D. J. [2009], 'Biological implications of polydimethylsiloxane-based microfluidic cell culture', *Lab on a Chip* **9**, 2132–2139.

[216] Rich, R. L. and Myszka, D. G. [2007], 'Higher-throughput, label-free, real-time molecular interaction analysis.', *Analytical Biochemistry* **361**(1), 1.

[217] Richter, B., Hahn, V., Bertels, S., Claus, T. K., Wegener, M., Delaittre, G., Barner-Kowollik, C. and Bastmeyer, M. [2017], 'Guiding cell attachment in 3d microscaffolds selectively functionalized with two distinct adhesion proteins', *Advanced Materials* **29**(5), 1604342.

[218] Richter, P. [1995], 'Estimating errors in least-squares fitting'.

[219] Robinson, C. V., Sali, A. and Baumeister, W. [2007], 'The molecular sociology of the cell', *Nature* **450**(7172), 973–982.

[220] Roman, M. C. and Brown, P. R. [1994], 'Free-flow electrophoresis as a preparative separation technique', *Analytical Chemistry* **66**(2), 86A–94A.

[221] Rowlands, C. J., Ströhl, F., Ramirez, P. P. V., Scherer, K. M. and Kaminski, C. F. [2018], 'Flat-field super-resolution localization microscopy with a low-cost refractive beam-shaping element', *Scientific Reports* **8**(1), 1–8.

[222] Ruggeri, F. S., Charmet, J., Kartanas, T., Peter, Q., Chia, S., Habchi, J., Dobson, C. M., Vendruscolo, M. and Knowles, T. P. [2018], 'Microfluidic deposition for resolving single-molecule protein architecture and heterogeneity', *Nature Communications* **9**(1), 1–12.

[223] Ruggeri, F., Zosel, F., Mutter, N., Różycka, M., Wojtas, M., Ożyhar, A., Schuler, B. and Krishnan, M. [2017], 'Single-molecule electrometry', *Nature Nanotechnology* **12**(5), 488.

[224] Ruschak, A. M. and Miranker, A. D. [2007], 'Fiber-dependent amyloid formation as catalysis of an existing reaction pathway.', *Proceedings of the National Academy of Sciences of the United States of America* **104**(30), 12341–6.

[225] Saar, K. L., Müller, T., Charmet, J., Challa, P. K. and Knowles, T. P. [2018], 'Enhancing the resolution of micro free flow electrophoresis through spatially controlled sample injection', *Analytical Chemistry* **90**(15), 8998–9005.

[226] Saar, K. L., Peter, Q., Müller, T., Challa, P. K., Herling, T. W. and Knowles, T. P. [2019], 'Rapid two-dimensional characterisation of proteins in solution', *Microsystems & Nanoengineering* **5**(1), 1–10.

[227] Saar, K.-L., Yates, E. V., Müller, T., Saunier, S., Dobson, C. M. and Knowles, T. P. [2016], 'Automated ex situ assays of amyloid formation on a microfluidic platform', *Biophysical Journal* **110**(3), 555 – 560.

[228] Saar, K. L., Zhang, Y., Müller, T., Kumar, C. P., Devenish, S., Lynn, A., Łapińska, U., Yang, X., Linse, S. and Knowles, T. P. [2018], 'On-chip label-free protein analysis with downstream electrodes for direct removal of electrolysis products', *Lab on a Chip* **18**(1), 162–170.

[229] Sackmann, E. K., Fulton, A. L. and Beebe, D. J. [2014], 'The present and future role of microfluidics in biomedical research', *Nature* **507**(7491), 181–189.

[230] Salgin, S., Salgin, U. and Bahadir, S. [2012], 'Zeta potentials and isoelectric points of biomolecules: the effects of ion types and ionic strengths', *International Journal of Electrochemical Science* **7**(12), 12404–12414.

[231] Sap, A., De Zitter, E., Van Meervelt, L. and Parac-Vogt, T. N. [2015], 'Structural characterization of the complex between hen egg-white lysozyme and zriv-substituted keggin polyoxometalate as artificial protease', *Chemistry – A European Journal* **21**(33), 11692–11695.

[232] Scarano, S., Mascini, M., Turner, A. P. and Minunni, M. [2010], 'Surface plasmon resonance imaging for affinity-based biosensors', *Biosensors and Bioelectronics* **25**(5), 957–966.

[233] Scheibel, T. and Serpell, L. C. [2008], 'Structural analysis of fibrous proteins', *Protein Science Encyclopedia: online* pp. 197–253.

[234] Scheidt, T., Kartanas, T., Peter, Q., Schneider, M. M., Saar, K. L., Müller, T., Challa, P. K., Levin, A., Devenish, S. and Knowles, T. P. [2020], 'Multidimensional protein characterisation using microfluidic post-column analysis', *Lab on a Chip* **20**(15), 2663–2673.

[235] Schmidt, C. and Robinson, C. V. [2014], 'Dynamic protein ligand interactions–insights from ms', *The FEBS journal* **281**(8), 1950–1964.

[236] Schoch, R. B., Han, J. and Renaud, P. [2008], 'Transport phenomena in nanofluidics', *Reviews of Modern Physics* **80**(3), 839.

[237] Schulze, P. and Belder, D. [2009], 'Label-free fluorescence detection in capillary and microchip electrophoresis', *Analytical and Bioanalytical Chemistry* **393**(2), 515–525.

[238] Schulze, P., Ludwig, M. and Belder, D. [2008], 'Impact of laser excitation intensity on deep UV fluorescence detection in microchip electrophoresis', *Electrophoresis* **29**(24), 4894–4899.

[239] Schwaber, J. and Cohen, E. P. [1973], 'Human× mouse somatic cell hybrid clone secreting immunoglobulins of both parental types', *Nature* **244**(5416), 444–447.

[240] Sear, R. P. [2019], 'Diffusiophoresis in cells: A general nonequilibrium, nonmotor mechanism for the metabolism-dependent transport of particles in cells', *Physical Review Letters* **122**(12), 128101.

[241] Sengupta, P., Garai, K., Balaji, J., Periasamy, N. and Maiti, S. [2003], 'Measuring size distribution in highly heterogeneous systems with fluorescence correlation spectroscopy', *Biophysical Journal* **84**(3), 1977–1984.

[242] Shalongo, W., Heid, P. and Stellwagen, E. [1993], 'Kinetic analysis of the hydrodynamic transition accompanying protein folding using size exclusion chromatography. 1. denaturant dependent baseline changes.', *Biopolymers* **33**(1), 127–34.

[243] Shin, S., Ault, J. T., Feng, J., Warren, P. B. and Stone, H. A. [2017], 'Low-cost zeta potentiometry using solute gradients', *Advanced Materials* .

[244] Shin, S., Ault, J. T., Warren, P. B. and Stone, H. A. [2017], 'Accumulation of colloidal particles in flow junctions induced by fluid flow and diffusiophoresis', *Physical Review X* **7**(4), 041038.

[245] Shin, S., Um, E., Sabass, B., Ault, J. T., Rahimi, M., Warren, P. B. and Stone, H. A. [2016], 'Size-dependent control of colloid transport via solute gradients in dead-end channels', *Proceedings of the National Academy of Sciences* **113**(2), 257–261.

[246] Siria, A., Bocquet, M.-L. and Bocquet, L. [2017], 'New avenues for the large-scale harvesting of blue energy', *Nature Reviews Chemistry* **1**(11), 1–10.

[247] Sluszny, C., He, Y. and Yeung, E. S. [2005], 'Light-emitting diode-induced fluorescence detection of native proteins in capillary electrophoresis.', *Electrophoresis* **26**(21), 4197–203.

[248] Song, Y., Shimanovich, U., Michaels, T. C. T., Ma, Q., Li, J., Knowles, T. P. J. and Shum, H. C. [2016], 'Fabrication of fibrillosomes from droplets stabilized by protein nanofibrils at all-aqueous interfaces', *Nature Communications* **7**, 12934 EP –.

[249] Sparreboom, W., van den Berg, A. and Eijkel, J. C. T. [2010], 'Transport in nanofluidic systems: a review of theory and applications', *New Journal of Physics* **12**(1), 015004.

[250] Spiga, M. and Morino, G. [1994], 'A symmetric solution for velocity profile in laminar flow through rectangular ducts', *International Communications in Heat and Mass Transfer* **21**(4), 469–475.

[251] Spindler, S., Ehrig, J., König, K., Nowak, T., Piliarik, M., Stein, H. E., Taylor, R. W., Garanger, E., Lecommandoux, S., Alves, I. D. and Sandoghdar, V. [2016], 'Visualization of lipids and proteins at high spatial and temporal resolution via interferometric scattering (iscat) microscopy', *Journal of Physics D: Applied Physics* **49**(27), 274002.

[252] Stocker, T. [2011], *Introduction to climate modelling*, Springer Science & Business Media.

[253] Streed, E. W., Jechow, A., Norton, B. G. and Kielpinski, D. [2012], 'Absorption imaging of a single atom', *Nature Communications* **3**(1), 1–5.

[254] Thiel, M., Rill, M. S., von Freymann, G. and Wegener, M. [2009], 'Three-dimensional bi-chiral photonic crystals', *Advanced Materials* **21**(46), 4680–4682.

[255] Timperman, A. T., Oldenburg, K. E. and Sweedler, J. V. [1995], 'Native fluorescence detection and spectral differentiation of peptides containing tryptophan and tyrosine in capillary electrophoresis', *Analytical Chemistry* **67**(19), 3421–3426.

[256] Toseland, C. P. [2013], 'Fluorescent labeling and modification of proteins', *Journal of Chemical Biology* **6**(3), 85–95.

[257] Toyama, B. H. and Weissman, J. S. [2011], 'Amyloid Structure: Conformational Diversity and Consequences', *Annual Review of Biochemistry* **80**(1), 557–585.

[258] Tripathi, A., Bozkurt, O. and Chauhan, A. [2005], 'Dispersion in microchannels with temporal temperature variations', *Physics of Fluids* **17**(10), 103607–103607.

[259] Ugaz, V. M. and Christensen, J. L. [2007], Electrophoresis in microfluidic systems, *in* 'Microfluidic Technologies for Miniaturized Analysis Systems', Springer, pp. 393–438.

[260] Ui, N. [1972], 'Electrophoretic mobility and isoelectric point of hog thyroglobulin', *Biochimica et Biophysica Acta (BBA)-Protein Structure* **257**(2), 350–364.

[261] Vanderpoorten, O., Peter, Q., Challa, P. K., Keyser, U. F., Baumberg, J., Kaminski, C. F. and Knowles, T. P. [2019], 'Scalable integration of nano-, and microfluidics with hybrid two-photon lithography', *Microsystems & Nanoengineering* **5**(1), 1–9.

[262] Velegol, D., Garg, A., Guha, R., Kar, A. and Kumar, M. [2016], 'Origins of concentration gradients for diffusiophoresis', *Soft Matter* **12**(21), 4686–4703.

[263] Vendruscolo, M., Zurdo, J., MacPhee, C. E. and Dobson, C. M. [2003], 'Protein folding and misfolding: a paradigm of self–assembly and regulation in complex biological systems', *Philosophical Transactions of the Royal Society of London. Series A: Mathematical, Physical and Engineering Sciences* **361**(1807), 1205–1222.

[264] Venturoli, D. and Rippe, B. [2005], 'Ficoll and dextran vs. globular proteins as probes for testing glomerular permselectivity: effects of molecular size, shape, charge, and deformability.', *American journal of physiology. Renal physiology* **288**(4), F605–13.

[265] Vigolo, D., Buzzaccaro, S. and Piazza, R. [2010], 'Thermophoresis and thermoelectricity in surfactant solutions', *Langmuir* **26**(11), 7792–7801.

[266] Vigolo, D., Rusconi, R., Stone, H. A. and Piazza, R. [2010], 'Thermophoresis: microfluidics characterization and separation', *Soft Matter* **6**(15), 3489–3493.

[267] Voller, A., Bidwell, D. et al. [1980], *The enzyme linked immunosorbent assay (ELISA). Vol. 2. A review of recent developments with abstracts of microplate applications.*, MicroSystems Ltd, Summerfield House, Vale, Guernsey, Channel Islands.

[268] Wales, D. J. and Doye, J. P. [1997], 'Global optimization by basin-hopping and the lowest energy structures of lennard-jones clusters containing up to 110 atoms', *The Journal of Physical Chemistry A* **101**(28), 5111–5116.

[269] Walsh, D. M., Thulin, E., Minogue, A. M., Gustavsson, N., Pang, E., Teplow, D. B. and Linse, S. [2009], 'A facile method for expression and purification of the Alzheimer's disease-associated amyloid β-peptide', *FEBS Journal* **276**(5), 1266–1281.

[270] Walsh, G. [2018], 'Biopharmaceutical benchmarks 2018', *Nature Biotechnology* **36**(12), 1136–1145.

[271] Westermark, G. T. and Westermark, P. [2010], 'Prion-like aggregates: Infectious agents in human disease', *Trends in Molecular Medicine* **16**(11), 501–507.

[272] Whitesides, G. M. [2006], 'The origins and the future of microfluidics', *Nature* **442**(7101), 368–373.

[273] Wienken, C. J., Baaske, P., Rothbauer, U., Braun, D. and Duhr, S. [2010], 'Protein-binding assays in biological liquids using microscale thermophoresis', *Nature Communications* **1**, 100.

[274] Wittig, I., Braun, H.-P. and Schägger, H. [2006], 'Blue native page', *Nature Protocols* **1**(1), 418.

[275] Wollhofen, R., Katzmann, J., Hrelescu, C., Jacak, J. and Klar, T. A. [2013], '120 nm resolution and 55 nm structure size in sted-lithography', *Optics Express* **21**(9), 10831–10840.

[276] Wu, D., Qin, J. and Lin, B. [2008], 'Electrophoretic separations on microfluidic chips', *Journal of Chromatography A* **1184**(1), 542–559.

[277] Xia, Y. and Whitesides, G. M. [1998], 'Soft lithography', *Annual Review of Materials Science* **28**(1), 153–184.

[278] Yates, E. V., Müller, T., Rajah, L., De Genst, E. J., Arosio, P., Linse, S., Vendruscolo, M., Dobson, C. M. and Knowles, T. P. J. [2015], 'Latent analysis of unmodified biomolecules and their complexes in solution with attomole detection sensitivity', *Nature Chemistry* **7**(10), 802–809.

[279] Young, G., Hundt, N., Cole, D., Fineberg, A., Andrecka, J., Tyler, A., Olerinyova, A., Ansari, A., Marklund, E. G., Collier, M. P. et al. [2018], 'Quantitative mass imaging of single biological macromolecules', *Science* **360**(6387), 423–427.

[280] Young, G. and Kukura, P. [2019], 'Interferometric scattering microscopy', *Annual Review of Physical Chemistry* **70**, 301–322.

[281] Yuan-Hui, L. and Gregory, S. [1974], 'Diffusion of ions in sea water and in deep-sea sediments', *Geochimica et Cosmochimica Acta* **38**(5), 703–714.

[282] Yusko, E. C., Johnson, J. M., Majd, S., Prangkio, P., Rollings, R. C., Li, J., Yang, J. and Mayer, M. [2011], 'Controlling protein translocation through nanopores with bio-inspired fluid walls', *Nature Nanotechnology* **6**(4), 253.

[283] Zhang, Y., Buell, A. K., Müller, T., De Genst, E., Benesch, J., Dobson, C. M. and Knowles, T. P. [2016], 'Protein aggregate-ligand binding assays based on microfluidic diffusional separation', *ChemBioChem* **17**(20), 1920–1924.

[284] Zhang, Y., Herling, T. W., Kreida, S., Peter, Q. A., Kartanas, T., Törnroth-Horsefield, S., Linse, S. and Knowles, T. P. [2020], 'A microfluidic strategy for the detection of membrane protein interactions', *Lab on a Chip* **20**(17), 3230–3238.

[285] Zhang, Y., Huang, Z., He, Y. and Miao, X. [2019], 'Enhancing the efficiency of energy harvesting from salt gradient with ion-selective nanochannel', *Nanotechnology* **30**(29), 295402.

[286] Zhang, Y., Yates, E. V., Hong, L., Saar, K. L., Meisl, G., Dobson, C. M. and Knowles, T. P. [2018], 'On-chip measurements of protein unfolding from direct observations of micron-scale diffusion', *Chemical Science* **9**(14), 3503–3507.

[287] Zhu, L., Lee, C. S. and DeVoe, D. L. [2006], 'Integrated microfluidic uv absorbance detector with attomol-level sensitivity for bsa.', *Lab on a chip* **6**(1), 115–20.

[288] Zia, R. N. and Brady, J. F. [2010], 'Single-particle motion in colloids: force-induced diffusion', *Journal of Fluid Mechanics* **658**, 188–210.